Structural flexibility in magnetocaloric RE_5T_4 (RE = rare-earth; T = Si, Ge, Ga) materials: Effect of chemical substitution on structure, bonding and properties

by

Sumohan Misra

A dissertation submitted to the graduate faculty

in partial fulfillment of the requirements for the degree of

DOCTOR OF PHILOSOPHY

Major: Inorganic Chemistry

Program of Study Committee:
Gordon J. Miller, Major Professor
John D. Corbett
Vitalij K. Pecharsky
Scott Chumbley
L. Keith Woo

Iowa State University

Ames, Iowa

2008

Dedicated to Ma and Bapi

ACKNOWLEDGMENTS

This is perhaps the easiest and at the same time the toughest piece of my dissertation that I have to write. It will be easy for me to name all the people that helped to get this done, but will be tough to thank them enough. I will nonetheless try.

My sincere thanks to my advisor, Professor Gordon J. Miller. His knowledge, perceptiveness, encouragement and persistence have helped me in accomplishing this milestone. His excellent guidance, insight and cooperation were extremely instrumental in increasing my knowledge and understanding of solid state chemistry and its applications. His encouragement and support all through this pivotal stage of my life cannot be expressed in words.

I would also like to express my sincere gratitude to Professor John D. Corbett, Professor Vitalij K. Pecharsky, Professor Scott Chumbley, Professor L. Keith Woo and Professor Victor Lin for serving on my thesis committee and for many helpful comments and guidance on my research and my career in chemistry.

Thanks are also due to Professor Karl A. Gschneidner Jr., Dr. Yaroslav Mudryk, Mr. Roger Rink, Professor Thomas A. Lograsso, Dr. Alexandra O. Pecharsky, Dr. Deborah L. Schlagel, Dr. Matt Besser and Dr. Arkady Ellern for helping me at various points of my research work. I would also like to thank Mr. Eric T. Poweleit, Ms. Ann S. Erickson and Professor Ian R. Fischer. I am also thankful to Ms. Maggie Haaland and the staff at the Chemistry Department Graduate Office – Ms. Renee M. Harris, Beverly A. Nutt, Carlene Enderson and Carla J. Holbrook.

I would like to acknowledge the financial support from Office of Basic Energy Sciences of the U. S. Department of Energy and Ames Laboratory.

Special thanks are due to "RG" Iyer for helping me at various stages of my graduate career. I am also thankful to the past and present members of the Miller and Corbett groups in expanding my knowledge and offering help at various stages: Professor Yurij Mozharivskyj, Dr. Bin Li, Dr. Qisheng Lin, Dr. Srinivasa Thimmaiah, Dr. Mi-Kyung Han, Dr. Hyunjin Ko, Dr. Tae-Soo You and Mr. Fei Wang.

I would also like to thank all my friends at both ISU and MSU whose companionship brought a lot of joy and laughter throughout my graduate studies especially Arpita, Pranaam, Ankur, Misha, Chetan, Anindya and the "Friday Night" gang – they deserve a special recognition for making life in both Ames and East Lansing so much more cherished.

Lastly, and most importantly, my family – who have been a strong pillar of support throughout the many years of my education. Their boundless love and affection continue to amaze me – I can never thank you enough.

Finally, my sincere gratitude to all my teachers who shaped my life and showed me this path.

TABLE OF CONTENTS

ABSTRACT

The binary, ternary and multicomponent intermetallic compounds of rare-earth metals (RE) with group 14 elements (*Tt*) at the RE_5Tt_4 stoichiometry have been known for over 30 years, but only in the past decade have these materials become a gold mine for solid-state chemistry, materials science and condensed matter physics. It all started with the discovery of a giant magnetocaloric effect in $Gd_5Si_2Ge_2$, along with other extraordinary magnetic properties, such as a colossal magnetostriction and giant magnetoresistance. The distinctiveness of this series is in the remarkable flexibility of the chemical bonding between well-defined, subnanometer-thick slabs and the resultant magnetic, transport, and thermodynamic properties of these materials. This can be controlled by varying either or both RE and *Tt* elements, including mixed rare-earth elements on the RE sites and different group 14 (or *T* = group 13 or 15) elements occupying the *Tt* sites. In addition to chemical means, the interslab interactions are also tunable by temperature, pressure, and magnetic field. Thus, this system provides a splendid "playground" to investigate the interrelationships among composition, structure, physical properties, and chemical bonding. The work presented in this dissertation involving RE_5T_4 materials has resulted in the successful synthesis, characterization, property measurements, and theoretical analyses of various new intermetallic compounds. The results provide significant insight into the fundamental magnetic and structural behavior of these materials and help us better understand the complex link between a compound's composition, its observed structure, and its properties.

Chapter 1

Introduction and Motivation

1.1. Introduction

One of the primary objectives for solid state chemists is to understand the complex link between a compound's composition, its observed structure and its properties. For such understanding, intermetallic compounds present a rich and diverse resource to study the relationships among chemical compositions, atomic structure, electronic structure, and physical properties. The complexity of this family of compounds is immense and is readily apparent from the *Pearson's Handbook of Intermetallic Phases*. In general, these compounds consist of two or more metallic or metalloid elements and often (though not necessary) the corresponding crystal structures are distinct from those of the component elements. They typically have small heats of formation (ca. −50 to −10 kJ / mol) when compared to salts and polymeric compounds (ca. −500 to −1000 kJ / mol), but for a single phase they frequently show finite ranges in composition, called homogeneity widths.[1] Regarding their structures, these compounds are formed as per the thermodynamic stability of certain types of crystal structures. The various metal constituents are usually ordered in different sublattices, each with its own distinct population of atoms. In this way, elements of differing sizes or electronegativities can combine to give new compounds.

The study of rare-earth intermetallic compounds represents an important part of the more general problem of metallic phases. As is well known, the rare-earths, due to their particular electronic structure, show a regular change of their properties, especially of atomic dimensions and electronegativities. Moreover, some of them exhibit different valence states in compounds with metallic character, which gives rise to interesting structural, electronic and magnetic properties.

Thus, an ideal starting point for this dissertation would be the basic knowledge of the various room temperature crystal structures and the high-temperature phases that exist for pure rare-earth elements.

1.2. Rare-Earth Metals

1.2.1. Crystal Structure, Lattice Constants, Atomic Volumes and Radii

The crystal structures, lattice parameters, atomic volumes, densities and metallic radii for pure rare-earth metals at room temperature (24°C) or below are presented in Table 1.1.

Table 1.1. Crystal structures and related properties of rare-earth metals at 24°C or below.[2]

Rare Earth Metal	Crystal Structure[a]	Lattice Constants (Å)			Atomic Volume (cm^3 / mol)	Density (g / cm^3)	Metallic radius CN = 12 (Å)
		a_0	b_0	c_0			
αLa	*dhcp*	3.7740	−	12.171	22.602	6.146	1.8791
αCe[b]	*fcc*	4.85[c]	−	−	28.5	8.16	1.71
βCe[b]	*dhcp*	3.6810	−	11.847	20.947	6.689	1.8321
γCe	*fcc*	5.1610	−	−	20.696	6.770	1.8247
αPr	*dhcp*	3.6721	−	11.8326	20.803	6.773	1.8279
αNd	*dhcp*	3.6582	−	11.7966	20.583	7.008	1.8214
αPm	*dhcp*	3.65	−	11.65	20.24	7.264	1.811
αSm	*rhomb*[d]	3.6290	−	26.207	20.000	7.520	1.8041
Eu	*bcc*	4.5827	−	−	28.979	5.244	2.0418
αGd	*hcp*	3.6336	−	5.7810	19.903	7.901	1.8013
α'Tb[e]	*ortho*	3.605	6.244	5.706	19.34	8.219	1.784
αTb	*hcp*	3.6055	−	5.6966	19.310	8.230	1.7833
α'Dy[f]	*ortho*	3.595	6.184	5.678	19.00	8.551	1.775
αDy	*hcp*	3.5915	−	5.6501	19.004	8.551	1.7740
Ho	*hcp*	3.5778	−	5.6178	18.752	8.795	1.7661
Er	*hcp*	3.5592	−	5.5850	18.449	9.066	1.7566
Tm	*hcp*	3.5375	−	5.5540	18.124	9.321	1.7462
αYb[g]	*hcp*	3.8799	−	6.3859	25.067	6.903	1.9451
βYb	*fcc*	5.4848	−	−	24.841	6.966	1.9392
Lu	*hcp*	3.5052	−	5.5494	17.779	9.841	1.7349
αSc	*hcp*	3.3088	−	5.2680	15.039	2.989	1.6406
αY	*hcp*	3.6482	−	5.7318	19.893	4.469	1.8012

[a]*dhcp* = double-*c* hexagonal close-packed; *fcc* = face-centered cubic; *bcc* = body-centered cubic; *hcp* = hexagonal close-packed. [b]After Koskenmaki and Gschneidner (1978).

[c]At 77 K (−196°C). [d]Rhomobohedral is the primitive cell. Lattice parameters are for the nonprimitive hexagonal cell. [e]At 220 K (−53°C), after Darnell (1963).

[f]At 86 K (−187°C), after Darnell and Moore (1963). [g]At 23°C.

1.2.2. Phase Transition and Melting Temperatures

Phase transformations and melting points for each rare-earth metals are presented in Table 1.2. All but five of the rare-earth elements exhibit one or more high temperature phase transitions.

Table 1.2. Transition temperatures, phases and melting point of rare-earth metals.[2]

Rare Earth Metal	Transition I ($\alpha-\beta$)[a]		Transition II ($\gamma-\delta$)[a]		Melting Point (°C)
	T (°C)	Phases	T (K)	Phases	
La[b]	310	*dhcp* → *fcc*	865	*fcc* $\overleftarrow{\rightarrow}$ *bcc*	918
Ce[c]	139	*dhcp* → *fcc* ($\beta-\gamma$)	726	*fcc* $\overleftarrow{\rightarrow}$ *bcc* ($\gamma-\delta$)	798
Pr	795	*dhcp* $\overleftarrow{\rightarrow}$ *bcc*	–	–	931
Nd	863	*dhcp* $\overleftarrow{\rightarrow}$ *bcc*	–	–	1021
Pm	890	*dhcp* $\overleftarrow{\rightarrow}$ *bcc*	–	–	1042
Sm[d]	734	*rhomb* → *hcp*	922	*hcp* $\overleftarrow{\rightarrow}$ *bcc*	1074
Eu	–	–	–	–	822
Gd	1235	*hcp* $\overleftarrow{\rightarrow}$ *bcc*	–	–	1313
Tb	1289	*hcp* $\overleftarrow{\rightarrow}$ *bcc*	–	–	1356
Dy	1381	*hcp* $\overleftarrow{\rightarrow}$ *bcc*	–	–	1412
Ho	–	–	–	–	1474
Er	–	–	–	–	1529
Tm	–	–	–	–	1545
Yb[e]	7	*hcp* $\overleftarrow{\rightarrow}$ *fcc*	795	*fcc* $\overleftarrow{\rightarrow}$ *bcc*	819
Lu	–	–	–	–	1663
Sc	1337	*hcp* $\overleftarrow{\rightarrow}$ *bcc*	–	–	1541
Y	1478	*hcp* $\overleftarrow{\rightarrow}$ *bcc*	–	–	1522

[a]For all the transformations listed, unless otherwise noted.

[b]On cooling, *fcc* → *dhcp* ($\beta \rightarrow \alpha$), 260°C.

[c]On cooling, *fcc* → *dhcp* ($\gamma \rightarrow \beta$), −16°C.

[d]On cooling, *hcp* → *rhomb* ($\beta \rightarrow \alpha$), 727°C.;

[e]On cooling, *fcc* → *hcp* ($\beta \rightarrow \alpha$), −13°C.

1.3. Intra Rare-Earth Phase Diagrams

In this dissertation, we have focused some of our studies on mixed rare-earth systems. Thus, it is imperative to include as a part of this introduction, the phase diagrams for the intra rare-earth binary alloys involved in this thesis. Neighboring rare-earth elements are known to exhibit similar chemical and physical properties and this is due to the fact that as the nuclear charge increases with increasing atomic number, the electrons occupy the inner 4*f* levels. This fact has a pertinent effect on the intra rare-earth binary alloys, which means that, if neighboring or near neighboring elements are alloyed, then they behave as ideal alloys at high temperatures. Thus, there is no measurable difference in the liquidus and solidus temperature. Moreover, the liquidus-solidus line between the two end-members is a straight line connecting the respective melting points of the pure metals. This ideal liquid and solid solution behavior only holds if the two components are trivalent and have atomic numbers within ca. ±4 of each other. In contrast, if the atomic numbers of the two rare-earth metals differ by more than ±4 or for binary alloys involving Y or Sc, then a deviation from the above ideal behavior is expected. Some of the phase diagrams important for this study are: (i) La-Gd, (ii) Nd-Er, (iii) Gd-Lu, and, (iv) Gd-Y and hence are discussed below.

1.3.1. Lanthanum-Gadolinium (La-Gd)

An intermediate phase which exists for this alloy system, adopts the same crystal structure as Sm metal. It is known as the "δ phase" and crystallizes as a primitive rhombohedral structure but is generally referred to in terms of its nonprimitive hexagonal axis. The *c*-axis for this nonprimitive hexagonal unit cell is 4.5 times that of the normal hexagonal structure. It exhibits a stacking sequence of ···*ABABCBCAC*·*ABABCBCAC*···, etc. In 1962, Spedding et al.[3] discovered the existence of this Sm-type crystal structure and is typically observed for an alloy system containing a light lanthanide (La, Ce, Pr or Nd) and a heavy lanthanide (Gd-Tm, Lu) or Y. They first proposed a phase diagram for the La-Gd system which indicated that this "δ phase" is formed by a peritectoidal reaction between *α*La and *α*Gd. But later on, based on the work of Lundin[4] and Koch,[5] it was established (Figure 1.1) that this "δ phase" forms congruently from *α*La(*dhcp*)-*α*Gd(*hcp*) solid solution. This

continuous change from *dhcp* to *hcp* can be accounted for through a stacking-fault mechanism.[2]

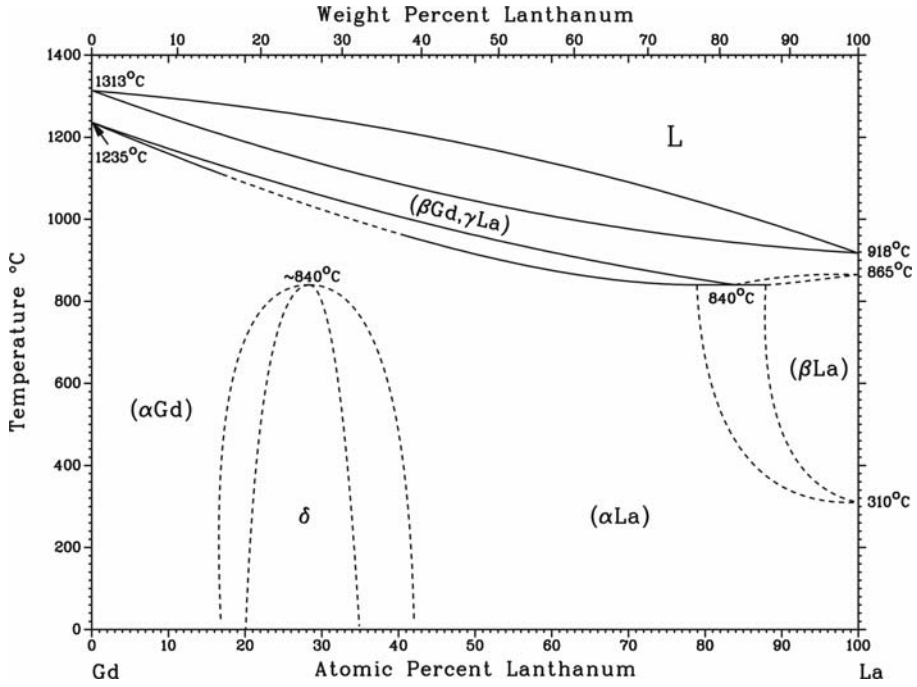

Figure 1.1. Phase Diagram of the lanthanum-gadolinium system.[6]

1.3.2. Neodymium-Erbium (Nd-Er)

In 1972, Kobzenko et al. studied the phase relationships in the neodymium-erbium system using X-ray diffraction, thermal analysis, and metallographic observations.[7] The phase diagram as shown in Figure 1.2 also reveals the existence of the Sm-type "δ phase". Kobzenko et al. also concluded that this structure was formed by a peritectoid reaction during the cooling of two phases based on the solid solutions of αNd (*dhcp*) and Er (*hcp*). But as was the case with La-Gd system, based on the work of Lundin,[4] this phase (see Figure 1.2) is formed by a congruent transformation.

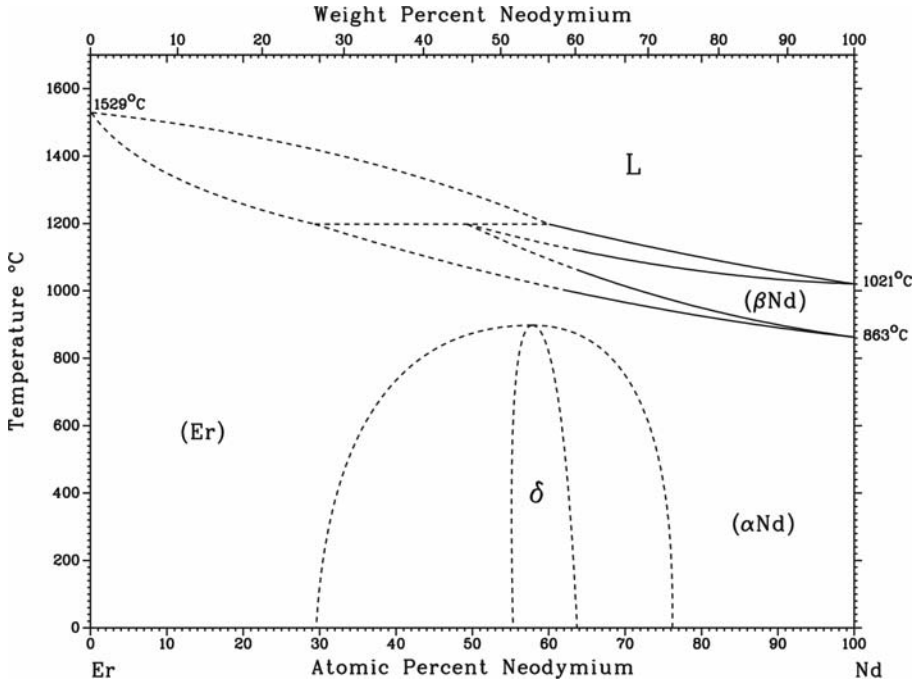

Figure 1.2. Phase Diagram of the neodymium-erbium system.[6]

1.3.3. Gadolinium-Lutetium (Gd-Lu)

In 1962, Smidt et al.[8] studied the phase relationships in the gadolinium-lutetium system. His studies established the presence of a complete solid solubility for the *hcp* phases (αGd and Lu) for this system. Due to the absence of any high temperature *bcc* phase for Lu, the βGd phase was estimated to terminate at ca. 40 at% Lu.[2] The phase diagram is shown in Figure 1.3.

1.3.4. Gadolinium-Yttrium (Gd-Y)

In 1962, Spedding et al.[3] examined the phase relationships in the gadolinium-yttrium system. The phase diagram for this system is shown in Figure 1.4 and reveals that there is complete solid solubility for both the room temperature (hcp) and high temperature (bcc) forms.

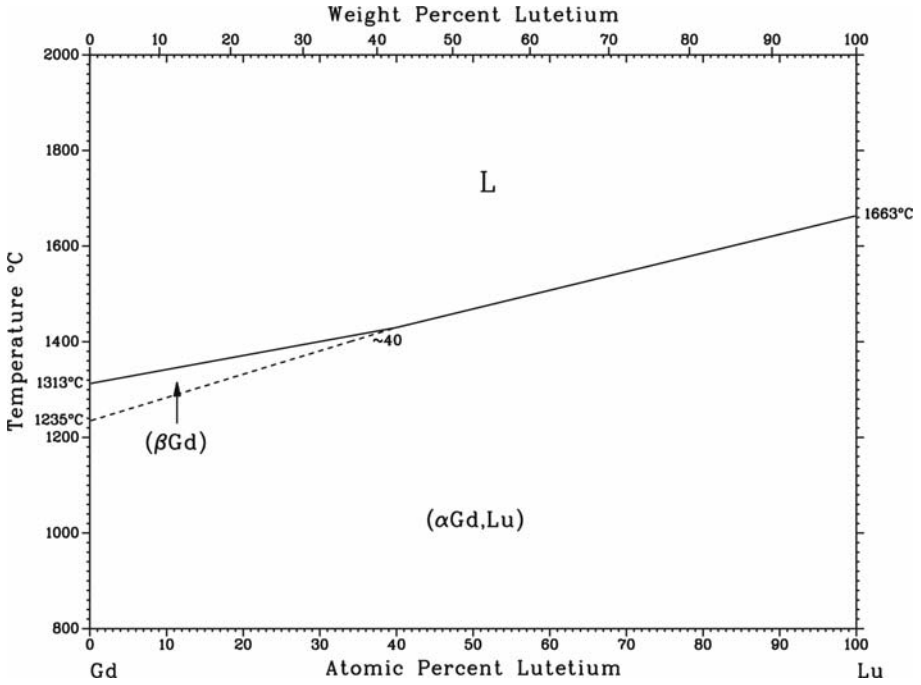

Figure 1.3. Phase Diagram of the gadolinium-lutetium system.[6]

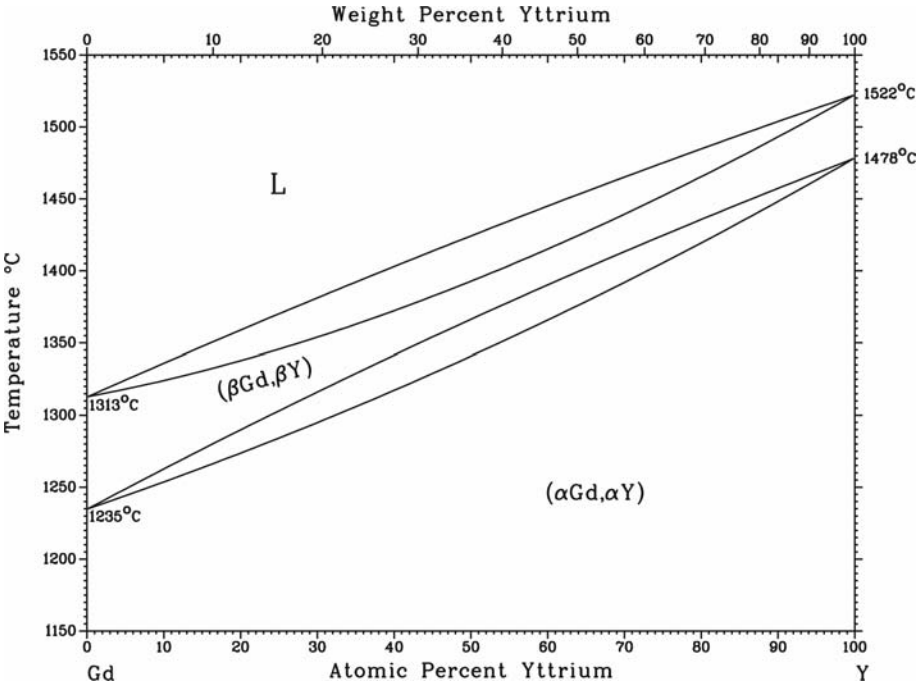

Figure 1.4. Phase Diagram of the gadolinium-yttrium system.[6]

1.4. Motivation to Study RE_5T_4 Materials

Since the last quarter of the 20th century there has been a significant increase in optimism that environmentally friendly, solid-state magnetic refrigeration may be a viable option to replace today's common gas compression/expansion technology. One of the momentous drawbacks for today's technologies, which achieve cooling efficiencies approaching 40% of the Carnot limit,[9] is its use of ozone depleting chemicals (ODCs) like hydrochlorofluorocarbons (HCFCs). Two of the most environmentally benign cooling techniques are thermoelectric and thermomagnetic cooling. The former technique utilizes the Peltier effect to create a heat difference through an applied potential across the ends of two dissimilar conductors. It finds its use in small volumes, as in integrated circuits. However, it achieves relatively low efficiency of 10% of the Carnot limit[10] and does not seem well suited for large scale cooling/refrigeration. On the other hand, magnetic refrigeration, or thermomagnetic cooling, which utilizes the magnetocaloric effect, achieves efficiency of 60% of the Carnot limit and is one of the most ecologically clean cooling techniques over a wide range of temperatures.[11] It can generate much savings in energy consumption and costs as it has the potential to achieve higher efficiencies. One of the attractive classes of materials that exhibit extraordinary magnetic responses and have the potential for applications in magnetic refrigeration is the RE_5T_4 (RE = rare-earth element; T = Si, Ge, Ga, Sn or their various combinations) materials.

1.4.1. Magnetocaloric Effect (MCE)

Magnetic refrigeration materials rely on the use of the magneto-thermodynamic phenomenon known as the **M**agneto**C**aloric **E**ffect (MCE), which is an intrinsic property of any magnetic material. This is characterized by a temperature change when a magnetic material is subjected to an adiabatic change of an external magnetic field on the material.[12] The effect was originally discovered by Warburg in iron in 1851.[13] In the late 1920s Debye[14] and Giauque[15] explained independently the origin of MCE. They also suggested the first practical use of the MCE: to reach lower temperatures than that of liquid helium by *adiabatic demagnetization*.

The physical origin of the MCE is a consequence of the coupling of the magnetic sublattice of a material with the magnetic field, which changes the magnetic part of the entropy of a solid. The effect as illustrated in Figure 1.5 closely resembles processes that occur in a gas in response to changing pressure. The isothermal compression of a gas decreases the positional disorder and, therefore, reduces the corresponding value of the entropy. This is analogous to the isothermal magnetization of a paramagnet (near absolute zero) or a ferromagnet material (near T_C) in which the magnetic part of the total entropy decrease as an external magnetic field is applied. In the reverse process, isothermal demagnetization restores the zero-field magnetic entropy of a system which is similar to isothermal expansion of a gas. The isothermal magnetic entropy change, $\Delta S_m = (T, \Delta H)$, an extensive parameter representing the MCE, can quantify the above transformations in a solid. Now, when a gas undergoes adiabatic expansion (compression), its total entropy remains constant but the velocity of its constituent molecules decrease (increase) thereby decreasing (increasing) its temperature. In the same manner, adiabatically demagnetizing (magnetizing) a material decreases (increases) both its lattice vibrations and temperature. An intensive parameter, the adiabatic temperature change, $\Delta T_{ad} = (S, \Delta H)$, provides a measure of the above transformation and is also used to express the MCE. The above two parameters can be determined either directly by thermometry [measuring $\Delta T_{ad} = (\Delta H)$] or indirectly by heat capacity measurements at different applied magnetic fields, or by different magnetization isotherms at different applied magnetic fields.

a.

b.

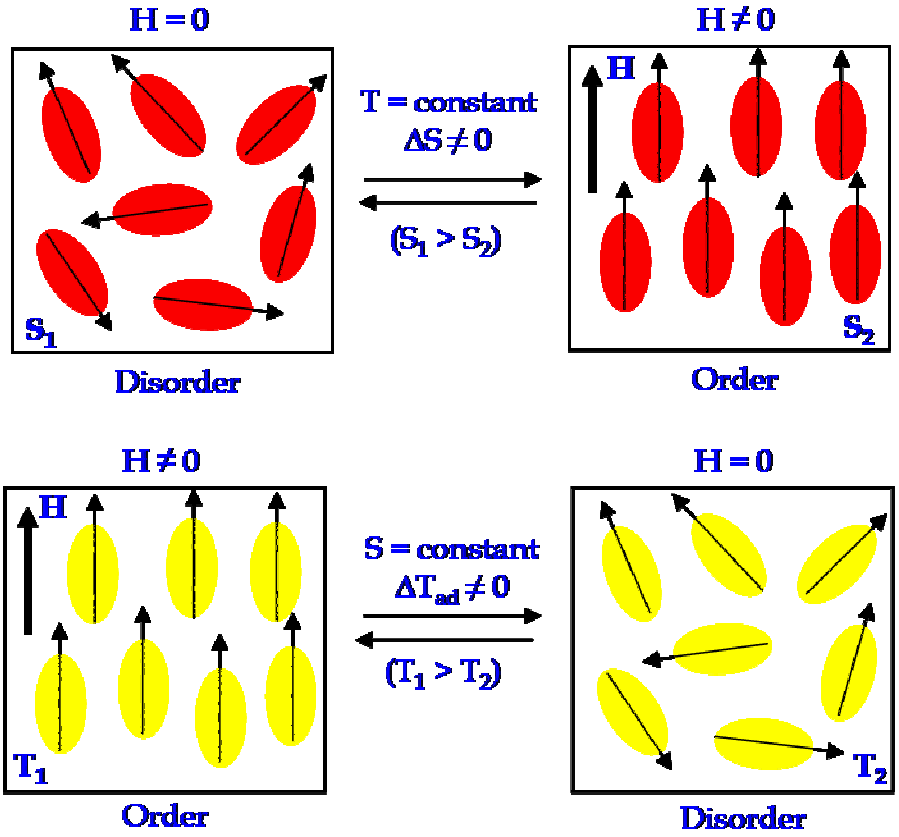

Figure 1.5. A schematic diagram showing two ways to characterize the magnetocaloric effect (MCE): (a) Isothermal entropy change, (b) Adiabatic temperature change.

In 1997 a giant MCE in the ternary compound, $Gd_5Si_2Ge_2$, was discovered by Pecharsky and Gschneidner showing Curie temperatures near room temperature.[16] According to both adiabatic temperature changes and isothermal magnetic entropy changes, $Gd_5Si_2Ge_2$ shows extraordinary behavior compared to elemental Gd. This discovery in the $Gd_5(Si_xGe_{1-x})_4$ system triggered a strong interest in the rare earth-tetrelide systems at 5:4 stoichiometry. From the perspective of a solid-state chemist the RE_5T_4 systems are a splendid "playground" to investigate structure-bonding-property relationships thereby providing significant insight into the fundamental magnetic and structural behavior of these systems which is important in understanding the higher values of MCE obtained in some of these systems. Since this discovery, the MCE has been studied for a number of different ferromagnetic phases showing Curie temperatures near room temperature.[17-19] A list of

materials with important MCE characteristics has been tabulated in Table 1.3. In all cases some form of structural change occurs in addition to ferromagnetic-paramagnetic transition.

Table 1.3. Summary of important MCE characteristics for several magnetic refrigeration materials with near room temperature T_C.[1]

Compound	T_C (K)	ΔT_{ad} (K); (ΔH = 2T)	$-\Delta S_m$ (J / mol K); (ΔH = 2T)
$Gd_5Si_2Ge_2$	276	7.2	15.8
$La(Fe_{0.89}Si_{0.11})_{13}H_{1.3}$	291	7.0	19.8
Gd	294	5.8	0.8
$MnFeP_{0.45}As_{0.55}$	302	3.0	2.5
$Fe_{0.49}Rh_{0.51}$	316	8.4	1.8
MnAs	318	4.9	4.2
$Ni_{54.8}Mn_{20.2}Ga_{25}$	351	1.0	0.9

1.4.2. The $Gd_5(Si_xGe_{1-x})_4$ System

This series was first reported by Holtzberg and coworkers at IBM in the late 1960s.[20] This family of intermetallic compounds shows interesting variations in crystal lattices and magnetic properties with changes in composition. The crystal structures of $Gd_5(Si_xGe_{1-x})_4$ and many other RE_5T_4 materials are built from slabs of two eclipsed 3^2434 nets of RE atoms. The arrangements of the atoms in the slabs and, in turn, the structural and magnetic properties depend on the presence and absence of interslab main group-main group chemical bonds. Three room temperature crystal structures exist for the $Gd_5(Si_xGe_{1-x})_4$ series. The Si-rich compounds ($x \geq 0.56$) adopt the orthorhombic, Gd_5Si_4-type [O(I)] crystal structure[21] and features interslab Si(Ge)-Si(Ge) bonds (distances ca. 2.4-2.6 Å); the Ge-rich compounds ($x \leq 0.3$) adopt the orthorhombic, Sm_5Ge_4-type [O(II)][20] and is characterized by the absence of any interslab Si(Ge)-Si(Ge) bonds (distances exceeds 3.4 Å). The materials in the intermediate composition range ($0.40 \leq x \leq 0.503$) crystallize in the monoclinic $Gd_5Si_2Ge_2$-

type (M) crystal structure[22] and has one pair of slabs connected by Si(Ge)–Si(Ge) bonds; however, the other pair do not show interslab Si(Ge) –Si(Ge) bonds.

Transformations between different crystal structures can be controlled by changing chemical composition, temperature, magnetic field, pressure and also by altering the valence electron concentration.[23-25] In order to explore the dependence of crystal structures on the Si/Ge ratio and also to probe the effect of chemical substitution on the structure, bonding and properties of these materials along with other RE_5T_4 materials, we have focused on these following projects. A short synopsis of each is given below.

1.5. Dissertation Organization

This dissertation has been organized in a format composed of original published papers or in a potentially publishable form. References cited within each chapter have been placed immediately after the chapter.

Chapter 2 covers the general experimental techniques used in this dissertation. It contains relevant information regarding the various equipments used along with an overview of the different analytical procedures used for characterizing the structures and properties.

Chapter 3 is an article titled "$Gd_{5-x}Y_xTt_4$ (*Tt* = Si or Ge): Effect of Metal Substitution on Structure, Bonding and Magnetism", published in the *Journal of the American Chemical Society*. It contains the results of X-ray diffraction, magnetic susceptibility and theoretical calculations on two new series of rare-earth tetrelides, $Gd_{5-x}Y_xTt_4$ (*Tt* = Si, Ge), which are related to magnetic refrigeration materials.

Chapter 4 is an article titled "On the Crystal Structure, Metal Atom Site Preferences and Magnetic Properties of $Nd_{5-x}Er_xTt_4$ (*Tt* = Si or Ge)" and is submitted for review in *Zeitschrift für Anorganische und Allegemeine Chemie*. It contains a crystallographic study of the Nd/Er site preferences in the $Nd_{5-x}Er_xTt_4$ (*Tt* = Si, Ge) series.

Chapter 5 is a paper titled "On the Distribution of Tetrelide Atoms (Si, Ge) in $Gd_5(Si_xGe_{1-x})_4$", published in the *Journal of Solid State Chemistry*. It presents a crystallographic study of the Si/Ge site preferences in the Si-rich regime of $Gd_5(Si_xGe_{1-x})_4$ and a crystal chemical analysis of these site preferences for the entire range.

Chapter 6 is a manuscript titled "Structural, Magnetic, and Thermal Characteristics of the Phase Transitions in $Gd_5Ga_xGe_{4-x}$ Magnetocaloric Materials", and is presented in a publishable format. It presents the temperature-dependent, single crystal and powder X-ray diffraction studies along with magnetization and heat capacity measurements on two phases of the $Gd_5Ga_xGe_{4-x}$ system.

Chapter 7 presents the conclusions that could be drawn from these studies and suggestions for future work.

1.6. References

(1) Gourdon, O.; Gout, D.; Miller, G. J., *Encyclopedia of Condensed Matter Physics, Elsevier, Amsterdam*, **2005**, 409.

(2) Gschneidner, K. A. Jr.; Calderwood, F. W., *Handbook on the Physics and Chemistry of Rare Earths*; Gschneidner, K. A. Jr.; Eyring, L., Elsevier Science Publishers B. V., Amsterdam, **1986**, *Vol. 8*. 1.

(3) Spedding, F. H.; Valletta, R. M.; Daane, A. H., *Trans. Quaterly (Am. Soc. Met.)* **1962**, *55*, 483.

(4) Lundin, C. E.; *Final Report, Denver Research Institute Rept. Ad-633558, Denver University, Denver, Co*, **1966**.

(5) Koch, C. C.; Mardon, P. G.; McHargue, C. J., *Metall. Trans*. **1971**, *2*, 1095.

(6) ASM Database

(7) Kobzenko, G. F.; Martynschuk, E. L.; Moiseeva, I. V., *Dopov. Akad. Nauk Ukr. RSR*, **1972**, *Ser. A*, 374.

(8) Smidt, F. A. Jr., *Ph.D. Thesis*, Iowa State University, Ames, IA, USA., **1962**.

(9) Miller, G. J., *Chem. Soc. Rev*. **2006**, *35*,799.

(10) Nolas, G. S.; Sharp, J.; Goldsmid, H. J., *Thermoelectrics: Basic Principles and New Materials Development*, Springer, Berlin, **2001**.

(11) Gschneidner, K. A. Jr.; Pecharsky, V. K.; Pecharsky, A. O.; Ivtchenko, V. V.; Levin, E. M., *J. Alloys Compd*. **2000**, *303-314*, 214.

(12) Pecharsky, V. K.; Gschneidner, K. A. Jr., *Encyclopedia of Condensed Matter Physics, Elsevier, Amsterdam*, **2005**, 236.

(13) Warburg, E., *Ann. Phys*. **1881**, *13*, 141.

(14) Debye, P., *Ann. Phys*. **1926**, *81*, 1154.

(15) Giauque, W. F., *J. Am. Chem. Soc*. **1927**, *49*, 1864.

(16) Pecharsky, V. K.; Gschneidner, K. A. Jr., *Phys. Rev. Lett*. **1997**, *78*, 4494.

(17) Gschneidner, K. A. Jr.; Pecharsky, V. K., *Ann. Rev. Mater. Sci*. **2000**, *30*, 387.

(18) Gschneidner, K. A. Jr.; Pecharsky, V. K., *Rep. Prog. Phys.* **2005**, *68*, 1479.

(19) Tegus, O.; Brück, E.; Zhang, L.; Dagula, Buschow, K . H. J.; de Boer, F. R., *Physica B* **2002**, *319*, 174.

(20) Holtzberg, F.; Gambino, R. J.; McGuire, T. R., *J. Phys. Chem. Solids* **1967**, *28*, 2283.

(21) Smith, G. S.; Johnson, Q.; Tharp, A. G., *Acta Crystallogr.* **1967**, *22*, 269.

(22) Pecharsky, V. K.; Gschneidner, K. A. Jr., *J. Alloys Compd*. **1997**, *260*, 98.

(23) Morellon, L.; Algarabel, P. A.; Ibara, M. R.; Blasco, J.; Garcia-Landa, B., *Phys. Rev. B* **1998**, *58*, R14721.

(24) Choe, W.; Pecharsky, V. K.; Pecharsky, A. O.; Gschneidner, K. A. Jr.; Young, V. G. Jr.; Miller, G. J., *Phys. Rev. Lett.* **2000**, *84*, 4617.

(25) Mozharivskyj, Y.; Choe, W.; Pecharsky, A. O.; Miller, G. J., *J. Am. Chem. Soc.* **2003**, *125*, 15183.

Chapter 2

Details of Synthesis, Characterization and Theoretical Calculations

2.1. Synthesis

2.1.1. Starting Materials

All starting materials were obtained from commercial sources. Table 2.1 lists their sources and some physical properties. The elements were used as received.

Table 2.1. Starting materials used in the syntheses.

Element	Purity (wt. %)	Source	Melting point (K)	Boiling point (K)
Nd	99.9	MPC, Ames Lab	1294	3347
Gd	99.9	MPC, Ames Lab	1586	3545
Tb	99.9	MPC, Ames Lab	1629	3500
Dy	99.9	MPC, Ames Lab	1685	2840
Ho	99.9	MPC, Ames Lab	1747	2968
Er	99.9	MPC, Ames Lab	1802	3140
Yb	99.9	MPC, Ames Lab	1092	1469
Zn	99.99	Fischer Scientific	692.73	1180
Ga	99.99	Aldrich	302.92	2478
Si	99.999	Alfa Aesar	2630	1683
Ge	99.999	Alfa Aesar	1211.5	3107
Sn	99.999	Aldrich	505.12	2876
Sb	99.99	Meldform Metals	903.91	1860

2.1.2. Reaction Containers

The highly reactive nature of the studied materials with silica at high temperature required the use of tantalum as a container material for reactions and heat-treatment processes. Prior to use, ⅜" Ta tubing was cut to size, usually to 1½"-long pieces, and were cleaned with an acidic mixture containing 55% concentrated sulfuric, 25% concentrated nitric and 20% concentrated hydrofluoric acid by volume. After thorough rinsing with deionized water and drying in oven, each tube was crimped at one end and was sealed under an argon atmosphere in an arc welder.[1] The reactants (or as-cast samples) were then loaded into the prepared tantalum tubes, either inside a dry-box or outside in air depending on the stability of the starting materials (or as-cast samples). The tubes were crimped shut and were sealed by arc welding as previously described, only if they were prepared inside the dry-box. The tubes were further sealed inside an evacuated silica jacket using a natural gas-oxygen mixture fueled torch. The silica jacket is used to protect the tantalum tubing from oxidation and breakdown at high temperatures. Before sealing, the silica jacket was heated with a natural gas torch to remove any moisture from the walls of the container.

Only reactions that were prepared using the induction furnace and as-cast materials that were heat-treated using a high-temperature furnace required the use of tantalum containers.

2.1.3. Synthetic Equipment

Two types of synthetic equipment were used for chemical reaction of the starting materials: an arc-melter and an induction furnace. High-temperature furnaces were used for heat-treatment of the as-cast materials.

2.1.3.1. Arc-melter. A majority of the intermetallic materials investigated in this thesis were prepared in an arc-melter. A Miller Maxstar 91 arc-melter, connected to the glovebox through a port was used to melt stoichiometric mixtures of the high purity elements on a water-cooled copper hearth. The arc-melter was loaded with the copper hearth and then evacuated and re-filled with argon three times before use. Under a flowing argon atmosphere, a zirconium getter was first melted and then the sample materials were arc-melted using a tungsten electrode, for approximately 20-30 seconds at 35-40 A. The resulting sample button

was remelted six times and turned over after each melting to ensure homogeneity. After cooling, the reactions were then moved back to the dry box.

2.1.3.2. Induction Furnace. Reactions involving elements with high vapor pressure were carried out using a high frequency induction furnace under a dynamic vacuum in the temperature range 1000°-1800°C with a holding time of 10-30 minutes. Prior to induction melting, stoichiometric mixtures of pure components were loaded into tantalum tubes and then the tubes were sealed under argon pressure by arc welding. The tubes were then set upright into a tantalum crucible positioned at the center of the induction furnace. The furnace was then evacuated using a combination of Welch Duoseal vacuum pump and a diffusion pump. A thermocouple was set close to the sample tube to monitor the temperature. The above procedure was repeated one more time with the sample tube turned upside down to ensure homogeneity.

2.1.3.3. High-temperature Furnace. To improve the overall crystallinity of the samples and also to investigate order-disorder in certain structures, the samples prepared using the arc-melter and the induction furnace were heat-treated in typical high-temperature furnaces equipped with programmable temperature controllers. The isotherm temperature and the length of the reaction time varied depending on requirements for different samples. Existing phase diagrams were used as a guide in determining the heat-treatment conditions.

2.2. Phase Analyses and Data Processing

2.2.1. Powder X-ray Diffraction

2.2.1.1. Room Temperature Powder X-ray Diffraction. Powder X-ray diffraction was employed as the first step to characterize the products. Powder patterns were obtained with an Enraf-Nonius Guinier camera using monochromatized Cu K_α radiation (λ = 1.54187 Å) at ambient (ca. 298 ± 1K) temperatures. The samples were ground in an agate mortar and pestle, and were then homogeneously dispersed over a Mylar film coated with a thin layer of petroleum jelly. All the diffractograms were recorded between $5° \leq 2\theta \leq 100°$ with a step size set at 0.005° and the exposure time for the samples were in the range between 30-120 minutes. The homogeneity and purity of all phases were identified by comparison of sample

powder patterns to those calculated from single-crystal data using the *POWDER CELL* software.[2]

2.2.1.2. Variable Temperature Powder X-ray Diffraction. Powder X-ray diffraction patterns in the temperature range 4-700 K were collected on a Rigaku TTRAX rotating anode diffractometer using monochromatized Mo K_α radiation (λ= 0.71075 Å) and equipped with either a sample heater in an evacuated chamber or a helium-flow cryostat. The scattered intensity was measured as a function of Bragg angle with a scintillation detector, in a step scan mode for 2θ ranging from 9° to 60° and a stepsize of 0.01° with the intensity measured for 2 second for each point. The sample temperature during low- and high-temperature diffraction experiments was stable within ±1K with respect to the value set for an experiment. All diffraction patterns collected at various temperatures were analyzed by a full-profile Rietveld refinement using *LHPM RIETICA* software.[3]

The samples for low temperature powder diffraction studies were prepared in the following manner: a fine powder of the samples with particle size less than 25 μm were obtained by grinding the ingot with an agate mortar and pestle and passing through a stainless steel sieve. The grounded powder was then mounted on a copper sample holder, mixed with a diluted GE varnish, air dried, and baked at 120°C for 1 hour to solidify the specimen, after which a flat surface was created by using a 280-grit sandpaper, thus minimizing preferred orientation near the surface and reducing surface roughness.

The samples for high temperature powder diffraction studies were prepared in a similar manner as above, without the use of GE varnish. The grounded powder was mounted on a copper sample holder and the sample was smoothed using a stainless steel razor blade.

2.2.2. Single Crystal X-ray Diffraction

Single crystal X-ray diffraction was used for the characterization of unknown structures and confirmation of structural aspects for known structures, aspects which include interatomic distances and atomic distributions.

2.2.2.1. Room-Temperature Single Crystal X-ray Diffraction Studies. Single crystals suitable for structure determination were selected from a crushed glittering product and were then mounted on the tips of glass fibers, which were then fixed onto 0.9 mm brass tubes

using wax. The diffraction intensities of crystals were collected on a Bruker Smart Apex CCD diffractometer with monochromatized Mo K_α radiation (λ = 0.71073 Å). Data were collected over a full sphere of reciprocal space by taking three sets of 606 frames with 0.3° scans in ω and an exposure time of 10 seconds per frame. The range of 2θ extended from 4° to 57°. The *SMART*[4] software was used for data acquisition. Intensities were extracted and then corrected for Lorentz and polarization effects by the *SAINT*[4] program. Empirical absorption corrections were accomplished with program *SADABS*,[4] which is based on modeling a transmission surface by spherical harmonics employing equivalent reflections with $I/\sigma > 3$. Structure solutions and refinements by full-matrix least squares fits on F^2 were performed with the *SHELXTL*[4] package of crystallographic programs. The refinement was based on F_0 using reflections with $I > 2(I)\sigma$. Program *XPREP*[4] was used for unit cell reductions and determinations of possible space groups according to the systematic absences and the internal R-values of the data based on appropriate equivalent reflections. Initial structural models were derived from direct methods calculations using *SHELXS*[4] or from the positional parameters of an isostructural compound. Full matrix least squares refinement of the crystal structures were employed using program *SHELXL*.[4,5] Atomic distances, angles and structural figures were obtained by using *DIAMOND*[6] and *ATOMS*[7] software.

2.2.2.2. Variable Temperature Single Crystal X-ray Diffraction. Variable temperature X-ray diffraction data in the temperature range 80-700 K were collected on a Bruker Smart Apex CCD diffractometer equipped with either a Nonius crystal heater (argon was used as the flow gas) or with an Oxford Cryosystems cooler using liquid nitrogen. During the high- and low-temperature diffraction experiments, the temperature was stable within ±1K with respect to the value set for an experiment.

For high-temperature data collection, a special crystal mounting procedure was used, which was developed in our research group, to prevent crystal decomposition at high temperature.[8] Neither glue nor cement was used to mount the crystals. Instead, first a suitable single crystal, for which a prior room temperature data set was collected, is placed at the bottom of a 0.2 mm capillary and is then fixed in place by a 0.1 mm capillary (all capillaries had wall thicknesses of 0.01 mm, glass # 50, Hampton Research). Freshly prepared Gd filings, acting as a getter, were put on the top of the inner 0.1 mm capillary and fixed by

another 0.1 mm capillary (Figure 2.1). The whole arrangement was evacuated while it was taken inside a drybox, where it was sealed with Apiezon-N grease. Then it was taken out of the drybox and the outer 0.2 mm capillary was flame-sealed using a microtorch and then mounted in 0.9 mm brass tubes using temperature resistant cement. Prior to a high temperature data collection, the center section (position of Gd filings) was heated to ca. 350°C for 3 seconds to absorb any remaining adventitious nitrogen and oxygen because crystal mounting was performed in air.

Figure 2.1. Mounting of a single crystal for high-temperature data collection

For low-temperature data collections, no special crystal mounting procedure was used. They were mounted in the same manner as the crystals on which room-temperature data were collected.

2.3. Physical Properties

2.3.1. Magnetic Susceptibility

Magnetic susceptibility measurements were carried out using a **S**uperconducting **QU**antum **I**nterference **D**evice magnetometer MPMS-XL manufactured by Quantum Design, Inc. on single and polycrystalline samples. The magnetic susceptibility of zero-magnetic-field cooled samples were measured as a function of temperature from 6 to 300 K and isothermal, field dependent magnetization data were collected in dc magnetic fields varying from 0 to 5 T. About 10-15 mg of the sample was used for each measurement.

The molar susceptibilities, χ_{mol}, of the samples were calculated as follows:

$$\chi_{mol} = \frac{M \cdot m_{mol}}{H \cdot m} \text{ cm}^3 \text{ mol}^{-1}$$

where: M = magnetic moment [emu] m = weight of the sample [g]

H = magnetic field [Oe] m_{mol} = Molar weight of the sample [g mol^{-1}]

The molar susceptibility χ_{mol} is fitted to a Curie-Weiss law which is given by:

$$\chi_{mol} = \frac{C}{(T - \Theta_w)}$$

where: C = Curie constant Θ_w = Curie-Weiss temperature

The Curie constant can be written in terms of the effective magnetic moment, μ_{eff}, as:

$$C = \frac{N \cdot \mu_{eff}^2}{3k_B}$$

where: N = no. of ions of magnetic elements k_B = Boltzman constant

Generally, the susceptibility is the sum of different contributions:

$$\chi_{mol} = \chi_{mol}^{para} + \chi_{mol}^{TIP} + \chi_{mol}^{dia}$$

χ_{mol} = molar susceptibility

χ_{mol}^{para} = T-dependent paramagnetic contribution

χ_{mol}^{TIP} = T-independent paramagnetic contribution (Pauli paramagnetism)

χ_{mol}^{dia} = T-dependent diamagnetic contribution

Using the above relation, all data were corrected for T-independent paramagnetic and T-dependent diamagnetic contributions.

2.3.2. Heat Capacity

Heat capacity measurements were carried out using a semiadiabatic heat-pulse calorimeter[9] between ca. 5 and 350 K in dc magnetic fields ranging from 0 to 10 T. During a heat pulse experiment the exact thermodynamic definition of the heat capacity (C_P), given by the following equation:

$$C_P = \left(\frac{\partial H}{\partial T}\right)_P$$

is modified, in practice, to:

$$C_P \cong \left(\frac{\Delta Q}{\Delta T}\right)_P$$

where H = enthalpy; T = absolute temperature; ΔQ = amount of heat introduced into the calorimeter during a heat pulse; ΔT = resulting temperature rise of the calorimeter, P = an index which indicates that the measurements were performed at a constant pressure.

The sample ingot was cut in the form of a rectangular block using a wire-saw. It was then mounted on a clamp-like sample holder, in which the sample is held tightly by a copper screw. A measured amount of a 50:50 (by volume) mixture of Apiezon-N and fine silver powder is placed between the sample and the main holder plate to improve the thermal connection. The whole setup is evacuated by a high speed vacuum pumping system which attains a pressure of 10^{-7} Torr. Conditions very close to adiabatic are maintained inside the vacuum chamber using a set of three concentric copper shields.

2.4. Electronic Structure Calculations

2.4.1. Tight-Binding Linear Muffin-Tin-Orbital Calculations

The electronic structures of many actual and hypothetical compounds were calculated self-consistently by using the tight-binding linear muffin-tin-orbital (TB-LMTO)[10-13] method within the atomic sphere approximation (ASA) using the LMTO version 47 program.[14] Exchange and correlation were treated in a local spin density approximation (LSDA).[15] All relativistic effects except spin-orbit coupling were taken into account using a scalar relativistic approximation.[16]

Within the ASA, space is filled with overlapping Wigner-Seitz (WS) atomic spheres. The radii of these WS spheres were obtained by requiring the overlapping potential to be the best possible approximation to the full potential according to an automatic procedure.[17] The Löwdin downfolding technique[10-13] allows the derivative of few-orbital effective Hamiltonians by keeping only the relevant degrees of freedom and integrating out the irrelevant ones. **k**-space integrations were carried out by the tetrahedron method[18] to determine the self-consistent charge density, density of states (DOS) and crystal orbital Hamiltonian populations (COHP).[19] The corresponding Fermi levels were chosen as an internal reference level in all cases.

2.5. References

(1) Miller, A. E.; Dane, A. H.; Haberman, C. E.; Beaudry, B. J., *Rev. Sci. Inst.* **1963**, *34*, 644.

(2) Kraus, W.; Nolze, G., *PowderCell for Windows*, *Version 2.4*, **2000**.

(3) Hunter, B. A., *International Union of Crystallography Commission on Powder Diffraction Newsletter*. **1998**, *20*, 21.

(4) XRD Single Crystal Software; Bruker Analytical X-ray Systems: Madison, USA, **2002**.

(5) Sheldrick, G. M.; *SHELXL-96. Program for the Refinement of Crystal Structures*; University of Göttingen; Germany, **1996**.

(6) Pennington, W. T., *J. Appl. Cryst*. **1999**, *32*, 1028.

(7) Dowty, E., 1999, http://www.shapesoftware.com/.

(8) Mozharivskyj, Y.; Pecharsky, A. O.; Pecharsky, V. K.; Miller, G. J., *J. Am. Chem. Soc.* **2005**, *127*, 317.

(9) Pecharsky, V. K.; Moorman, J. O.; Gschneidner, K. A. Jr., *Rev. Sci. Inst.* **1997**, *68*, 4196.

(10) Andersen, O. K., *Phys. Rev. B* **1975**, *12*, 3060.

(11) Andersen, O. K.; Jepsen, O., *Phys. Rev. Lett.* **1984**, *53*, 2571.

(12) Andersen, O. K.; Jepsen, O.; Glötzel, D., in *Highlights of Condensed-Matter Theory*; Bassani, F.; Fumi, F.; Tosi, M. P., Eds.; North-Holland: New York, **1985**.

(13) Andersen, O. K., *Phys. Rev. B* **1986**, *34*, 2439.

(14) Tank, R. W.; Jepsen, O.; Burckhardt. A.; Andersen, O. K., *TB-LMTO-ASA program*, *Version 4.7c*; Max-Planck-Institut für Festkörperforschung: Stuttgart, Germany, **1994**.

(15) Von Barth, U.; Hedin, L., *J. Phys. C* **1972**, *5*, 1629.

(16) Koelling, D. D.; Harmon, B. N., *J. Phys. C* **1977**, *10*, 3107.

(17) Jepsen, O.; Andersen, O. K., *Z. Phys. B* **1995**, *97*, 35.

(18) Dronskowski,R.; Blöchl, P., *J. Phys. Chem.* **1993**, *97*, 8617.

(19) Blöchl, P.; Jepsen, O. Andersen, O. K., *Phys. Rev. B* **1994**, *49*, 16223.

Chapter 3

$Gd_{5-x}Y_xTt_4$ (*Tt* = Si or Ge): Effect of Metal Substitution on Structure, Bonding and Magnetism

A paper published in the *Journal of the American Chemical Society*

J. Am. Chem. Soc. **2008**, *130*, 13900–13911.

Sumohan Misra and Gordon J. Miller

3.1. Abstract

A crystallographic study and theoretical assessment of the Gd/Y site preferences in the $Gd_{5-x}Y_xTt_4$ (*Tt* = Si, Ge) series prepared by high-temperature methods is presented. All structures for the $Gd_{5-x}Y_xSi_4$ system belong to the orthorhombic, Gd_5Si_4-type (space group *Pnma*). For the $Gd_{5-x}Y_xGe_4$ system, phases with $x < 3.6$ and $x \geq 4.4$ adopt the orthorhombic, Sm_5Ge_4-type structure. For the composition range of $3.6 \leq x \leq 4.2$, a monoclinic, $U_2Mo_3Si_4$-type structure (space group $P2_1/c$) occurs as the majority phase. This structure type has not been previously observed in the RE_5T_4 (*T* = Si, Ge, Ga) system, and differs from the known monoclinic structure of $Gd_5Si_2Ge_2$-type (space group $P2_1/a$) because all Ge···Ge contacts between slabs are equivalent. The structural relationships between the Sm_5Ge_4-type and the $U_2Mo_3Si_4$-type structures are discussed. Single crystal refinements of the occupancies for the three sites for Gd/Y atoms in the asymmetric unit reveal a partially ordered arrangement of Gd and Y atoms. TB-LMTO-ASA calculations were performed to study these atomic distributions as well as to elucidate possible electronic forces that might drive the structural variation. These results illustrate the importance of one of the Gd/Y-sites in shaping the magnetic and structural features observed in $Gd_{5-x}Y_xTt_4$ system. The magnetic properties of some of the $Gd_{5-x}Y_xTt_4$ phases are also reported. Germanides with $x \leq 2$ show a metamagnetic-type transition similar to Gd_5Ge_4 from 57-92(2) K. As the Y concentration

increases ($3 \leq x \leq 4$), these phases exhibit at least ferrimagnetic ordering with transition temperatures ranging from 15-31(2) K to the paramagnetic state.

3.2. Introduction

The $RE_5(Si_xGe_{1-x})_4$ (RE = rare-earth element) family of compounds is characterized by an intimate relationship between chemical composition, crystal structure and magnetism.[1-8] There is an intriguing interplay between several different, yet closely related crystal structures, all of which are based on characteristic slabs and the nature of their spontaneous magnetic ordering. During the past decade, the discovery of a giant magnetocaloric effect (MCE) in $Gd_5Si_2Ge_2$, along with other extraordinary magnetic properties such as a colossal magnetostriction and giant magnetoresistance,[9-16] has encouraged the rare-earth–tetrelide systems at the 5:4 stoichiometry to be subjects of broad interest, especially $Gd_5(Si_xGe_{1-x})_4$.

Most of the research activity to date has emphasized the chemistry, physics and materials science of Gd_5T_4 systems where T = Si, Ge, Ga, Sn or their various combinations.[17-23] For $Gd_5(Si_xGe_{1-x})_4$, as the Si/Ge ratio varies, it shows two amazing changes for their room temperature structures (Figure 3.1). All structures involve stackings of $[Gd_5T_4]$ slabs. At low Si concentrations ($x \leq 0.30$), the orthorhombic Sm_5Ge_4-type structure exists, which is characterized by the absence of any interslab Si(Ge)–Si(Ge) bonds; at high Si concentrations ($x \geq 0.56$), the orthorhombic Gd_5Si_4-type structure occurs and features the presence of interslab Si(Ge)–Si(Ge) covalent bonds. At intermediate Si compositions ($0.40 \leq x \leq 0.503$), the monoclinic $Gd_5Si_2Ge_2$-type structure exists, which displays only one-half of the Si(Ge)–Si(Ge) pairs, short enough for covalent bonding. The structural transition in this series is due to a correlation between the distribution of Si and Ge at the *Tt*-sites between the slabs (Si has a preference for the intraslab sites and Ge prefers the interslab positions) and the nature of the *Tt*···*Tt* interslab contacts.[24] The dependence of the crystal structure on valence electron counts have also been investigated, as in the $Gd_5Ga_xGe_{4-x}$ system,[22] where a decrease in valence electron concentration through substitution of three-valent, size equivalent Ga for four-valent Ge results in lower population of antibonding *T*-*T* (interslab) states with subsequent shortening and formation of *T*-*T* interslab dimers, thereby leading to a structural transition.

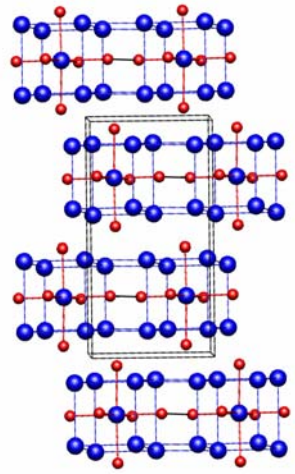

ORTHORHOMBIC

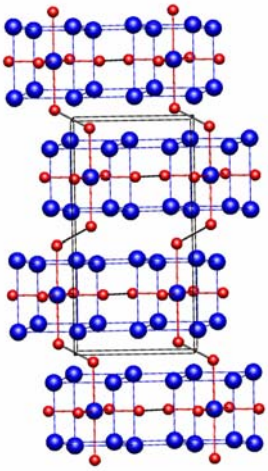

Sm_5Ge_4-type **Gd_5Si_4-type**

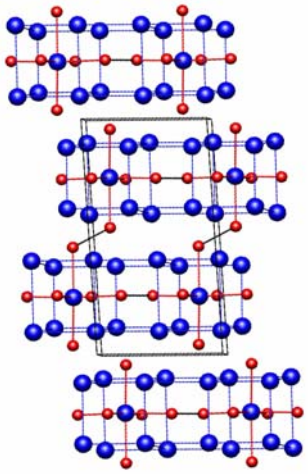

MONOCLINIC

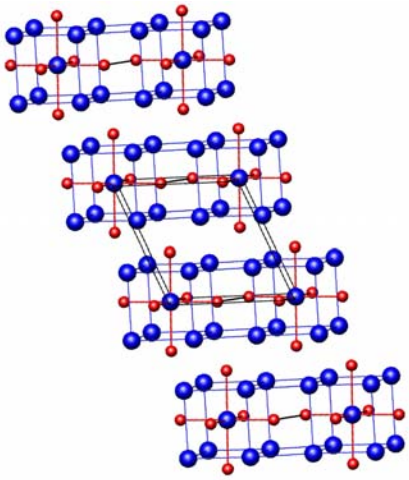

$Gd_5Si_2Ge_2$-type **$U_2Mo_3Si_4$-type**

Figure 3.1. Projections of four crystal structures observed for various RE_5T_4 (T = Si, Ge, Ga) systems. Blue atoms represent RE metal and red atoms represent T atoms.

The physical and chemical properties of tetrelides for other rare-earth or mixtures of rare-earth elements at the 5:4 stoichiometry have been explored to a much lesser extent, especially when RE = Y, La or Lu.[25, 26] We report here the results obtained for a systematic investigation of the effect of replacing Gd with Y on the structural features and magnetic properties in both pseudobinary Si and Ge systems. Not only is Y smaller than Gd,[27] but Y has no f electrons, although both Gd and Y are isoelectronic in their valance shell

configurations. Hence, Y will dilute the magnetic moments associated with Gd and should affect magnetic ordering patterns as well as ordering temperatures. Such behavior also exists in the binary Gd-Y alloys.[28] Gd and Y both adopt the *hcp* crystal structure type and form a continuous series of solid solutions.[28] These alloys show ferromagnetic behavior for Gd content exceeding 60 atomic % but antiferromagnetic ordering below 60 atomic %; Y itself is Pauli paramagnetic. Furthermore, the Curie temperatures for the ferromagnetic phases increase from ca. 95(2) K to 281(1) K as Gd content increases above 60 atomic %.[28] The Néel temperatures for alloys with Gd content less than 60 % were in the range of ca. 111(2) K-197(2) K.[28] Therefore, dilution of Gd with Y changes the magnetic properties continuously, but then undergoes a significant change in long-range order at a specific composition.

In the Gd-Y-Ge system, there are variations in the magnetic ordering as well as a transformation from the orthorhombic Sm_5Ge_4-type[29] to a new monoclinic $U_2Mo_3Si_4$-type[30] (Figure 3.1) structure for certain compositions. This structure is different from the known monoclinic structure of $Gd_5Si_2Ge_2$-type, and has not been reported before in the RE_5T_4 system. Thus, this structure becomes the eighth structure type established for the RE_5T_4 system.[4, 22]

3.3. Experimental Section

3.3.1. Syntheses: Samples of $Gd_{5-x}Y_xSi_4$, where x = 0, 1, 2, 3 and 4, and $Gd_{5-x}Y_xGe_4$, where x = 0, 1, 2, 3, 3.2, 3.4, 3.6, 3.8, 4, 4.2, 4.4, 4.6, 4.8 and 5.0, were prepared by arc-melting its constituent elements in an argon atmosphere on a water-cooled copper hearth. The starting materials were pieces of Gadolinium (99.99 wt. %, Materials Preparation Center, Ames Laboratory), Yttrium (99.99 wt. %, Materials Preparation Center, Ames Laboratory), Silicon (99.9999 wt. %, Alfa Aesar) and Germanium (99.9999 wt. %, Alfa Aesar). Each ingot had a total weight of ca. 1g and was remelted six times to ensure homogeneity. Weight losses during melting were less than 0.1 wt. %. To check for possible phase transformation and the distribution of rare earth atoms among the metal sites upon annealing, the samples were heated in evacuated silica tubes, at a rate of 4°C/min to 800°C and were then annealed for 1 week. In the end, the tubes were quenched in ice water.

3.3.2. Powder X-ray diffraction: The as-cast samples were examined by powder X-ray diffraction for identification and to assess phase purity. Powder patterns were obtained using an Enraf-Nonius Guinier camera using monochromatized Cu K_α radiation (λ = 1.54187 Å). To probe the purity and homogeneity of all phases, all diffraction patterns were analyzed by full-profile Rietveld refinement using *LHPM RIETICA* software.[31] Only the scale factor and the lattice parameters of each phase were refined. The isotropic displacement parameters of all atoms in each phase were assumed to be the same. For $Gd_{5-x}Y_xSi_4$, the profile residuals, R_p, varied from ca. 1.89 to 4.24 and derived Bragg residuals, R_B, varied from ca. 1.56 to 6.58. For $Gd_{5-x}Y_xGe_4$, the profile residuals, R_p, varied from ca. 2.33 to 4.73 (for pure phases) and from ca. 2.36 to 9.68 (for mixed phases). Their derived Bragg residuals, R_B, varied from ca. 2.29 to 5.15 (for pure phases) and from ca. 2.45 to 15.90 (for mixed phases). Figure 2 shows a schematic plot of the diffraction patterns for the four different phases existing in the RE_5T_4 system, patterns which were used for phase identification. There is a significant difference among these plots in the 2θ range 22-32°, which, therefore, acts as a fingerprinting region to identify the different phases.

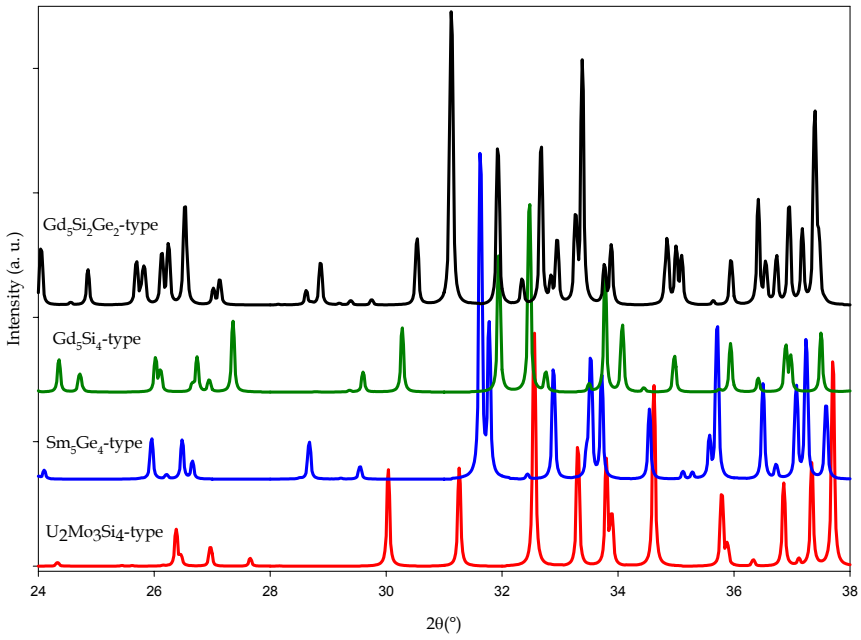

Figure 3.2. Schematic representation of powder X-ray diffraction patterns of four different types of structure types existing in the RE_5T_4 system.

3.3.3. Single-Crystal X-ray Crystallography: Several single crystals from the as-cast samples were mounted on the tips of glass fibers. Room temperature intensity data were collected on a Bruker Smart Apex CCD diffractometer with Mo K_α radiation (λ= 0.71073 Å) and a detector-to-crystal distance of 5.990 cm. Data were collected over a full sphere of reciprocal space by taking three sets of 606 frames with 0.3° scans in ω with an exposure time of 10 seconds per frame. The 2θ range extended from 4° to 57°. The *SMART*[32] software was used for data acquisition. Intensities were extracted and then corrected for Lorentz and polarization effects by the *SAINT*[32] program. Empirical absorption corrections were accomplished with *SADABS*,[32] which is based on modeling a transmission surface by spherical harmonics employing equivalent reflections with $I > 3\sigma(I)$. Structure solutions and refinements were performed with the *SHELXTL*[32] package of crystallographic programs.

3.3.4. Magnetic Property Measurements: Magnetic measurements were carried out using a Lake Shore ac / dc susceptometer-magnetometer, model 7225 on polycrystalline samples weighing ca. 0.25 g. These included dc magnetic susceptibility measurements between ca. 4 and 300 K and isothermal magnetization measurements in dc magnetic fields varying from 0 to 50 kOe. For the susceptibility measurements, the samples were first cooled under zero magnetic field (zfc) and then the measurements were carried out on heating under a 10 kOe magnetic field. The measurements were then repeated upon cooling with the magnetic field turned on (fc). All data were corrected for T-independent contributions.

3.3.5. Electronic Structure Calculations: Tight-binding, linear muffin-tin orbital (TB-LMTO) electronic band structure calculations with the atomic spheres approximation (ASA) were carried out using the Stuttgart program[33] on various models of Gd_5Ge_4, Gd_4YGe_4 GdY_4Ge_4 and Y_5Ge_4. Exchange and correlation were treated in a local spin density approximation. All relativistic effects except spin-orbit coupling were taken into account using a scalar relativistic approximation. The radii of the Wigner-Seitz (WS) spheres were obtained by requiring the overlapping potential to be the best possible approximation to the full potential according to an automatic procedure – no empty spheres were necessary.[34] The WS radii determined by this procedure are in the ranges 1.791-2.001 Å for Gd, 1.799-2.090

Å for Y, and 1.516-1.686 Å for Ge. The basis set included Gd 6*s*, 6*p* and 5*d* orbitals, Y 5*s*, 5*p* and 4*d* orbitals, and Ge 4*s*, 4*p* and 4*d* orbitals. The Gd 4*f* orbitals were treated as core wavefunctions occupied by seven valence electrons. Furthermore, the Ge 4*d* orbitals were treated by the Löwdin downfolding technique.[33] The **k**-space integrations to determine total energies and densities of states were evaluated by the tetrahedron method using 75-136 **k**-points (orthorhombic) and 170-512 **k**-points (monoclinic) in the irreducible wedges of the first Brillouin zones.

3.4. Results and Discussion

3.4.1. Structural Features. The powder X-ray diffraction patterns for all $Gd_{5-x}Y_xSi_4$ samples ($0.0 \leq x \leq 4.0$) could be completely indexed by the orthorhombic (space group *Pnma*), Gd_5Si_4-type structure. The lattice parameters obtained from powder X-ray diffraction is presented in Table 3.1. The crystallographic data, atomic coordinates, site occupancies and isotropic displacement parameters obtained from single crystal X-ray diffraction are listed in the supporting information. Previously, Elbicki and co-workers[25] had reported powder X-ray diffraction results on these phases for $0.0 \leq x \leq 2.0$. In our investigation with both powder and single crystal X-ray diffraction for $0.0 \leq x \leq 4.0$, we obtain similar results. Moreover, we also observe that Gd and Y are nonrandomly distributed over the three RE metal sites: there is preferential occupation of Y at the M3 site (center of the pseudo-cube); whereas Gd prefers the M1 sites. As expected, due to the smaller size of Y compared to Gd,[27] the unit-cell volume gradually decreases with increasing concentration of Y.

Table 3.1. Lattice parameters for $Gd_{5-x}Y_xSi_4$ as obtained by powder X-ray diffraction (Gd_5Si_4-type, space group *Pnma* (No. 62), Cu K_α radiation, 2θ range = 10-100°, T = 298(2) K, Z = 4).

x	***a* (Å)**	***b* (Å)**	***c* (Å)**	***V′* (Å^3)[a]**
0	7.4880(6)	14.750(1)	7.7476(6)	213.9(1)
1	7.4634(4)	14.7123(9)	7.7421(4)	212.53(8)

Table 3.1. (continued)

x	*a* (Å)	*b* (Å)	*c* (Å)	*V′* (Å^3)[a]
2	7.4411(4)	14.6754(9)	7.7301(4)	211.03(8)
3	7.4245(4)	14.6419(8)	7.7170(4)	209.73(8)
4	7.4105(4)	14.6087(8)	7.7062(4)	208.56(8)

[a] *V′* = Unit cell volume per formula unit.

For the $Gd_{5-x}Y_xGe_4$ system, three distinct composition ranges exist as identified by powder X-ray diffraction. For $x < 3.6$ and $x \geq 4.4$, the orthorhombic, Sm_5Ge_4-type structure forms as the majority phase, and for the composition range of $3.6 \leq x \leq 4.2$, the monoclinic $U_2Mo_3Si_4$-type structure is observed as the majority phase. The lattice parameters obtained from Rietveld refinement of the powder data is presented in Table 3.2. The crystallographic data, atomic coordinates, site occupancies and isotropic displacement parameters from single crystal X-ray diffraction are shown in Tables 3.3-3.7. To check for possible phase transformation upon annealing, the sample with $x = 4.0$, having the monoclinic $U_2Mo_3Si_4$-type structure was annealed at 800°C for 1 week and then a powder diffraction pattern was measured. The diffraction pattern was similar to the pattern before annealing with no additional peaks.

Table 3.2. Lattice parameters for $Gd_{5-x}Y_xGe_4$ as obtained by powder X-ray diffraction (space group for Sm_5Ge_4-type ($Z = 4$) and $U_2Mo_3Si_4$-type ($Z = 2$) structures are *Pnma* (No. 62) and $P2_1/c$ (No. 14) respectively, Cu K_α radiation, 2θ range = 10-100°, $T = 298(2)$ K).

x	*Structure Type(s)*	*a* (Å)	*b* (Å)	*c* (Å)	*β* (°)	*V′* (Å^3)[a]
0	Sm_5Ge_4	7.6984(4)	14.8372(8)	7.7872(4)		222.4(1)
1	Sm_5Ge_4	7.6842(4)	14.8070(8)	7.7690(4)		221.0(1)
2	Sm_5Ge_4	7.6675(4)	14.7795(8)	7.7504(4)		219.6(1)
3	Sm_5Ge_4* + *$U_2Mo_3Si_4$*	7.6559(9)	14.7553(18)	7.7346(10)		218.4(2)
		present in trace amounts				
3.2	Sm_5Ge_4* + *$U_2Mo_3Si_4$*	7.6519(6)	14.7476(11)	7.7319(6)		218.1(1)
		present in trace amounts				

Table 3.2. (continued)

x	*Structure Type(s)*	*a* (Å)	*b* (Å)	*c* (Å)	*β* (°)	*V′* (Å^3)[a]
3.4	Sm_5Ge_4* +	7.6441(3)	14.7354(6)	7.7210(3)		217.4(0)
	$U_2Mo_3Si_4$	*8.097(7)*	*7.723(6)*	*7.690(6)*	*113.32(5)*	*220.8(6)*
3.6	*Sm_5Ge_4* +	*7.646(1)*	*14.738(2)*	*7.718(1)*		*217.4(2)*
	$U_2Mo_3Si_4$*	8.0277(31)	7.7401(28)	7.6501(28)	113.08(3)	218.6(3)
3.8	*Sm_5Ge_4* +	*7.644(1)*	*14.738(2)*	*7.712(1)*		*217.2(2)*
	$U_2Mo_3Si_4$*	7.9971(22)	7.7562(24)	7.6235(20)	113.09(2)	217.5(2)
4	*Sm_5Ge_4* +	*7.735(1)*	*14.759(1)*	*7.679(1)*		*219.15(3)*
	$U_2Mo_3Si_4$*	8.0067(9)	7.7540(10)	7.6174(8)	113.04(1)	217.6(1)
4.2	*Sm_5Ge_4* +	*7.720(3)*	*14.717(5)*	*7.676(3)*		*218.0(6)*
	$U_2Mo_3Si_4$*	8.0022(5)	7.7460(5)	7.6061(5)	113.00(1)	217.0(0)
4.4	Sm_5Ge_4* +	7.6389(8)	14.7196(15)	7.7103(9)		216.7(2)
	$U_2Mo_3Si_4$	*8.031(2)*	*7.730(3)*	*7.619(2)*	*113.14(2)*	*217.5(3)*
4.6	Sm_5Ge_4	7.6373(5)	14.7097(10)	7.7037(5)		216.4(1)
4.8	Sm_5Ge_4	7.6335(5)	14.6985(9)	7.6982(5)		215.9(1)
5	Sm_5Ge_4	7.6316(2)	14.6976(3)	7.6966(2)		215.8(0)

[a] *V′* = Unit cell volume per formula unit; * Majority phase as determined from Rietveld refinement. Lattice parameters for the minority phases are shown in italics.

Table 3.3. Crystallographic data for $Gd_{5-x}Y_xGe_4$ (x = 0, 1, 2, 3, 3.2, and 3.4) as obtained by single crystal X-ray diffraction (space group *Pnma* (No. 62), Mo K_α radiation, 2θ range = 4-57°, T = 298(2) K, Z = 4).

x	0	1	2	3	3.2	3.4
Loaded Composition	Gd_5Ge_4	Gd_4YGe_4	$Gd_3Y_2Ge_4$	$Gd_2Y_3Ge_4$	$Gd_{1.8}Y_{3.2}Ge_4$	$Gd_{1.6}Y_{3.4}Ge_4$
Refined Composition	Gd_5Ge_4	$Gd_{4.02(6)}Y_{0.98}Ge_4$	$Gd_{2.96(5)}Y_{2.04}Ge_4$	$Gd_{1.91(4)}Y_{3.09}Ge_4$	$Gd_{1.74(5)}Y_{3.26}Ge_4$	$Gd_{1.55(6)}Y_{3.45}Ge_4$
Independent Reflections	1098	1081	1083	1068	1072	1061
No. of Parameters	47	50	50	50	50	50
Final R indices [I > 2σ(I)]	R1 =0.0385, wR2 = 0.0831	R1 = 0.0461, wR2 = 0.0864	R1 = 0.0485, wR2 = 0.0881	R1 = 0.0503, wR2 = 0.0799	R1 = 0.0493, wR2 = 0.0895	R1 = 0.0628, wR2 = 0.1179

Table 3.2. (continued)

x	0	1	2	3	3.2	3.4
Peak/hole, (*e*/Å^3)	3.085 / −1.817	2.570 / –2.138	2.332 / –2.332	2.183 / –2.326	2.743 / –2.284	3.593 / –2.331

Table 3.4. Crystallographic data for $Gd_{5-x}Y_xGe_4$ (x = 3.6, 4.4, 4.6, 4.8 and 5.0) as obtained by single crystal X-ray diffraction (space group *Pnma* (No. 62), Mo K_α radiation, 2θ range = 4-57°, T = 298(2) K, Z = 4).

x	3.6	4.4	4.6	4.8	5.0
Loaded Composition	$Gd_{1.4}Y_{3.6}Ge_4$	$Gd_{0.6}Y_{4.4}Ge_4$	$Gd_{0.4}Y_{4.6}Ge_4$	$Gd_{0.2}Y_{4.8}Ge_4$	Y_5Ge_4
Refined Composition	$Gd_{1.26(4)}Y_{3.74}Ge_4$	$Gd_{0.61(5)}Y_{4.39}Ge_4$	$Gd_{0.29(3)}Y_{4.71}Ge_4$	$Gd_{0.17(3)}Y_{4.83}Ge_4$	Y_5Ge_4
Independent Reflections	1076	1078	1091	1069	1070
No. of Parameters	50	50	50	50	47
Final R indices [I > 2σ(I)]	R1 = 0.0524, wR2 = 0.0914	R1 = 0.0611, wR2 = 0.1109	R1 = 0.0437, wR2 = 0.0758	R1 = 0.0423, wR2 = 0.0838	R1 = 0.0482, wR2 = 0.0798
Peak/hole, (*e*/Å^3)	2.225 / –1.902	3.442 / –2.025	1.841 / –1.626	3.196 / –1.489	1.730 / –1.642

Table 3.5. Atomic coordinates, site occupancies and isotropic displacement parameters for $Gd_{5-x}Y_xGe_4$ ($x \leq 3.6$; $x \geq 4.4$) as obtained by single crystal X-ray diffraction. Coordinates are represented in accordance with similar previously reported structure types.

Atom		***x***	***y***	***z***	**occupancy[a]**	**U_{eq}, (Å^2)[b]**
			Gd_5Ge_4			
M1	8d	0.9758(1)	0.4000(1)	0.1782(1)	1	0.009(1
M2	8d	0.6233(1)	0.3832(1)	0.8387(1)	1	0.008(1)
M3	4c	0.2097(1)	¾	0.4992(1)	1	0.008(1)
Ge1	8d	0.7821(2)	0.4560(1)	0.5332(2)	1	0.009(1)
Ge2	4c	0.0817(2)	¾	0.1127(2)	1	0.010(1)
Ge3	4c	0.3261(2)	¾	0.8657(2)	1	0.009(1)

Table 3.5. (continued)

Atom		*x*	*y*	*z*	occupancy[a]	U_{eq}, (Å^2)[b]
			$Gd_{4.02(6)}Y_{0.98}Ge_4$			
M1	8d	0.9755(1)	0.4001(1)	0.1781(1)	0.88(1)	0.010(1)
M2	8d	0.6235(1)	0.3831(1)	0.8387(1)	0.76(1)	0.009(1)
M3	4c	0.2101(2)	¾	0.4988(2)	0.72(1)	0.009(1)
Ge1	8d	0.7822(2)	0.4562(1)	0.5336(2)	1	0.010(1)
Ge2	4c	0.0819(3)	¾	0.1135(3)	1	0.010(1)
Ge3	4c	0.3273(3)	¾	0.8653(3)	1	0.010(1)
			$Gd_{2.96(5)}Y_{2.04}Ge_4$			
M1	8d	0.9749(1)	0.4002(1)	0.1779(1)	0.71(1)	0.010(1)
M2	8d	0.6234(1)	0.3831(1)	0.8388(1)	0.53(1)	0.009(1)
M3	4c	0.2105(2)	¾	0.4990(2)	0.46(1)	0.009(1)
Ge1	8d	0.7825(2)	0.4560(1)	0.5335(2)	1	0.010(1)
Ge2	4c	0.0816(3)	¾	0.1144(3)	1	0.010(1)
Ge3	4c	0.3284(3)	¾	0.8647(3)	1	0.010(1)
			$Gd_{1.91(4)}Y_{3.09}Ge_4$			
M1	8d	0.9744(1)	0.4002(1)	0.1777(1)	0.56(1)	0.010(1)
M2	8d	0.6233(1)	0.3829(1)	0.8391(1)	0.29(1)	0.008(1)
M3	4c	0.2116(2)	¾	0.4990(2)	0.20(1)	0.008(1)
Ge1	8d	0.7823(2)	0.4559(1)	0.5331(2)	1	0.009(1)
Ge2	4c	0.0811(2)	¾	0.1155(2)	1	0.009(1)
Ge3	4c	0.3299(2)	¾	0.8639(2)	1	0.010(1)
			$Gd_{1.74(5)}Y_{3.26}Ge_4$			
M1	8d	0.9737(1)	0.4001(1)	0.1772(1)	0.49(1)	0.011(1)
M2	8d	0.6228(1)	0.3830(1)	0.8390(1)	0.27(1)	0.009(1)
M3	4c	0.2118(2)	¾	0.4992(2)	0.22(1)	0.009(1)
Ge1	8d	0.7817(2)	0.4558(1)	0.5331(2)	1	0.010(1)
Ge2	4c	0.0818(3)	¾	0.1155(3)	1	0.009(1)
Ge3	4c	0.3309(3)	¾	0.8642(3)	1	0.010(1)

Table 3.5. (continued)

Atom		*x*	*y*	*z*	occupancy[a]	U_{eq}, (Å^2)[b]
			$Gd_{1.55(6)}Y_{3.45}Ge_4$			
M1	8d	0.9737(2)	0.4002(1)	0.1773(2)	0.47(1)	0.014(1)
M2	8d	0.6229(2)	0.3830(1)	0.8391(2)	0.22(1)	0.011(1)
M3	4c	0.2119(3)	¾	0.4990(3)	0.15(1)	0.010(1)
Ge1	8d	0.7815(3)	0.4559(1)	0.5333(3)	1	0.013(1)
Ge2	4c	0.0814(3)	¾	0.1159(3)	1	0.012(1)
Ge3	4c	0.3306(3)	¾	0.8637(3)	1	0.013(1)
			$Gd_{1.26(4)}Y_{3.74}Ge_4$			
M1	8d	0.9730(1)	0.4001(1)	0.1772(1)	0.39(1)	0.011(1)
M2	8d	0.6227(1)	0.3829(1)	0.8392(1)	0.18(1)	0.009(1)
M3	4c	0.2122(2)	¾	0.4992(2)	0.12(1)	0.008(1)
Ge1	8d	0.7815(2)	0.4558(1)	0.5326(2)	1	0.010(1)
Ge2	4c	0.0819(3)	¾	0.1155(2)	1	0.010(1)
Ge3	4c	0.3315(2)	¾	0.8638(2)	1	0.011(1)
			$Gd_{0.61(5)}Y_{4.39}Ge_4$			
M1	8d	0.9702(2)	0.3992(1)	0.1758(2)	0.15(1)	0.013(1)
M2	8d	0.6205(2)	0.3835(1)	0.8389(2)	0.14(1)	0.011(1)
M3	4c	0.2141(3)	¾	0.4989(3)	0.03(1)	0.009(1)
Ge1	8d	0.7801(2)	0.4555(1)	0.5304(2)	1	0.013(1)
Ge2	4c	0.0840(3)	¾	0.1168(3)	1	0.011(1)
Ge3	4c	0.3338(3)	¾	0.8642(3)	1	0.011(1)
			$Gd_{0.29(3)}Y_{4.71}Ge_4$			
M1	8d	0.9700(1)	0.3995(1)	0.1760(1)	0.07(1)	0.010(1)
M2	8d	0.6205(1)	0.3831(1)	0.8394(1)	0.07(1)	0.009(1)
M3	4c	0.2143(2)	¾	0.4989(2)	0.01(1)	0.008(1)
Ge1	8d	0.7796(1)	0.4556(1)	0.5311(1)	1	0.010(1)
Ge2	4c	0.0839(2)	¾	0.1164(2)	1	0.010(1)
Ge3	4c	0.3350(2)	¾	0.8635(2)	1	0.010(1)

Table 3.5. (continued)

Atom		*x*	*y*	*z*	occupancy[a]	U_{eq}, (Å^2)[b]
			$Gd_{0.17(3)}Y_{4.83}Ge_4$			
M1	8d	0.9696(1)	0.3992(1)	0.1759(1)	0.04(1)	0.011(1)
M2	8d	0.6205(1)	0.3832(1)	0.8392(1)	0.04(1)	0.009(1)
M3	4c	0.2143(1)	¾	0.4988(2)	0.01(1)	0.009(1)
Ge1	8d	0.7798(1)	0.4556(1)	0.5310(1)	1	0.011(1)
Ge2	4c	0.0840(2)	¾	0.1167(2)	1	0.010(1)
Ge3	4c	0.3352(2)	¾	0.8633(2)	1	0.009(1)
			Y_5Ge_4			
M1	8d	0.9692(1)	0.3993(1)	0.1758(1)	1	0.010(1)
M2	8d	0.6204(1)	0.3829(1)	0.8396(1)	1	0.008(1)
M3	4c	0.2145(2)	¾	0.4988(2)	1	0.008(1)
Ge1	8d	0.7797(1)	0.4556(1)	0.5314(1)	1	0.009(1)
Ge2	4c	0.0840(2)	¾	0.1163(2)	1	0.009(1)
Ge3	4c	0.3353(2)	¾	0.8635(2)	1	0.009(1)

[a] All M1, M2 and M3 sites are fully occupied with a mixture of Gd and Y atoms. Only Gd occupations are listed. The only exception is Gd_5Ge_4 and Y_5Ge_4 where the M1, M2 and M3 sites are fully occupied by Gd and Y atoms respectively.

[b] U(eq) is defined as one-third of the trace of the orthogonalized U_{ij} tensor.

Table 3.6. Crystallographic data for $Gd_{5-x}Y_xGe_4$ (x = 3.8, 4.0 and 4.2) as obtained by single crystal X-ray diffraction (space group $P2_1/c$ (No. 14), Mo K_α radiation, 2θ range = 4-57°, T = 298(2) K, Z = 2).

x	3.8	4.0	4.2
Loaded Composition	$Gd_{1.2}Y_{3.8}Ge_4$	GdY_4Ge_4	$Gd_{0.8}Y_{4.2}Ge_4$
Refined Composition	$Gd_{1.11(3)}Y_{3.89}Ge_4$	$Gd_{1.00(3)}Y_{4.00}Ge_4$	$Gd_{0.77(3)}Y_{4.23}Ge_4$

Table 3.6. (continued)

x	3.8	4.0	4.2
Independent Reflections	1014	1021	1010
No. of Parameters	47	47	47
Final R indices [I > 2σ(I)]	R1 = 0.0434, wR2 = 0.0826	R1 = 0.0426, wR2 = 0.0769	R1 = 0.0332, wR2 = 0.0574
Peak/hole, (*e*/Å^3)	1.979 / –1.496	1.623 / –1.439	1.408 / –1.092

Table 3.7. Atomic coordinates, site occupancies and isotropic displacement parameters for $Gd_{5-x}Y_xGe_4$ (x = 3.8, 4.0 and 4.2) as obtained by single crystal X-ray diffraction. Coordinates are represented in accordance with similar previously reported structure types.

Atom		***x***	***y***	***z***	**occupancy**[a]	**U_{eq}, (Å^2)**[b]
			$Gd_{1.11(3)}Y_{3.89}Ge_4$			
M1	4e	0.7006(1)	0.3217(1)	0.0574(1)	0.35(1)	0.010(1)
M2	4e	0.2659(1)	0.3371(1)	0.2775(1)	0.15(1)	0.009(1)
M3	2a	0	0	0	0.11(1)	0.009(1)
Ge1	4e	0.4115(2)	0.0314(2)	0.1807(2)	1	0.010(1)
Ge2	4e	0.0082(2)	0.6300(2)	0.1286(2)	1	0.010(1)
			$Gd_{1.00(3)}Y_{4.00}Ge_4$			
M1	4e	0.7007(1)	0.3219(1)	0.0571(1)	0.32(1)	0.011(1)
M2	4e	0.2658(1)	0.3373(1)	0.2776(1)	0.13(1)	0.009(1)
M3	2a	0	0	0	0.09(1)	0.009(1)
Ge1	4e	0.4112(2)	0.0312(1)	0.1807(2)	1	0.010(1)
Ge2	4e	0.0083(2)	0.6300(1)	0.1286(2)	1	0.011(1)
			$Gd_{0.77(3)}Y_{4.23}Ge_4$			
M1	4e	0.7008(1)	0.3219(1)	0.0569(1)	0.25(1)	0.010(1)
M2	4e	0.2656(1)	0.3371(1)	0.2779(1)	0.10(1)	0.009(1)

Table 3.7. (continued)

Atom		*x*	*y*	*z*	occupancy[a]	U_{eq}, (Å^2)[b]
M3	2a	0	0	0	0.07(1)	0.008(1)
Ge1	4e	0.4112(1)	0.0314(1)	0.1809(1)	1	0.010(1)
Ge2	4e	0.0083(1)	0.6302(1)	0.1287(1)	1	0.010(1)

[a] All M1, M2 and M3 sites are fully occupied with a mixture of Gd and Y atoms. Only Gd occupations are listed.

[b] U(eq) is defined as one-third of the trace of the orthogonalized U_{ij} tensor.

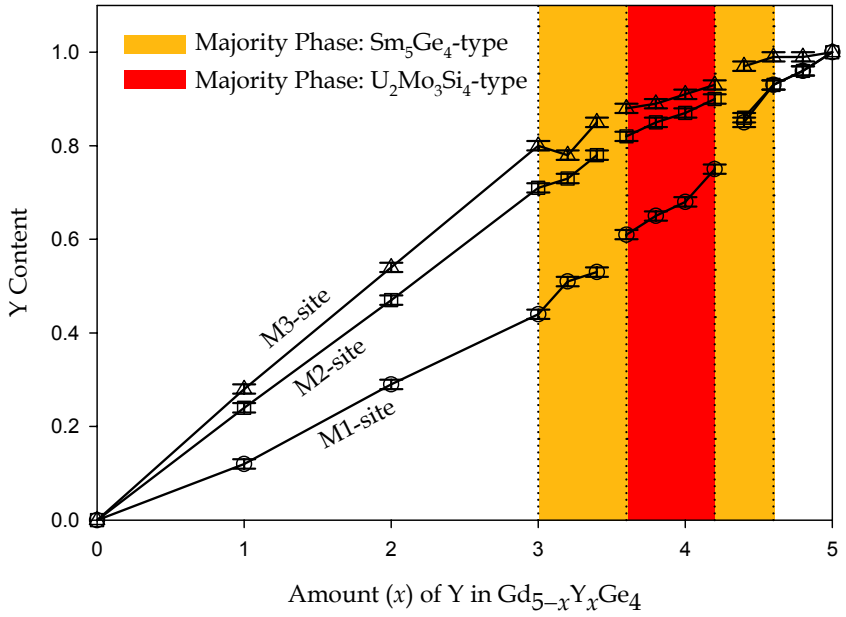

Figure 3.3. Y occupation in each M site of $Gd_{5-x}Y_xGe_4$ as a function of Y concentration, *x*, as obtained from single crystal X-ray diffraction. The shaded regions delineate the two-phase regions as observed from powder X-ray diffraction.

The orthorhombic crystal structure has six atoms in the asymmetric unit: three crystallographically independent sites for Gd or Y metal atoms, and three distinct sites for the tetrelide atoms. All three rare earth metal sites (in both structures) exhibit mixed site occupancies, with Gd (or the larger rare-earth atom) having a preference for the M1 site and

Y (or the smaller rare-earth atom) having a preference for the M3 site (see Figure 3.3) as observed in Gd-Y-Si, Gd-La-Ge,[26] Gd-Lu-Ge[26] and Gd-Sc-Ge[35] systems. In comparison to the orthorhombic structure, the asymmetric unit of the monoclinic structure has five atoms: three distinct sites for Gd or Y metal atoms and just two distinct sites for the tetrelide atoms. This monoclinic structure has never been previously reported in RE_5T_4 systems. However, it has been observed in various ternary compounds with lanthanide and actinide elements, e.g., in $RE_2Mo_3Si_4$ where RE = Dy, Er, Ho, Tb, Tm, Y[36] and also in $U_2M_3Tt_4$ where *M* = V, Mo, W and *Tt* = Si, Ge.[37] Nevertheless, the monoclinic $U_2Mo_3Si_4$ structure-type shows remarkable similarities with the Sm_5Ge_4-type structure. Both crystal structures are built from nearly identical 3^2434 nets of Gd/Y atoms. Two such nets are placed over one another to form two-dimensional slabs with additional Gd/Y atoms in pseudo-cubic coordination (M3 site) and Ge2, Ge3 (in case of orthorhombic structure) and Ge2 atoms (in case of monoclinic structure) in trigonal prismatic voids. These crystal structures differ from one other in the manner in which these neighboring slabs stack with respect to each other. In the orthorhombic structure, each slab has reflection symmetry through the M3, T2 and T3 sites, and the first and the second slabs are shifted but related by inversion symmetry. This results in the slabs being arranged in a way that the interslab Ge1···Ge1 contacts form a herring-bone pattern along the *b*-direction. In the monoclinic $U_2Mo_3Si_4$-type structure, each slab has inversion symmetry at the M3 sites, and adjacent layers are related by translational symmetry resulting in a stacking pattern which creates inversion symmetry between slabs along the stacking direction. Due to these different symmetry characteristics the arrangements of the M1 and M2 metal positions are different in the two structures, although every cube surrounding the M3 positions contains 4 M1 and 4 M2 sites. In the orthorhombic structure, the two faces of the cube perpendicular to the *c*-direction are either all M1 or all M2. On the other hand, for the monoclinic structure, the two faces of the cube perpendicular to the *b*-direction are 50 % M1 and 50 % M2 in an alternating pattern, which preserves the inversion center at the M3 site.

The other monoclinic structure observed in the RE_5T_4 system, the $Gd_5Si_2Ge_2$-type, adopts the space group $P2_1/a$, which is a proper subgroup of *Pnma*, and contains nine atoms in the asymmetric unit with the M1 and M2 sites each splitting into two pairs (M1a, M1b and

M2a, M2b) and the *T*1 site also splitting into a pair of distinct sites (*T*1a, *T*1b). Hence, when compared with the monoclinic $U_2Mo_3Si_4$-type structure, the $Gd_5Si_2Ge_2$-type forms two sets of inequivalent interslab (*T*1-*T*1) contacts, resulting in one-half of these pairs short enough for covalent bonding. The stacking pattern of the slabs remains similar to the Sm_5Ge_4-type structure.

Variations of selected interatomic distances across the $Gd_{5-x}Y_xGe_4$ series ($3.0 \leq x \leq 5.0$) near the crystal structure changes are illustrated in Figure 3.4. The structural figures display the various contacts, matching the color code of the plots. The vertical dotted lines delineate the region where the monoclinic phase is observed. For all plots there are distinct deviations when x = 3.8-4.2, marking the region for the structural transition. The largest variations occur for certain intraslab M···M and M···Ge distances, and arise because the change in symmetry (orthorhombic to monoclinic) creates equidistant bond lengths. These are marked as black open triangles and inverted triangles in the plots and as dashed bonds in the figures. The graphs, moreover, identify certain pervasive features of the entire series: (a) Ge-Ge contacts between adjacent slabs are nonbonding, or, at most, weakly bonding; (b) M1-Ge and M2-Ge contacts between adjacent slabs are more significant (solid orange bonds in Figure 4b) for holding the slabs together than the Ge-Ge contacts; (c) there is a single M-M (M1-M2) interaction between slabs (solid blue bonds in Figure 4a) that occurs at each M1 or M2 site and exhibits a very short distance (ca. 3.50 Å); and (d) the most significant M-M interactions within each slab involve the M3 sites. We will discuss some of the impacts of these geometrical features in more detail in the subsequent section on electronic structure.

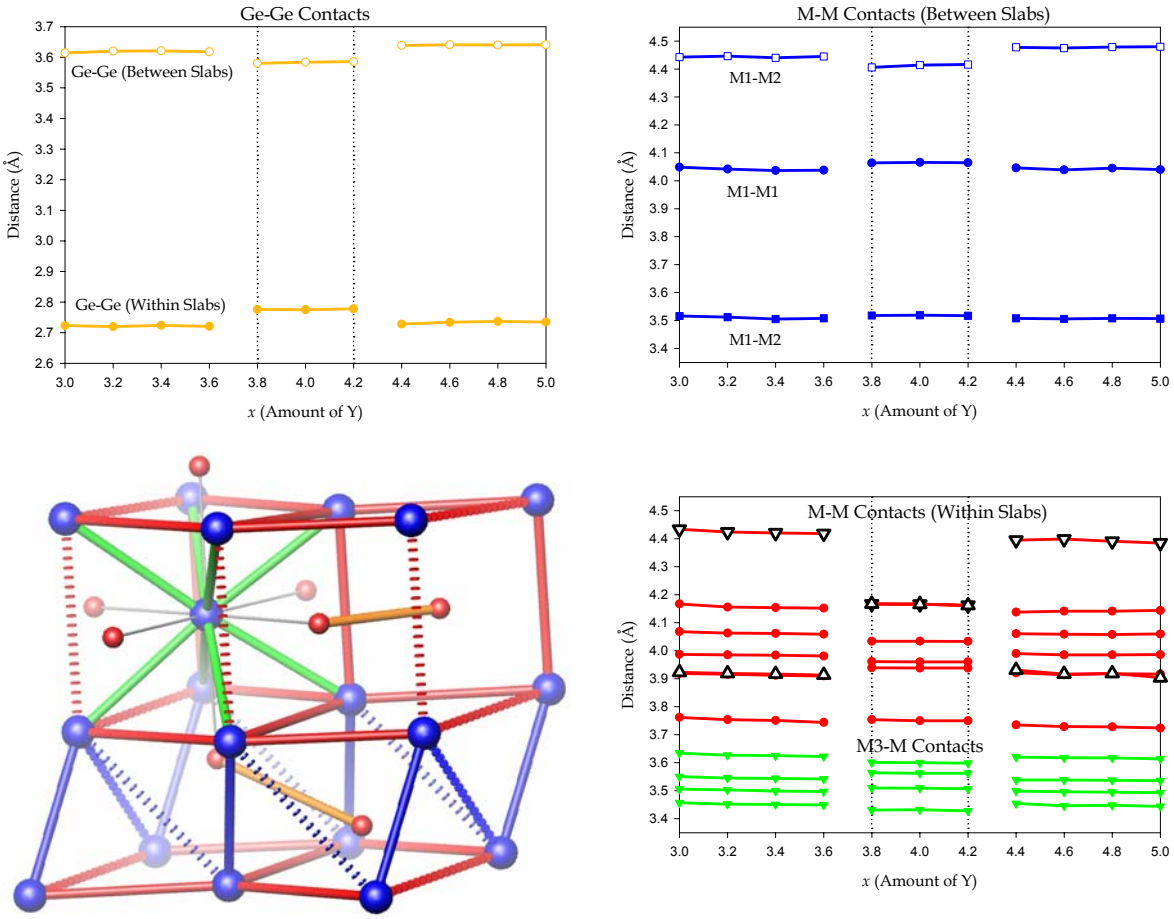

Figure 3.4a. Interatomic distance variations in $Gd_{5-x}Y_xGe_4$ as a function of Y concentration, x. These graphs illustrate trends in Ge-Ge and M-M distances. The distance scales on all M-M graphs are identical to illustrate the relative magnitudes. The structural figure shows the various interatomic distances presented by the graphs in their respective colors. Blue spheres are metal (Gd/Y), and red spheres are Ge sites.

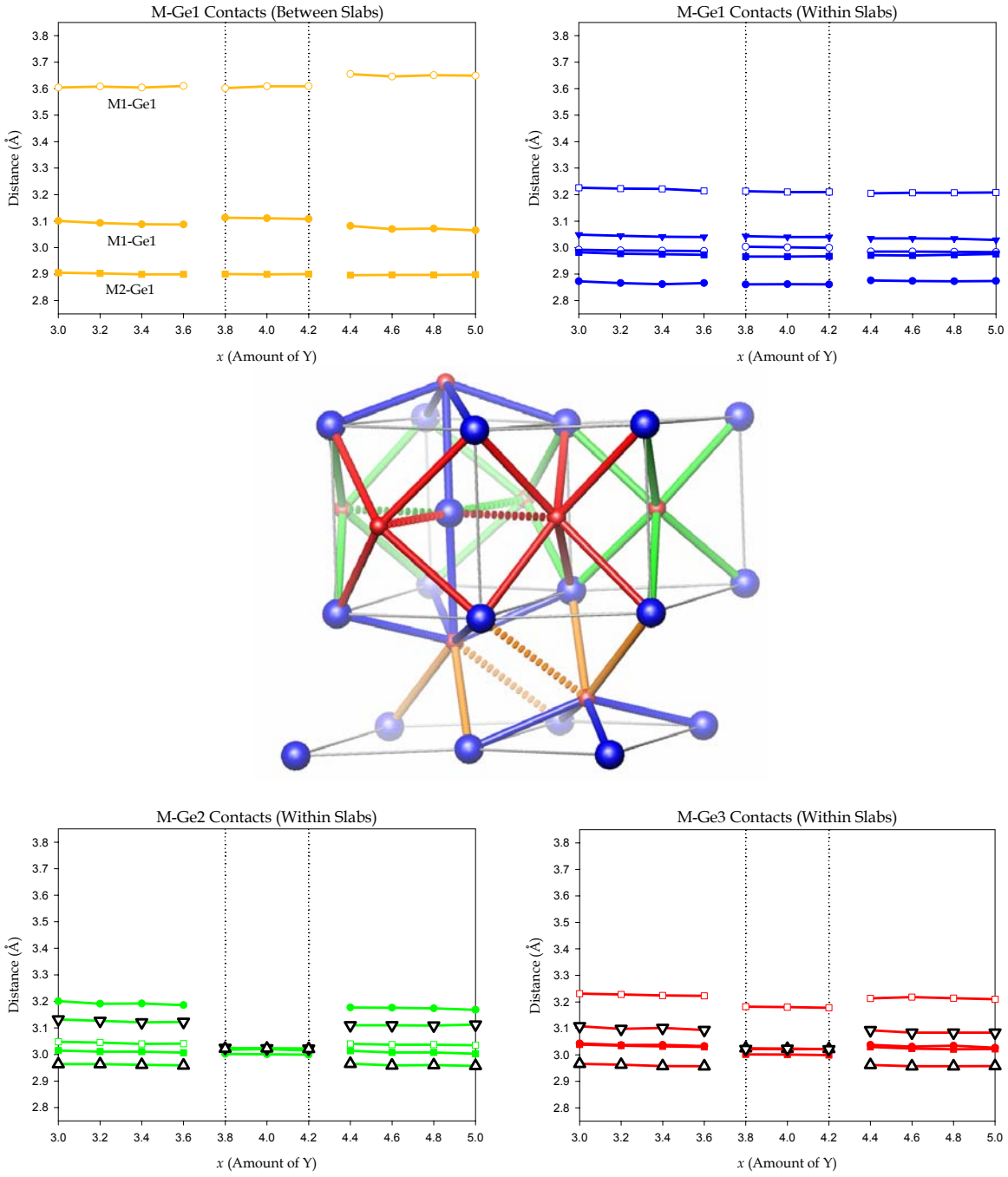

Figure 3.4b. Interatomic distance variations in $Gd_{5-x}Y_xGe_4$ as a function of Y concentration, x. These graphs illustrate trends in M-Ge distances. The distance scales on all graphs are identical to illustrate the relative magnitudes. The structural figure shows the various interatomic distances presented by the graphs in their respective colors. Blue spheres are metal (Gd/Y), and red spheres are Ge sites.

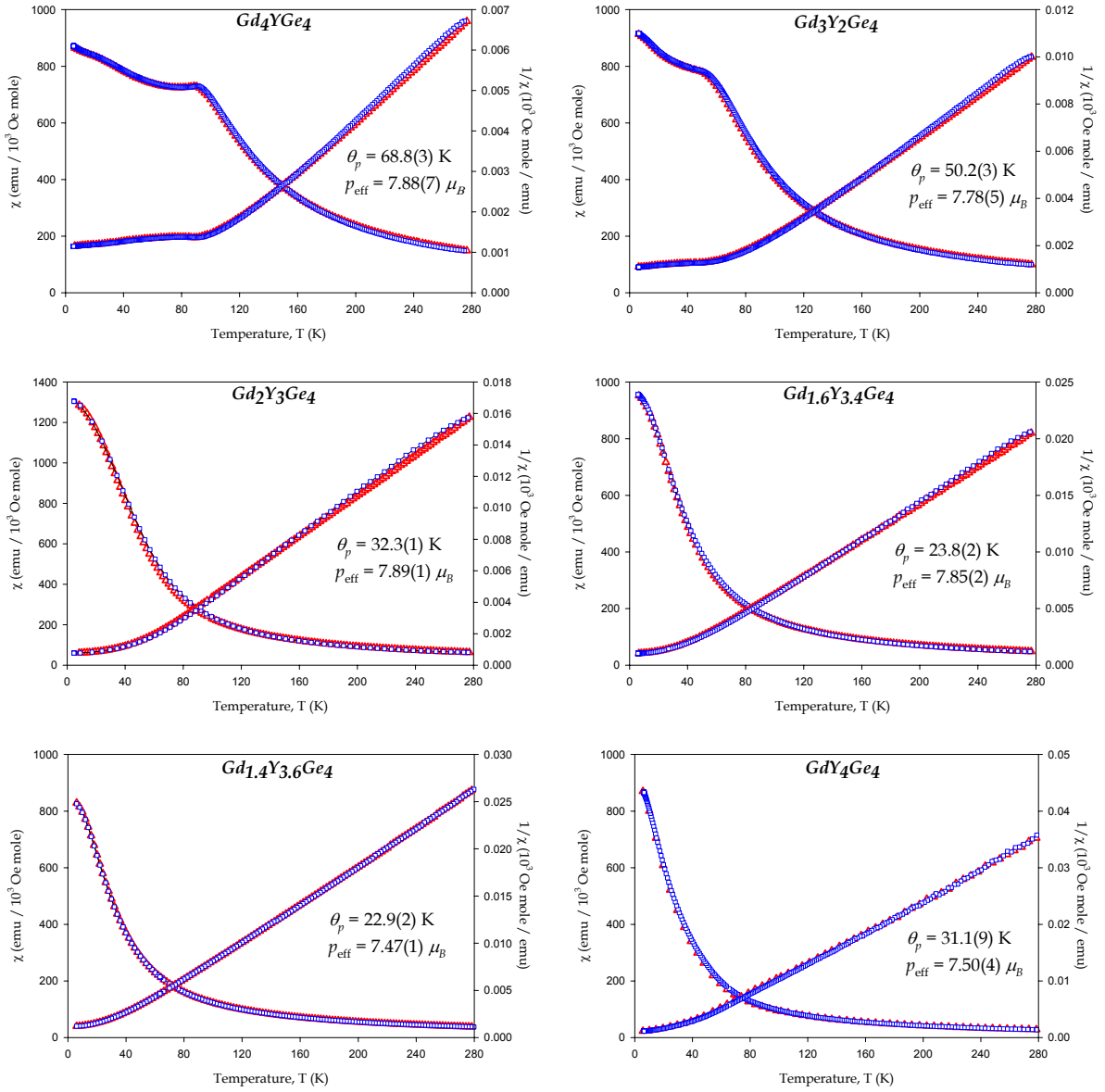

Figure 3.5. Magnetic susceptibility plots for $Gd_{5-x}Y_xGe_4$ series. Red triangles are data for the heating cycles (zfc) and blue circles are data for the cooling cycles (fc) with H = 10 kOe.

3.4.2. Magnetism

Figure 3.5 illustrates the magnetic susceptibility measurements in a 10 kOe field for the $Gd_{5-x}Y_xGe_4$ series. The Gd-rich phases (x = 1 and 2) show a metamagnetic-type transition at 92 K and 57 K respectively, similar to Gd_5Ge_4, which shows this transition at 128 K (T_N). The reduction in transition temperature can be explained by dilution of the magnetic Gd sites

by Y in this system.[28] The curves also show a Curie-Weiss behavior above these transitions. The Y-rich phases (x = 3-4), in contrast, undergo ferrimagnetic-type ordering showing Curie-Weiss behavior at high temperatures. The $M(H)$ plots for the above phases are available in the supporting information, which also reiterates the presence of metamagnetic and ferrimagnetic-type behavior as none of the phases show saturation in fields upto 50 kOe. The paramagnetic Curie temperatures, θ_p, decrease with increasing Y concentration, but increases for x = 4. The Curie temperatures, T_C, were estimated for the ferrimagnetic phases (x = 3.0, 3.4, 3.6 and 4.0) from dM/dT vs. T plots to be 31(2), 24(2), 20(2) and 15(2) K, respectively. The effective magnetic moments for the series were determined to be 7.89(1)-7.47(1) μ_B/Gd ion (theoretical value for Gd^{3+} = 7.94 μ_B) based on numerical fits for the data between 150 and 270 K. The effective magnetic moments for the two Y-rich phases are lower than the expected value and the reason is not well understood. But since the results were reproducible, it could probably be attributed due to the presence of some unidentified non-crystalline minority phases.

Magnetic susceptibility measurements for the $Gd_{5-x}Y_xSi_4$ series were also carried out between 6 and 300 K. All phases undergo ferromagnetic ordering showing Curie-Weiss behavior at high temperatures. This transition for Gd_4YSi_4 exceeds 300 K, but for $Gd_3Y_2Si_4$ (T_C = 203(2) K), $Gd_2Y_3Si_4$ (T_C = 133(2) K), and GdY_4Si_4 (T_C = 50(2) K), the Curie temperatures decrease almost linearly with increasing Y concentration. These susceptibility plots are included in the Supporting Information.

3.4.3. Theoretical Electronic Structure

Substitution at the RE metal sites raises a number of questions. In this paper, we specifically focus on the problems for the Ge-system. For this, electronic structure calculations were carried out on two, near-end members of the $Gd_{5-x}Y_xGe_4$ series, Gd_4YGe_4 and GdY_4Ge_4, to gain an understanding as to how electronic forces affect the following three issues: (1) the distribution of Gd and Y among the three metal sites, which is known as the coloring problem;[38] (2) the structural transformation from orthorhombic to monoclinic crystal class; and (3) the magnetic ordering behavior.

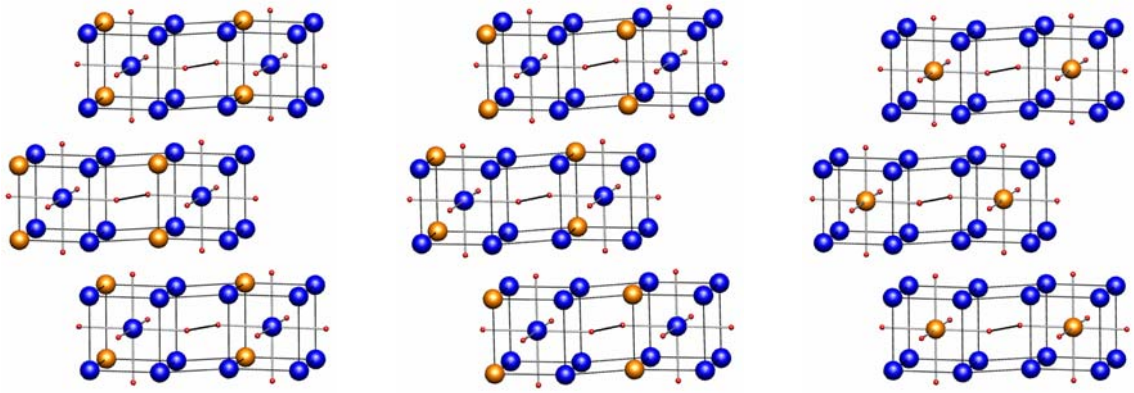

Model 1: Y in M1 site **Model 2:** Y in M2 site **Model 3:** Y in M3 site

Figure 3.6. Three model structures of Gd_4YGe_4 studied by TB-LMTO-ASA and LSDA calculations. Blue spheres are Gd, orange spheres are Y, and smaller red spheres are Ge.

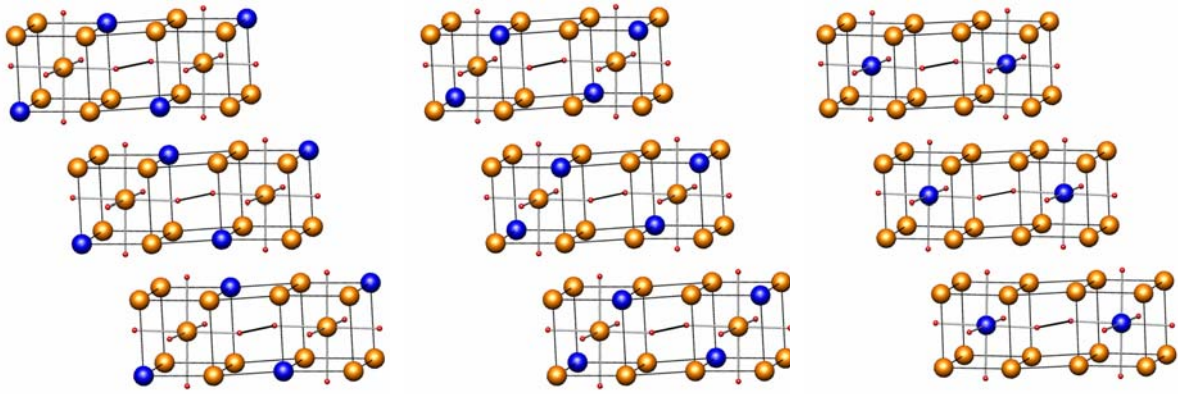

Model 4: Gd in M1 site **Model 5:** Gd in M2 site **Model 6:** Gd in M3 site

Figure 3.7. Three model structures of GdY_4Ge_4 studied by TB-LMTO-ASA and LSDA calculations. Blue spheres are Gd, orange spheres are Y, and smaller red spheres are Ge.

3.4.3.1. Coloring Problem. For all $Gd_{5-x}Y_xTt_4$ systems where *Tt* = Si, Ge, the M sites are all fractionally occupied by Gd and Y atoms: the M3 sites are Y-rich, the M1 sites are Gd-rich. To probe the distribution of Gd and Y atoms among the M sites, we examined three model structures based on the experimentally determined orthorhombic Gd_4YGe_4 and monoclinic GdY_4Ge_4: Model **1 (4)** contains Y (Gd) in 50% of M1 sites and Gd (Y) in M2 and M3 sites; Model **2 (5)** contains Y (Gd) in 50% of M2 sites and Gd (Y) in M1 and M3 sites; Model **3 (6)** contains Y (Gd) in M3 site and Gd (Y) in M1 and M2 sites. These model structures are

illustrated in Figures 3.6 and 3.7; the coloring schemes of Gd and Y atoms were selected to maintain either the mirror plane or inversion center, respectively, within the slabs building up Gd_4YGe_4 and GdY_4Ge_4. According to the total energies per formula unit, which are listed in Table 3.8, Models **3** and **4**, respectively, are the preferred arrangements of Gd and Y atoms for Gd_4YGe_4 and GdY_4Ge_4. Both energetic conclusions indicate that it is most favorable for the Y atoms to occupy the M3 sites and Gd atoms to occupy the M1 sites. This fact is consistent with the refined site occupancies obtained from single crystal diffraction results (see Figure 3.4), as well as from size arguments as based upon the local coordination environments for the different M sites. The M3 site shows the shortest M-M contacts and has the smallest volume of the different M sites in these structures. Nevertheless, the calculated total energies also suggest an influence from the local electronic structure towards influencing the observed coloring.

Table 3.8. Summary of relative total energies and magnetic moments per Gd atom calculated for the models of Gd_4YGe_4 and GdY_4Ge_4 by TB-LMTO-ASA and LSDA.

Model	Minority Atom Site	LDA (meV)	LSDA (meV)	Moment/ Gd (BM)
		Gd_4YGe_4		
1	M1	+268	+267	7.27
2	M2	+281	+275	7.29
3	M3	0	0	7.27
		GdY_4Ge_4		
4	M1	0	0	7.38
5	M2	+127	+138	7.29
6	M3	+355	+355	7.52

An alternative way to study the coloring problem in this series by electronic structure calculations is to compare the valence electron numbers assigned to each M site for the binary examples, Gd_5Ge_4 and Y_5Ge_4, both of which crystallize in the orthorhombic structure at room temperature. For semi-empirical methods, valence electron numbers correspond to

Mulliken populations, for example; in TB-LMTO-ASA, we can approximate these numbers for each atomic site by the sum of integrated electron densities within each WS sphere for the atoms, which are called QVAL values. An alternative approach is to integrate the occupied density of states for each site, which we call IDOS. As a qualitative interpretation, QVAL values are determined from real-space electron densities; IDOS values from reciprocal-space electron densities. The sum of either QVAL or IDOS values will equal the total number of valence electrons in the chemical formula. The TB-LMTO-ASA results for Gd_5Ge_4 and Y_5Ge_4 are listed in Table 3.9. In both cases, the greatest build up of valence electrons at the M sites, as indicated by the highest QVAL value, occurs at the M3 site (center) and the fewest at the M1 and M2 sites (edges). From the diffraction and coloring problem results, Y prefers to occupy the M3 sites and Gd prefers to occupy the M1 sites. According to this alternative perspective for ternary $Gd_{5-x}Y_xGe_4$ phases, Y also prefers the site which has a highest density of valence electrons, whereas Gd prefers the site(s) which has a lower density of valence electrons.

Table 3.9. QVAL and IDOS values evaluated for each site in the asymmetric units for Gd_5Ge_4 and Y_5Ge_4. The location of the sites is indicated in parentheses: edge = edge of slabs; center = center of slabs; BeS = between slabs; WiS = within slabs. V' = volume per formula unit.

	Gd_5Ge_4 [V' = 222.4 Å^3]		**Y_5Ge_4 [V' = 215.8 Å^3]**	
	QVAL	*IDOS*	*QVAL*	*IDOS*
M1 (edge)	2.916	2.899	2.844	2.843
M2 (edge)	2.916	2.899	2.844	2.843
M3 (center)	3.355	3.322	3.333	3.334
Ge1 (BeS)	4.167	4.157	4.283	4.280
Ge2 (WiS)	3.824	3.816	3.863	3.861
Ge3 (WiS)	3.824	3.815	3.863	3.861

These results corroborate well with the trends in the sequence of ionization energies to form M^{3+} ions from the gaseous atoms. The first three ionization energies for Gd are, respectively, 595, 1172, and 1999 kJ/mol, whereas those for Y are 616, 1181 and 1980 kJ/mol.[39] In chemically reduced environments for Gd and Y when both elements occur simultaneously, as observed for $Gd_{5-x}Y_xGe_4$, Gd atoms will tend to lose valence electrons more readily than Y atoms. Thus, in such structures, Gd atoms will occupy sites with lower valence electron concentrations than Y atoms. However, the results listed in Table 3.9 for Gd_5Ge_4 and Y_5Ge_4 cannot be directly compared as the QVAL or IDOS values were calculated for different unit cell volumes, atomic positions, and basis functions for the atomic orbitals.

An additional observation from Table 3.9 is that the Ge sites separate clearly into two chemically distinct environments, which is in accord with earlier electronic structure calculations.[21] The Ge1 sites attract greater electron density than the Ge2 and Ge3 sites within the slabs. The long Ge1-Ge1 distance between slabs but the shorter Ge2-Ge3 contact within slabs have rationalized the Zintl-type formalism $(Gd^{3+})_5(Ge_2)^{6-}(Ge^{4-})_2$: in Table 3.9, the Ge1 sites correspond to the more reduced Ge sites (Ge^{4-}) and the Ge2, Ge3 sites are less reduced and share a valence electron pair.(Ge_2^{6-}).

3.4.3.2. Structural Transformation Problem. To elucidate possible electronic factors that might influence the structural variation in the $Gd_{5-x}Y_xGe_4$ series, idealized model structures of monoclinic GdY_4Ge_4 and orthorhombic Gd_4YGe_4 were constructed from topologically identical slabs. An idealized, isolated slab would have tetragonal symmetry with the fourfold rotation axes intersecting the M3 sites at the centers of every cube of M sites. However, this rotational symmetry is destroyed when the slabs form the various structures in $Gd_{5-x}Y_xGe_4$. In the monoclinic GdY_4Ge_4 structure, space group $P2_1/c$, there is one slab per unit cell with the M3 site coincident with an inversion center; in the orthorhombic Gd_4YGe_4 structure, space group *Pnma*, there are two slabs per unit cell and each slab contains a mirror plane through the middle of each slab intersecting the M3, Ge2, and Ge3 sites. Therefore, to take into account these features as well as the results of the coloring problem for Gd and Y atom, our models have the following common features: (i) the two lattice constants identifying the

periodicity within each slab are set equal, i.e., $b_M = c_M$ in the monoclinic case with β = 113.042° and $a_O = c_O$ in the orthorhombic case;[40] (ii) the lattice metrics and site positions are selected to mimic as closely as possible the nearest neighbor distances in the observed structures; (iii) the 3^2434 nets formed by the M1 and M2 sites in each slab are strictly planar; and (iv) the distribution of Gd and Y atoms are in accord with the results of the coloring problem. For these calculations the WS radii for each atomic site in the asymmetric units were kept the same in the different models, which encompassed both monoclinic and orthorhombic crystal classes for the two compositions.

3.4.3.2.1. GdY_4Ge_4. Figure 3.8 illustrates the four structural models studied. The lattice parameters for the different crystal classes were also restricted as follows: $a_O = c_O = b_M = c_M$ and $a_O \cdot b_O \cdot c_O = 2(a_M \cdot \sin \beta) \cdot b_M \cdot c_M$, where a_O, b_O, c_O are the lattice parameters for a hypothetical orthorhombic structure; a_M, b_M, c_M, β are the lattice parameters for the monoclinic structure of GdY_4Ge_4 obtained from PXRD. As evident from Figure 3.8, to obtain the formula GdY_4Ge_4, each 3^2434 metal layer contains 25% Gd atoms. Furthermore, the Gd distribution in Models **Ia** and **IV** locate inversion centers at the M3 sites (this inversion center in **IV** is strictly lost in the complete 3D structure); [41] for Models **II** and **III**, each slab shows local mirror symmetry containing the M3 sites (again, this mirror plane in **II** is lost in the complete 3D structure). The total energies listed in Table 3.10 show that Model **Ia**, which has a monoclinic structure with its inversion center intact, is the most favorable configuration, which matches our experimental results very well; in fact, the two monoclinic models give the lowest energies.

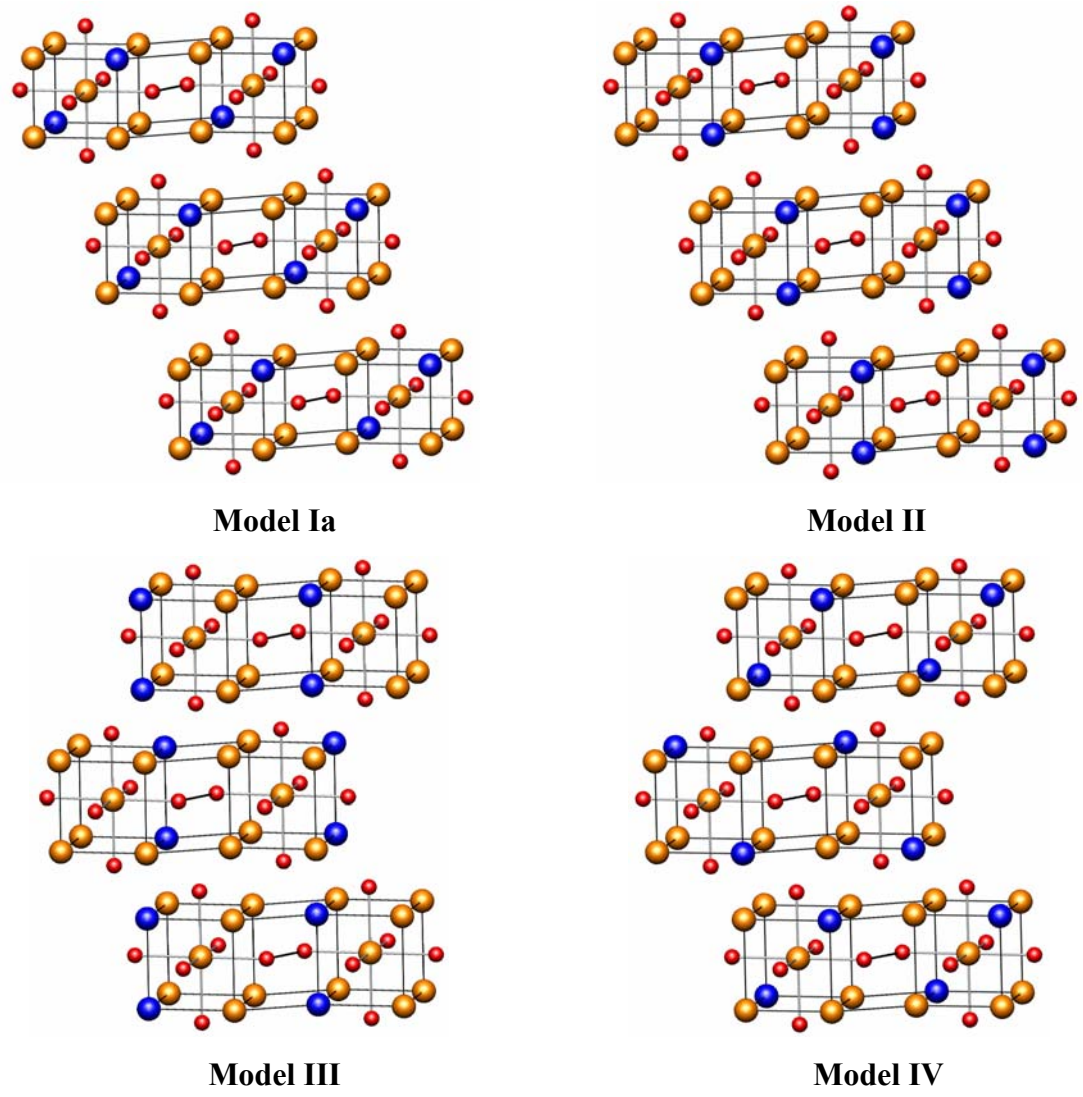

Figure 3.8. Structural models of GdY_4Ge_4. Blue spheres are Gd, orange spheres are Y and red spheres are Ge sites.

Table 3.10. Relative total energies, average QVAL and IDOS values for each of the metal and Ge-sites in the model structures for GdY_4Ge_4. The location of the sites is indicated in parentheses: edge = edge of slabs; center = center of slabs; BeS = between slabs; WiS = within slabs. (f.u. = formula unit).

E / f.u. (meV)	**Monoclinic (Model Ia)**		**Monoclinic (Model II)**	
	0		+133.33	
	QVAL	*IDOS*	*QVAL*	*IDOS*
M1 (edge)	3.278	3.263	3.277	3.262
M2 (edge)	2.599	2.585	2.606	2.592
M3 (center)	3.750	3.730	3.749	3.730
Ge1 (BeS)	3.975	3.968	3.973	3.966
Ge2 (WiS)	3.772	3.765	3.770	3.763

E / f.u. (meV)	**Orthorhombic (Model III)**		**Orthorhombic (Model IV)**	
	+160.82		+361.58	
	QVAL	*IDOS*	*QVAL*	*IDOS*
M1 (edge)	3.312	3.300	3.311	3.295
M2 (edge)	2.576	2.567	2.583	2.570
M3 (center)	3.747	3.733	3.749	3.727
Ge1 (BeS)	3.967	3.963	3.962	3.956
Ge2 / Ge3 (WiS)	3.772	3.766	3.769	3.761

3.4.3.2.2. Gd_4YGe_4. Following to the results of the coloring problem, Y was placed at the M3 site, which is the center of the pseudo-cubes of Gd atoms. The orthorhombic model (**V**) is Model **3**, as shown in Figure 3.6; the monoclinic model (**VI**) is Model **6** (see Figure 3.7) but with orange spheres representing Gd and blue spheres representing Y. The lattice parameters for the two structures also followed the restrictions: $a_O = c_O = b_M = c_M$ and $(a_M \cdot \sin \beta) \cdot b_M \cdot c_M = ½\ a_O \cdot b_O \cdot c_O$, where a_M, b_M, c_M, β are the lattice parameters for the hypothetical monoclinic structure; a_O, b_O, c_O are the lattice parameters for the orthorhombic

structure of Gd_4YGe_4 obtained from PXRD. The total energies listed in Table 3.11 show that Model **V** is energetically more favorable, which also matches well with our experimental results.

Table 3.11. Relative total energies, average QVAL and IDOS values for each of the metal and Ge-sites in the model structures for Gd_4YGe_4. The location of the sites is indicated in parentheses: edge = edge of slabs; center = center of slabs; BeS = between slabs; WiS = within slabs. (f.u. = formula unit).

E / f.u. (meV)	**Orthorhombic (Model V)**		**Monoclinic (Model VI)**	
	0		+331.72	
	QVAL	*IDOS*	*QVAL*	*IDOS*
M1 (edge)	2.910	2.898	2.878	2.871
M2 (edge)	2.910	2.897	2.983	2.976
M3 (center)	3.364	3.341	3.360	3.349
Ge1 (BeS)	4.172	4.163	4.140	4.135
Ge2 / Ge3 (WiS)	3.826	3.819	3.818	3.815

These preliminary theoretical results suggest the interplay among the site preferences for Gd and Y, the local symmetry features of an individual slab, and the local electronic structures of Gd and Y atoms. In GdY_4Ge_4, the minority Gd atoms seek the M1 or M2 sites. These sites accumulate the lowest electron density, so we infer that electrostatic factors maximize the separation between adjacent Gd atoms, and this creates the inversion center for an isolated slab. The valence electron numbers (QVAL values) listed in Table 3.10 confirms this charge distribution: Y sites are electron rich whereas Gd sites are electron poor. The stacking mode thus follows monoclinic symmetry. For Gd_4YGe_4, the majority Gd atoms also seek the M1 and M2 sites; Y prefers the M3 sites at the interior of the slabs. Again, the Gd sites are electron poor; the Y sites are electron rich. In this structural configuration, each slab has both mirror and inversion symmetry. In this case, the mirror plane is retained while the

inversion center is lost for the orthorhombic stacking pattern (**V**). In this situation, further theoretical assessment is required.

The DOS plots for two models each of GdY_4Ge_4 and Gd_4YGe_4 are shown, respectively, in Figures 3.9 and 3.10. Common features to all four curves include (i) three peaks between −9.0 and −7.0 eV, with the two end peaks representing the bonding σ_s and antibonding σ_s^* states of the short Ge_2 dimers and the middle peak being the nonbonding state of the interslab Ge monomers, all with contributions from Gd and Y orbitals; (ii) states between −4.5 eV to just below the Fermi level, involving significant combinations of Ge 4*p*, Y 5*s* and 4*d*, and Gd 6*s* and 5*d* orbitals; and (iii) states just above the Fermi level, which are largely Y 5*s* and 4*d* and Gd 6*s* and 5*d* orbitals. Also, all of them show two pseudogaps in the region between −4.5 eV to just below the Fermi level: these states are derived from the 4*p* bonding states and 4*p* lone pairs of Ge_2 dimers that interact in a bonding manner with the metal *s* and *d* orbitals, which are also involved in M−M bonding. From integration of the DOS curves, the electron count at the lower energy pseudogap is ca. 12 electrons per formula unit for both GdY_4Ge_4 and Gd_4YGe_4; the pseudogap closer to the Fermi level ranges from ca. 29-30 valence electrons per formula unit. Since the interslab Ge-Ge contacts exceed ca. 3.6 Å, we can treat each Ge atom as isoelectronic with noble gas atoms and would, therefore, carry a formal charge of −4. The intraslab Ge_2 dimers can be treated to be isoelectronic with halogen dimers and hence would carry a formal charge of −6. Hence we can write the chemical formula of $(Gd/Y)_5Ge_4$ as $(Gd^{3+}/Y^{3+})_5(Ge_2^{6-})(Ge^{4-})_2(1e^-)$. This formalism accounts for 30 valence electrons per formula unit needed to occupy states up to the second pseudogap, just below the Fermi level. Now, as $(Gd/Y)_5Ge_4$ has 31 valence electrons per formula unit, the additional electron will occupy the narrow band just above this second pseudogap.

The insets in all the DOS plots show the contributions of the M1 and M2 sites to the total DOS with respect to that from the M3 sites, i.e., (M1+M2)/M3. Now, since the ratio of the number of metal sites at the edges (M1/M2) to the number of metal sites at the center (M3) in both orthorhombic and monoclinic structures is 4:1, these curves have a baseline at $y = 4$, which is indicated by the dashed horizontal line. The interesting feature that stands out from these plots is that the contribution to the DOS from the M3 sites near the Fermi level is

about twice that from (M1+M2) sites, in spite of the 4:1 ratio. Moreover, LSDA+U calculations[26, 42] show that the magnetic moment for the M3 site is greater than that for either the M1 or M2 site. Hence, we can conclude that the M3 site acts decisively in shaping the magnetic and structural features observed in these RE_5T_4 systems.

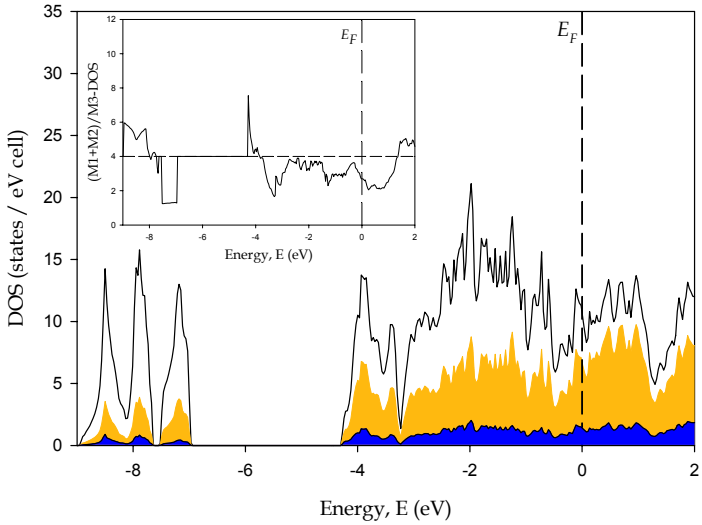

Model Ia

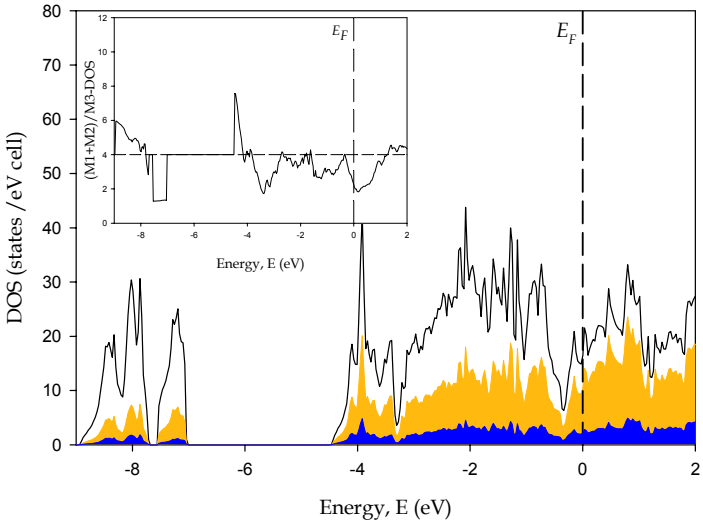

Model IV

Figure 3.9. DOS plots for GdY_4Ge_4. Total DOS (white region), Y PDOS (orange region) Gd PDOS (blue region). The insets show the variation of (M1+M2)/M3-DOS with energy.

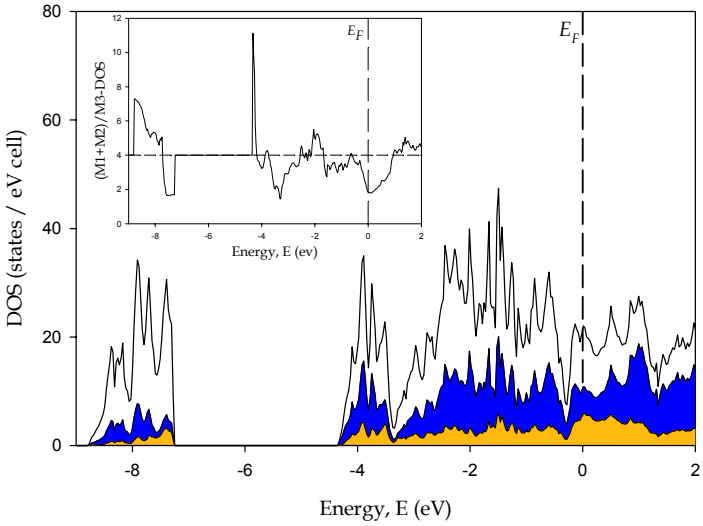

Model V

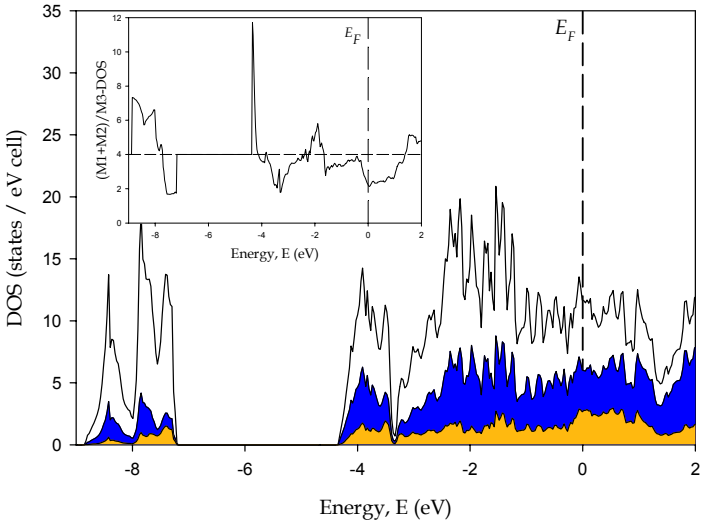

Model VI

Figure 3.10. DOS plots for Gd_4YGe_4. Total DOS (white region), Gd PDOS (blue region), Y PDOS (orange region). The insets show the variation of (M1+M2)/M3-DOS with energy.

3.4.3.3. Magnetic Ordering Problem. The results of LSDA calculations for the lowest energy models of GdY_4Ge_4 (Model **Ia**) and Gd_4YGe_4 (Model **V**) are presented in Table 3.12. In both cases, magnetically ordered patterns achieve lower total energies self-consistently than the corresponding nonmagnetic cases. This approach successfully agrees with our

experimental results: GdY_4Ge_4 prefers ferromagnetic ordering; Gd_4YGe_4 prefers antiferromagnetic ordering. The lowest energy magnetic ordering patterns show completely ferromagnetic coupling within the structural slabs that serve as the building blocks for the entire $Gd_{5-x}Y_xGe_4$ series. Orthorhombic Gd_4YGe_4, therefore, exhibits antiferromagnetic coupling between adjacent slabs; ferromagnetic coupling within slabs for a net zero magnetization.

Table 3.12 also summarizes the local magnetic moments obtained by each calculation. Local moments at the Ge sites are negligibly small and there is a slight polarization occurring at the Y sites. For all models, Y atoms at the M3 sites (center of the pseudocubes within each slab) show the greater local moments than for Y atoms located at the M1 or M2 sites. Since the DOS curves in Figures 3.9 and 3.10 emphasize the significance of valence *s* and *d* orbitals of the M3 sites at the Fermi levels in this series, their magnetic behavior is strongly influenced by exchange coupling between the M3 sites and the M1 or M2 sites of the slabs. With just a single effective conduction electron in $Gd_{5-x}Y_xGe_4$, ferromagnetic coupling within the slab is anticipated by this low band filling.[43] Further calculations, however, are required to elucidate the factors contributing to the magnetic exchange between slabs. Nevertheless, other substitution patterns in various $Gd_{5-x}RE_xGe_4$ examples (RE = La, Lu, Sc)[26, 35] also show interesting variations in magnetic behavior.

Table 3.12. Summary of relative total energies and local magnetic moments calculated for two different models of GdY_4Ge_4 and Gd_4YGe_4 by TB-LMTO-ASA.

	GdY_4Ge_4		**Gd_4YGe_4**	
	Monoclinic (Model **Ia**): E_{NM} = 8690 meV		*Orthorhombic* (Model **V**): E_{NM} = 34760 meV	
	Ferromagnetic	Antiferromagnetic	Ferromagnetic	Antiferromagnetic
E (meV)	0.000	7.68	11.98	0
μ (M1)	Gd: 7.243	Gd: ±7.242	Gd: 7.228	Gd: ±7.245
μ (M2)	Y: 0.009	Y: ±0.002	Gd: 7.228	Gd: ±7.244
μ (M3)	Y: 0.043	Y: ±0.043	Y: 0.133	Y: ±0.146
μ (Ge1)	–0.003	∓ 0.002	–0.028	∓ 0.019
μ (Ge2)	–0.003	∓ 0.003	–0.029	∓ 0.028
μ (Ge3)	---	---	–0.029	∓ 0.028

3.5. Conclusions

A crystal chemical analysis of the distribution of Gd and Y atoms over the various metal sites in the $Gd_{5-x}Y_xTt_4$ (*Tt* = Si, Ge) series has been presented. All silicides adopt the orthorhombic Gd_5Si_4-type structure with short Si-Si contacts between the slabs, which form the primary structural building blocks for these structures. All germanides exhibit long Ge-Ge contacts between these slabs at room temperature, but do show a change in stacking pattern near GdY_4Ge_4 to a monoclinic, $U_2Mo_3Si_4$-type structure. Single crystal diffraction results reveal a preference of the smaller Y atoms to occupy the M3 sites (centers of slabs) whereas the larger Gd atoms prefer to occupy the M1 sites (edges of slabs). Furthermore, the calculated electronic structures for $Gd_{5-x}Y_xGe_4$ show that this preference can also be attributed to the density of valence electrons at the various M-sites: Y prefers the site with the highest density of valence electrons (M3), whereas Gd prefers the site(s) with a lower density of valence electrons (M1/M2). It is this interaction among the site preferences and electronic factors that drives the structural transformation from orthorhombic, Sm_5Ge_4-type to a previously unreported monoclinic, $U_2Mo_3Si_4$-type structure in the $Gd_{5-x}Y_xGe_4$ series. The calculation results also illustrate the central importance of the M3 site in molding the magnetic properties and the structural features observed for these RE_5T_4 systems. It is, therefore, further emphasized and confirmed that these nanometer-sized slabs, centered by the M3 site, can truly be regarded as the fundamental building blocks for many of the structures observed within these systems.

The differences, however, between $Gd_{5-x}Y_xGe_4$ and $Gd_{5-x}Y_xSi_4$ remain to be understood, as the silicides phases retain the robust O(I) structure for compositions with $x < 5$ (Y_5Si_4 adopts the monoclinic $Gd_5Si_2Ge_2$ structure[44]) whereas the germanides phases exhibit the monoclinic $U_2Mo_3Si_4$-type structure for values of x close to 4.0. Although one can speculate about chemical pressure imposed by replacing Ge atoms with the smaller Si atoms, changes in specific RE-RE, RE-*Tt*, and *Tt*-*Tt* interactions have not been evaluated. Investigations of mixed metal and mixed tetrelide systems, i.e., $Gd_{5-x}Y_x(Si,Ge)_4$, as well as additional theoretical study of the site preferences and electronic structures of $Gd_{5-x}Y_xSi_4$ are underway.

3.6. Acknowledgements

The authors thank Prof. Vitalij Pecharsky and Mr. Roger Rink for using the Lakeshore Magnetometer. This work was carried out at the Ames Laboratory, which is operated for the U.S. Department of Energy by Iowa State University under Contract No. DE-AC02-07CH11358. This work was supported by the Materials Sciences Division of the Office of Basic Energy Sciences of the U.S. Department of Energy.

3.7. References

(1) Pecharsky, V. K.; Gschneidner, K. A. Jr., *Phys. Rev. B* **1997**, *78*, 4494.

(2) Pecharsky, V. K.; Gschneidner, K. A. Jr., *Appl. Phys. Lett.* **1997**, *70*, 3299.

(3) Pecharsky, V. K.; Gschneidner, K. A. Jr., *J. Magn. Magn. Mater.* **1997**, *167*, L179.

(4) Miller, G. J., *Chem. Soc. Rev.* **2006**, *35*, 799.

(5) Giguere, A.; Foldeaki, M.; Ravi Gopal, R.; Bose, T. K.; Frydman, A., *Phys. Rev. Lett.* **1999**, *83*, 2262.

(6) Gschneidner, K. A. Jr., Pecharsky, V. K.; Duijin, H. G. M.; Levin. E. M., *Phys. Rev. Lett.* **2000**, *85*, 4190.

(7) Pecharsky, A. O.; Gschneidner, K. A. Jr.; Pecharsky, V. K., *J. Appl. Phys.* **2003**, *93*, 4722.

(8) Gschneidner, K. A. Jr.; Pecharsky, V. K.; Tsokol, A. O., *Rep. Prog. Phys.* **2005**, *68*, 1479.

(9) Morellon, L.; Blasco, J.; Algarabel, P. A.; Ibara, M. R., *Phys. Rev. B* **2000**, *62*, 1022.

(10) Morellon, L.; Algarabel, P. A.; Ibara, M. R.; Blasco, J.; Garcia-Landa, B., *Phys. Rev. B* **1998**, *58*,R14721.

(11) Magen, C.; Morellon, L.; Algarabel, P. A.; Marquina, C.; Ibara, M. R., *J. Phys.: Condens. Matter* **2003**, *15*, 2389.

(12) Morellon, L.; Stankiewicz, J.; Garcia-Landa, B.; Algarabel, P. A.; Ibara, M. R., *Appl. Phys. Lett.* **1998**, *73*, 3462.

(13) Levin. E. M.; Pecharsky, V. K.; Gschneidner, K. A. Jr., *Phys. Rev. B* **1999**, *60*,7993.

(14) Levin. E. M.; Pecharsky, V. K.; Gschneidner, K. A. Jr., *J. Magn. Magn. Mater.* **2000**, *210*, 181.

(15) Levin. E. M.; Pecharsky, V. K.; Gschneidner, K. A. Jr., *Phys. Rev. B* **2001**, *63*, 174110.

(16) Stankiewicz, J.; Morellon, L.; Algarabel, P. A.; Ibara, M. R., *Phys. Rev. B* **2000**, *61*, 12651.

(17) Choe, W.; Pecharsky, V. K.; Pecharsky, A. O.; Gschneidner, K. A. Jr.; Young, V. G. Jr.; Miller, G. J., *Phys. Rev. Lett.* **2000**, *84*, 4617.

(18) Choe, W.; Miller, G. J.; Meyers, J.; Chumbley, S.; Pecharsky, A. O., *Chem. Mater.* **2003**, *15*, 1413.

(19) Smith, G. S.; Johnson, Q.; Tharp, A. G. *Acta Crystallogr*. **1967**, *22*, 269.

(20) Pecharsky, A. O.; Gschneidner, K. A. Jr.; Pecharsky, V. K.; Schindler, C. E., *J. Alloys Compd.* **2002**, *338*, 126.

(21) Choe, W.; Pecharsky, A. O.; Wörle, M.; Miller, G. J., *Inorg. Chem.* **2003**, *42*, 8223.

(22) Mozharivskyj, Y.; Choe, W.; Pecharsky, A. O.; Miller, G. J., *J. Am. Chem. Soc.* **2003**, *125*, 15183.

(23) Mozharivskyj, Y.; Tsokol, A. O.; Miller, G. J., *Z. Kristallogr*. **2006**, *221*, 493.

(24) Misra, S.; Miller, G. J., *J. Solid State Chem.* **2006**, *179*, 2290.

(25) Elbicki, J. M.; Zhang, L. Y.; Obermyer, R. T.; Wallace, W. E., *J. Appl. Phys.* **1991**, *69*, 5571.

(26) Mudryk, Ya.; Paudayl, D.; Pecharsky, V. K.; Gschneidner, K. A. Jr.; Misra, S.; Miller, G. J., in preparation.

(27) Shannon, R. D., *Acta Cryst. A*, **1976**, *32*, 751.

(28) Thoburn, W. C.; Legvold, S.; Spedding, F. H., *Phys. Rev.* **1958**, *110*, 1298.

(29) Holtzberg, F.; Gambino, R. J.; McGuire, T. R., *J. Phys. Chem. Solids* **1967**, *28*, 2283.

(30) Richter, K. W.; Franzen, H. F., *J. Solid State Chem*. **2000**, *150*, 347.

(31) Hunter, B. A., *International Union of Crystallography Commission on Powder Diffraction Newsletter*. **1998**, *20*, 21.

(32) *XRD Single Crystal Software*; Bruker Analytical X-ray Systems: Madison, USA, **2002**.

(33) (a) Andersen, O. K., *Phys. Rev. B* **1975**, *12*, 3060; (b) Andersen, O. K.; Jepsen, O., *Phys. Rev. Lett.* **1984**, *53*, 2571; (c) Andersen, O. K.; Jepsen, O.; Glötzel, D., in *Highlights of Condensed-Matter Theory*; Bassani, F.; Fumi, F.; Tosi, M. P., Eds.; North-Holland: New York, **1985**; (d) Andersen, O. K., *Phys. Rev. B* **1986**, *34*, 2439; (e)

Tank, R. W.; Jepsen, O.; Burckhardt. A.; Andersen, O. K., *TB-LMTO-ASA program*, *Version 4.7c*; Max-Planck-Institut für Festkörperforschung: Stuttgart, Germany, **1994**.

(34) Jepsen, O.; Andersen, O. K., *Z. Phys. B* **1995**, *97*, 35.

(35) Misra, S.; Miller, G. J., to be published.

(36) Bodak, O. I.; Gorelenko, Y. K.; Yarovets, V. I.; Skolozdra, R. V., *Inorg. Mater. (transl. Izv. Akad. Nauk. SSSR)* **1984**, *20*, 741.

(37) Bihan, T. L.; Nöel, H, *J. Alloys Comp.* **1995**, *227*, 44.

(38) Miller, G. J., *Eur. J. Inor. Chem*. **1998**, *5*, 523.

(39) Greenwood, N. N.; Earnshaw, A., *Chemistry of the Elements*, Elsevier Butterworth-Heinemann, Oxford, **1997**.

(40) The coordinates and the lattice parameters used for building both orthorhombic and monoclinic structural models are provided in Supporting Information.

(41) A different coloring of Gd atom in the monoclinic structure was also studied as Model **Ib**. The calculation results and the structural figure are included in Supporting Information.

(42) Paudayl, D.; Pecharsky, V. K.; Gschneidner, K. A. Jr.; Harmon, B. N., *Phys. Rev. B* **2007**, *75*, 094427.

(43) (a) Samolyuk, G.; Fokwa, B. P. T.; Dronskowski, R.; Miller, G.J., *Phys. Rev. B* **2007**, *76*, 094404; (b) Samolyuk, G.; Miller, G. J., *J. Computational Chem.*, **2008**, *29*, 2177.

(44) Pecharsky, A.O.; Pecharsky, V. K.; Gschneidner, K.A., Jr. *J. Alloys Comp.* **2004**, *379*, 127.

3.8. Supporting Information

Table 3.S1. Crystallographic data for $Gd_{5-x}Y_xSi_4$ (x = 0-4) as obtained by single crystal X-ray diffraction (space group *Pnma* (No. 62), Mo $K\alpha$ radiation, 2θ range = 4-57°, T = 298(2) K, Z = 4).

x	0	1	2	3	4
Loaded Composition	Gd_5Si_4	Gd_4YSi_4	$Gd_3Y_2Si_4$	$Gd_2Y_3Si_4$	GdY_4Si_4
Refined Composition	Gd_5Si_4	$Gd_{3.92(9)}Y_{1.08}Si_4$	$Gd_{2.9(1)}Y_{2.1}Si_4$	$Gd_{1.97(6)}Y_{3.03}Si_4$	$Gd_{0.98(4)}Y_{4.02}Si_4$
***a*, Å**	7.482(2)	7.464(2)	7.435(2)	7.429(5)	7.415(4)
***b*, Å**	14.738(4)	14.708(5)	14.690(4)	14.696(9)	14.607(7)
***c*, Å**	7.746(2)	7.742(2)	7.739(2)	7.738 (5)	7.713(4)
***V*, Å^3**	854.2(4)	849.9(5)	845.3(4)	844.8(9)	835.4(7)
Independent Reflections	1067	1063	1036	1044	1032
No. of Parameters	47	50	50	50	50
Final R indices [I>2sigma(I)]	R1 = 0.0326, wR2 = 0.0591	R1 = 0.0356, wR2 = 0.0702	R1 = 0.0484, wR2 = 0.0912	R1 = 0.0351, wR2 = 0.0655	R1 = 0.0350, wR2 = 0.0610
Peak/hole, e/Å^3	2.061 / −1.898	2.700 / −1.802	2.323 / −1.764	1.650 / −1.338	1.516 / −1.162

Table 3.S2. Atomic coordinates, site occupancies and isotropic displacement parameters for $Gd_{5-x}Y_xSi_4$ (x = 0-4) as obtained by single crystal X-ray diffraction. Coordinates are represented in accordance with similar previously reported structure types.

Atom		***x***	***y***	***z***	**occupancy[a]**	**U_{eq}, (Å^2)[b]**
			Gd_5Si_4			
M1	8d	0.0289(1)	0.4028(1)	0.1827(1)	1	0.009(1)
M2	8d	0.6837(1)	0.3777(1)	0.8204(1)	1	0.008(1)
M3	4c	0.1442(1)	¾	0.5112(1)	1	0.007(1)
Si1	8d	0.8562(4)	0.4602(2)	0.5281(4)	1	0.010(1)
Si2	4c	0.0210(5)	¾	0.0998(5)	1	0.009(1)
Si3	4c	0.2589(6)	¾	0.8748(6)	1	0.010(1)

Table 3.S2. (continued)

Atom		*x*	*y*	*z*	occupancy[a]	U_{eq}, (Å^2)[b]
			$Gd_{3.92(9)}Y_{1.08}Si_4$			
M1	8d	0.0276(1)	0.4030(1)	0.1820(1)	0.87(2)	0.010(1)
M2	8d	0.6833(1)	0.3776(1)	0.8203(1)	0.74(2)	0.008(1)
M3	4c	0.1462(1)	¾	0.5124(1)	0.69(2)	0.008(1)
Si1	8d	0.8553(4)	0.4606(2)	0.5283(4)	1	0.010(1)
Si2	4c	0.0214(6)	¾	0.1017(6)	1	0.011(1)
Si3	4c	0.2620(6)	¾	0.8755(6)	1	0.011(1)
			$Gd_{2.9(1)}Y_{2.1}Si_4$			
M1	8d	0.0265(1)	0.4033(1)	0.1816(1)	0.71(2)	0.010(1)
M2	8d	0.6826(1)	0.3775(1)	0.8205(1)	0.50(2)	0.009(1)
M3	4c	0.1474(1)	¾	0.5131(2)	0.45(2)	0.009(1)
Si1	8d	0.8540(5)	0.4605(3)	0.5284(4)	1	0.012(1)
Si2	4c	0.0226(7)	¾	0.1029(6)	1	0.012(1)
Si3	4c	0.2645(7)	¾	0.8736(7)	1	0.011(1)
			$Gd_{1.97(6)}Y_{3.03}Si_4$			
M1	8d	0.0252(1)	0.4033(1)	0.1812(1)	0.54(1)	0.010(1)
M2	8d	0.6820(1)	0.3775(1)	0.8207(1)	0.32(1)	0.008(1)
M3	4c	0.1488(1)	¾	0.5132(1)	0.26(1)	0.009(1)
Si1	8d	0.8529(3)	0.4604(2)	0.5287(3)	1	0.011(1)
Si2	4c	0.0215(4)	¾	0.1041(4)	1	0.009(1)
Si3	4c	0.2658(4)	¾	0.8736(4)	1	0.011(1)
			$Gd_{0.98(4)}Y_{4.02}Si_4$			
M1	8d	0.0244(1)	0.4034(1)	0.1809(1)	0.31(1)	0.010(1)
M2	8d	0.6814(1)	0.3774(1)	0.8208(1)	0.13(1)	0.008(1)
M3	4c	0.1498(1)	¾	0.5131(1)	0.09(1)	0.008(1)
Si1	8d	0.8516(3)	0.4604(1)	0.5289(2)	1	0.010(1)
Si2	4c	0.0225(4)	¾	0.1040(4)	1	0.010(1)
Si3	4c	0.2675(4)	¾	0.8725(4)	1	0.009(1)

[a] All M1, M2 and M3 sites are fully occupied with a mixture of Gd and Y atoms. Only Gd occupations are listed. The only exception is Gd_5Si_4 where the M1, M2 and M3 sites are fully occupied by Gd

[b] U(eq) is defined as one-third of the trace of the orthogonalized U_{ij} tensor.

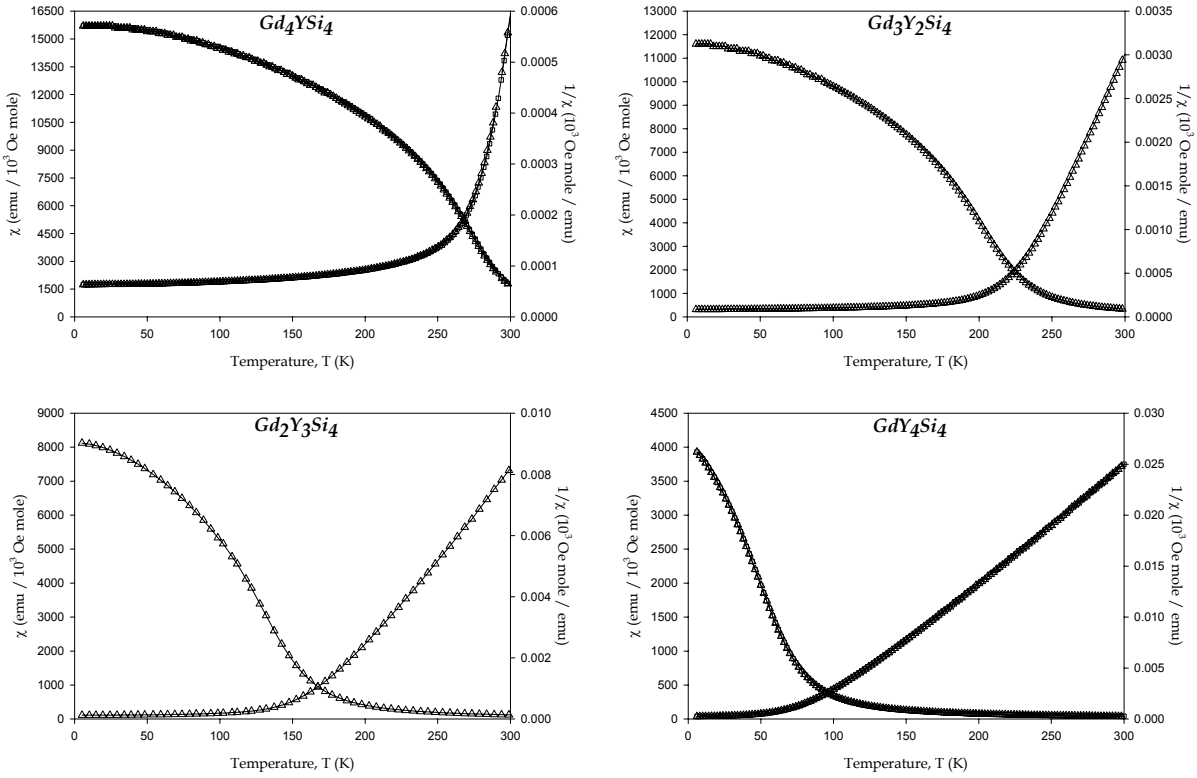

Figure 3.S1. Magnetic susceptibility plots for $Gd_{5-x}Y_xSi_4$ series. The measurements were carried out under a magnetic filed, H = 10 kOe.

Table 3.S3. Crystallographic data for $Gd_{5-x}Y_xGe_4$ (x = 0, 1, 2, 3, 3.2, & 3.4) as obtained by single crystal X-ray diffraction (space group *Pnma* (No. 62), Mo K_α radiation, 2θ range = 4-57°, T = 298(2) K, Z = 4).

x	0	1	2	3	3.2	3.4
Loaded Composition	Gd_5Ge_4	Gd_4YGe_4	$Gd_3Y_2Ge_4$	$Gd_2Y_3Ge_4$	$Gd_{1.8}Y_{3.2}Ge_4$	$Gd_{1.6}Y_{3.4}Ge_4$
Refined Composition	Gd_5Ge_4	$Gd_{4.02(6)}Y_{0.98}Ge_4$	$Gd_{2.96(5)}Y_{2.04}Ge_4$	$Gd_{1.91(4)}Y_{3.09}Ge_4$	$Gd_{1.74(5)}Y_{3.26}Ge_4$	$Gd_{1.55(6)}Y_{3.45}Ge_4$
***a* (Å)**	7.691(2)	7.676(2)	7.663(3)	7.653(4)	7.647(1)	7.645(2)
***b* (Å)**	14.820(3)	14.787(4)	14.772(6)	14.758(8)	14.741(2)	14.720(4)
***c* (Å)**	7.780(2)	7.763(2)	7.748(3)	7.741(4)	7.726(1)	7.720(2)
***V* (Å^3)**	886.8(3)	881.1(4)	877.1(6)	874.3(9)	870.8(2)	868.7(4)

Table 3.S4. Crystallographic data for $Gd_{5-x}Y_xGe_4$ (x = 3.6, 4.4, 4.6, 4.8 & 5.0) as obtained by single crystal X-ray diffraction (space group *Pnma* (No. 62), Mo K_α radiation, 2θ range = 4-57°, T = 298(2) K, Z = 4).

x	3.6	4.4	4.6	4.8	5.0
Loaded Composition	$Gd_{1.4}Y_{3.6}Ge_4$	$Gd_{0.6}Y_{4.4}Ge_4$	$Gd_{0.4}Y_{4.6}Ge_4$	$Gd_{0.2}Y_{4.8}Ge_4$	Y_5Ge_4
Refined Composition	$Gd_{1.26(4)}Y_{3.74}Ge_4$	$Gd_{0.61(5)}Y_{4.39}Ge_4$	$Gd_{0.29(3)}Y_{4.71}Ge_4$	$Gd_{0.17(3)}Y_{4.83}Ge_4$	Y_5Ge_4
***a* (Å)**	7.638(2)	7.645(3)	7.636(1)	7.636(1)	7.637(2)
***b* (Å)**	14.723(4)	14.728(6)	14.713(3)	14.713(2)	14.695(4)
***c* (Å)**	7.714(2)	7.711(3)	7.705(1)	7.708(1)	7.711(2)
***V* (Å^3)**	867.4(4)	868.2(6)	865.7(3)	866.0(2)	865.3(4)

Table 3.S5. Crystallographic data for $Gd_{5-x}Y_xGe_4$ (x = 3.8, 4.0 & 4.2) as obtained by single crystal X-ray diffraction (space group $P2_1/c$ (No. 14), Mo K_α radiation, 2θ range = 4-57°, T = 298(2) K, Z = 2).

x	3.8	4.0	4.2
Loaded Composition	$Gd_{1.2}Y_{3.8}Ge_4$	GdY_4Ge_4	$Gd_{0.8}Y_{4.2}Ge_4$
Refined Composition	$Gd_{1.11(3)}Y_{3.89}Ge_4$	$Gd_{1.00(3)}Y_{4.00}Ge_4$	$Gd_{0.77(3)}Y_{4.23}Ge_4$
***a* (Å)**	7.996(2)	8.001(3)	7.998(1)
***b* (Å)**	7.757(2)	7.754(3)	7.751(1)
***c* (Å)**	7.602(2)	7.601(3)	7.600(1)
***β* (°)**	112.879(5)	112.945(6)	112.952(2)
***V* (Å^3)**	434.5(2)	434.2(3)	433.8(1)

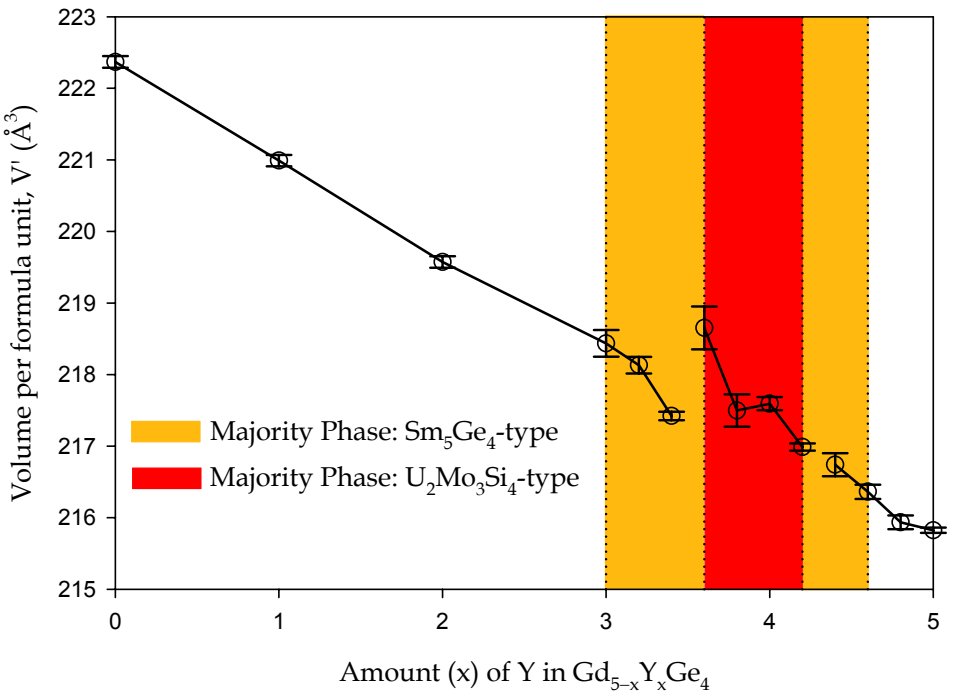

Figure 3.S2. Variation of the unit cell volume per formula unit, V', for $Gd_{5-x}Y_xGe_4$ phases as a function of Y amount as obtained from powder X-ray diffraction. The shaded regions delineate the two-phase region.

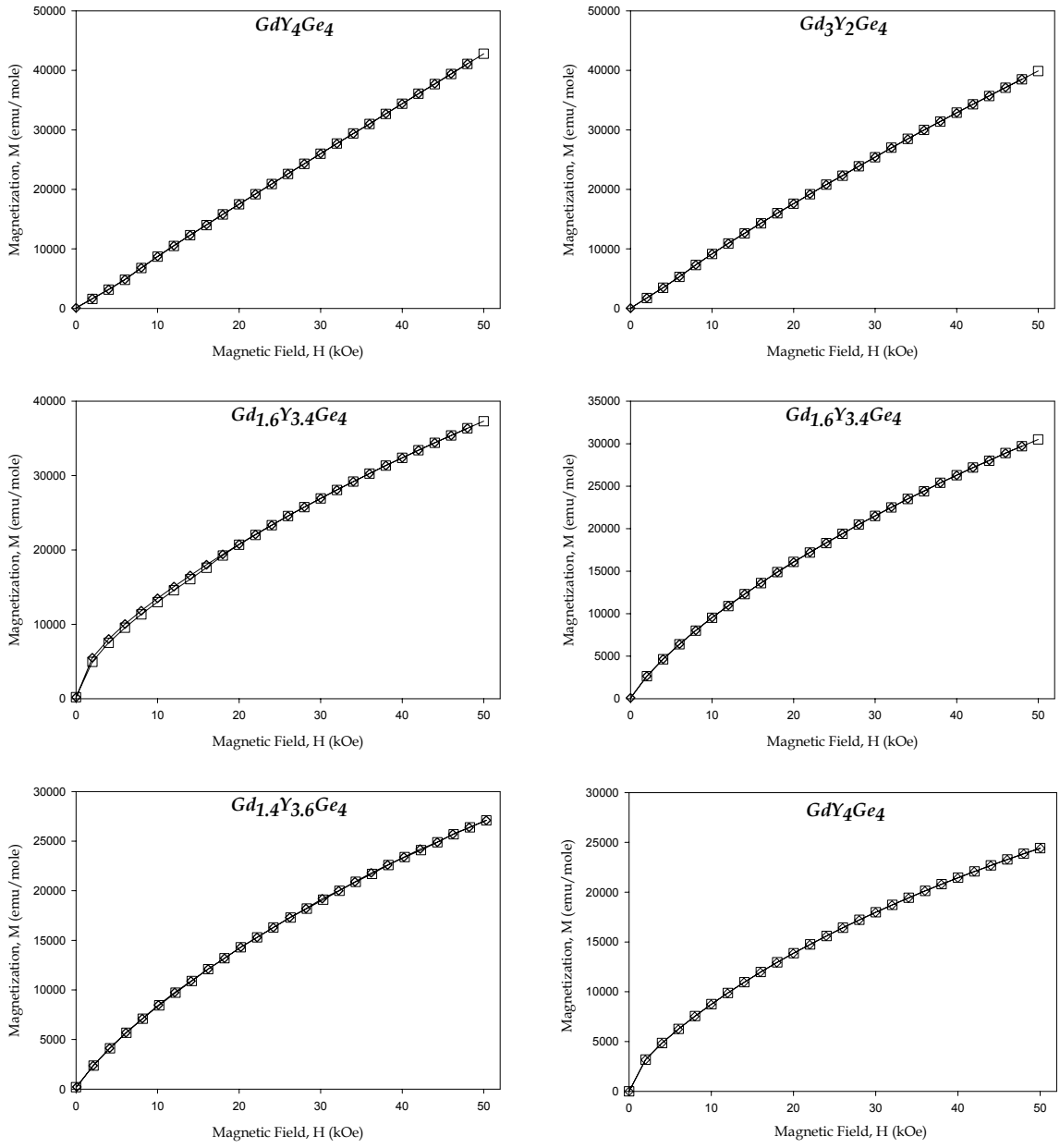

Figure 3.S3. The magnetization isotherms measured for H = 0-50 kOe at T = 5 K. Squares represent data for increasing magnetic field and diamonds are data for decreasing magnetic field.

Table 3.S6. Coordinates for the monoclinic structural models, Model **Ia**, Model **Ib**, Model **II** and Model **VI**. (Lattice parameters for Model **Ia**, **Ib** and **II**: a_M = 8.0067 Å; b_M = c_M = 7.685396515* Å; β = 113.042°; space group = $P2_1/c$)

Atom	***x***	***y***	***z***
M1	− 0.283162	0.317000	0.183 − 0.25 tan (β−90°)
M2	0.283162	0.317000	0.183 + 0.25 tan (β−90°)
M3	0	0	0
Ge1	0.412363	0	0.412363 tan (β−90°)
Ge2	0	0.615700	0.115700

* To ensure the errors of the calculations due to the accuracy of the input lattice constants are kept to a minimum, a greater number of significant digits were used.

Table 3.S7. Total energy, average QVAL and IDOS values for each of the metal and Ge-sites in the model structure for GdY_4Ge_4 (BeS = between slabs; WiS = within slabs).

	Monoclinic (Model Ib)	
E / f.u. (meV)	+ 0.87	
	QVAL	*IDOS*
M1 (edge)	3.278	3.263
M2 (edge)	2.599	2.585
M3 (center)	3.750	3.730
Ge1 (BeS)	3.974	3.968
Ge2 (WiS)	3.772	3.765

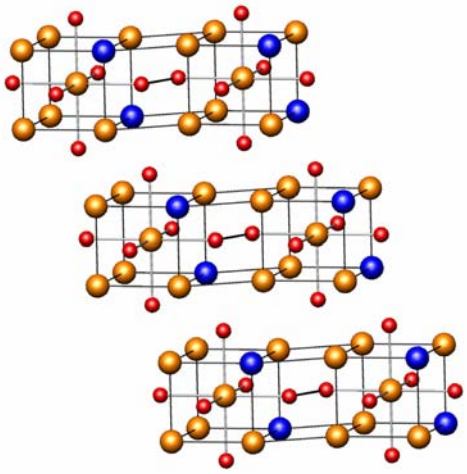

Model Ib

Figure 3.S4. Structural model of GdY_4Ge_4. Blue spheres are Gd, orange spheres are Y and red spheres are Ge sites.

Table 3.S8. Coordinates for the orthorhombic structural models, Model **III**, Model **IV** and Model **V**. (Lattice parameters for Model **V**: $a_O = c_O = 7.726483663^*$ Å; $b_O = 14.8070$ Å; space group = *Pnma*)

Atom	***x***	***y***	***z***
M1	− 0.06700	0.39158	0.18300
M2	0.56700	0.39158	− 0.18300
M3	¼	¼	0
Ge1	¼	0.45618	0
Ge2	0.86570	¼	− 0.11570
Ge3	− 0.36570	¼	0.11570

* To ensure the errors of the calculations due to the accuracy of the input lattice constants are kept to a minimum, a greater number of significant digits were used.

Chapter 4

On the Crystal Structure, Metal Atom Site Preferences and Magnetic Properties of $Nd_{5-x}Er_xTt_4$ (*Tt* = Si or Ge)

An article submitted in *Zeitschrift für Anorganische und Allegemeine Chemie*

Sumohan Misra, Eric T. Poweleit, Gordon J. Miller

4.1. Abstract

A crystallographic study of the Nd/Er site preferences in the $Nd_{5-x}Er_xTt_4$ (*Tt* = Si, Ge) series prepared by high-temperature methods is presented. For $Nd_{5-x}Er_xSi_4$, phases with $x \leq 1.0$ adopt the tetragonal Zr_5Si_4-type structure. On the other hand, phases in the composition range of $2.0 \leq x \leq 5.0$ exhibits the Gd_5Si_4-type structure. For all silicides, all Si atoms belong to Si-Si dimers. In the $Nd_{5-x}Er_xGe_4$ system, phases with $x < 3.2$ and $x = 4.0$ adopt the orthorhombic Sm_5Ge_4-type structure. For the composition range of $3.2 \leq x \leq 4.0$, a monoclinic $U_2Mo_3Si_4$-type structure (space group $P2_1/c$) occurs as the majority phase. This monoclinic structure, until recently, was not reported for similar RE_5T_4 systems, and differs from the known monoclinic $Gd_5Si_2Ge_2$-type (space group $P2_1/a$) because all Ge···Ge contacts between slabs are equivalent. The structural relationships between the Zr_5Si_4-type, Gd_5Si_4-type, Sm_5Ge_4-type, and $U_2Mo_3Si_4$-type structures are discussed. Single crystal refinements of the metal atom occupancies for the three different metal sites in the asymmetric unit of all structure types reveal a partially ordered nonstatistical arrangement of Nd and Er atoms. The magnetic properties of some $Nd_{5-x}Er_xGe_4$ phases are also reported. Nd_4ErGe_4 shows an antiferromagnetic-type transition similar to Gd_5Ge_4. As the Er concentration increases ($2 \leq x \leq 4$), these phases exhibit, at least, ferrimagnetic-type ordering.

4.2. Introduction

The last quarter of the 20th century has seen a growing interest in environmentally friendly, alternative technologies for refrigeration from ambient temperature to the temperatures of helium and hydrogen liquefaction (ca. 4.2-20 K). These new technologies should potentially help to replace today's common gas compression/expansion technology, which achieves cooling efficiencies approaching 40% of the Carnot limit[1] and uses ozone depleting chemicals (ODCs) like hydrochlorofluorocarbons (HCFCs). One such environmentally benign cooling technique is magnetic refrigeration or thermomagnetic cooling, which utilizes the magnetocaloric effect (MCE) and can achieve an efficiency of ca. 60% of the Carnot limit and is one of the most ecologically clean cooling techniques over a wide range of temperatures.[2] One of the attractive classes of materials that exhibit extraordinary magnetic responses and have the potential for applications in magnetic refrigeration is the rare-earth tetrelides, RE_5Tt_4 (RE = rare-earth element; "*Tt*" or "tetrelide" corresponds to Group 14/IVB element viz. Si and Ge).[1, 3-4]

This series was first reported by Holtzberg and coworkers in the late 1960s.[5] These intermetallic compounds are characterized by an intimate relationship between crystal chemistry and physical properties, e.g., magnetism. Recent studies reveal that the rich chemistry and physics associated with these compounds are closely related to their two-dimensional structural building blocks and strong magnetoelastic coupling present in these materials.[6] Features that have captured the attention of solid-state chemists include microscopic twinning,[7] dependence of crystal structures on the Si/Ge ratio,[8] valence electron count,[9-10] and their ability to break and re-form covalent bonds existing between pairs of *Tt* atoms on heating and cooling near the corresponding magnetic transition temperatures. Such structural behavior has been termed "nanoscale zippers".[11] The crystal structures of $Gd_5(Si_xGe_{1-x})_4$ and many other RE_5T_4 (RE = rare earth; *T* = Si, Ge, Ga, Sn or their various combinations) materials are built from slabs of two eclipsed 3^2434 nets of RE atoms. The arrangements of the atoms in the slabs and, in turn, the structural and magnetic properties depend on the presence or absence of interslab main group-main group chemical bonds. Theoretical and experimental investigations indicate that the giant MCE found in these materials is due to a first-order phase transformation, e.g., as observed in $Gd_5Si_2Ge_2$ at ca.

277 K at which a transition between ferromagnetic and paramagnetic behavior is coupled with, respectively, an orthorhombic Gd_5Si_4-type and monoclinic $Gd_5Si_2Ge_2$-type crystallographic transition.[6, 11]

The majority of research activity, however, has emphasized the chemistry, physics and materials science of Gd_5T_4 or $Gd_{5-x}RE_xT_4$ systems.[1-4, 6-14] The physical and chemical properties of tetrelides for other rare-earth or mixtures of rare-earth elements at the 5:4 stoichiometry have been explored to a much lesser extent.[15-17] For mixed rare-earth systems in particular, e.g., as in $Gd_{5-x}Y_xTt_4$, the different crystallographic sites for the metal atoms show distinct site preferences that significantly influence structural and magnetic characteristics.[15] We report herein the results obtained for a systematic investigation of a mixed rare-earth system comprised of a lighter and larger rare-earth, Nd, and a heavier and smaller rare-earth, Er, on the structural features and magnetic properties in both pseudobinary Si and Ge systems.

In the Nd-Er-Si system we observe a structural transition from the tetragonal Zr_5Si_4-type[18] crystal structure (which is a typical structure type for the silicon-rich, lighter rare-earth cases) to the orthorhombic Gd_5Si_4-type[19] structure (which is a typical structure type for the silicon-rich, heavier rare-earth cases). For the Nd-Er-Ge system, together with variations in magnetic ordering, we also observe a structural transformation from the orthorhombic Sm_5Ge_4-type[20] to a new monoclinic $U_2Mo_3Si_4$-type[21] structure for certain compositions. This structure is different from the known monoclinic structure of $Gd_5Si_2Ge_2$-type[6] and, until recently, was not reported for other RE_5T_4 systems.[15]

4.3. Experimental Section

4.3.1. Syntheses: Samples of $Nd_{5-x}Er_xSi_4$ where x = 1, 2, 3, and 4 and $Nd_{5-x}Er_xGe_4$ where x = 1, 2, 3, 3.2, 3.6, and 4 were prepared by arc-melting its constituent elements in an argon atmosphere on a water-cooled copper hearth. The starting materials were pieces of neodymium (99.99 wt. %, Materials Preparation Center, Ames Laboratory), erbium (99.99 wt. %, Materials Preparation Center, Ames Laboratory), silicon (99.9999 wt. %, Alfa Aesar) and germanium (99.9999 wt. %, Alfa Aesar). Each ingot had a total weight of ca. 1.5 g and was remelted six times with the button being turned over after each melting to ensure

homogeneity. Weight losses during melting were less than 0.1 wt. percent. At room temperature the as-cast samples were stable to decomposition on exposure to air and moisture. A powder X-ray diffraction pattern for an exposed sample did not reveal any additional peaks compared to one for an unexposed sample.

4.3.2. Powder X-ray Diffraction: The as-cast samples were examined by powder X-ray diffraction for identification and to assess phase purity. Powder patterns were obtained using an Enraf-Nonius Guinier camera with monochromatized Cu K_α radiation (λ = 1.54187 Å). To probe the purity and homogeneity of all phases, all diffraction patterns were analyzed by full-profile Rietveld refinement using *LHPM RIETICA* software.[22] Only the scale factor and the lattice parameters of each phase were refined. The isotropic displacement parameters of all atoms in each phase were assumed to be the same. For $Nd_{5-x}Er_xSi_4$, the profile residuals, R_p, varied from ca. 2.01 to 3.53 and derived Bragg residuals, R_B, varied from ca. 2.51 to 4.06. For $Nd_{5-x}Er_xGe_4$, the profile residuals, R_p, varied from ca. 2.03 to 3.32 and their derived Bragg residuals, R_B, varied from ca. 3.90 to 6.52.

4.3.3. Single-Crystal X-ray Crystallography: Several single crystals from the as-cast samples were mounted on the tip of a glass fiber. Room temperature intensity data were collected on a Bruker Smart Apex CCD diffractometer with Mo K_α radiation (λ = 0.71073 Å) and a detector-to-crystal distance of 5.990 cm. Data were collected over a full sphere of reciprocal space by taking three sets of 606 frames with 0.3° scans in ω with an exposure time of 10 seconds per frame. The 2θ range extended from 4° to 57°. The *SMART*[23] software was used for data acquisition. Intensities were extracted and then corrected for Lorentz and polarization effects by the *SAINT*[23] program. Empirical absorption corrections were accomplished with the program *SADABS*,[23] which is based on modeling a transmission surface by spherical harmonics employing equivalent reflections with $I > 3\sigma(I)$. Structure solutions and refinements were performed with the *SHELXTL*[23] package of crystallographic programs.

4.3.4. Magnetic Property Measurements: Magnetic measurements were carried out using a Lake Shore ac / dc susceptometer-magnetometer, model 7225 on polycrystalline samples. These included dc magnetic susceptibility measurements between ca. 4 and 300 K and isothermal magnetization measurements in dc magnetic fields varying from 0 to 50 kOe. For the susceptibility measurements, the samples were first cooled under zero magnetic field (zfc) and then the measurements were carried out on heating under a 10 kOe magnetic field. The measurements were then repeated upon cooling with the magnetic field turned on (fc). All data were corrected for T-independent contributions.

4.4. Results and Discussion

4.4.1. Structural Features of $Nd_{5-x}Er_xSi_4$. Powder X-ray diffraction investigation of $Nd_{5-x}Er_xSi_4$ samples reveals that two distinct phases exist in this system. For $x \leq 1.0$, the tetragonal Zr_5Si_4-type structure forms as the majority phase; and for $x \geq 2.0$, the orthorhombic Gd_5Si_4-type structure is observed as the majority phase. The lattice parameters obtained from Rietveld refinement of the powder data are presented in Table 4.1. Selected crystallographic data, atomic coordinates, site occupancies and isotropic displacement parameters from single crystal X-ray diffraction experiments are presented in Tables 4.2 and 4.3. The distances of the nearest atom from the highest residual peak for each structural solution are listed in parentheses (Table 4.2). As expected, due to the smaller size of Er compared to Nd,[24] the unit cell volume gradually decreases with increasing Er content.

The tetragonal, Zr_5Si_4-type crystal structure has five atoms in the asymmetric unit: three crystallographically independent sites for Nd or Er metal atoms and only two distinct sites for the tetrelide atoms and is typically found for the lighter rare-earth, silicon-rich 5:4 cases.[1] The projection of the crystal structure along the *a*-axis is shown in Figure 4.1. The tetrelide atoms (Si1 and Si2) are surrounded by tricapped trigonal prisms; each prism is formed by six RE (M1 and M2) atoms while the capping atoms are two RE (M3) atoms and one Si atom. Therefore, two of these Si-centered prisms share a common rectangular face, which creates rhombic prisms. Furthermore, the Si atoms are slightly displaced from the center of the prisms toward each other, which may be formulated as Si_2^{6-} dimers. The structure may be considered as a complex, three-dimensional packing of these rhombic

prisms. The local coordination environment at each RE site, in terms of end-on/side-on coordination to Si–Si dimers, reveals a separate picture for the two 8*b* (M1 and M2) and one 4*a* (M3) sites. Due to the nature of the rhombic prisms, the Si–Si dimers are coordinated both end-on and side-on by four 8*b* (2 M1 and 2M2) sites, respectively. The 4*a* (M3) sites, in comparison, coordinate the Si–Si dimers only in an end-on fashion.

Table 4.1. Lattice parameters for $Nd_{5-x}Er_xSi_4$ as obtained by powder X-ray diffraction (space group for Zr_5Si_4-type (Z = 4) and Gd_5Si_4-type (Z = 4) structures are respectively $P4_12_12$ (No. 92) and *Pnma* (No. 62), Cu K_α radiation, 2θ range = 10–100°, T = 298(2) K).

x	***Structure Type(s)***	***a* (Å)**	***b* (Å)**	***c* (Å)**	***V′* (Å^3)[a]**
0[b]	Zr_5Si_4	7.8694(0)	7.8694(0)	14.8077(1)	229.25(1)
1	Zr_5Si_4	7.8255(5)	7.8255(5)	14.551(1)	222.8(1)
2	*Zr_5Si_4 +*	*7.7153(8)*	*7.7153(8)*	*14.275 (8)*	*212.4(6)*
	Gd_5Si_4*	7.4723(8)	14.753(2)	7.7894(9)	214.7(2)
3	*Zr_5Si_4 +*	*7.830(3)*	*7.830(3)*	*13.48(1)*	*206.5(7)*
	Gd_5Si_4*	7.4042(3)	14.6164(7)	7.7237(3)	209.0(1)
4	Gd_5Si_4	7.3473(4)	14.4859(9)	7.6570(5)	203.7(1)
5[c]	Gd_5Si_4	7.2940(6)	14.374(1)	7.5973(5)	199.1(1)

[a]*V′* = Unit cell volume per formula unit; [b]Reference (25); [c]Reference (28); *Majority phase as determined from Rietveld refinement. Lattice parameters for the minority phases are shown in italics.

Table 4.2. Crystallographic data for $Nd_{5-x}Er_xSi_4$ (x = 1–4) as obtained by single crystal X-ray diffraction (space group for Zr_5Si_4-type (Z = 4) and Sm_5Ge_4-type (Z = 4) structures are respectively $P4_12_12$ (No. 92) and *Pnma* (No. 62), Mo $K\alpha$ radiation, 2θ range = 4–57°, T = 298(2) K).*

x	1	2	3	4
Loaded Composition	Nd_4ErSi_4	$Nd_3Er_2Si_4$	$Nd_2Er_3Si_4$	$NdEr_4Si_4$
Refined Composition	$Nd_{3.92}Er_{1.08(5)}Si_4$	$Nd_{2.94}Er_{2.06(7)}Si_4$	$Nd_{2.01}Er_{2.99(33)}Si_4$	$Nd_{0.96}Er_{4.04(36)}Si_4$
Structure Type	Zr_5Si_4	Gd_5Si_4	Gd_5Si_4	Gd_5Si_4
No. of Independent Reflections	1080	1069	1035	1018
No. of Parameters	45	49	50	50
Final R indices [I > 2sigma(I)]	R1 = 0.0303, wR2 = 0.0532	R1 = 0.0358, wR2 = 0.0661	R1 = 0.0372, wR2 = 0.0801	R1 = 0.0346, wR2 = 0.0636
Peak/hole, e/Å^3	1.765 / –1.362 [1.19 Å from Si2]	3.028 / –1.863 [0.92 Å from M3]	2.070 / –1.964 [0.76 Å from Si2]	2.430 / –2.666 [1.37 Å from Si2]

Table 4.3. Atomic coordinates, site occupancies and isotropic displacement parameters for $Nd_{5-x}Er_xSi_4$ (x = 1–4) as obtained by single crystal X-ray diffraction. Coordinates are represented in accordance with similar previously reported structure types.[24, 25]

Atom		x	y	z	**Occupancy**[a]	U_{eq}, (Å^2)[b]
			$Nd_{3.92}Er_{1.08(5)}Si_4$			
Nd1	8b	0.0101(1)	0.3651(1)	0.0438(1)	1	0.009(1)
M2	8b	0.0125(1)	0.8659(1)	0.1255(1)	0.32(2)	0.008(1)
M3	4a	0.6857(1)	0.6857(1)	0	0.44(2)	0.009(1)
Si1	8b	0.1590(4)	0.2022(4)	0.8078(2)	1	0.013(1)
Si2	8b	0.0683(4)	0.7089(4)	0.9400(2)	1	0.009(1)

* Further details of the crystal structure investigations are available from the Fachinformationszentrum Karlsruhe, D-76344 Eggenstein-Leopoldshafen (Germany), on quoting the depository number CSD 380261, 380262, 380263, 380264, the name of the author(s), and citation of the paper.

Table 4.3. (continued)

Atom		*x*	*y*	*z*	Occupancy[a]	U_{eq}, (Å^2)[b]
			$Nd_{2.94}Er_{2.06(7)}Si_4$			
Nd1	8d	0.0221(1)	0.4028(1)	0.1798(1)	1	0.009(1)
M2	8d	0.6807(1)	0.3771(1)	0.8216(1)	0.65(2)	0.008(1)
M3	4c	0.1518(1)	¾	0.5123(1)	0.76(3)	0.008(1)
Si1	8d	0.8532(4)	0.4609(2)	0.5312(4)	1	0.010(1)
Si2	4c	0.0239(6)	¾	0.1086(6)	1	0.011(1)
Si3	4c	0.2700(6)	¾	0.8752(6)	1	0.011(1)
			$Nd_{2.01}Er_{2.99(33)}Si_4$			
M1	8d	0.0201(1)	0.4033(1)	0.1787(1)	0.17(6)	0.009(1)
M2	8d	0.6790(1)	0.3769(1)	0.8219(1)	0.87(7)	0.008(1)
M3	4c	0.1538(1)	¾	0.5118(1)	0.90(7)	0.008(1)
Si1	8d	0.8506(4)	0.4609(2)	0.5308(4)	1	0.010(1)
Si2	4c	0.0253(6)	¾	0.1103(6)	1	0.009(1)
Si3	4c	0.2726(6)	¾	0.8746(6)	1	0.011(1)
			$Nd_{0.96}Er_{4.04(36)}Si_4$			
M1	8d	0.0199(1)	0.4034(1)	0.1794(1)	0.56(6)	0.008(1)
M2	8d	0.6779(1)	0.3769(1)	0.8217(1)	0.98(6)	0.007(1)
M3	4c	0.1549(1)	¾	0.5116(1)	0.97(6)	0.007(1)
Si1	8d	0.8483(4)	0.4612(2)	0.5311(4)	1	0.009(1)
Si2	4c	0.0265(6)	¾	0.1088(5)	1	0.009(1)
Si3	4c	0.2740(6)	¾	0.8726(6)	1	0.009(1)

[a]All M1, M2 and M3 sites are fully occupied with a mixture of Nd and Er atoms. Only Er occupations are listed.

[b]U(eq) is defined as one third of the trace of the orthogonalized U_{ij} tensor.

In contrast, the orthorhombic Gd_5Si_4-type crystal structure has six atoms in the asymmetric unit: three crystallographically independent sites for Nd or Er metal atoms, and three distinct sites for the tetrelide atoms and is typically found for the silicon-rich heavier

rare-earth systems.[1] A detailed description of the Gd_5Si_4-type structure can be found elsewhere.[5] In both of these structures all Si atoms belong to Si–Si dimers, in spite of the fact that the former forms a three-dimensional network structure while the latter has a layered morphology (NOTE: although the orthorhombic structure can be described as "layered", with the interslab Si-Si bonds, it is really a 3D network, too).

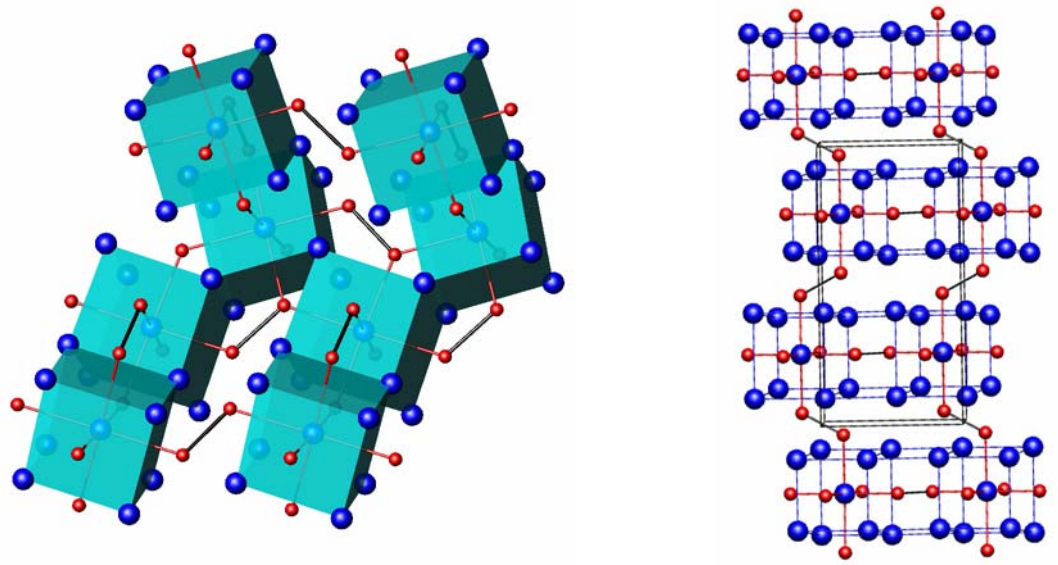

Tetragonal, Zr_5Si_4-type ($P4_12_12$) **Orthorhombic, Gd_5Si_4-type (*Pnma*)**

Figure 4.1. Projections of the two crystal structures observed for $Nd_{5-x}Er_xSi_4$ systems. Blue atoms represent RE metals and red atoms represent Si atoms.

One of the common structural units present in both structures is the M3-centered cube of rare-earth atoms (made of M1 and M2 sites) that is capped on all faces with Si atoms, i.e., $M(M_8)(Si_6)$ units. Alternatively, this unit can be viewed as an octahedral coordination polyhedron of six Si atoms about the M3 site with M1 and M2 atoms capping the eight triangular faces. In both cases, these units are condensed according to the formulation, $M(M_{8/2})[(Si)_2(Si)_{4/2}]$. The different structures are formed by fusing four edges of each cube with adjacent units in two different ways, as shown in Figure 4.2. In the tetragonal Zr_5Si_4-type structure, the fused edges occur on two opposite faces and are oriented perpendicular to one another, which creates a three-dimensional network involving 4_1 screw axes. On the

other hand, in the orthorhombic Gd_5Si_4-type structure, the four fused edges are parallel with one another, which forms layers of these units condensed within the *ac*-planes.

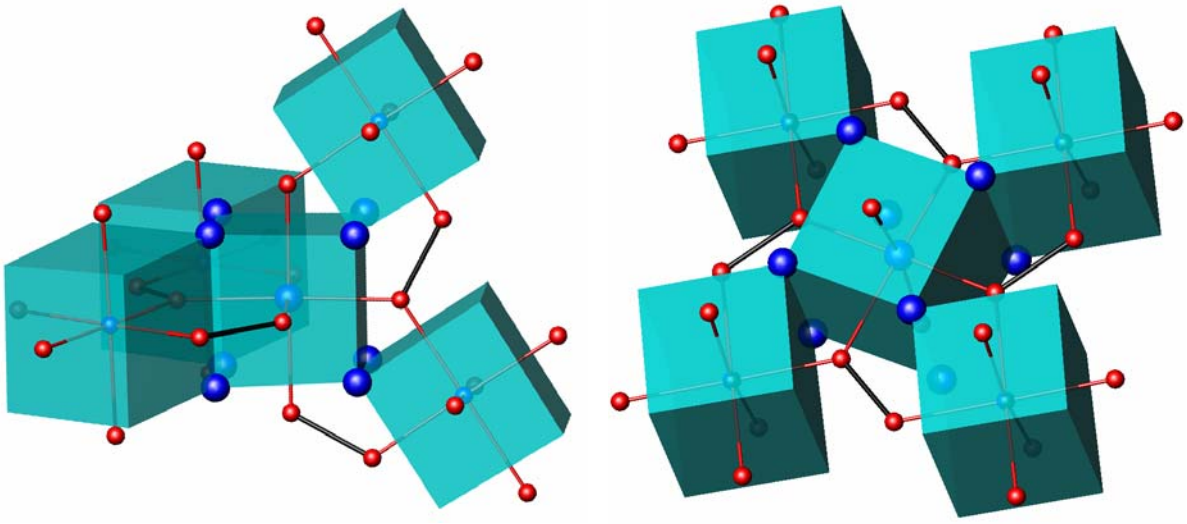

Tetragonal, Zr_5Si_4-type ($P4_12_12$) **Orthorhombic, Gd_5Si_4-type (*Pnma*)**

Figure 4.2. The two different ways the edges of the cube are fused with adjacent units to form the tetragonal and orthorhombic structure. Blue atoms represent RE metals and red atoms represent Si atoms.

All three rare-earth metal sites for $3 \leq x \leq 4$ exhibit mixed site occupancies, with Nd (or the larger rare-earth atom) having a preference for the M1 site and Er (or the smaller rare-earth atom) having a preference for the M3 site, as also observed for Gd-Y-*Tt* (*Tt* = Si, Ge),[15] Gd-La-Ge,[16] Gd-Lu-Ge[16] and Gd-Sc-Ge[17] systems. For $1 \leq x \leq 2$, the M1 site is exclusively occupied by the larger Nd atom. The other two rare-earth metal sites (M2 and M3) display mixed site occupancies with the smaller Er atom showing a distinct preference for the M3 site.

Figure 4.3 includes the variations of Si1–Si1 (orthorhombic interslab contacts) and Si2–Si3 (orthorhombic intraslab contacts) as the Er content changes. A distinct deviation in the monotonic trends in these distances occurs for $x = 1.0$, which marks the region for structural transition between the tetragonal and orthorhombic structures.

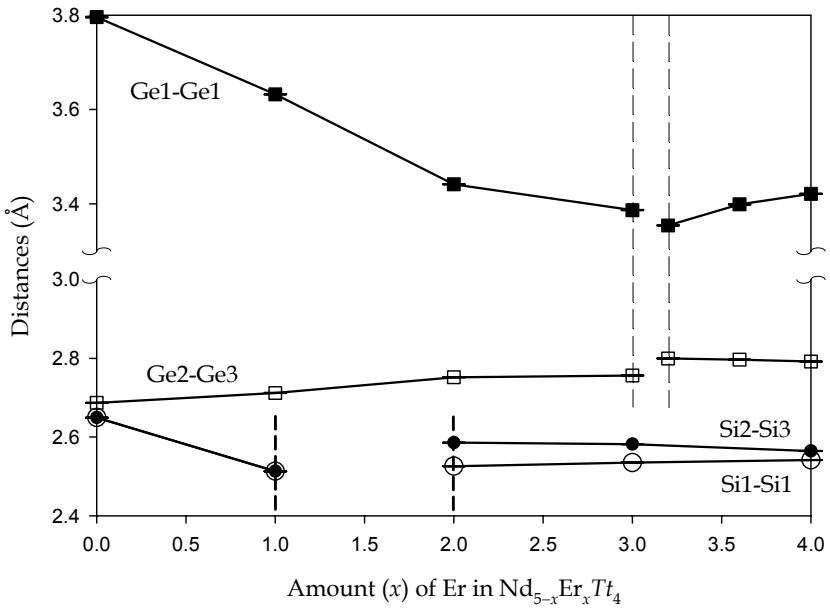

Figure 4.3. Interatomic distance variations in $Nd_{5-x}Er_xTt_4$ as a function of Er content, x. Circles represent data for $Nd_{5-x}Er_xSi_4$ and squares represent data for $Nd_{5-x}Er_xGe_4$. The dotted lines delineate the region where the crystal structure changes.

4.4.2. Structural Features of $Nd_{5-x}Er_xGe_4$. Two distinct phases exist in this system as identified by powder X-ray diffraction. For $x < 3.2$, the orthorhombic Sm_5Ge_4-type structure forms as the majority phase, and for the composition range $3.2 \leq x \leq 4.0$, the monoclinic $U_2Mo_3Si_4$-type structure is observed as the majority phase. The lattice parameters obtained from Rietveld refinement of the powder data are listed in Table 4. Selected crystallographic data, atomic coordinates, site occupancies, and isotropic displacement parameters from single crystal X-ray diffraction are presented in Tables 4.5–4.8. The distances of the nearest atom from the highest residual peak for each structural solution are listed in parentheses (Table 4.5 and 4.7).

Table 4.4. Lattice parameters for $Nd_{5-x}Er_xGe_4$ as obtained by powder X-ray diffraction (space group for Sm_5Ge_4-type (Z = 4) and $U_2Mo_3Si_4$-type (Z = 2) structures are respectively *Pnma* (No. 62) and $P2_1/c$ (No. 14), Cu K_α radiation, 2θ range = 10–100°, T = 298(2) K).

x	***Structure Type(s)***	***a* (Å)**	***b* (Å)**	***c* (Å)**	***β* (°)**	***V′* (Å^3)[a]**
0[b]	Sm_5Ge_4	7.8631(1)	15.1163(3)	7.9559(1)		236.41(2)
1	Sm_5Ge_4	7.7904(5)	15.0062(10)	7.8983(5)		230.8(1)
2	Sm_5Ge_4	7.6893(7)	14.8517(13)	7.8192(3)		223.2(1)
3	Sm_5Ge_4* +	7.6101(7)	14.7284(15)	7.7595(7)		217.4(1)
	$U_2Mo_3Si_4$	*7.898(1)*	*7.792(1)*	*7.599(1)*	*111.09(1)*	*218.2(1)*
3.2	$U_2Mo_3Si_4$	7.8880(7)	7.7695(6)	7.5733(6)	111.344(4)	216.1(1)
3.6	$U_2Mo_3Si_4$	7.8850(4)	7.7549(3)	7.5582(3)	111.553(2)	214.92(3)
4	$U_2Mo_3Si_4$	7.8842(4)	7.7261(4)	7.5388(3)	111.886(2)	213.06(4)
5[c]	Sm_5Ge_4	7.5448(3)	14.515(1)	7.6081(3)		208.3(1)

[a]*V′* = Unit cell volume per formula unit; [b]Reference (27); [c]Reference (28); ***** Majority phase as determined from Rietveld refinement. Lattice parameters for the minority phases are shown in italics.

Table 4.5. Crystallographic data for $Nd_{5-x}Er_xGe_4$ (x = 1–3) as obtained by single crystal X-ray diffraction (Sm_5Ge_4-type, space group *Pnma* (No. 62), Mo $K\alpha$ radiation, 2θ range = 4–57°, T = 298(2) K, Z = 4).*

x	1	2	3
Loaded Composition	Nd_4ErGe_4	$Nd_3Er_2Ge_4$	$Nd_2Er_3Ge_4$
Refined Composition	$Nd_{4.09}Er_{0.91(10)}Ge_4$	$Nd_{3.06}Er_{1.94(9)}Ge_4$	$Nd_{1.94}Er_{3.06(13)}Ge_4$
No. of Independent Reflections	1164	1111	1092
No. of Parameters	49	49	50
Final R indices [I > 2sigma(I)]	R1 = 0.0495, wR2 = 0.0944	R1 = 0.0445, wR2 = 0.0823	R1 = 0.0337, wR2 = 0.0609
Peak/hole, e/Å^3	3.329 / –3.447 [0.96 Å from M3]	2.989 / –2.423 [1.00 Å from Ge3]	2.680 / –2.250 [1.24 Å from M3]

Table 4.6. Atomic coordinates, site occupancies and isotropic displacement parameters for $Nd_{5-x}Er_xGe_4$ (x = 1–3) as obtained by single crystal X-ray diffraction. Coordinates are represented in accordance with similar previously reported structure types.[15]

Atom		***x***	***y***	***z***	**occupancy**[a]	**U_{eq}, (Å^2)**[b]
			$Nd_{4.09}Er_{0.91(10)}Ge_4$			
Nd1	8d	0.9814(1)	0.4005(1)	0.1803(1)	1	0.010(1)
M2	8d	0.6280(1)	0.3831(1)	0.8392(1)	0.23(3)	0.009(1)
M3	4c	0.2069(2)	¾	0.4982(1)	0.45(4)	0.009(1)
Ge1	8d	0.7863(2)	0.4554(1)	0.5355(2)	1	0.011(1)
Ge2	4c	0.0774(3)	¾	0.1131(3)	1	0.011(1)
Ge3	4c	0.3197(3)	¾	0.8665(3)	1	0.010(1)
			$Nd_{3.06}Er_{1.94(9)}Ge_4$			
Nd1	8d	0.9875(1)	0.4021(1)	0.1802(1)	1	0.010(1)
M2	8d	0.6377(1)	0.3811(1)	0.8376(1)	0.58(3)	0.009(1)

* Further details of the crystal structure investigations are available from the Fachinformationszentrum Karlsruhe, D-76344 Eggenstein-Leopoldshafen (Germany), on quoting the depository number CSD 380265, 380266, 380267, the name of the author(s), and citation of the paper.

Table 4.6. (continued)

Atom		*x*	*y*	*z*	occupancy[a]	U_{eq}, (Å^2)[b]
M3	4c	0.1990(1)	¾	0.4992(1)	0.77(3)	0.009(1)
Ge1	8d	0.7963(2)	0.4565(1)	0.5385(2)	1	0.012(1)
Ge2	4c	0.0667(3)	¾	0.1179(3)	1	0.011(1)
Ge3	4c	0.3164(3)	¾	0.8657(3)	1	0.010(1)
			$Nd_{1.94}Er_{3.06(13)}Ge_4$			
M1	8d	0.9876(1)	0.4022(1)	0.1794(1)	0.16(2)	0.011(1)
M2	8d	0.6384(1)	0.3804(1)	0.8372(1)	0.90(3)	0.011(1)
M3	4c	0.1983(1)	¾	0.4997(1)	0.94(3)	0.011(1)
Ge1	8d	0.7976(2)	0.4568(1)	0.5387(2)	1	0.013(1)
Ge2	4c	0.0648(2)	¾	0.1200(2)	1	0.012(1)
Ge3	4c	0.3170(2)	¾	0.8650(2)	1	0.011(1)

[a]All M1, M2 and M3 sites are fully occupied with a mixture of Nd and Er atoms. Only Er occupations are listed.

[b]U(eq) is defined as one third of the trace of the orthogonalized U_{ij} tensor.

Table 4.7. Crystallographic data for $Nd_{5-x}Er_xGe_4$ (x = 3.2, 3.6, and 4.0) as obtained by single crystal X-ray diffraction ($U_2Mo_3Si_4$-type, space group $P2_1/c$ (No. 14), Mo K_α radiation, 2θ range = 4–57°, T = 298(2) K, Z = 2).*

x	3.2	3.6	4.0
Loaded Composition	$Nd_{1.8}Er_{3.2}Ge_4$	$Nd_{1.4}Er_{3.6}Ge_4$	$NdEr_4Ge_4$
Refined Composition	$Nd_{1.86}Er_{3.14(18)}Ge_4$	$Nd_{1.19}Er_{3.81(15)}Ge_4$	$Nd_{1.00}Er_{4.00(13)}Ge_4$

* Further details of the crystal structure investigations are available from the Fachinformationszentrum Karlsruhe, D-76344 Eggenstein-Leopoldshafen (Germany), on quoting the depository number CSD 380268, 380269, 380270, the name of the author(s), and citation of the paper.

Table 4.7. (continued)

x	3.2	3.6	4.0
No. of Independent Reflections	1019	997	995
No. of Parameters	47	47	47
Final R indices [I > 2σ(I)]	R1 = 0.0393, wR2 = 0.0707	R1 = 0.0364, wR2 = 0.0702	R1 = 0.0294, wR2 = 0.0593
Peak/hole, (*e*/Å^3)	2.100 / –2.288 [0.82 Å from Ge1]	2.638 / –3.520 [0.91 Å from M1]	2.238 / –1.899 [0.96 Å from M2]

Table 4.8. Atomic coordinates, site occupancies and isotropic displacement parameters for $Nd_{5-x}Er_xGe_4$ (x = 3.2, 3.6, and 4.0) as obtained by single crystal X-ray diffraction. Coordinates are represented in accordance with similar previously reported structure types [15, 21].

Atom		***x***	***y***	***z***	**occupancy**[a]	**U_{eq}, (Å^2)**[b]
			$Nd_{1.86}Er_{3.14(18)}Ge_4$			
M1	4e	0.6953(1)	0.3198(1)	0.0630(1)	0.25(3)	0.010(1)
M2	4e	0.2602(1)	0.3356(1)	0.2672(1)	0.89(4)	0.009(1)
M3	2a	0	0	0	0.87(4)	0.009(1)
Ge1	4e	0.4138(2)	0.0383(2)	0.1686(2)	1	0.012(1)
Ge2	4e	0.0078(2)	0.6306(2)	0.1301(2)	1	0.011(1)
			$Nd_{1.19}Er_{3.81(15)}Ge_4$			
M1	4e	0.6959(1)	0.3201(1)	0.0619(1)	0.43(3)	0.011(1)
M2	4e	0.2608(1)	0.3362(1)	0.2688(1)	0.99(3)	0.010(1)
M3	2a	0	0	0	0.98(3)	0.010(1)
Ge1	4e	0.4131(2)	0.0368(2)	0.1707(2)	1	0.012(1)
Ge2	4e	0.0080(2)	0.6309(2)	0.1301(2)	1	0.011(1)
			$Nd_{1.00}Er_{4.00(13)}Ge_4$			
M1	4e	0.6967(1)	0.3203(1)	0.0606(1)	0.54(2)	0.010(1)

M2	4e	0.2616(1)	0.3363(1)	0.2708(1)	0.98(3)	0.009(1)
M3	2a	0	0	0	0.96(3)	0.009(1)
Ge1	4e	0.4132(2)	0.0361(1)	0.1736(2)	1	0.011(1)
Ge2	4e	0.0086(2)	0.6313(1)	0.1303(2)	1	0.010(1)

[a]All M1, M2 and M3 sites are fully occupied with a mixture of Nd and Er atoms. Only Er occupations are listed.

[b]U(eq) is defined as one third of the trace of the orthogonalized U_{ij} tensor.

The orthorhombic Sm_5Ge_4-type crystal structure has six atoms in the asymmetric unit: three crystallographically independent sites for Nd or Er metal atoms, and three distinct sites for the tetrelide atoms. In comparison to the orthorhombic structure, the asymmetric unit of the monoclinic $U_2Mo_3Si_4$-type structure has five atoms: three distinct sites for Nd or Er metal atoms and just two distinct sites for the tetrelide atoms. This monoclinic structure, until recently, was not reported for the RE_5T_4 systems. However, our recent work has shown the existence of this structure in the $Gd_{5-x}Y_xGe_4$ system for Y-rich phases.[15] The projections of these two crystal structures are shown in Figure 4.4.

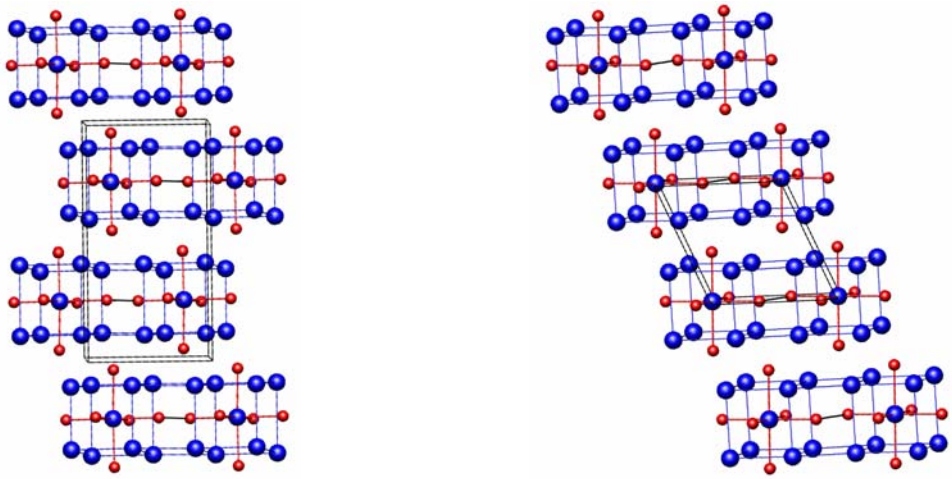

Orthorhombic, Sm_5Ge_4-type (*Pnma*) **Monoclinic, $U_2Mo_3Si_4$-type ($P2_1/c$)**

Figure 4.4. Projections of the two crystal structures observed for $Nd_{5-x}Er_xGe_4$ systems. Blue atoms represent RE metal and red atoms represent Si atoms.

All three rare-earth metal sites (in both structures) for $x \geq 3$ exhibit mixed site occupancies, with Nd (or the larger rare-earth atom) having a preference for the M1 site and Er (or the smaller rare-earth atom) having a preference for the M3 site (see Figure 4.4) as observed in Nd-Er-Si and the other systems mentioned above. For $1 \leq x \leq 2$, as was the case with Nd-Er-Si, the M1 site is exclusively occupied by the larger Nd atom while the other two rare-earth metal sites (M2 and M3) displays mixed site occupancies with the smaller Er atom showing a preference for the M3 site.

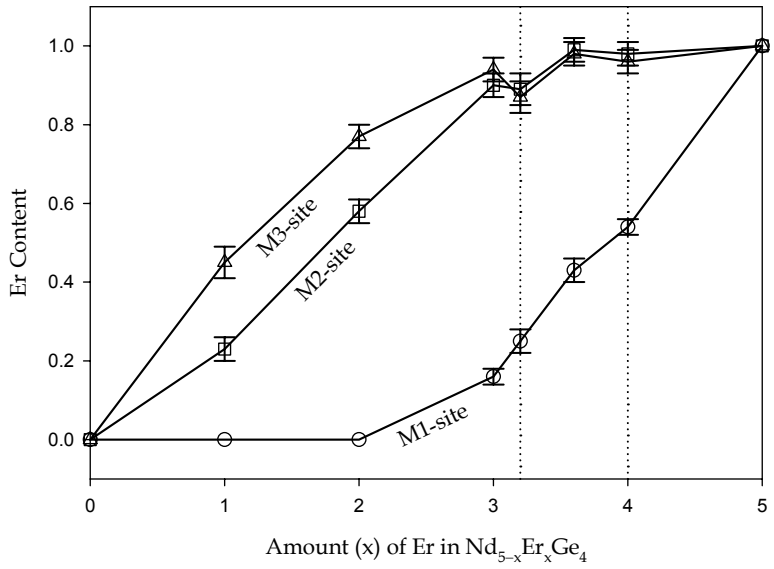

Figure 4.5. Er occupation in each M site of $Nd_{5-x}Er_xGe_4$ as a function of Er concentration, x, as obtained from single crystal X-ray diffraction. The vertical dotted lines delineate the region where the monoclinic phase is observed.

The monoclinic $U_2Mo_3Si_4$-type structure shows striking similarities to the Sm_5Ge_4-type structure. Both crystal structures are built from nearly identical 3^2434 nets of Nd/Er atoms. Two such nets are placed over one another to form two-dimensional slabs with additional Nd/Er atoms in pseudo-cubic coordination (the M3 site) and Ge2, Ge3 (in the orthorhombic structure) and Ge2 atoms (in the monoclinic structure) in trigonal prismatic voids. These crystal structures differ from one other in the manner in which these

neighboring slabs stack with respect to each other. In the orthorhombic structure, space group *Pnma*, there are two slabs per unit cell and each slab has reflection symmetry through the plane formed by M3, Ge2, and Ge3 sites. The two slabs are structurally related to each other by inversion symmetry. This stacking arrangement creates a herringbone pattern along the *b*-direction for the interslab Ge1···Ge1 contacts. On the other hand, in the monoclinic structure, space group $P2_1/c$, there is one slab per unit cell with the M3 site coincident with an inversion center. The adjacent layers are related by translational symmetry resulting in a stacking pattern which creates inversion symmetry between slabs as well. Due to these different symmetry characteristics, the arrangements of the M1 and M2 metal positions are different in the two structures, although every cube surrounding the M3 positions contains 4 M1 and 4 M2 sites. In the orthorhombic structure, the two faces of the cube perpendicular to the *c*-direction are either all M1 or all M2. On the other hand, for the monoclinic structure, the two faces of the cube perpendicular to the *b*-direction are 50% M1 and 50% M2 in an alternating pattern, which preserves the inversion center at the M3 site.

The variations in Ge1–Ge1 (interslab) and Ge2–Ge3 (intraslab) as the Er content changes are also presented in Figure 3. As seen in the silicides, there are distinct deviations in the distance trends at the region when the structure type changes, i.e., between $x = 3$ and 4.

4.4.3. Magnetism. Figure 4.6 illustrates the magnetic susceptibility measurements in a 10 kOe field for some members of the $Nd_{5-x}Er_xGe_4$ series. The Nd-rich phase, Nd_4ErGe_4, shows an antiferromagnetic type (AFM) transition at 23(2) K similar to Gd_5Ge_4, which shows this transition at 128 K (T_N). The remaining phases (x = 2–4) undergo a ferrimagnetic type ordering showing Curie-Weiss behavior at high temperatures. The Curie temperatures, T_C, were estimated for the ferrimagnetic phases (x = 2–4) from dM/dT vs. T plots to be 6(2), 12(2) and 11(2) K, respectively. The effective magnetic moments, μ_{eff}, for the series were determined based on the numerical fits for the data between 150 and 270 K and are listed within the plots. The expected μ_{eff} for a mixture of noninteracting trivalent ions comprised of: 0.8Nd+0.2Er is 5.37 μ_B/RE^{3+}, 0.6Nd+0.4Er is 6.68 μ_B/RE^{3+}, 0.4Nd+0.6Er is 7.76 μ_B/RE^{3+} and 0.2Nd+0.8Er is 8.72 μ_B/RE^{3+} (RE = rare-earth). As evident, the measured μ_{eff} values matches quite well with these theoretical values.

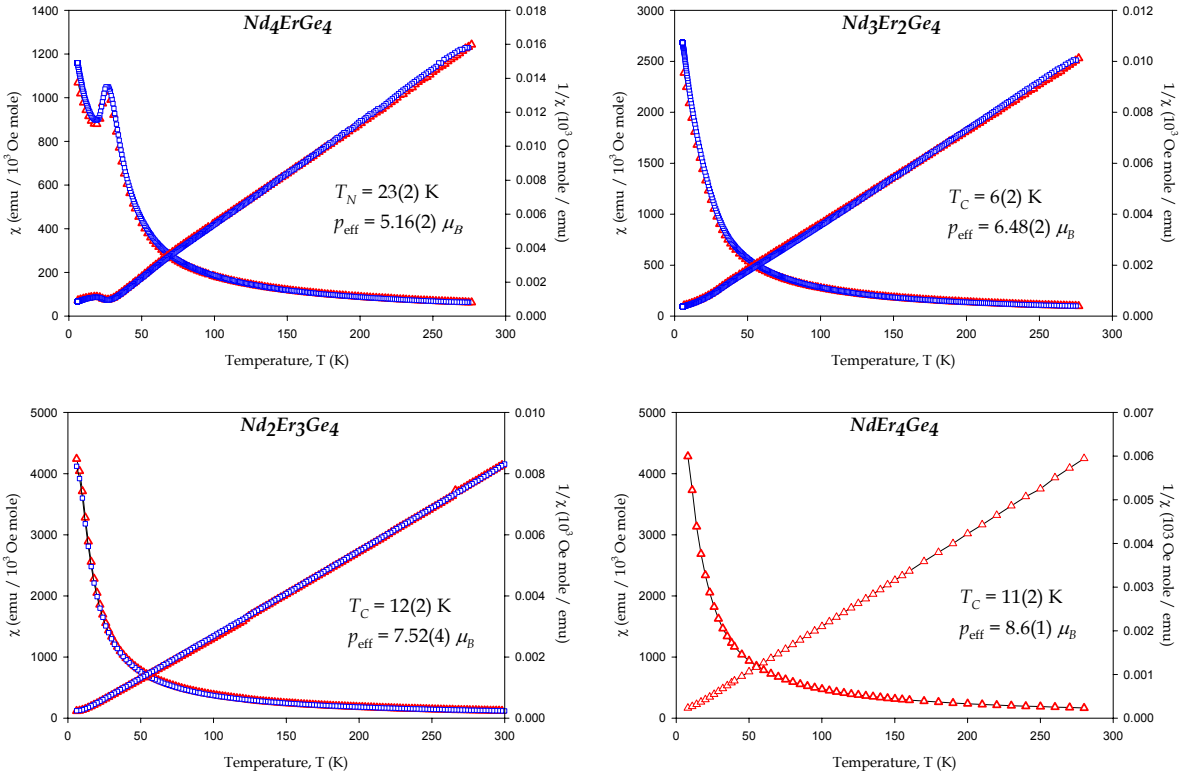

Figure 4.6. Magnetic susceptibility plots for $Nd_{5-x}Er_xGe_4$ series. The measurements were carried out under a magnetic field, H = 10 kOe.

4.5. Conclusions

The crystal structures and the corresponding distributions of Nd and Er atoms over the various metal sites in the $Nd_{5-x}Er_xTt_4$ (*Tt* = Si, Ge) series have been presented. All silicides adopt either the tetragonal Zr_5Si_4-type three-dimensional network structure or the orthorhombic Gd_5Si_4-type structure, both of which contain short Si-Si contacts. All germanides exhibit a mixture of short and long Ge-Ge contacts, and adopt either the orthorhombic Sm_5Ge_4-type or monoclinic $U_2Mo_3Si_4$-type structure. The different stacking patterns occur for Er contents between 3.2 and 4. Single crystal diffraction results reveal a preference of the smaller Er atoms to occupy the M3 sites (centers of slabs) whereas the larger Nd atoms prefer to occupy the M1 sites (edges of slabs). These results match well with our recent investigations in the $Gd_{5-x}RE_xTt_4$ (RE = Sc, Y, La, Lu; Tt = Si, Ge).

4.6. Acknowledgements

The authors thank Prof. Vitalij Pecharsky for using the Lakeshore Magnetometer. E.T.P. acknowledges support from the Science Undergraduate Laboratory Internship (SULI) from the U.S. DOE. This work was carried out at the Ames Laboratory, which is operated for the U.S. Department of Energy by Iowa State University under Contract No. DE-AC02-07CH11358. This work was supported by the Materials Sciences Division of the Office of Basic Energy Sciences of the U.S. Department of Energy.

4.7. References

(1) Miller, G. J., *Chem. Soc. Rev.* **2006**, *35*, 799.

(2) Gschneidner, K. A. Jr.; Pecharsky, V. K.; Pecharsky, A. O.; Ivtchenko, V. V.; Levin, E. M., *J. Alloys Compd.* **2000**, *303-304*, 214.

(3) Gschneidner, K. A. Jr.; Pecharsky, V. K.; Tsokol, A. O., *Rep. Prog. Phys.* **2005**, *68*, 1479.

(4) Pecharsky, V. K.; Gschneidner, K. A. Jr., *Pure Appl. Chem*., **2007**, *79*, 1383.

(5) Holtzberg, F.; Gambino, R. J.; McGuire, T. R., *J. Phys. Chem. Solids* **1967**, *28*, 2283.

(6) Choe, W.; Pecharsky, V. K.; Pecharsky, A. O.; Gschneidner, K. A. Jr.; Young, V. G. Jr.; Miller, G. J., *Phys. Rev. Lett.* **2000**, *84*, 4617.

(7) Meyer, J.; Chumbley, S.; Choe, W.; Miller, G. J., *Phys. Rev. B* **2002**, *66*, 012106/012101.

(8) Choe, W.; Pecharsky, A. O.; Wörle, M.; Miller, G. J., *Inorg. Chem.* **2003**, *42*, 8223.

(9) Mozharivskyj, Y.; Choe, W.; Pecharsky, A. O.; Miller, G. J., *J. Am. Chem. Soc.* **2003**, *125*, 15183.

(10) Wu, L. M.; Kim, S. H.; Seo, D. K., *J. Am. Chem. Soc*. **2005**, *127*, 15682.

(11) Choe, W.; Miller, G. J.; Meyers, J.; Chumbley, S.; Pecharsky, A. O., *Chem. Mater.* **2003**, *15*, 1413.

(12) Singh, N. K.; Pecharsky, V. K.; Gschneidner, K. A. Jr., *Phys. Rev. B* **2008**, *77*, 054414/1-10.

(13) Nirmala, R.; Kundaliya, D. C.; Shinde, S. R.; Joshi, A. G.; Morozkin, A. V.; Malik, S. K., *J. Appl. Phys*. **2007**, *101*, 123901/1-4.

(14) Elbicki, J. M.; Zhang, L. Y.; Obermyer, R. T.; Wallace, W. E., *J. Appl. Phys.* **1991**, *69*, 5571.

(15) Misra, S.; Miller, G. J., *J. Am. Chem. Soc*. **2008**, submitted.

(16) Mudryk, Ya.; Paudayl, D.; Misra, S.; Pecharsky, V. K.; Gschneidner, K. A. Jr.; Miller, G. J., in preparation.

(17) Misra, S.; Miller, G. J., unpublished results.

(18) Pfeifer, H. -U.; Schubert, K.; *Z. Metallkunde* **1966**, *57*, 884.

(19) Iglesias, J. E.; Steinfink, H., *J. Less-Common Met*. **1972**, *26*, 45.

(20) Smith, G. S.; Johnson, Q.; Tharp, A. G. *Acta Crystallogr*. **1967**, *22*, 269.

(21) Richter, K. W.; Franzen, H. F., *J. Solid State Chem*. **2000**, *150*, 347.

(22) Kraus, W.; Nolze, G., *Powder Cell for Windows, Version 2.4*, **2000**.

(23) *XRD Single Crystal Software*; Bruker Analytical X-ray Systems: Madison, USA, **2002**.

(24) Shannon, R. D., *Acta Cryst. A*, **1976**, *32*, 751.

(25) Yang, H. F.; Rao, G. H.; Chu, W. G.; Liu, G. Y.; Ouyang, Z. W.; Liang, J. K., *J. Alloys Compds.* **2002**, *334,* 131.

(26) Misra, S.; Miller, G. J., *J. Solid State Chem.* **2006**, *179*, 2290.

(27) Yang, H. F.; Rao, G. H.; Liu, G. Y.; Ouyang, Z. W.; Liu, W. F.; Feng, X. M.; Chu, W. G.; Liang, J. K., *J. Alloys Compds.* **2002**, *346,* 190.

(28) Pecharsky, A. O.; Gschneidner, K. A. Jr.; Pecharsky, V. K.; Schlagel, D. L.; Lograsso, T. A., *Phys. Rev. B* **2008**, *70*, 144419.

4.8. Supporting Information

Table 4.S1. Crystallographic data for $Nd_{5-x}Er_xSi_4$ (x = 1–4) as obtained by single crystal X-ray diffraction (Gd_5Si_4-type, space group *Pnma* (No. 62), Mo $K\alpha$ radiation, 2θ range = 4–57°, T = 298(2) K, Z = 4)

x	1	2	3	4
Loaded Composition	Nd_4ErSi_4	$Nd_3Er_2Si_4$	$Nd_2Er_3Si_4$	$NdEr_4Si_4$
Refined Composition	$Nd_{3.92}Er_{1.08(5)}Si_4$	$Nd_{2.94}Er_{2.06(7)}Si_4$	$Nd_{2.01}Er_{2.99(33)}Si_4$	$Nd_{0.96}Er_{4.04(36)}Si_4$
***a*, Å**	7.818(1)	7.457(1)	7.394(1)	7.346(1)
***b*, Å**	7.818(1)	14.735(3)	14.612(3)	14.488(3)
***c*, Å**	14.550(4)	7.778(1)	7.718(1)	7.661(1)
***V*, Å^3**	889.3(3)	854.6(3)	833.9(3)	815.4(3)

Table 4.S2. Crystallographic data for $Nd_{5-x}Er_xGe_4$ (x = 1–3) as obtained by single crystal X-ray diffraction (Sm_5Ge_4-type, space group *Pnma* (No. 62), Mo $K\alpha$ radiation, 2θ range = 4–57°, T = 298(2) K, Z = 4)

x	1	2	3
Loaded Composition	Nd_4ErGe_4	$Nd_3Er_2Ge_4$	$Nd_2Er_3Ge_4$
Refined Composition	$Nd_{4.09}Er_{0.91(10)}Ge_4$	$Nd_{3.06}Er_{1.94(9)}Ge_4$	$Nd_{1.94}Er_{3.06(13)}Ge_4$
***a*, Å**	7.780(1)	7.652(2)	7.624(2)
***b*, Å**	14.986(2)	14.807(4)	14.710(3)
***c*, Å**	7.885(1)	7.800(2)	7.760(2)
***V*, Å^3**	919.3(2)	883.7(4)	870.3(3)

Table 4.S3. Crystallographic data for $Nd_{5-x}Er_xGe_4$ (x = 3.2, 3.6, and 4.0) as obtained by single crystal X-ray diffraction ($U_2Mo_3Si_4$-type, space group $P2_1/c$ (No. 14), Mo K_α radiation, 2θ range = 4–57°, T = 298(2) K, Z = 2).

x	3.2	3.6	4.0
Loaded Composition	$Nd_{1.8}Er_{3.2}Ge_4$	$Nd_{1.4}Er_{3.6}Ge_4$	$NdEr_4Ge_4$
Refined Composition	$Nd_{1.86}Er_{3.14(18)}Ge_4$	$Nd_{1.19}Er_{3.81(15)}Ge_4$	$Nd_{1.00}Er_{4.00(13)}Ge_4$
***a* (Å)**	7.892(5)	7.898(1)	7.878(2)
***b* (Å)**	7.767(5)	7.749(1)	7.715(2)
***c* (Å)**	7.562(5)	7.561(1)	7.531(2)
***β* (°)**	111.490(9)	111.749(3)	112.014(4)
***V* (Å^3)**	431.3(5)	429.8(1)	424.4(2)

Chapter 5

On the Distribution of Tetrelide Atoms (Si, Ge) in $Gd_5(Si_xGe_{1-x})_4$

A paper published in the *Journal of Solid State Chemistry*

J. Solid State Chem. **2006**, *179*, 2290–2297.

Sumohan Misra and Gordon J. Miller

5.1. Abstract

A crystallographic study of the Si/Ge site preferences in the Si-rich regime of $Gd_5(Si_xGe_{1-x})_4$ and a crystal chemical analysis of these site preferences for the entire range is presented. The room temperature crystal structure of Gd_5Si_4 as well as four pseudobinary phases, $Gd_5(Si_xGe_{1-x})_4$ for $x \geq 0.6$, is reported. All structures are orthorhombic (space group *Pnma*), Gd_5Si_4-type and show decreasing volume as the Si concentration increases. Refinements of the site occupancies for the three crystallographic sites for Si/Ge atoms in the asymmetric unit reveal a nonrandom, but still incompletely ordered arrangement of Si and Ge atoms. The distribution of Si and Ge atoms at each site impacts the fractions of possible homonuclear and heteronuclear Si-Si, Si-Ge and Ge-Ge dimers in the various structures. This distribution correlates with the observed room temperature crystal structures for the entire series of $Gd_5(Si_xGe_{1-x})_4$.

5.2. Introduction

There has been a renaissance in the $RE_5(Si_xGe_{1-x})_4$ systems during the past decade due to discovery of a giant magnetocaloric effect (MCE) in $Gd_5Si_2Ge_2$[1-7] and extraordinary magnetic responses exhibited by many examples.[8-15] Most of the effort has emphasized the $Gd_5(Si_xGe_{1-x})_4$ system because not only was this the first system to show extraordinary behavior, but the orbitally nondegenerate ground state of the Gd atom eliminates orbital

contributions to the local magnetic moment. Numerous experimental and theoretical investigations indicate that the giant MCE is associated with a first-order magnetic transition,[16-17] which typically means a structural transition accompanying the change in magnetic order, although the two transitions need not be intrinsically coupled, as seen, e.g., in Er_5Si_4.[18] It is often observed that changes in magnetic structure also show magnetostriction, but the structural transitions in $Gd_5(Si_xGe_{1-x})_4$ involve changes in crystal symmetry by making or breaking main group-main group chemical bonds.

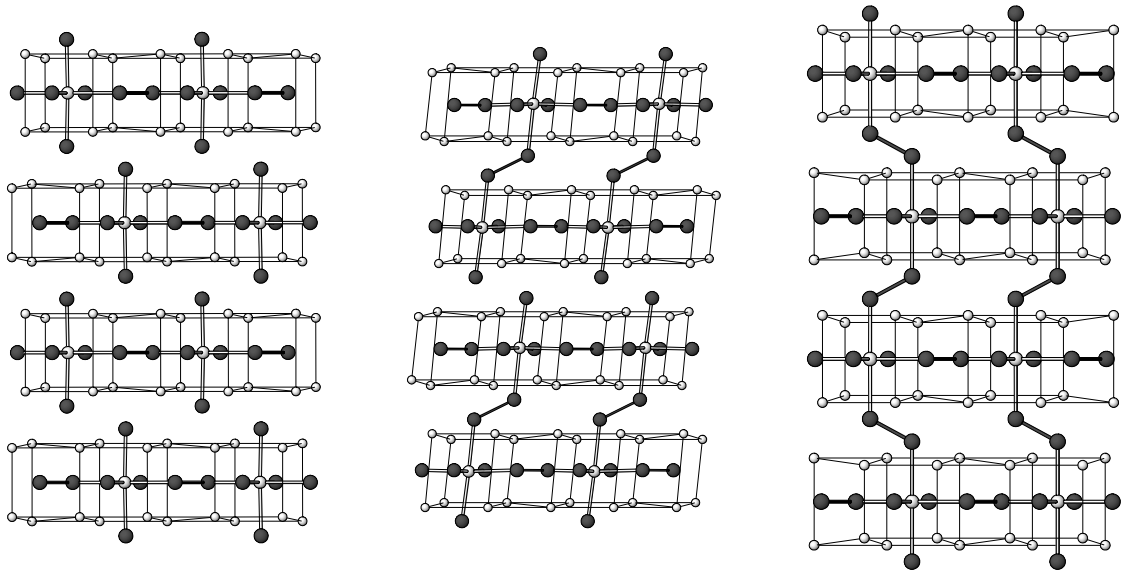

O(II) **M** **O(I)**

(Sm_5Ge_4-Type) **($Gd_5Si_2Ge_2$-Type)** **(Gd_5Si_4-Type)**

Figure 5.1. Projections of the three crystal structures observed for the $Gd_5(Si_xGe_{1-x})_4$ series, which emphasizes the slabs and their interconnections. Shaded circles are Si or Ge sites; larger open circles are Gd3 sites; smaller open circles are Gd1 and Gd2 sites at vertices of the polyhedral frameworks. Lines are drawn to highlight the $[Gd_5(Si_xGe_{1-x})_4]$ slabs as well to emphasize Tt-Tt and Gd3-Tt bonds.

$Gd_5(Si_xGe_{1-x})_4$ shows two remarkable changes for their room-temperature structures as the Si content varies, shown in Figure 5.1. At low Si concentrations ($x \leq 0.30$; Ge-rich

phases), the orthorhombic Sm_5Ge_4-structure type (O(II)-type) exists;[19] at high Si concentrations ($x \geq 0.56$; Si-rich phases), the orthorhombic Gd_5Si_4-structure type (O(I)-type) occurs.[20] At intermediate Si compositions, $0.40 \leq x \leq 0.503$, the monoclinic $Gd_5Si_2Ge_2$-structure (M) type,[21] which is a distorted version of either orthorhombic end phase, is found, but appears to be metastable. Heat treatment of samples for $x = 0.50$ at temperatures below 1000 K showed transformation to the O(I)-type structure and partial eutectoidal decomposition into $Gd_5(Si_xGe_{1-x})_3$ and $Gd(Si_xGe_{1-x})$.[22] Nevertheless, this decomposition occurs slowly and once cooled below ca. 570 K, the monoclinic phase remains. Furthermore, there are two regions, $0.30 < x < 0.40$ and $0.503 < x < 0.56$, where two respective boundary phases are observed.[22] All three structure types are constructed from topologically identical layers that can be stitched together by main group-main group Tt-Tt bonds (Tt = tetrelide element; Si or Ge). In the Sm_5Ge_4-type, these bonds are not really bonds at all: the Ge-Ge separations exceed 3.5 Å; in the Gd_5Si_4-type, the distances fall well within Si-Si single-bonded distances of 2.6 Å. The monoclinic $Gd_5Si_2Ge_2$ shows both types of interactions. These different structures can occur for a given composition by changing temperature or magnetic field, and are at the heart of the giant MCE in $Gd_5Si_2Ge_2$: the monoclinic structure transforms into the O(I)-type at the Curie temperature of 276 K.[22]

Previous single crystal X-ray diffraction studies[23] for the Ge-rich phases in the $Gd_5(Si_xGe_{1-x})_4$ system showed that the Si and Ge distributions were not completely random nor completely ordered among the crystallographic sites occupied by these main group elements. This phenomenon could be explained by a competition between enthalpic and entropic factors: enthalpy favors segregation of Si and Ge into the different sites whereas entropy favors mixing, especially with increasing temperature. To obtain a complete characterization of this series and to attempt an understanding of the structural changes, the phase behavior and the physical properties in this system, we have continued these single crystal investigations into the Si-rich region and report these results and conclusions in this paper.

5.3. Experimental Section

5.3.1. Syntheses: The $Gd_5(Si_xGe_{1-x})_4$ samples, where x = 0.6, 0.7, 0.8, 0.9 and 1.0, were prepared by arc-melting its constituent elements in an argon atmosphere on a water-cooled copper hearth. The starting materials were pieces of Gadolinium (99.99 wt. %, Materials Preparation Center, Ames Laboratory), Silicon (99.9999 wt. %, Alfa Aesar) and Germanium (99.9999 wt. %, Alfa Aesar). Each ingot had a total weight of ca. 1.9 g and was remelted several times to ensure homogeneity. Weight losses during melting were less than 0.1 weight percent.

5.3.2. X-ray powder diffraction: The as-cast samples were examined by X-ray powder diffraction for identification and to assess phase purity. Powder patterns were obtained using an Enraf-Nonius Guinier camera using monochromatized Cu K_α radiation. The purity and homogeneity of all phases was confirmed by comparison of X-ray powder diffraction patterns to those calculated from single-crystal data using the *PowderCell* software.[24] The X-ray powder diffraction patterns for all samples could be completely indexed by orthorhombic Gd_5Si_4-type structures and the refined lattice parameters are listed in Table 5.1.

Table 5.1. Lattice parameters for $Gd_5(Si_xGe_{1-x})_4$ ($x \geq 0.6$) as obtained by X-ray powder diffraction (space group *Pnma* (No. 62), Cu K_α radiation, 2θ range = 4-100°, T = 273(2) K, Z = 4). The refined compositions arise from refinements from single crystal X-ray diffraction.

x	0.6	0.7	0.8	0.9	1.0
Loaded Composition (Gd : Si : Ge)	5 : 2.4 : 1.6	5 : 2.8 : 1.2	5 : 3.2 : 0.8	5 : 3.6 : 0.4	5 : 4 : 0
Refined Composition	$Gd_5Si_{2.40}Ge_{1.60(4)}$	$Gd_5Si_{2.79}Ge_{1.21(4)}$	$Gd_5Si_{3.16}Ge_{0.84(4)}$	$Gd_5Si_{3.59}Ge_{0.41(5)}$	Gd_5Si_4
***a* (Å)**	7.514(2)	7.508(2)	7.503(2)	7.500(2)	7.500(3)
***b* (Å)**	14.775(5)	14.777(4)	14.775(4)	14.770(5)	14.756(6)
***c* (Å)**	7.797(2)	7.779(2)	7.767(2)	7.765(3)	7.735(3)
***V* (Å^3)**	865.6(5)	863.0(4)	861.0(4)	860.2(5)	856.0(6)

5.3.3. Single-crystal X-ray crystallography: Multiple single crystals from the as-cast samples (without annealing) were mounted on the tip of a glass fiber. To check for possible effects of annealing on the distribution of Si and Ge atoms, the sample with x = 0.6 was annealed at 800°C for 1 week and then room temperature intensity data were collected on a single crystal. The refined composition was $Gd_5Si_{2.39}Ge_{1.61(3)}$, which is in agreement with the refined composition without annealing (See Table 5.2). The refined occupancy for the T1 site is 0.456(7), for the T2 site is 0.323(10), and for the T3 site is 0.369(10). Room temperature intensity data were collected on a Bruker Smart Apex CCD diffractometer with Mo K_α radiation (λ= 0.71073 Å) and a detector-to-crystal distance of 5.990 cm. Data were collected over full spheres of reciprocal space by taking three sets of 606 frames with 0.3° scans in ω with an exposure time of 10 seconds per frame. The ranges of 2θ extended from 4° to 57°. The SMART[25] software was used for data acquisition. Intensities were extracted and then corrected for Lorentz and polarization effects through the SAINT[25] program. Empirical absorption corrections were accomplished with SADABS,[25] which is based on modeling a transmission surface by spherical harmonics employing equivalent reflections with $I/\sigma > 3$. Crystallographic data, fractional atomic coordinates and isotropic displacement parameters for all crystals are presented in Tables 5.2 and 5.3.

Table 5.2. Crystallographic data for $Gd_5(Si_xGe_{1-x})_4$ ($x \geq 0.6$) as obtained by single crystal X-ray diffraction (space group *Pnma* (No. 62), Mo K_α radiation, 2θ range = 4-57°, T = 273(2) K, Z = 4).

x	0.6	0.7	0.8	0.9	1.0
Refined Composition	$Gd_5Si_{2.40}Ge_{1.60(4)}$	$Gd_5Si_{2.79}Ge_{1.21(4)}$	$Gd_5Si_{3.16}Ge_{0.84(4)}$	$Gd_5Si_{3.59}Ge_{0.41(5)}$	Gd_5Si_4
***a* (Å)**	7.507(2)	7.506(2)	7.498(3)	7.494(2)	7.482(2)
***b* (Å)**	14.767(5)	14.789(4)	14.751(5)	14.774(5)	14.738(4)
***c* (Å)**	7.786(3)	7.790(2)	7.784(3)	7.756(2)	7.746(2)
***V* (Å^3)**	863.2(5)	864.7(4)	861.0(5)	858.8(4)	854.2(4)
Independent Reflections	1064	1071	1069	1074	1067
No. of Parameters	50	50	50	50	47
Final R indices [I > 2σ(I)]	R1 = 0.0372, wR2 = 0.0686	R1 = 0.0432, wR2 = 0.0847	R1 = 0.0341, wR2 = 0.0655	R1 = 0.0452, wR2 = 0.0842	R1 = 0.0326, wR2 = 0.0591
Peak/hole, (*e*/Å^3)	2.305 / –2.272	2.884 / –2.849	2.101 / –2.597	2.468 / –2.462	2.061 / –1.898

*Further details of the crystal structure investigation(s) can be obtained from the Fachinformationszentrum Karlsruhe, 76344 Eggenstein-Leopoldshafen, Germany, (fax: (49) 7247-808-666; e-mail: crysdata@fiz.karlsruhe.de) on quoting the depository number CSD 416225, 416226, 416227, 416228 and 416229.

Table 5.3. Atomic coordinates, site occupancies and isotropic displacement parameters for $Gd_5(Si_xGe_{1-x})_4$ ($x \geq 0.6$) as obtained by single crystal X-ray diffraction.

Atom		*x*	*y*	*z*	occupancy[a]	U_{eq}, ($Å^2$)[b]
			$Gd_5Si_{2.40}Ge_{1.60(4)}$			
Gd1	8d	0.0237(1)	0.4031(1)	0.1820(1)	1	0.010(1)
Gd2	8d	0.6800(1)	0.3775(1)	0.8218(1)	1	0.009(1)
Gd3	4c	0.1498(1)	3/4	0.5112(1)	1	0.009(1)
T1	8d	0.8469(3)	0.4602(1)	0.5297(2)	0.467(9)	0.012(1)
T2	4c	0.0228(4)	3/4	0.1036(4)	0.312(13)	0.010(1)
T3	4c	0.2683(4)	3/4	0.8709(4)	0.349(13)	0.008(1)
			$Gd_5Si_{2.79}Ge_{1.21(4)}$			
Gd1	8d	0.0249(1)	0.4031(1)	0.1823(1)	1	0.011(1)
Gd2	8d	0.6810(1)	0.3774(1)	0.8215(1)	1	0.009(1)
Gd3	4c	0.1484(1)	3/4	0.5112(1)	1	0.009(1)
T1	8d	0.8489(3)	0.4604(2)	0.5291(3)	0.366(9)	0.013(1)
T2	4c	0.0222(5)	3/4	0.1028(4)	0.223(12)	0.010(1)
T3	4c	0.2666(4)	3/4	0.8724(4)	0.252(12)	0.009(1)
			$Gd_5Si_{3.16}Ge_{0.84(4)}$			
Gd1	8d	0.0261(1)	0.4030(1)	0.1825(1)	1	0.010(1)
Gd2	8d	0.6820(1)	0.3775(1)	0.8211(1)	1	0.008(1)
Gd3	4c	0.1470(1)	3/4	0.5113(1)	1	0.008(1)
T1	8d	0.8512(3)	0.4603(2)	0.5288(3)	0.247(8)	0.012(1)
T2	4c	0.0219(4)	3/4	0.1017(4)	0.165(11)	0.010(1)
T3	4c	0.2637(4)	3/4	0.8727(4)	0.177(11)	0.009(1)
			$Gd_5Si_{3.59}Ge_{0.41(5)}$			
Gd1	8d	0.0279(1)	0.4029(1)	0.1827(1)	1	0.010(1)
Gd2	8d	0.6828(1)	0.3776(1)	0.8207(1)	1	0.009(1)
Gd3	4c	0.1456(1)	3/4	0.5115(1)	1	0.008(1)
T1	8d	0.8538(5)	0.4604(2)	0.5280(5)	0.118(11)	0.010(1)
T2	4c	0.0221(7)	3/4	0.1011(7)	0.087(15)	0.011(2)
T3	4c	0.2623(7)	3/4	0.8749(7)	0.090(15)	0.011(2)

Table 5.3. (continued)

Atom		*x*	*y*	*z*	occupancy[a]	U_{eq}, (Å^2)[b]
			Gd_5Si_4			
Gd1	8d	0.0289(1)	0.4028(1)	0.1827(1)	1	0.009(1)
Gd2	8d	0.6837(1)	0.3777(1)	0.8204(1)	1	0.008(1)
Gd3	4c	0.1442(1)	3/4	0.5112(1)	1	0.007(1)
T1	8d	0.8562(4)	0.4602(2)	0.5281(4)	0	0.010(1)
T2	4c	0.0210(5)	3/4	0.0998(5)	0	0.009(1)
T3	4c	0.2589(6)	3/4	0.8748(6)	0	0.010(1)

[a] All T1, T2 and T3 sites are fully occupied with a mixture of Ge and Si atoms. Only Ge occupations are listed. The only exception is Gd_5Si_4 where the T1, T2 and T3 sites are fully occupied by Si atoms.

[b] U(eq) is defined as one third of the trace of the orthogonalized U_{ij} tensor.

5.3.4. Electronic Structure Calculations: Tight-binding, linear muffin-tin orbital (TB-LMTO) electronic band structure calculations in the atomic sphere approximation (ASA) were carried out using the LMTO47 program.[26] Exchange and correlation were treated in a local density approximation. All relativistic effects except spin-orbit coupling were taken into account using a scalar relativistic approximation. The radii of the Wigner-Seitz (WS) spheres were obtained by requiring the overlapping potential to be the best possible approximation to the full potential according to an automatic procedure – no empty spheres were necessary.[27] The WS radii determined by this procedure for the atoms in $Gd_5(Si_xGe_{1-x})_4$ are in the ranges 1.886-2.120 Å for Gd, 1.430-1.442 Å for Si, and 1.440-1.451 Å for Ge. The basis set included Gd 6*s*, 6*p* and 5*d* orbitals, Si 3*s*, 3*p* and 3*d* orbitals, and Ge 4*s*, 4*p* and 4*d* orbitals. The Gd 4*f* orbitals were treated as core wavefunctions occupied by seven valence electrons. Furthermore, the Si 3*d* and Ge 4*p* orbitals were treated by the Löwdin downfolding technique.[26] The **k**-space integrations to determine total energies and densities of states were evaluated by the tetrahedron method using 78 **k**-points in the irreducible wedges of the first Brillouin zones.

5.4. Results and Discussion

The Si-rich region of the $Gd_5(Si_xGe_{1-x})_4$ phase diagram shows a single, orthorhombic Gd_5Si_4-structure type at all temperatures. These phases give a continuous paramagnetic-ferromagnetic transition without change in crystal structure[21] The surprising issue is that their Curie temperatures exceed that of elemental Gd,[19] and increase essentially linearly with increasing Si concentration. This phenomenon is unusual because the Gd atoms are "diluted" by nonmagnetic main group elements and still cannot be explained by appropriate theory. The orthorhombic crystal structure has six atoms in the asymmetric unit: three distinct sites for Gd atoms; and three distinct sites for Si or Ge atoms. Our single crystal diffraction experiments elucidated the distribution of Si and Ge atoms among the three crystallographic sites for these elements. We label these sites as T1 for between slabs and T2, T3 for within slabs. In accord with earlier work on the Ge-rich examples,[23] the distributions of Si and Ge atoms are not completely random, nor are they completed ordered. Nevertheless, there is a clear preference for Ge atoms in the T1 sites and for Si atoms in the T2 and T3 sites. Naturally, as the Si concentration increases, all sites become rich in Si atoms.

Now, the diffraction experiment provides a coarse-grained average of atomic distributions over several thousand unit cells and the occupations of various crystallographic sites are based upon independent probability distributions and not conditional probability distributions. Therefore, we can calculate the fractions of allowed homonuclear Si-Si and Ge-Ge and heteronuclear Si-Ge dimers present in these structures for the various compositions by using a binomial distribution, which assumes that no short range order exists throughout the sample. For example, if the site occupancy factor for Ge at site T1 is u, then the corresponding factor for Si at site T1 is $v = 1-u$, and we can work out the distribution of Ge-Ge, Ge-Si and Si-Si dimers by $(u + v)^2 = u^2 + 2uv + v^2$. In this expression, u^2 = fraction of Ge-Ge dimers; $2uv$ = fraction of Si-Ge dimers; and v^2 = fraction of Si-Si dimers found at T1-T1 sites throughout the crystal. The Ge site occupancy factors for the T1, T2 and T3 sites as a function of x in $Gd_5(Si_xGe_{1-x})_4$ are plotted in Figure 5.2. A completely random distribution of Si and Ge atoms among the sites would produce 3 coincident, linear plots. The graph also indicates the boundaries between the various structural regions.

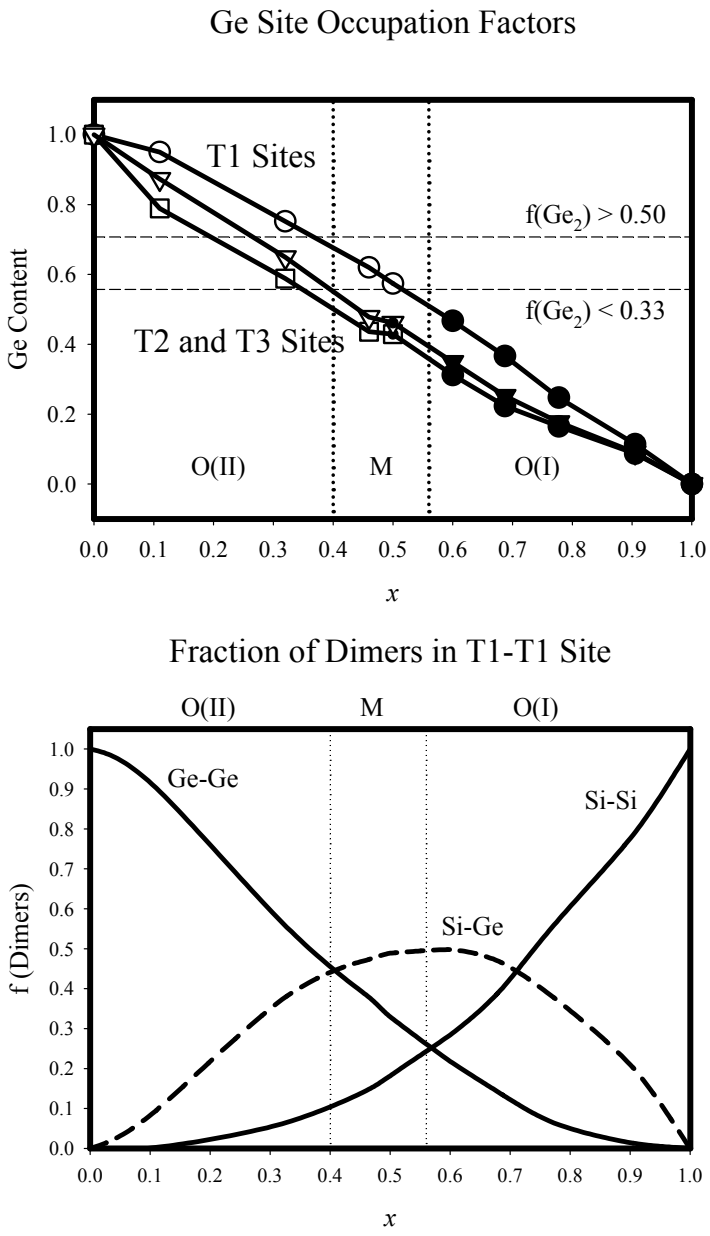

Figure 5.2. (Top) Ge occupation in each T site in $Gd_5(Si_xGe_{1-x})_4$ as a function of Si concentration, *x*. The dark symbols are from this work; the open symbols come from reference 23. The three different structure regimes at room temperature are noted by vertical dotted lines. See text for explanation of the horizontal dashed lines. (Bottom) Fraction of Ge-Ge (solid), Si-Ge (dashed) and Si-Si (solid) dimers at the T1-T1 sites as a function of Si concentration, x.

Note that the Gd_5Si_4-type structure with short T1-T1 contacts occurs as long as the fraction of Ge-Ge dimers in these sites is below 33%, which means that the fraction of Ge in the T1 site, $u <$ 57.7%. When the fraction of Ge-Ge dimers exceeds 50%, i.e., $u >$ 71.4%, then these T1-T1 bonds are completely severed in the room temperature structures. For intermediate concentrations, 57.7% $< u <$ 71.4%, the monoclinic structure is observed in which one-half of the T1-T1 contacts are short and one-half of them are long.

From a different perspective, we plot the fractions of Ge-Ge, Si-Ge, and Si-Si dimers that occur at the T1-T1 sites as a function of x. Since there is a preference for Ge atoms in the T1 sites, these graphs are skewed away from the midpoint, $x = ½$. According to the graph, in the range $0 \le x \le 0.4$, Ge-Ge dimers are most abundant; from $0.4 \le x \le 0.7$, Si-Ge dimers dominate; and then for $0.7 \le x \le 1.0$, Si-Si dimers are most abundant. Furthermore, the fraction of Si-Si dimers exceeds that of Ge-Ge dimers for $x \ge 0.56$. We, therefore, see a correlation between the observed room-temperature structure in the $Gd_5(Si_xGe_{1-x})_4$ series and the distribution of Si and Ge atoms at the T1 positions. The O(II) structure, with no T1-T1 bonds, exists when the concentration of Ge-Ge dimers is highest; the O(I) structure, with all T1-T1 bonds, occurs when the concentration of Si-Si dimers exceeds that of the Ge-Ge dimers. The monoclinic M structure exists for intermediate values. In our opinion, size arguments cannot provide the entire rationale for the distinctive changes in interatomic T1-T1 distances with composition. Nevertheless, the effects of size are clearly seen in trends in unit cell volumes with x. Using volume increments for zero valent Si and Ge from Biltz's compendium (19.98 $Å^3$/atom for Si; 22.43 $Å^3$/atom for Ge),[28] one obtains a consistent range of volume increments for Gd (26.5-26.8 $Å^3$/atom) from the observed volumes for $Gd_5(Si_xGe_{1-x})_4$. Furthermore, the trends in T1-T1 and T2-T3 distances that are shown in Figure 5.3, show the size effect, but point out the distinct difference in chemical bonding that occurs in these two sets of dimers.

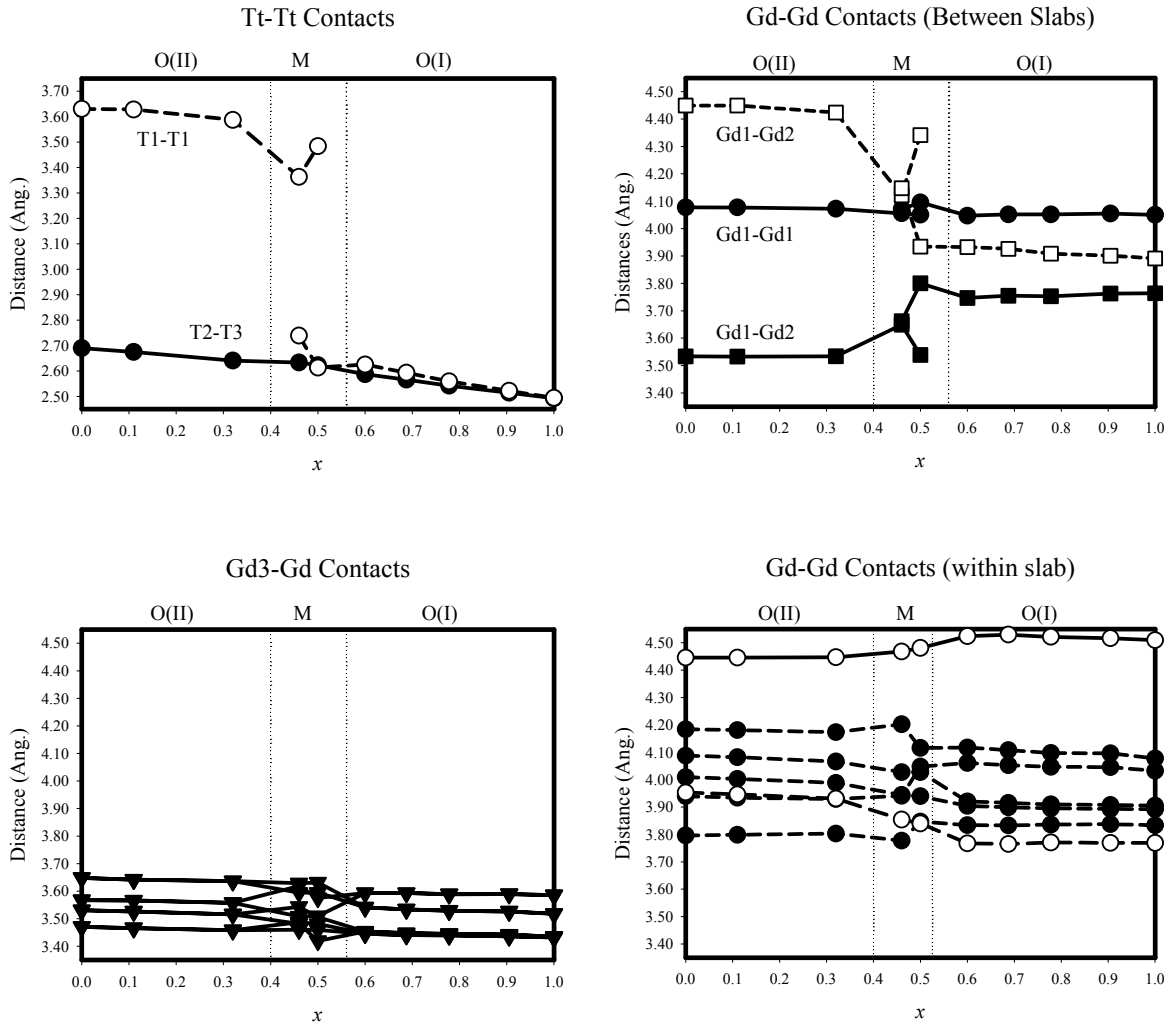

Figure 5.3a. Interatomic distance variations in $Gd_5(Si_xGe_{1-x})_4$ as a function of Si concentration, *x*. These graphs illustrate trends in Tt-Tt and Gd-Gd distances. The distance scale on all Gd-Gd graphs are identical to illustrate the relative magnitudes.

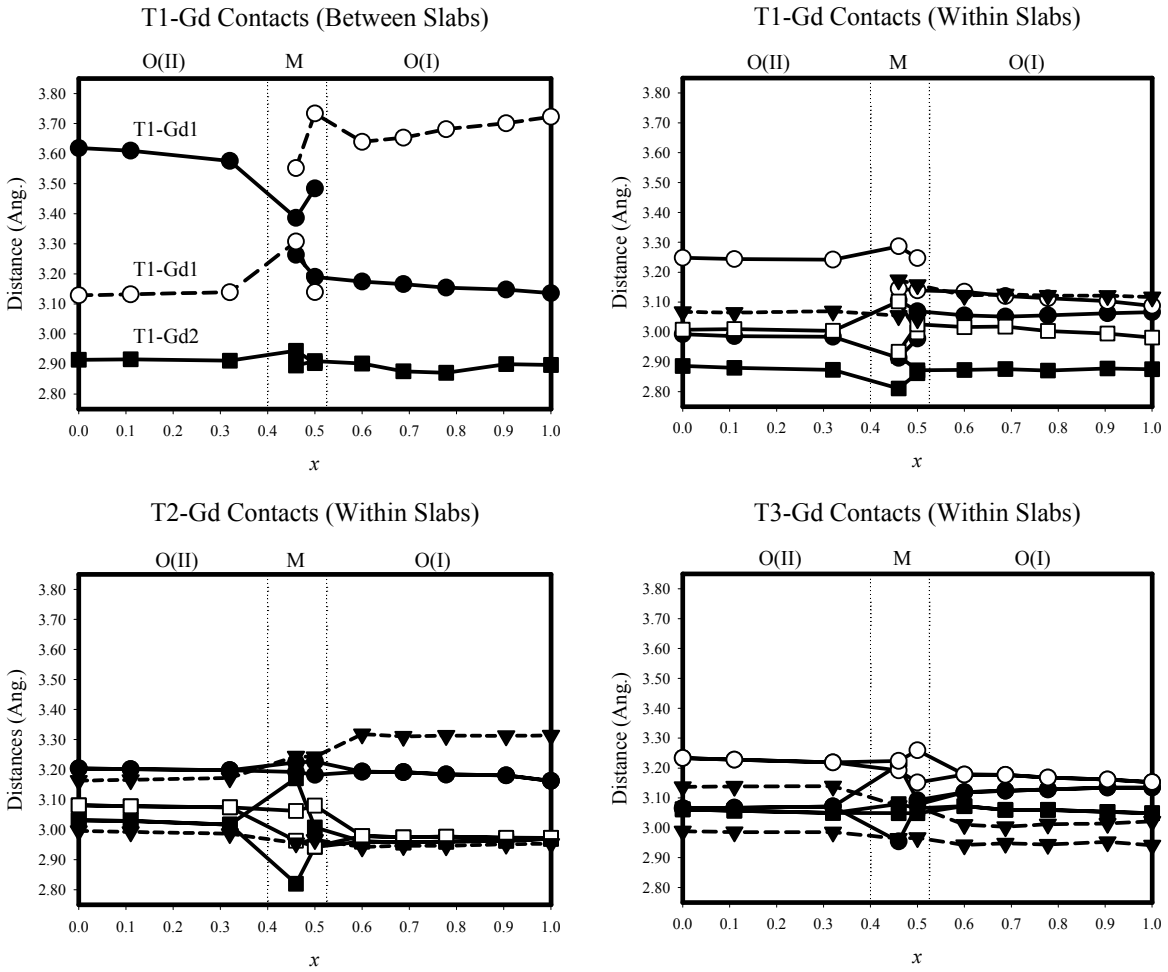

Figure 5.3b. Interatomic distance variations in $Gd_5(Si_xGe_{1-x})_4$ as a function of Si concentration, x. These graphs illustrate trends in Tt-Gd distances. The distance scale on all Tt-Gd graphs are identical to illustrate the relative magnitudes.

In an earlier paper, we showed that the site preferences for Si and Ge atoms could be explained by a site energy and bond energy argument.[23] The site energy argument concludes that the T1 sites are attractive for the more electronegative element (Ge). The bond energy argument shows that the site symmetry of the T1-T1 contacts allows mixing between σ_p* and π molecular orbitals of the T1-T1 dimer. Thus, the weaker Ge-Ge bond pair loses less energy by occupying the T1-T1 site than the Si-Si bond pair does. Therefore, these two distinct arguments give consistent predictions, but there are other significant changes in Gd-(Si,Ge) and Gd-Gd interactions as the structure type varies along the $Gd_5(Si_xGe_{1-x})_4$ series.

Trends for the various interatomic distances across the entire $Gd_5(Si_xGe_{1-x})_4$ series are illustrated in Figure 5.3 (data for Ge-rich samples are taken from reference 23; data for Si-rich samples come from this work). Although the most notable change occurs for the T1-T1 distance along the series O(II)-M-O(I) as x increases, there are also significant distance variations associated with the Gd1 sites. The graphs of distances show clear trends, with some irregularities among the monoclinic structures, which can be attributed to the occurrence of merohedral twins in all cases and the inherent difficulties to obtain well resolved parameters for such samples.[16] Nevertheless, as the T1-T1 distance decreases sharply from the O(II) to the O(I) structure, there is a distinct switch in length between two T1-Gd1 contacts. Figure 5.4 illustrates the coordination environments for the T1 sites in both the O(I) and O(II) structures to highlight these changes. In both cases the T1 atom is surrounded by a tricapped trigonal prism: the prism is formed by six Gd atoms while the capping atoms are another T1 site, one Gd3 site, and another Gd1 site. In the O(I) structure, with the short T1-T1 contact (ca. 2.49 Å), the T1-Gd1 contact capping the trigonal prism is long (ca. 3.73 Å). In the O(II) structure, the corresponding T1-Gd1 contact has decreased to 3.13 Å while the T1-T1 distance is now ca. 3.63 Å. Note in the figure that one of the T1-Gd1 distances within the trigonal prism also increases from ca. 3.14 to 3.62 Å as the structure switches from O(I)-type to O(II)-type.

The other significant change arises for Gd-Gd interslab distances: in the O(II) structure, there is a short Gd1-Gd1 contact (ca. 3.53 Å) that expands to ca. 3.76 Å in the O(I) structure type (Figure 5.5). Thus, we can simply state that Tt-Tt bonds in the O(I) structure are exchanged for Tt-Gd and Gd-Gd bonds in the O(II) structure. In Gd_5Ge_4, these short Gd-Gd bonds were used to explain the observed metal-semiconductor transition at 110 K,[29] and they can also help explain the antiferromagnetic ordering observed for the low-temperature O(II) phases in the Ge-rich $Gd_5(Si_xGe_{1-x})_4$. In general, however, the shortest Gd-Gd distances in these structures are found between Gd3 and Gd1/Gd2 atoms (the pseudo-cubic coordination sphere) – see Figure 5.3.

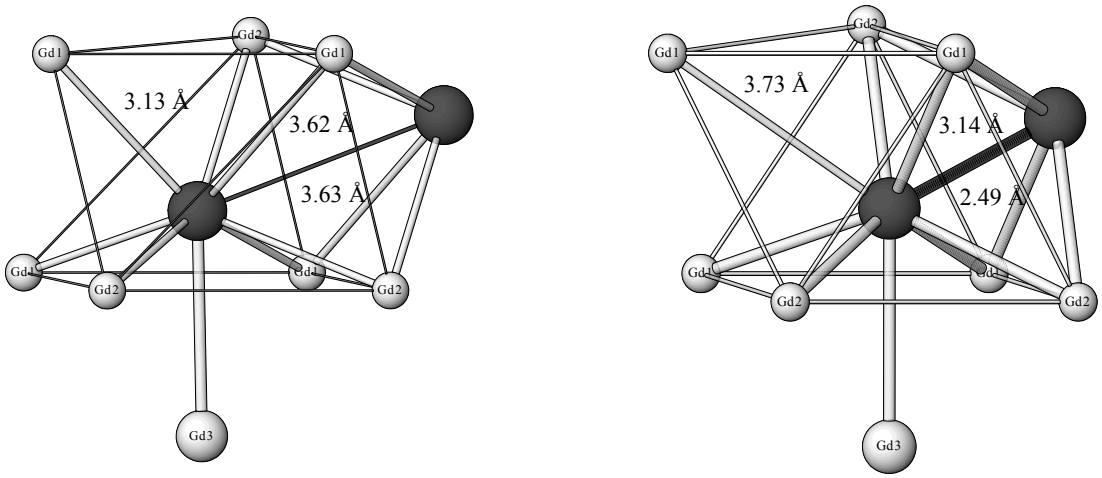

O(II)-Type **O(I)-Type**

Figure 5.4. Coordination environments surrounding the T1 sites in the orthorhombic O(II) and O(I) structures. Interatomic distances showing significant differences between the structures are included.

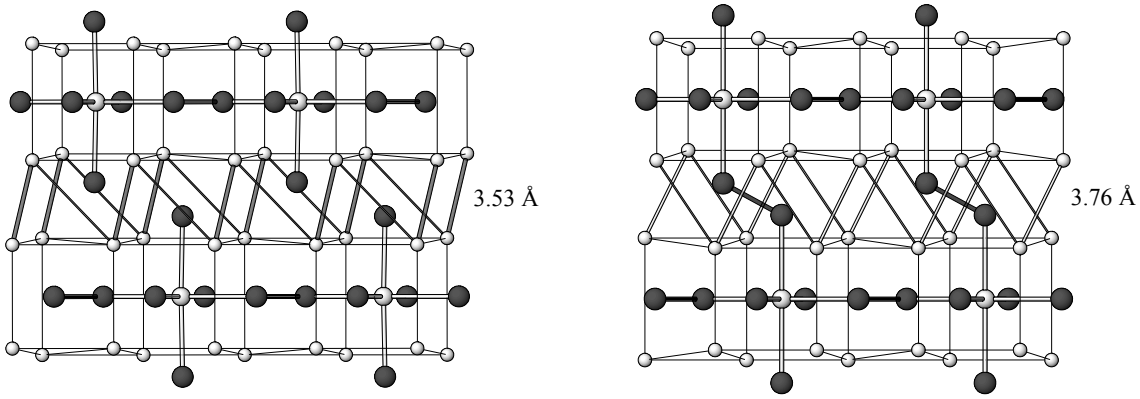

O(II)-Type **O(I)-Type**

Figure 5.5. Interslab contacts for the O(II) and O(I) structure types

As a final comment about the variations in interatomic distances shown in Figure 5.3, many experimental and theoretical discussions concerning this $Gd_5(Si_xGe_{1-x})_4$ series rely on the slabs remaining intact. This distance analysis essentially confirms this picture, although there are some subtle distance rearrangements across the series. Nevertheless, changes in these interatomic contacts are not as noticeable as those changes occurring between slabs.

Completing this structural analysis and distribution of Si and Ge atoms in the $Gd_5(Si_xGe_{1-x})_4$ series of structures sheds further light on the importance of chemical bonding factors influencing their structures and physical properties. The changes in crystal structure, which can be driven by temperature, magnetic field and temperature, as well as by chemical substitutions, occur due to the subtle differences in chemical bonding strengths. Electronic structure calculations using the TB-LMTO-ASA approach on different arrangements of Si and Ge atoms distributed among the T1, T2 and T3 sites consistently give lower energies to those arrangements where Ge occupies the T1 sites.[23] As part of this study, we explored the total electronic energy differences for $Gd_5Si_2Ge_2$ in the three different structure types: O(I), M and O(II) and for two distinct arrangements of Si and Ge atoms: (i) Ge in T1, Si in T2 and T3; or (ii) Si in T1, Ge in T2 and T3. These results are summarized in Table 5.4. In all cases, Ge atoms prefer the T1 sites, but the energy differences increase from O(I)-type to M-type to O(II)-type: ca. 0.02 eV/formula unit for O(I); ca. 0.11 eV/formula unit for M; and ca. 0.17 eV/formula unit for O(II). Thus, there is a greater tendency for Si and Ge mixing for the O(I)-type structures with short T1-T1 contacts. We also examined the relative total energies for Gd_5Si_4, $Gd_5Si_2Ge_2$ and Gd_5Ge_4 in the three structure types. For these calculations, hypothetical structures were necessary in which the unit cell volumes were held constant for a given composition while the structural parameters were scaled isotropically to maintain constant relative distances and angles. As Table 5.4 indicates, for the entire series, the calculated ground state structure of $Gd_5(Si_xGe_{1-x})_4$ is the orthorhombic O(I)-type, which agrees with earlier calculations.[30] The orthorhombic O(II)-type is more competitive with Ge-rich examples, as is observed experimentally, and its calculated total electronic energy increases relative to the O(I)-type with increasing Si concentration. The monoclinic phase lies intermediate in energy between the O(I) and O(II)-type structures – note that earlier calculations[30] found the monoclinic phase to be lower in energy than the O(I)-type but for a smaller monoclinic angle than the experimentally determined one (ca. 91.7° vs. 93.2°). Nevertheless, the computational results allow us to conclude that there is a strong correlation between the occupation of the T1 sites and the observed structures or possible phase behavior of $Gd_5(Si_xGe_{1-x})_4$. Further efforts to clarify these models for other rare-earth systems are underway.

Table 5.4. Summary of relative total energies calculated for various models of Gd_5Ge_4, $Gd_5Si_2Ge_2$ and Gd_5Si_4 by TB-LMTO-ASA. All energies are given in units of eV/formula unit, and are expressed relative to the lowest energy arrangement for each composition.

Model		Gd_5Ge_4	$Gd_5Si_2Ge_2$	Gd_5Si_4
O(I):	Ge in T1	0.000	0.000	---
O(I):	Si in T1	---	0.027	0.000
M:	Ge in T1	0.043	0.097	---
M:	Si in T1	---	0.205	0.242
O(II):	Ge in T1	0.177	0.250	---
O(II):	Si in T1	---	0.420	0.437

5.5. Summary

The distribution of Si and Ge atoms among the various Tt sites in the $Gd_5(Si_xGe_{1-x})_4$ series has been completed by single crystal X-ray diffraction experiments. With the results from reference 23, we see a clear correlation between the distribution of Si and Ge atoms at the T1 sites between the slabs and the nature of the T1-T1 contacts at room temperature. A thorough analysis of the interatomic distances for the series indicated significant changes in some T1-Gd and Gd-Gd interactions between slabs as the structure varies, and these variations can have significant effects on their physical properties. Electronic structure calculations provide a rationale for these observations, but still do not give a clear understanding of the complex phase behavior in these compounds.

5.6. Acknowledgements

The authors thank Prof. Yurij Mozharivskyj for informative discussions. This work was carried out at the Ames Laboratory, which is operated for the U.S. Department of Energy by Iowa State University under Contract No. W-7405-ENG-82. This work was supported by the Materials Sciences Division of the Office of Basic Energy Sciences of the U.S. Department of Energy.

5.7. References

(1) Pecharsky, V. K.; Gschneidner, K. A., Jr. *Phys. Rev. B* **1997**, *78*, 4494.

(2) Pecharsky, V. K.; Gschneidner, K. A., Jr. *Appl. Phys. Lett.* **1997**, *70*, 3299.

(3) Pecharsky, V. K.; Gschneidner, K. A., Jr. *J. Magn. Magn. Mater.* **1997**, *167*, L179.

(4) Giguere, A.; Foldeaki, M.; Gopal, R. R.; Bose, T. K.; Frydman, A., *Phys. Rev. Lett.* **1999**, *83*, 2262.

(5) Gschneidner, K.A., Jr.; Pecharsky, V. K.; Duijin, H. G. M.; Levin. E. M., *Phys. Rev. Lett.* **2000**, *85*, 4190.

(6) Pecharsky, A. O.; Gschneidner, K. A., Jr.; Pecharsky, V. K., *J. Appl. Phys.* **2003**, *93*, 4722.

(7) Gschneidner, K.A., Jr.; Pecharsky, V. K.; Tsokol, A. O., *Rep. Prog. Phys.* **2005**, *68*, 1479.

(8) Morellon, L.; Blasco, J.; Algarabel, P. A.; Ibara, M. R., *Phys. Rev. B* **2000**, *62*, 1022.

(9) Morellon, L.; Algarabel, P. A.; Ibara, M. R.; Blasco, J.; Garcia-Landa, B., *Phys. Rev. B* **1998**, *58*, R14721.

(10) Magen, C.; Morellon, L.; Algarabel, P. A.; Marquina, C.; Ibara, M. R., *J. Phys.: Condens. Matter* **2003**, *15*, 2389.

(11) Morellon, L.; Stankiewicz, J.; Garcia-Landa, B.; Algarabel, P. A.; Ibara, M. R., *Appl. Phys. Lett.* **1998**, *73*, 3462.

(12) Levin, E. M.; Pecharsky, V. K.; Gschneidner, K. A., Jr. *Phys. Rev. B* **1999**, *60*, 7993.

(13) Levin, E. M.; Pecharsky, V. K.; Gschneidner, K. A., Jr. *J. Magn. Magn. Mater.* **2000**, *210*, 181.

(14) Levin, E. M.; Pecharsky, V. K.; Gschneidner, K. A., Jr. *Phys. Rev. B* **2001**, *63*, 174110.

(15) Stankiewicz, J.; Morellon, L.; Algarabel, P. A.; Ibara, M. R., *Phys. Rev. B* **2000**, *61*, 12651.

(16) Choe, W.; Pecharsky, V. K.; Pecharsky, A. O.; Gschneidner, K. A., Jr.; Young V. G., Jr.; Miller, G. J., *Phys. Rev. Lett.* **2000**, *84*, 4617.

(17) Choe, W.; Miller, G. J.; Meyers, J.; Chumbley, S.; Pecharsky, A. O., *Chem. Mater.* **2003**, *15*, 1413.

(18) Mozharivskyj, Y.; Pecharsky, A. O.; Pecharsky, V. K.; Miller, G. J.; Gschneidner K. A., Jr. *Phys. Rev. B* **2004**, *69*, 144102.

(19) Holtzberg, F.; Gambino, R. J.; McGuire, T. R., *J. Phys. Chem. Solids* **1967**, *28*, 2283.

(20) Smith, G. S.; Johnson, Q.; Tharp, A. G., *Acta Crystallogr.* **1967**, *22*, 269.

(21) Pecharsky, V. K.; Gschneidner, K. A., Jr. *J. Alloys Compd.* **1997**, *260*, 98.

(22) Pecharsky, A .O.; Gschneidner K. A., Jr.; Pecharsky, V. K.; Schindler, C. E., *J. Alloys Compd.* **2002**, *338*, 126.

(23) Choe, W.; Pecharsky, A. O.; Wörle, M.; Miller, G. J., *Inorg. Chem.* **2003**, *42*, 8223.

(24) Kraus, W.; Nolze, G., *PowderCell for Windows, Version 2.4*; **2000**.

(25) *XRD Single Crystal Software*; Bruker Analytical X-ray Systems: Madison, USA, **2002**.

(26) (a) Andersen, O. K., *Phys. Rev. B* **1975**, *12*, 3060; (b) Andersen, O. K.; Jepsen, O., *Phys. Rev. Lett.* **1984**, *53*, 2571; (c) Andersen, O. K.; Jepsen, O.; Glötzel, D., in *Highlights of Condensed-Matter Theory*; Bassani, F.; Fumi, F.; Tosi, M .P., Eds.; North-Holland: New York, **1985**; (d) Andersen, O. K., *Phys. Rev. B* **1986**, *34*, 2439.

(27) Jepsen, O.; Andersen, O. K., *Z. Phys. B* **1995**, *97*, 35.

(28) (a) Biltz, W., *Raumchemie der festen Stoffe*, Verlag von Leopold Voss, Leipzig, **1934**; (b) Dronskowski, R., *Computational Chemistry of Solid State Materials*, Wiley-VCH, Weinheim, **2005**.

(29) Levin, E. M.; Pecharsky, V. K.; Gschneidner K. A., Jr.; Miller, G. J., *Phys. Rev. B* **2001**, *64*, 235103.

(30) Pecharsky, V. K.; Samolyuk, G. D.; Antropov, V. P.; Pecharsky, A. O.; Gshneidner, K. A., Jr. *J. Solid State Chem.* **2003**, *171*, 57.

Chapter 6

Structural, Magnetic, and Thermal Characteristics of the Phase Transitions in $Gd_5Ga_xGe_{4-x}$ Magnetocaloric Materials

An article prepared to be published in a journal

Sumohan Misra, Yurij Mozharivskyj, Alexandra O. Tsokol, Deborah L. Schlagel, Thomas A. Lograsso, Gordon J. Miller

6.1. Abstract

Temperature-dependent, single crystal and powder X-ray diffraction studies as well as magnetization and heat capacity measurements were carried out on two phases of the $Gd_5Ga_xGe_{4-x}$ system: for x = 0.7 and 1.0. $Gd_5Ga_{0.7}Ge_{3.3}$, shows three structure types as a function of temperature: (i) from 165 K to room temperature, the orthorhombic Sm_5Ge_4-type crystal structure exists; (ii) below 150 K, it transforms to a orthorhombic Gd_5Si_4-type structure; and (iii) a monoclinic $Gd_5Si_2Ge_2$-type component is observed at the intermediate temperature range of 150 K $\leq T \leq$ 165 K. This is the first time that all these three structure types have been observed for the same composition. For $Gd_5Ga_{1.0}Ge_{3.0}$, the room temperature phase belongs to orthorhombic Pu_5Rh_4-type structure with interslab contacts between main group atoms of 2.837(4) Å. Upon heating above T > 523 K, it transforms to a Gd_5Si_4-type structure with this distance decreasing to 2.521(7) Å before decomposing at T > 573 K.

6.2. Introduction

Since the discovery of a giant magnetocaloric effect in the pseudobinary $Gd_5(Si_xGe_{1-x})_4$ system,[1-8] many intriguing magnetic, crystallographic and electronic responses have been observed in this family of metal-rich compounds.[9-16] Recent studies reveal that the rich chemistry and physics associated with these compounds are closely related to their two-dimensional structural building blocks and strong magnetoelastic

coupling present in these materials.[17] The features that have captured the attention of solid-state chemists are microscopic twinning,[18] dependence of crystal structures on the Si/Ge ratio[19,20] and valence electron count, [21,22] and their ability to break and re-form covalent bonds existing between pairs of Si/Ge atoms on heating and cooling near the corresponding transition temperatures. Such structural behavior has been termed "nanoscale zippers".[23] The crystal structures of $Gd_5(Si_xGe_{1-x})_4$ and many other RE_5Tt_4 (RE = rare earth; *Tt* = Si and/or Ge) materials are built from slabs of two eclipsed 3^2434 nets of RE atoms separated by ca. 0.7 nm. The arrangements of the atoms in the slabs and, in turn, the structural and magnetic properties depend on the presence or absence of interslab main group-main group chemical bonds. Three room temperature crystal structures exist for the $Gd_5(Si_xGe_{1-x})_4$ series. The Si-rich compounds ($x \geq 0.56$) adopt the orthorhombic, Gd_5Si_4-type crystal structure[24] and features interslab Si(Ge)-Si(Ge) bonds (distances ca. 2.4-2.6 Å); the Ge-rich compounds ($x \leq 0.3$) adopt the orthorhombic, Sm_5Ge_4-type crystal structure[25] and is characterized by the absence of any interslab Si(Ge)-Si(Ge) bonds (distances exceeds 3.4 Å). The materials in the intermediate composition range ($0.40 \leq x \leq 0.503$) crystallize in the monoclinic $Gd_5Si_2Ge_2$-type crystal structure[26] and has one pair of slabs connected by Si(Ge)–Si(Ge) bonds; however, the other pair do not show interslab Si(Ge)–Si(Ge) bonds. Transformations between different crystal structures can be controlled by changing chemical composition, temperature, magnetic field and pressure[17,10] and very recently, our research group demonstrated the same control by altering the valence electron concentration.[21]

Electronic structure calculations have suggested the close connection between the structure and magnetic behavior of $Gd_5(Si_xGe_{1-x})_4$ with the number of valence electrons available for metallic bonding.[17,27] Recently, this idea was tested on $Gd_5Ga_xGe_{4-x}$.[21] It was found that a decrease in valence electron concentration through substitution of three-valent, size-equivalent gallium for four-valent germanium results in reduced population of T1-T1 (Ge-Ge) antibonding states and this leads to steady formation of T1-T1 interslab dimers.* This resulted in a structural transformation from the Sm_5Ge_4-type ($0 \leq x \leq 0.9$) to an intermediate, previously unreported, Pu_5Rh_4-type[28] ($0.7 \leq x \leq 1.0$), and then finally to the

* T1-T1 are main group-main group dimers between $_\infty^2[Gd_5T_4]$ slabs. The various structure types observed for the $Gd_5Ga_xGe_{4-x}$ system can be differentiated by the length of these T1-T1 dimer distances.

Gd_5Si_4-type ($1.2 \leq x \leq 2.2$), which is indicated by a plot of the lattice constant ratio c/a vs. Ga content x, shown in Figure 6.1. Now, to investigate a possible effect of temperature on the $Gd_5Ga_xGe_{4-x}$ system, we focused on two compositions, $Gd_5Ga_{0.7}Ge_{3.3}$ and $Gd_5Ga_{1.0}Ge_{3.0}$, which lie, respectively, at the bottom and top ends of the discontinuous part of the c/a vs. x plot (the plotted lattice parameters for $Gd_5Ga_{0.7}Ge_{3.3}$ from powder data belong to Pu_5Rh_4-type and from single crystal data belong to Sm_5Ge_4-type structures. For details see reference 21).

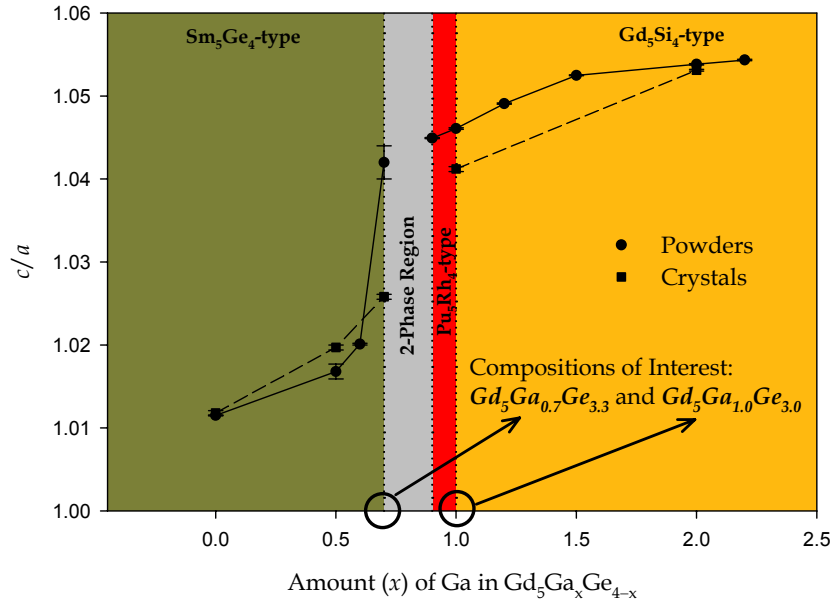

Figure 6.1. Variation of c/a with the amount (x) of Ga in $Gd_5Ga_xGe_{4-x}$. Also shown are the two compositions of interest, $Gd_5Ga_{0.7}Ge_{3.3}$ and $Gd_5Ga_{1.0}Ge_{3.0}$, for the present study. (Plot modified from reference 21)

In situ single crystal X-ray diffraction experiments show that $Gd_5Ga_{0.7}Ge_{3.3}$ transforms to a Gd_5Si_4-type structure for temperatures below 150 K. Between 150 K and 165 K the monoclinic $Gd_5Si_2Ge_2$-type is also observed. On the other hand, *in situ* powder and single crystal X-ray diffraction experiments show that $Gd_5Ga_{1.0}Ge_{3.0}$ adopts a Pu_5Rh_4-type structure at room temperature and transforms to a Gd_5Si_4-type structure above ca. 523 K. In addition to structural details, we also report results of magnetization and heat capacity measurements for these two compositions.

6.3. Experimental Section

6.3.1. Syntheses: All weighings were done in air and were then taken inside a glove-box (conc. of H_2O = 60-80 ppm) equipped with an arc-melter. All samples studied here were not subjected to any heat treatments.

6.3.1.1. $Gd_5Ga_{0.7}Ge_{3.3}$**:** Samples were prepared by arc-melting stoichiometric mixtures of high purity constituent elements on a water-cooled copper hearth in an argon atmosphere. The starting materials, pieces of Gadolinium (99.99 wt. %, Materials Preparation Center, Ames Laboratory), Gallium (99.99 wt. %, Aldrich), and Germanium (99.9999 wt. %, Alfa Aesar), were used as obtained. The buttons were then re-melted six times to ensure compositional homogeneity throughout the ingot and the alloy drop cast into a copper chill cast mold. Then the as-cast ingot with a total weight of 74g was electron beam welded in a tungsten Bridgman style crucible for crystal growth. The ingot was heated in a tungsten mesh resistance furnace under a pressure of 8.8×10^{-5} Pa up to 1700°C and held at this temperature for 30 minutes to degas the crucible and charge. The chamber was then backfilled to a pressure of 3.4×10^{4} Pa with high purity argon. The ingot was then heated to 1900°C followed by withdrawal from the heat zone at a rate of 8 mm/hr. The loaded composition for the samples grown by Bridgman method was $Gd_5Ga_{1.0}Ge_{3.0}$ but due to elemental separation of Ga and Ge during Bridgman growth, the top part of the ingot was Ga-rich and the bottom part of the ingot was Ge-rich (discussed in detail in later sections). $Gd_5Ga_{0.7}Ge_{3.3}$ single crystals were extracted from both the as-cast ingot as well as the bottom part of the as-solidified ingot grown by the Bridgman method.

6.3.1.2. $Gd_5Ga_{1.0}Ge_{3.0}$**:** Samples were prepared by arc-melting stoichiometric mixtures of high purity constituent elements on a water-cooled copper hearth in an argon atmosphere. The purity of the starting materials was the same as mentioned above. Each ingot had a total weight between 1-3g and was remelted six times to ensure homogeneity. Weight losses during melting were less than 0.1 wt. %. $Gd_5Ga_{1.0}Ge_{3.0}$ single crystals were extracted only from the as-cast samples.

6.3.2. Powder X-ray Diffraction: The as-cast samples were examined by powder X-ray diffraction for identification and to assess phase purity. These initial powder patterns were

obtained using an Enraf-Nonius Guinier camera using monochromatized Cu K_α radiation (λ = 1.54187 Å) at 298 K. The purity and homogeneity of all phases were confirmed by comparison of powder X-ray diffraction patterns to those calculated from single-crystal data using the *POWDER CELL* software.[29] Powder patterns at high temperature were collected on a Rigaku TTRAX rotating anode diffractometer using Mo K_α radiation (λ = 0.71075 Å) and equipped with a sample heater in an evacuated chamber. Fine $Gd_5Ga_{1.0}Ge_{3.0}$ powder with particle size less than 38 μm was obtained by grinding the ingot in an Agate mortar and pestle and then passed through a stainless steel sieve. The grounded powder was mounted on a copper sample holder and the sample was smoothed using a stainless steel razor blade. The scattered intensity was measured as a function of Bragg angle with a scintillation detector, in a step scan mode for 2θ ranging from 9.00° to 42.00° and a stepsize of 0.01° with the intensity measured for 2 sec. for each point. The sample temperature remained stable within ± 1K with respect to the value set for an experiment. All diffraction patterns collected at various temperatures were analyzed by a full-profile Rietveld refinement using *LHPM RIETICA* software.[30] The scale factor and the lattice parameters of each phase were refined. The coordinates of individual atoms were refined if the amount of the corresponding phase was at least 20 mole percent. The isotropic displacement parameters of all atoms in each phase were assumed to be the same. The profile residuals, R_p were from 10.74 to 12.72, and the derived Bragg residuals, R_B were from 6.29 to 7.43.

6.3.3. Single-Crystal X-ray Crystallography: Variable-temperature diffraction experiments were performed on $Gd_5Ga_{0.7}Ge_{3.3}$ and $Gd_5Ga_{1.0}Ge_{3.0}$. Several single crystals were extracted from $Gd_5Ga_{0.7}Ge_{3.3}$ (samples grown by Bridgman method and as-cast samples) and $Gd_5Ga_{1.0}Ge_{3.0}$ (as-cast samples) products. To prevent contamination of the crystals at high temperatures, neither glue nor cement was used to mount the crystals; instead, a special procedure was used (Figure 6.2), the details of which have been described elsewhere.[31] Room- and high-temperature X-ray diffraction data were collected on a Bruker Smart Apex CCD diffractometer with Mo K_α radiation (λ = 0.71075 Å) and a detector-to-crystal distance of 5.990 cm equipped with a Nonius crystal heater. Low-temperature data were collected on a similar instrument equipped with an Oxford Cryosystems cooler. During

the high- and low- temperature diffraction experiments, the temperature remained stable within ±1K with respect to the value set for an experiment. Single crystal diffraction data at 143, 293, 298 and 533 K were collected for a maximum 2θ value of 57° either over a full sphere or a hemisphere of reciprocal space, with 0.3° scans in ω and an exposure time of 10 seconds per frame. Also collected were three sets of 30 frames with similar specifications to obtain the corresponding lattice parameters for high temperature and low temperature diffraction experiments on $Gd_5Ga_{0.7}Ge_{3.3}$ and $Gd_5Ga_{1.0}Ge_{3.0}$ respectively (see Supporting Information). The *SMART*[32] software was used for data acquisition. Intensities were extracted and then corrected for Lorentz and polarization effects by the *SAINT*[32] program. Empirical absorption corrections were accomplished with *SADABS*,[32] which is based on modeling a transmission surface by spherical harmonics employing equivalent reflections with $I > 3\sigma(I)$. Structure solutions and refinements were performed with the *SHELXTL*[32] package of crystallographic programs. Because Ga and Ge atoms could not be unequivocally distinguished by X-ray diffraction techniques in these systems due to the one-electron difference in their electron densities, statistical mixtures of Ga and Ge atoms consistent with sample stoichiometry were assumed on all main group sites during the refinement procedures.

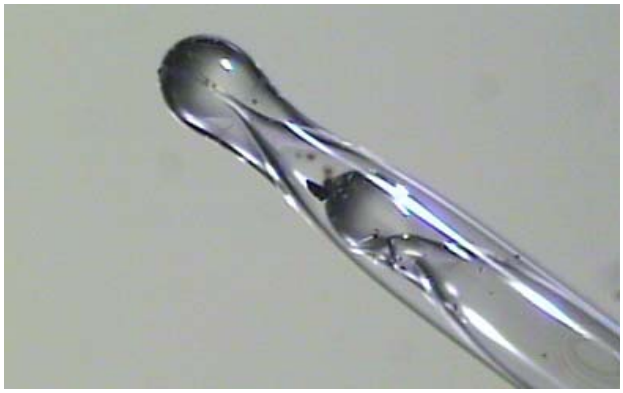

Figure 6.2. A picture of a single crystal of $Gd_5Ga_{1.0}Ge_{3.0}$ prepared for high temperature X-ray diffraction experiments.

6.3.4. Magnetic Property Measurements: Magnetic measurements were carried out using a **S**uperconducting **QU**antum **I**nterference **D**evice (SQUID) magnetometer MPMS-XL

manufactured by Quantum Design, Inc. on single and polycrystalline samples. The measurements included dc magnetic susceptibility measurements between ca. 4 and 300 K and isothermal magnetization measurements in dc magnetic fields varying from 0 to 50 kOe. For the susceptibility measurements, the samples were first cooled under zero magnetic field (zfc) and then the measurements were carried out on heating under a 10 kOe magnetic field. The measurements were then repeated upon cooling with the magnetic field turned on (fc). All data were corrected for temperature-independent contributions.

6.3.5. Heat Capacity Measurements: The heat capacities for both $Gd_5Ga_{0.7}Ge_{3.3}$ and $Gd_5Ga_{1.0}Ge_{3.0}$ were measured using a semi-adiabatic heat-pulse calorimeter[33] between ca. 5 and 400 K in dc magnetic fields ranging from 0 to 10 T. Rectangular blocks weighing 0.3833 g and 1.2615 g, respectively, for $Gd_5Ga_{0.7}Ge_{3.3}$ and $Gd_5Ga_{1.0}Ge_{3.0}$ were used for the above measurements. For $Gd_5Ga_{0.7}Ge_{3.3}$, oriented single crystals along its [001], [010] and [100] axes were used, whereas for $Gd_5Ga_{1.0}Ge_{3.0}$, as-cast polycrystalline samples were used.

6.4. Results and Discussion

6.4.1. Phase Transformation in $Gd_5Ga_{0.7}Ge_{3.3}$: Detailed descriptions of the orthorhombic Sm_5Ge_4-type (O(II)), monoclinic $Gd_5Si_2Ge_2$-type (M), and orthorhombic Gd_5Si_4-type (O(I)) structures can be found elsewhere.[21,23,25,26,28] Lattice parameters and atomic coordinates for $Gd_5Ga_{0.7}Ge_{3.3}$ at 293 and 143 K, are listed in Tables 6.1 and 6.2. The room temperature crystal structure of $Gd_5Ga_{0.7}Ge_{3.3}$ belongs to the Sm_5Ge_4-type with a T1-T1 distance of 3.405(2) Å and c/a = 1.02252(9) (see Table 6.1), which places it near the bottom of the discontinuous part of the c/a vs. x plot (see Figure 6.1) for $Gd_5Ga_xGe_{4-x}$.

Further exchange of Ga for Ge lowers the valence electron count, which removes electrons from T1-T1 antibonding states, thus decreasing the T1-T1 dimer distance, resulting in the intermediate Pu_5Rh_4-type structure and eventually, at x = 1.2, changes to the Gd_5Si_4-type crystal structure.[21] Now, without changing the composition of $Gd_5Ga_{0.7}Ge_{3.3}$, a similar effect was observed by lowering the temperature. The result, as shown in Figure 6.3, is a transformation, first to the monoclinic $Gd_5Si_2Ge_2$-type structure for the temperature range 165 K $\geq T \geq$ 150 K, and then to the orthorhombic Gd_5Si_4-type structure for temperatures

below 150 K, where we have short T1-T1 dimers, e.g. a distance of 2.687(8) Å measured at 143 K.

Table 6.1. Crystallographic data for $Gd_5Ga_{0.7}Ge_{3.3}$ as obtained by single crystal X-ray diffraction (space group *Pnma* (No. 62), Mo *Kα* radiation, 2θ range = 4-57°, $Z = 4$)

Temperature (K)	293	143
Structure Type	Sm_5Ge_4	Gd_5Si_4
***a* (Å)**	7.6359(5)	7.525(2)
***b* (Å)**	14.855(1)	14.829(4)
***c* (Å)**	7.8079(5)	7.840(2)
***V* (Å^3)**	885.7(1)	874.8(4)
No. of Independent Reflections	1117	798
No. of Parameters	46	46
Final R indices [I>2σ(I)]	R1 = 0.0247, wR2 = 0.0557	R1 = 0.0684, wR2 = 0.1413
Peak/hole (e/Å^3)	1.714 / –1.695	3.812 / –5.926
b*/*a	1.94542(9)	1.9706(4)
c*/*a	1.02252(9)	1.0419(4)
T1-T1 (Å)	3.405(2)	2.687(8)

Table 6.2. Atomic coordinates and isotropic displacement parameters for $Gd_5Ga_{0.7}Ge_{3.3}$ as obtained by single crystal X-ray diffraction at 293 K and 143 K.

Atom		***x***	***y***	***z***	**U_{eq}, (Å^2)[a]**
			293 K		
Gd1	8d	0.0106(1)	0.5976(1)	0.1804(1)	0.013(1)
Gd2	8d	0.3619(1)	0.1188(1)	0.1642(1)	0.013(1)
Gd3	4c	0.1962(1)	¼	0.5023(1)	0.012(1)
T1	8d	0.2038(1)	0.0426(1)	0.4642(1)	0.016(1)
T2	4c	0.0668(2)	¼	0.1111(2)	0.014(1)
T3	4c	0.3119(2)	¼	0.8662(2)	0.013(1)

Table 6.2. (continued)

Atom		*x*	*y*	*z*	U_{eq}, (Å^2)[a]
			143 K		
Gd1	8d	0.0194(3)	0.5954(1)	0.1819(2)	0.004(1)
Gd2	8d	0.3228(3)	0.1226(1)	0.1753(2)	0.003(1)
Gd3	4c	0.1530(4)	¼	0.5106(2)	0.003(1)
T1	8d	0.1568(6)	0.0403(2)	0.4697(3)	0.003(1)
T2	4c	0.0249(7)	¼	0.1041(5)	0.003(1)
T3	4c	0.2735(8)	¼	0.8690(5)	0.003(1)

[a] U(eq) is defined as one third of the trace of the orthogonalized U_{ij} tensor.

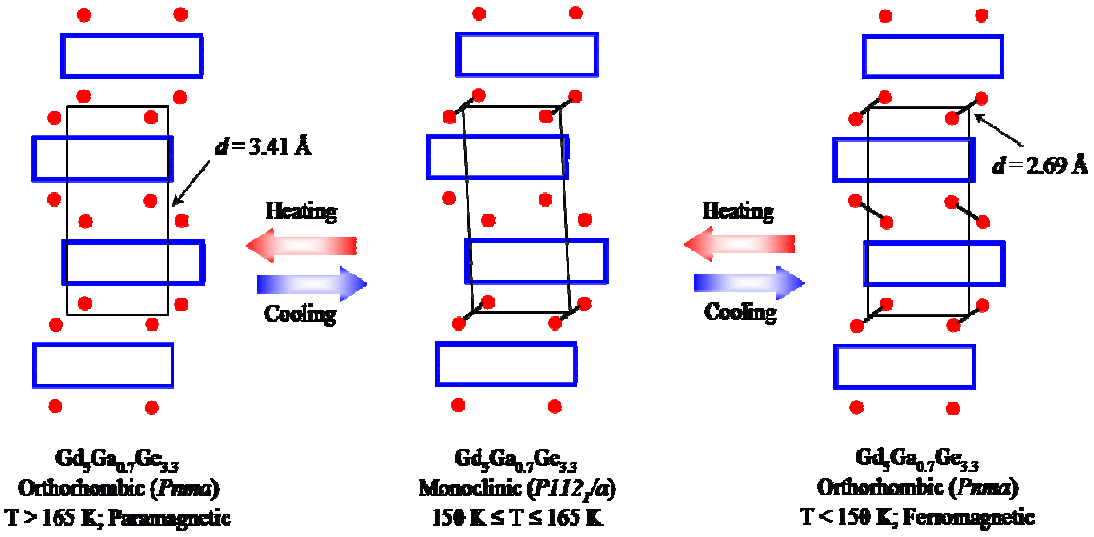

Figure 6.3. Phase transformation in $Gd_5Ga_{0.7}Ge_{3.3}$ as the sample is cooled. The Gd1 and Gd2 network in each slab is shown as the blue "lattice".

There are, seven crystal structures in total, that are reported for RE_5T_4 (RE = rare-earth; *T* = Ga, Si, Ge, Sn, Sb,) materials for various temperatures. They are (i) orthorhombic Sm_5Ge_4-type, (ii) monoclinic $Gd_5Si_2Ge_2$-type, (iii) orthorhombic Gd_5Si_4-type, (iv) tetragonal Zr_5Si_4-type, (v) hexagonal Ti_5Ga_4-type (vi) orthorhombic Eu_5As_4-type and (vii) orthorhombic Pu_5Rh_4-type.[4,21] An eighth crystal structure, adopting the monoclinic $U_2Mo_3Si_4$-type,[34] also

exists for mixtures of rare-earth elements.[35] The materials undergo transitions between different crystal structures with changing chemical composition, temperature, magnetic field, pressure, and valence electron concentration. But, as yet we have only seen a maximum of two crystal structure types being stabilized for a particular chemical composition, when the other parameters are varying. To our knowledge, $Gd_5Ga_{0.7}Ge_{3.3}$ is the first example that exhibits the existence of three structures: the orthorhombic Sm_5Ge_4-type, monoclinic $Gd_5Si_2Ge_2$-type, and orthorhombic Gd_5Si_4-type for the same composition. This exemplifies the degree of flexibility that $Gd_5Ga_xGe_{4-x}$ system possesses and the ability of this system to stabilize various types of crystal structures.

In the 150-165 K range, we always observe the presence of two phases. Near 165 K the monoclinic $Gd_5Si_2Ge_2$-type phase coexists with the Sm_5Ge_4-type structure, while near 150 K, coexists with the Gd_5Si_4-type structure. Additionally, as we have observed before, the orthorhombic and monoclinic phases can coexist as separate crystalline domains within a "single crystal".[23] Hence, due to the presence of these three components: two twinned monoclinic components[17] and one orthorhombic component; we were unable to refine the monoclinic structure thoroughly.

Figure 6.4 illustrates the coordination environments surrounding the T1 sites above and below the phase transition. These are similar to what we observe when the phase changes from Sm_5Ge_4-type to Gd_5Si_4-type for $Gd_5(Si_xGe_{1-x})_4$ materials.[20] In both structures the T1 site is surrounded by a tricapped trigonal prism of eight Gd atoms and one T1 atom. In the Sm_5Ge_4-type structure, with long T1-T1 contacts (ca. 3.405(2) Å), the T1-Gd1 contact capping the trigonal prism is short (ca. 3.220(1) Å). In the Gd_5Si_4-type structure, the corresponding T1-Gd1 contact increases to 3.593(1) Å while the T1-T1 distance decreases to 2.687(8) Å. The figure also highlights one of the T1-Gd1 distances within the trigonal prism which decreases from ca. 3.453(1) to 3.194(3) Å. Also, as we have seen with $Gd_5(Si_xGe_{1-x})_4$ materials,[20] the low-temperature structure has a higher symmetry (*Pnma*) than the high-temperature structure ($P11_2/a$). This is in violation of the Gibbs free energy / entropy relationship, which would imply a reverse structural sequence,[35] and it may be due to large magnetic exchange energy and subsequent magnetic ordering for the orthorhombic phase, which overcomes the unfavorable entropy contribution.[17, 27]

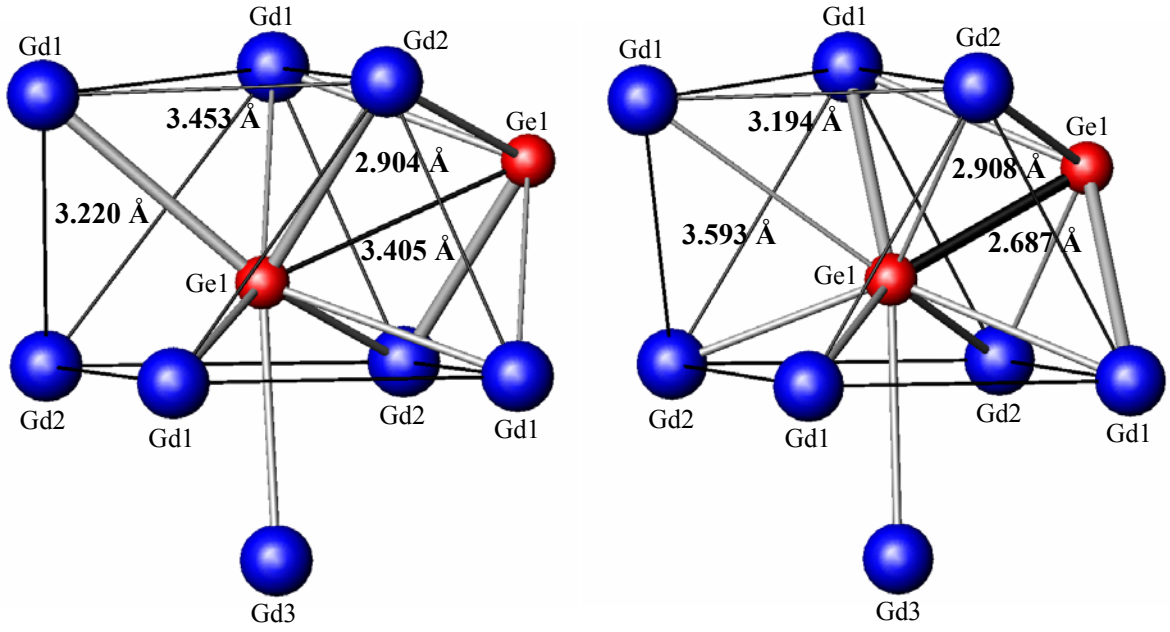

At 293 K **At 143 K**

Figure 6.4. Coordination environments surrounding the T1 sites for $Gd_5Ga_{0.7}Ge_{3.3}$ as it changes with temperature. Interatomic distances showing significant differences between the structures are included.

Magnetic measurements were carried out on single crystalline samples extracted from the bottom part of an ingot grown by the Bridgman method. Figure 6.5 shows the temperature dependency of the dc magnetization measured in a magnetic field of 20 kOe in the temperature range of ca. 5-320 K. The plot portrays two interesting features: (1) a dip in magnetization (shown by the arrow) at ca. 160 K probably corresponds to the structural phase transition from Gd_5Si_4-type → $Gd_5Si_2Ge_2$-type → Sm_5Ge_4-type; and (2) a change in slope (shown by the arrow) at ca 195 K corresponds to the phase transition between paramagnetic and ferromagnetic states.

Figure 6.6 show the temperature variation of the MCE, calculated in terms of the isothermal magnetic entropy change for various field changes (ΔH). The magnetic entropy change was calculated from the $M(H)$ data collected at various temperatures and employing Maxwell's relation as described in reference 37. $Gd_5Ga_{0.7}Ge_{3.3}$ shows a maximum peak at ca.

170 K with a peak value of 14 J/kg K. In comparison, $-\Delta S_M$ for $Gd_5Si_2Ge_2$ shows a peak value of 20 J/kg K for ΔH = 0-5 T at 277 K.[7]

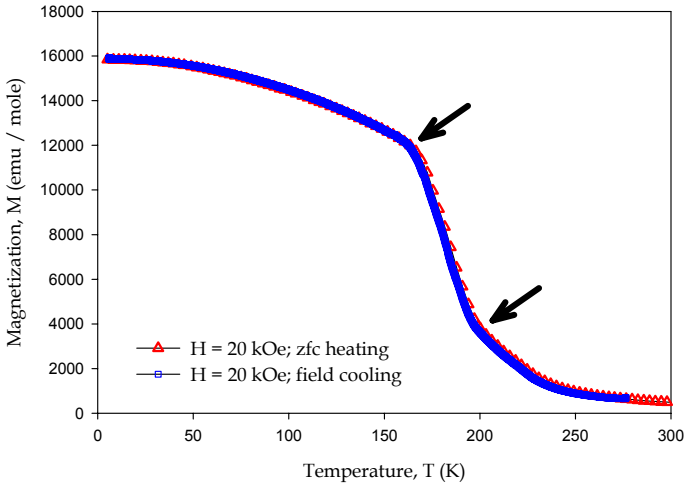

Figure 6.5. The magnetization of zero-magnetic-field cooled samples of $Gd_5Ga_{0.7}Ge_{3.3}$ measured as a function of temperature in a stable dc magnetic field of 20 kOe.

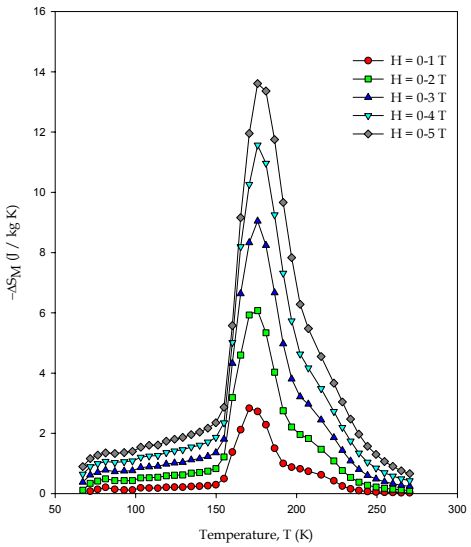

Figure 6.6. The magnetic entropy change ($-\Delta S_M$) of single crystalline $Gd_5Ga_{0.7}Ge_{3.3}$ as a function of temperature calculated from magnetic measurements for 1, 2, 3, 4, and 5 T magnetic field changes.

In order to further understand the magnetic properties of this compound, we also measured the temperature variation of the heat capacity (C_p), shown in Figure 6.7. The $C_p(T)$ data show a non λ-type anomaly peaking at ca. 200 K. The peak width is ca. 50 K and reveals that the phase transitions (both structural and magnetic) are occurring over a wide range of temperature. Both the behavior and location of this anomaly are commensurate with the magnetic measurements shown above.

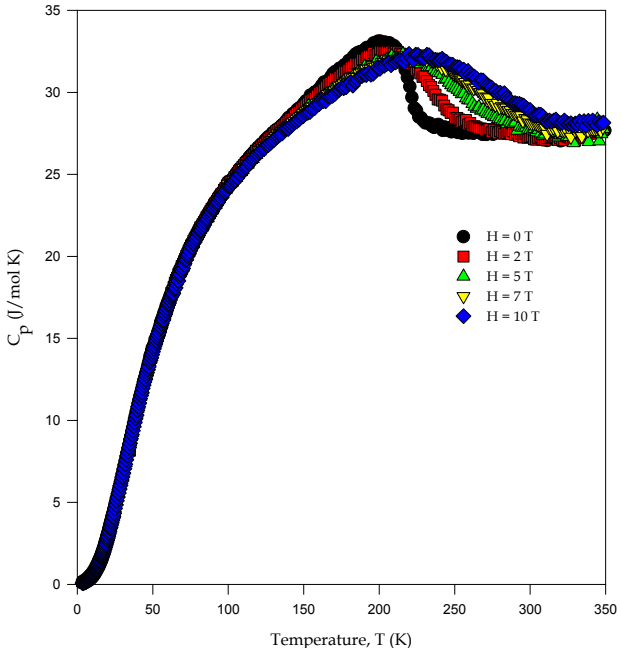

Figure 6.7. The heat capacity of a single crystalline sample of $Gd_5Ga_{0.7}Ge_{3.3}$ oriented along its (001) axis as a function of temperature in 0, 2, 5, 7, and 10 T magnetic fields.

One of the problems that we have encountered during the preparation of this material is its purity. Since it lies near the boundary of a two-phase region (Figure 6.1), preparation of this material typically produces a second Pu_5Rh_4-type phase. The concentration of this second phase is much smaller in samples prepared by the Bridgman method compared to the as-cast samples. This is probably due to elemental separation of Ga and Ge during Bridgman growth, in which the top part of the ingot becomes Ga-rich and the bottom part becomes Ge-rich. We speculate that this phenomenon inhibits the growth of the second Pu_5Rh_4-type phase

in the bottom part of the ingot from which the sample was extracted for the present study, as this second phase only shows up when the Ga content is between 0.7 and 1 for $Gd_5Ga_xGe_{4-x}$. The crystallographic results are similar for both as-cast and samples grown by Bridgman method but the magnetic properties, especially $-\Delta S_M(T)$, depreciate significantly for the as-cast samples. Hence, only the results for samples grown by the Bridgman method are presented here.

To check any possible structural implications of high temperature, we also performed single crystal X-ray diffraction on $Gd_5Ga_{0.7}Ge_{3.3}$ (see Supporting Information) from 298-533 K. These experiments do not reveal any structural transition upto 523 K; and, then, the crystal decomposes at 533 K.

6.4.2. Phase Transformation in $Gd_5Ga_{1.0}Ge_{3.0}$: Lattice parameters and atomic coordinates for $Gd_5Ga_{1.0}Ge_{3.0}$ at 298 and 533 K from single crystal X-ray diffraction experiments are given in Tables 6.3 and 6.4. Figure 6.8 shows the lattice parameters plot for $Gd_5Ga_{1.0}Ge_{3.0}$ obtained from both powder X-ray diffraction in the temperature range 298-623 K. The room-temperature crystal structure of $Gd_5Ga_{1.0}Ge_{3.0}$ belongs to the Pu_5Rh_4-type, which is made up of $_\infty^2[Gd_5T_4]$ (T = Ge and/or Ga) slabs, similar to those found in any of the established crystal structures found for $Gd_5(Si_xGe_{1-x})_4$ series of materials. The interslab dimer distances for the Pu_5Rh_4-type structure lie between the O(I)- and O(II)-type structures. From previous investigations,[21] we have observed that this particular phase is placed at the top end of the discontinuity of the c/a vs. x plot (Figure 6.1). Combined with this, the results of low-temperature X-ray diffraction of $Gd_5Ga_{0.7}Ge_{3.3}$ directed us to expect that upon heating $Gd_5Ga_{1.0}Ge_{3.0}$, the interslab T1-T1 bond distances would increase and possibly cleave, leading to a O(II)-type structure.

Table 6.3. Crystallographic data for $Gd_5Ga_{1.0}Ge_{3.0}$ as obtained by single crystal X-ray diffraction (space group *Pnma* (No. 62), Mo K_α radiation, 2θ range = 4-57°, $Z = 4$).

Temperature (K)	298	533
Structure Type	Pu_5Rh_4	Gd_5Si_4
***a* (Å)**	7.562(4)	7.672(2)
***b* (Å)**	14.929(7)	15.210(5)
***c* (Å)**	7.904(4)	7.834(2)
***V* (Å^3)**	892.3(7)	914.2(5)
No. of Independent Reflections	1095	1142
No. of Parameters	47	47
Final R indices [I > 2σ(I)]	R1 = 0.0527, wR2 = 0.0990	R1 = 0.0711, wR2 = 0.1169
Peak/hole (*e*/Å^3)	2.896 / –2.859	4.011 / –2.795
b*/*a	1.9742(7)	1.9825(4)
c*/*a	1.0452(7)	1.0211(4)
T1-T1 (Å)	2.837(4)	2.521(7)

Table 6.4. Atomic coordinates and isotropic displacement parameters for $Gd_5Ga_{1.0}Ge_{3.0}$ as obtained by single crystal X-ray diffraction at 298 and 533 K.

Atom		***x***	***y***	***z***	**U_{eq}, (Å^2)[a]**
			298 K		
Gd1	8d	0.0136(1)	0.5954(1)	0.1819(1)	0.013(1)
Gd2	8d	0.3285(1)	0.1219(1)	0.1730(1)	0.013(1)
Gd3	4c	0.1633(2)	¼	0.5109(2)	0.014(1)
T1	8d	0.1664(3)	0.4597(1)	0.4672(2)	0.016(1)
T2	4c	0.0324(4)	¼	0.1086(3)	0.015(1)
T3	4c	0.2819(4)	¼	0.8686(3)	0.013(1)
			533 K		
Gd1	8d	0.0294(2)	0.5904(1)	0.1649(2)	0.021(1)
Gd2	8d	0.3066(2)	0.1167(1)	0.1833(2)	0.018(1)
Gd3	4c	0.1343(3)	¼	0.5155(3)	0.018(1)
T1	8d	0.1350(4)	0.4532(2)	0.4878(4)	0.022(1)
T2	4c	0.0078(6)	¼	0.1082(6)	0.021(1)
T3	4c	0.2529(7)	¼	0.8784(6)	0.025(1)

[a] U(eq) is defined as one third of the trace of the orthogonalized U_{ij} tensor.

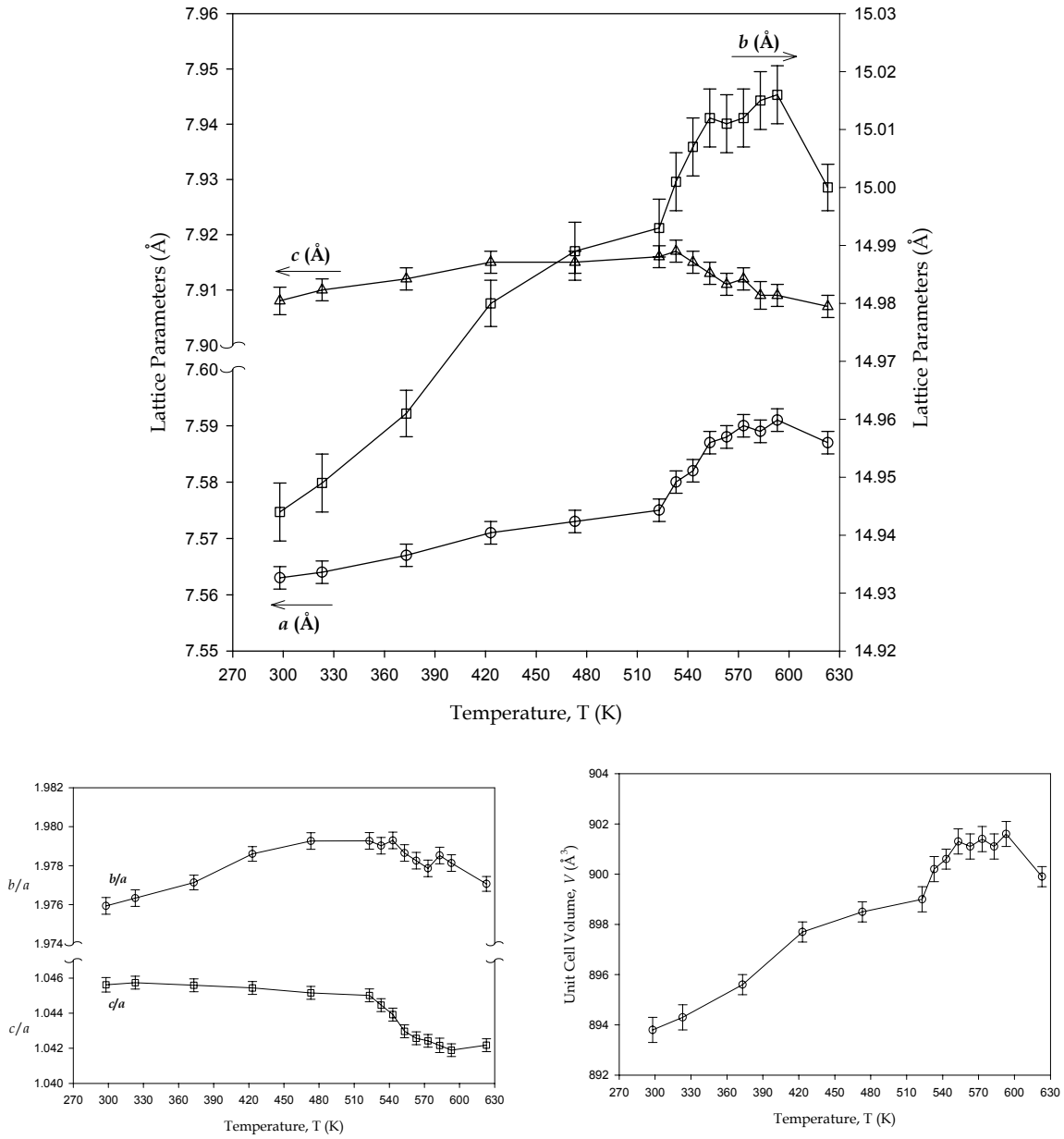

Figure 6.8. Lattice Parameters of $Gd_5Ga_{1.0}Ge_{3.0}$ as a function of temperature as obtained from powder X-ray diffraction.

In fact, a first look at the variations of *b*/*a*, *c*/*a*, and *V* (Figure 6.8) with temperature based on high-temperature powder X-ray diffraction experiments indicates a similar sort of phase transformation as the lattice parameter ratios decrease and the unit cell volume

increases abruptly for $T > 523$ K. This could be attributed to an increase in the *a* lattice parameter and, hence, an increase in the T1-T1 dimer distance. A closer look at the processed data from both powder and single crystal X-ray diffraction shows that an increase in the *a* parameter is accompanied, as expected, by an increase in the *b* parameter, but, unlike what have been observed in other RE_5Tt_4 materials,[19] the *c* parameter decreases. Between 523-593 K, the powder X-ray data shows that there is 0.21% and 0.15% increase in the *a* and *b* lengths respectively. On the other hand, for the same temperature range, there is 0.09% decrease in the *c*-axis. Combining these three trends produces a 0.29% increase in the unit cell volume. This change can be visualized as applying a pressure to an oriented metal block along the *c*-direction with no restrictions along the *a*- and *b*-direction. This forces the slabs to slide closer to each other along the *c*-direction. The result is a decrease in the T1-T1 interslab distance, which lies perpendicular to the *c*-direction, from 2.837(4) Å to 2.521(7) Å (Table 6.3). On closer look, apart from this severe change in interslab dimer distance, there are some subtle structural changes which helps us better understand this phase transition from the Pu_5Rh_4-type to Gd_5Si_4-type structure.

First, consider the fragment, shown in Figure 6.9a and based on single crystal X-ray diffraction at 298 and 533 K. The T1-Gd3-T1 bond angle increases by 4.6(1)°. As evident from the figure, the fragment T1-Gd3-T1 from slab-I is oriented in a 'V' form whereas the fragment T1-Gd3-T1 from slab-II is oriented in an 'inverted V' form and then these two fragments are linked by T1-T1 bonds. As temperature rises, the T1-Gd3-T1 bond angle moves closer to linearity as the *c*-parameter decreases, both of which bring these two linker T1 atoms of the two fragments closer to each other (Figure 6.9b). Also affected are the interslab Gd-Gd contacts as shown in Figure 6.10: at 298 K the longer (4.025 Å) Gd1-Gd2 distances shrinks to 3.802 Å at 533 K. This feature is in stark contrast to what we observe for the $Gd_5(Si_xGe_{1-x})_4$ series of materials, when O(II)-type (short Gd1-Gd1 interslab distance) transforms to O(I)-type structure (long Gd1-Gd1 interslab distance). This probably is due to the fact that in the present scenario the *a*- and *c*-parameter change in the opposite direction, which is not the case for the $Gd_5(Si_xGe_{1-x})_4$ series of materials.

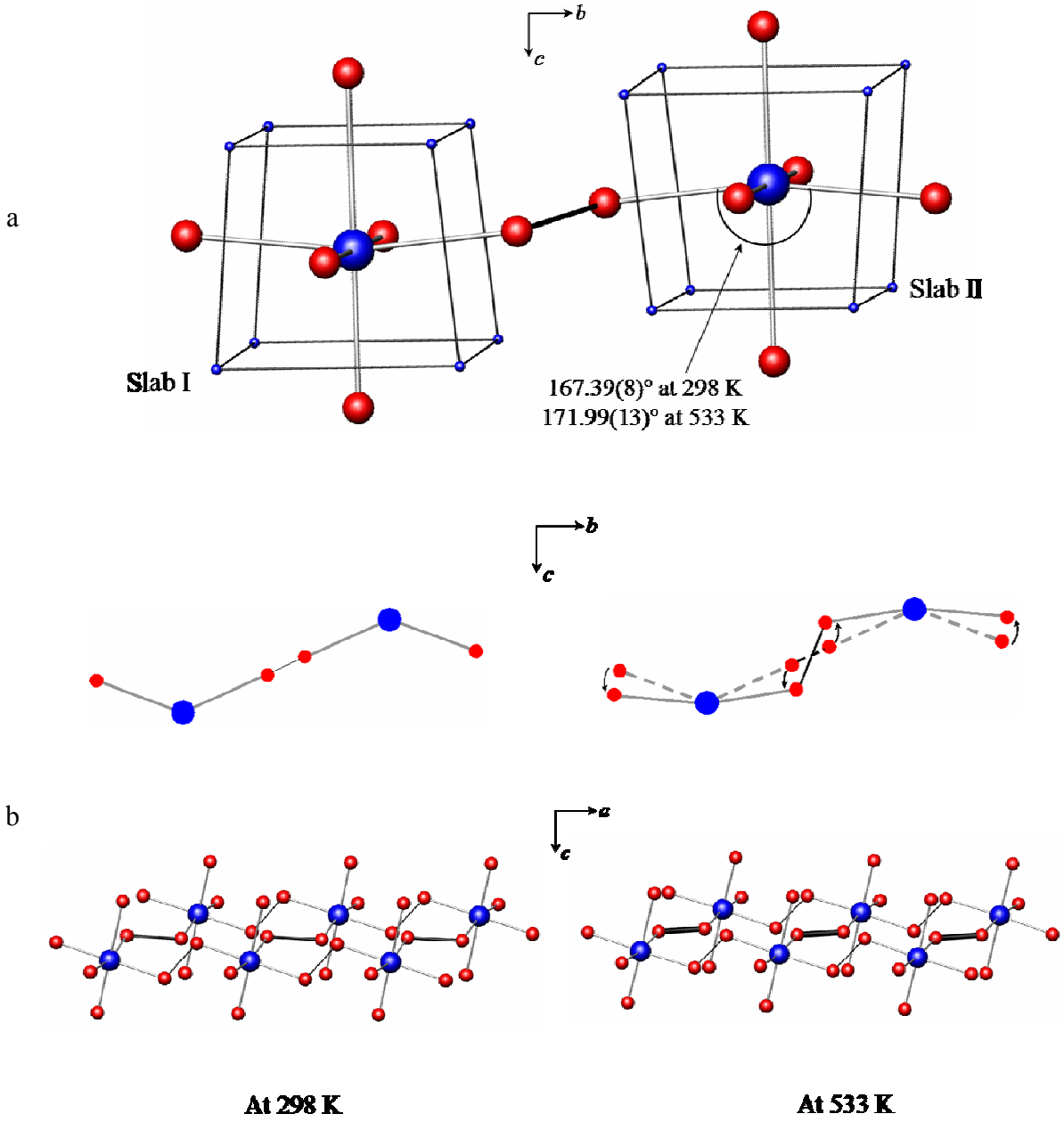

Figure 6.9. a) Change in T1-Gd3-T1 bond angle for $Gd_5Ga_{1.0}Ge_{3.0}$ as the temperature varies from 298 K to 533 K and b) Schematic diagram in two different orientations depicting how the change in bond angle decreases the T1-T1 distance.

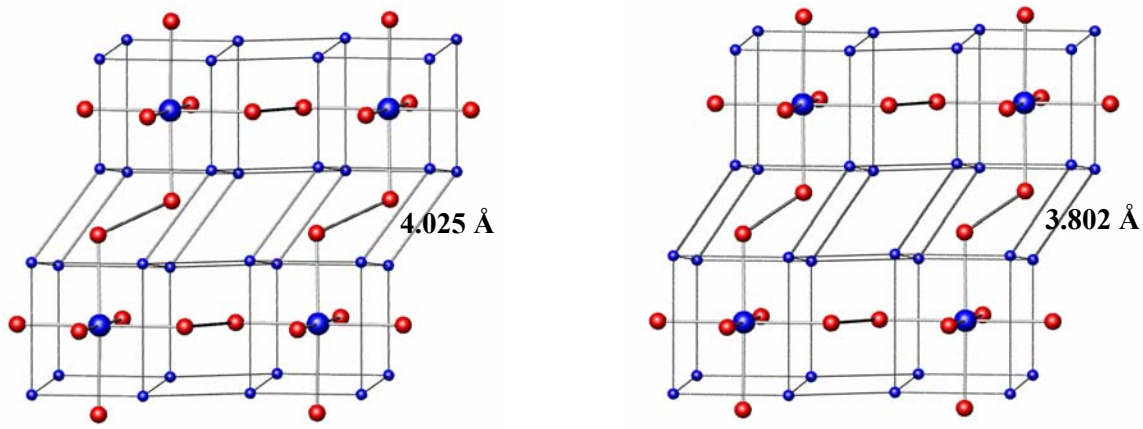

At 298 K **At 533 K**

Figure 6.10. Variation of interslab contacts with temperature for $Gd_5Ga_{1.0}Ge_{3.0}$.

The other significant change arises in the coordination environments surrounding the T1 sites as shown in Figure 6.11. On heating, the T1-T1 distance decreases for reasons mentioned above, and this promotes the increase of three interslab T1-Gd distances. The T1-Gd1 contact capping the trigonal prism increases from 3.519 Å to 3.865 Å. The other two, T1-Gd1 and T1-Gd2 contacts, within the trigonal prism also increase to 3.378(4) Å and 2.954(4) Å, respectively. Thus, we observe that Gd-T bonds in the Pu_5Rh_4-type structure are exchanged for T-T and Gd-Gd bonds in the Gd_5Si_4-type structure. Figure 6.12 illustrates the trends for some interatomic distances as the material is heated from 298 to 623 K. Related plots for other interatomic distances as the temperature increases are compiled in Supporting Information. For all plots the distances change abruptly above 523 K, which is the temperature at which the phase transition begins. Although the most notable changes occur for T1-T1 and T2-T3 distances, there are significant changes associated with Gd-T contacts, especially the Gd3-T contacts.

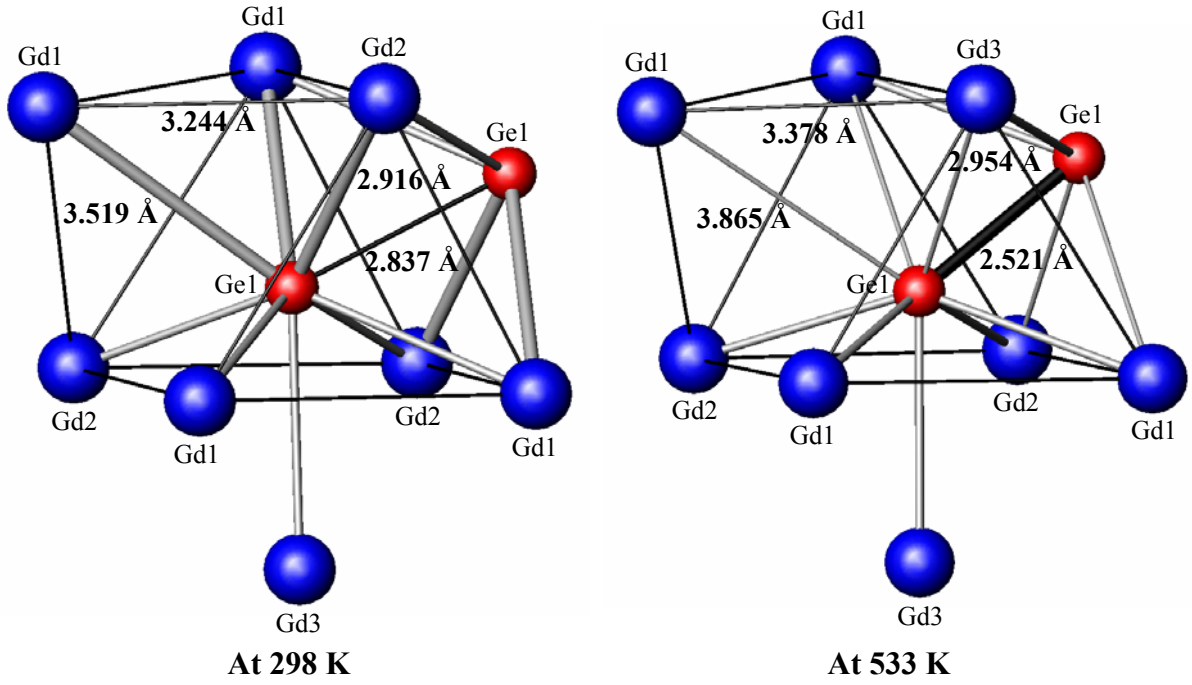

Figure 6.11. Coordination environments surrounding the T1 sites for $Gd_5Ga_{1.0}Ge_{3.0}$ as it changes with temperature. Interatomic distances showing significant differences between the structures are included.

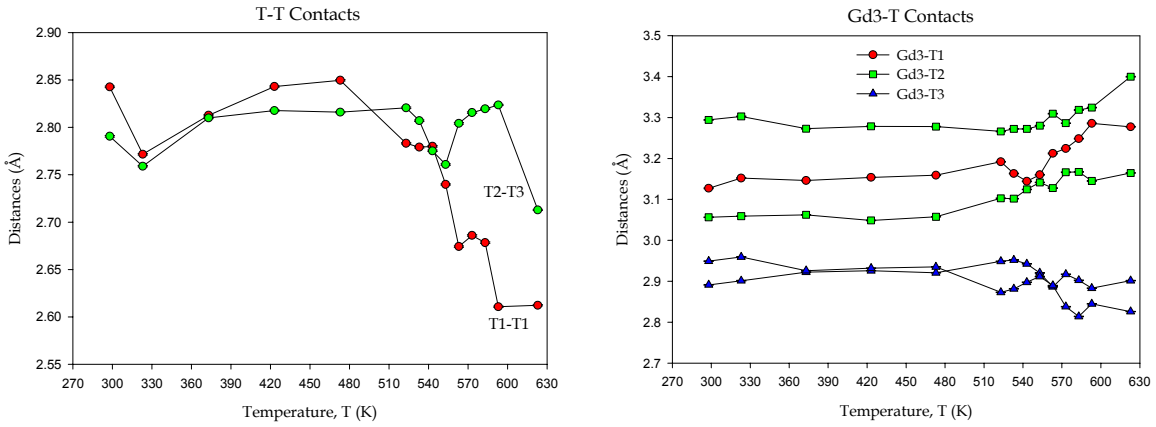

Figure 6.12. T-T contact distance variations with temperature in $Gd_5Ga_{1.0}Ge_{3.0}$ as obtained from powder X-ray diffraction experiment.

The difference between the Pu_5Rh_4- and Gd_5Si_4-type structures is rather small, as they both adopt the same space group as well as similar lattice constants and atomic arrangements. Nonetheless we do observe subtle changes in the atomic coordinates (mostly along *a*; Figure 6.13).

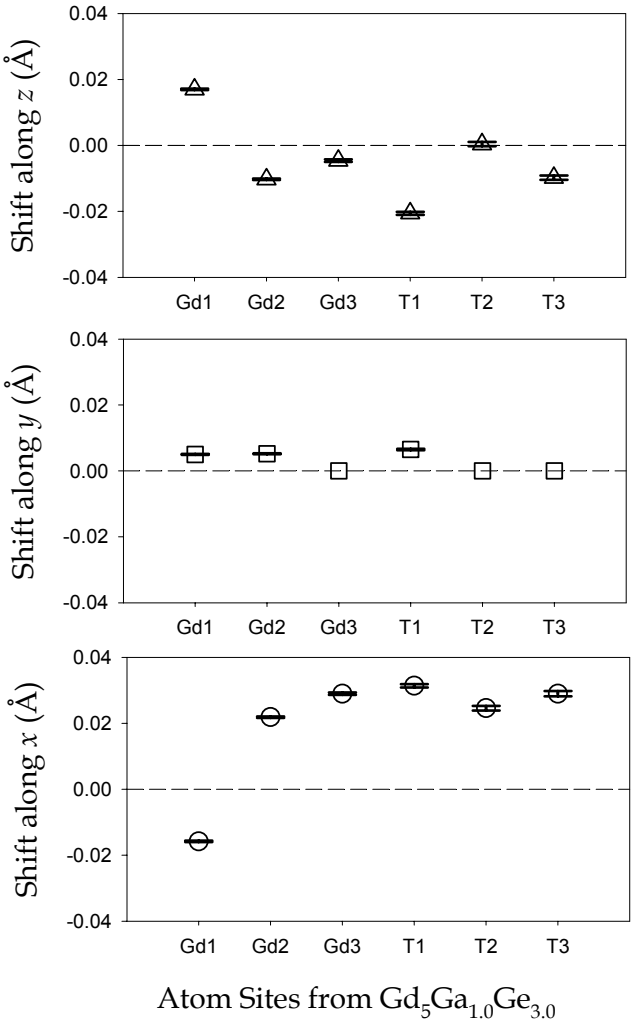

Figure 6.13. Atomic shifts along *a*-, *b*-, *c*-axes in the crystal structure of $Gd_5Ga_{1.0}Ge_{3.0}$ at 533 K relative to the initial positions in the room temperature (298 K) structure.

To check the possible implications of low temperatures, we also performed single crystal X-ray diffraction on $Gd_5Ga_{1.0}Ge_{3.0}$ (see Supporting Information) from 298-120 K. These experiments do not show any structural transitions down to 120 K.

The temperature dependence of the inverse magnetic susceptibility corrected for the diamagnetic and temperature independent paramagnetic susceptibility contribution is shown in Figure 6.14a. The paramagnetic Curie temperature, θ_p = 206.8(2) K, was calculated from the Curie-Weiss behavior of $1/\chi(T)$ dependency observed between ca. 250-300 K, above the magnetic ordering temperature. Figure 6.14b shows the isothermal magnetization plot at a temperature of 5.5 K for varying dc magnetic fields in the range 0-50 kOe.

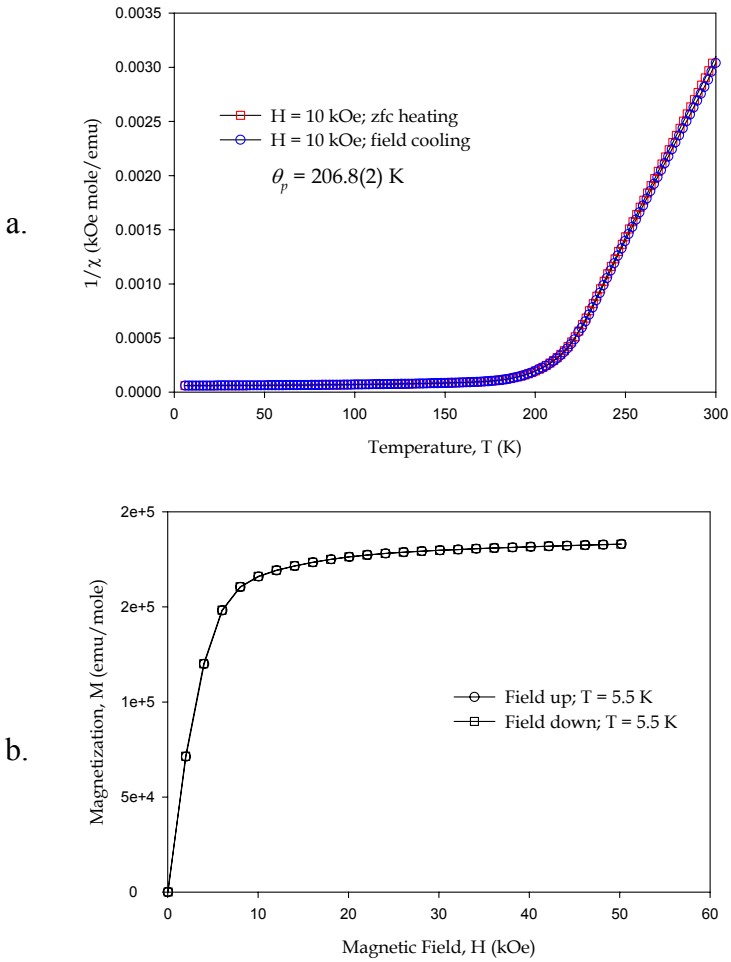

Figure 6.14. a) Dc inverse magnetic susceptibility vs. temperature plot and b) isothermal magnetization plot with varying dc magnetic fields measured on a polycrystalline sample of $Gd_5Ga_{1.0}Ge_{3.0}$.

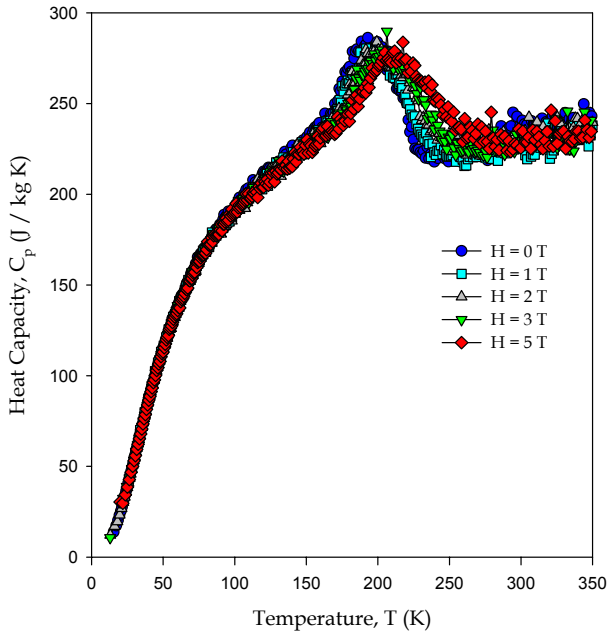

Figure 6.15. The heat capacity of a polycrystalline sample of $Gd_5Ga_{1.0}Ge_{3.0}$ measured in 0, 1, 2, 3, and 5 T magnetic fields after zero-field cooling the sample to ca. 5 K

The temperature variation of the heat capacity (C_p) of a polycrystalline sample of $Gd_5Ga_{1.0}Ge_{3.0}$ is shown in Figure 6.15. The $C_p(T)$ data also show a non λ-type anomaly peaking at ca. 190 K similar to $Gd_5Ga_{0.7}Ge_{3.3}$. The peak signifies a phase transition between the paramagnetic and ferromagnetic states. Its broad feature may be due to the inhomogeneity of as-cast samples which were used for these measurements.

6.5. Conclusions

In situ low-temperature diffraction experiments on $Gd_5Ga_{0.7}Ge_{3.3}$ show a structural phase transition from Sm_5Ge_4-type to $Gd_5Si_2Ge_2$-type and then to Gd_5Si_4-type as temperature decreases. On the other hand, *in situ* high-temperature diffraction experiments on $Gd_5Ga_{1.0}Ge_{3.0}$ show a structural phase transition from Pu_5Rh_4-type to Gd_5Si_4-type as temperature rises. These temperature-induced structural transformations in the $Gd_5Ga_xGe_{4-x}$ system reveal the immense flexibility of this system. These results also present, for the first time, the existence of orthorhombic Sm_5Ge_4-, monoclinic $Gd_5Si_2Ge_2$- and Gd_5Si_4-type, for the same composition.

6.6. Acknowledgements

The authors thank Prof. Vitalij Pecharsky, Dr. Y. Mudryk and Mr. R. Rink for using the SQUID magnetometer, semi-adiabatic heat-pulse calorimeter and Rigaku TTRAX diffractometer. This work was carried out at the Ames Laboratory, which is operated for the U.S. Department of Energy by Iowa State University under Contract No. DE-AC02-07CH11358. This work was supported by the Materials Sciences Division of the Office of Basic Energy Sciences of the U.S. Department of Energy.

6.7. References

(1) Pecharsky, V. K.; Gschneidner, K. A. Jr., *Phys. Rev. B* **1997**, *78*, 4494.

(2) Pecharsky, V. K.; Gschneidner, K. A. Jr., *Appl. Phys. Lett.* **1997**, *70*, 3299.

(3) Pecharsky, V. K.; Gschneidner, K. A. Jr., *J. Magn. Magn. Mater.* **1997**, *167*, L179.

(4) Miller, G. J., *Chem. Soc. Rev.* **2006**, *35*, 799.

(5) Giguere, A.; Foldeaki, M.; Ravi Gopal, R.; Bose, T. K.; Frydman, A., *Phys. Rev. Lett.* **1999**, *83*, 2262.

(6) Gschneidner, K. A. Jr., Pecharsky, V. K.; Duijin, H. G. M.; Levin. E. M., *Phys. Rev. Lett.* **2000**, *85*, 4190.

(7) Pecharsky, A. O.; Gschneidner, K. A. Jr.; Pecharsky, V. K., *J. Appl. Phys.* **2003**, *93*, 4722.

(8) Gschneidner, K. A. Jr.; Pecharsky, V. K.; Tsokol, A. O., *Rep. Prog. Phys.* **2005**, *68*, 1479.

(9) Morellon, L.; Blasco, J.; Algarabel, P. A.; Ibara, M. R., *Phys. Rev. B* **2000**, *62*, 1022.

(10) Morellon, L.; Algarabel, P. A.; Ibara, M. R.; Blasco, J.; Garcia-Landa, B., *Phys. Rev. B* **1998**, *58*, R14721.

(11) Magen, C.; Morellon, L.; Algarabel, P. A.; Marquina, C.; Ibara, M. R., *J. Phys.: Condens. Matter* **2003**, *15*, 2389.

(12) Morellon, L.; Stankiewicz, J.; Garcia-Landa, B.; Algarabel, P. A.; Ibara, M. R., *Appl. Phys. Lett.* **1998**, *73*, 3462.

(13) Levin. E. M.; Pecharsky, V. K.; Gschneidner, K. A. Jr., *Phys. Rev. B* **1999**, *60*,7993.

(14) Levin. E. M.; Pecharsky, V. K.; Gschneidner, K. A. Jr., *J. Magn. Magn. Mater.* **2000**, *210*, 181.

(15) Levin. E. M.; Pecharsky, V. K.; Gschneidner, K. A. Jr., *Phys. Rev. B* **2001**, *63*, 174110.

(16) Stankiewicz, J.; Morellon, L.; Algarabel, P. A.; Ibara, M. R., *Phys. Rev. B* **2000**, *61*, 12651.

(17) Choe, W.; Pecharsky, V. K.; Pecharsky, A. O.; Gschneidner, K. A. Jr.; Young, V. G. Jr.; Miller, G. J., *Phys. Rev. Lett.* **2000**, *84*, 4617.

(18) Meyer, J.; Chumbley, S.; Choe, W.; Miller, G. J., *Phys. Rev. B* **2002**, *66*, 012106/012101.

(19) Choe, W.; Pecharsky, A. O.; Wörle, M.; Miller, G. J., *Inorg. Chem.* **2003**, *42*, 8223.

(20) Misra, S; Miller, G. J., *J. Solid State Chem*. **2006**, *179*, 2290.

(21) Mozharivskyj, Y.; Choe, W.; Pecharsky, A. O.; Miller, G. J., *J. Am. Chem. Soc.* **2003**, *125*, 15183.

(22) Wu, L. M.; Kim, S. H.; Seo, D. K., *J. Am. Chem. Soc.* **2005**, *127*, 15682.

(23) Choe, W.; Miller, G. J.; Meyers, J.; Chumbley, S.; Pecharsky, A. O., *Chem. Mater.* **2003**, *15*, 1413.

(24) Smith, G. S.; Johnson, Q.; Tharp, A. G. *Acta Crystallogr*. **1967**, *22*, 269.

(25) Holtzberg, F.; Gambino, R. J.; McGuire, T. R., *J. Phys. Chem. Solids* **1967**, *28*, 2283.

(26) Pecharsky, A. O.; Gschneidner, K. A. Jr., *J. Alloys Compd.* **1997**, *260*, 98.

(27) Pecharsky, V. K.; Samolyuk, G. D.; Antropov, V. P.; Pecharsky, A. O.; Gschneidner, K. A. Jr., *J. Solid State Chem*. **2003**, *171*, 57.

(28) Le Roy, J.; Moreau, J. M.; Paccard, D.; Parthe, E. *Acta Crystallogr*. **1978**, *B34*, 3315.

(29) Kraus, W.; Nolze, G., *Powder Cell for Windows, Version 2.4*, **2000**.

(30) Hunter, B. A., *IUCR Powder Diffraction* **1997**, *22*.

(31) Mozharivskyj, Y.; Pecharsky, A. O.; Pecharsky, V. K.; Miller, G. J., *J. Am. Chem. Soc.* **2005**, *123*, 317.

(32) *XRD Single Crystal Software*; Bruker Analytical X-ray Systems: Madison, USA, **2002**.

(33) Pecharsky, V. K.; Moorman, J. O.; Gschneidner, K. A. Jr., *Rev. Sci. Instrum.* **1997**, *68*, 4196.

(34) Richter, K. W.; Franzen, H. F., *J. Solid State Chem.*, **2000**, *150*, 347.

(35) Misra, S.; Miller, G. J. *J. Am. Chem. Soc.* **2008**, submitted.

(36) Franzen, H. F. *Physical Chemistry of Inorganic Crystalline Solids*; Springer-Verlag: New York, 1986.

(37) Pecharsky, V. K.; Gschneidner, K. A. Jr., *J. Appl. Phys.* **1999**, *86*, 565.

6.8. Supporting Information

Table 6.S1. Lattice parameters for $Gd_5Ga_{0.7}Ge_{3.3}$ as obtained by single crystal X-ray diffraction. The data are from the matrix composed of 3 runs of 30 frames each.

Temperature (K)	***a*, Å**	***b*, Å**	***c*, Å**	***V*, Å^3**	***b*/*a***	***c*/*a***
298	7.647(1)	14.862(5)	7.822(2)	889.0(5)	1.9435(4)	1.0229(3)
373	7.651(2)	14.882(5)	7.833(3)	891.9(6)	1.9451(4)	1.0238(5)
473	7.650(2)	14.897(8)	7.845(3)	894.0(7)	1.9473(6)	1.0255(5)
523	7.643(9)	14.91(4)	7.87(2)	897(7)	1.951(3)	1.030(3)
533	Crystal Decomposed					

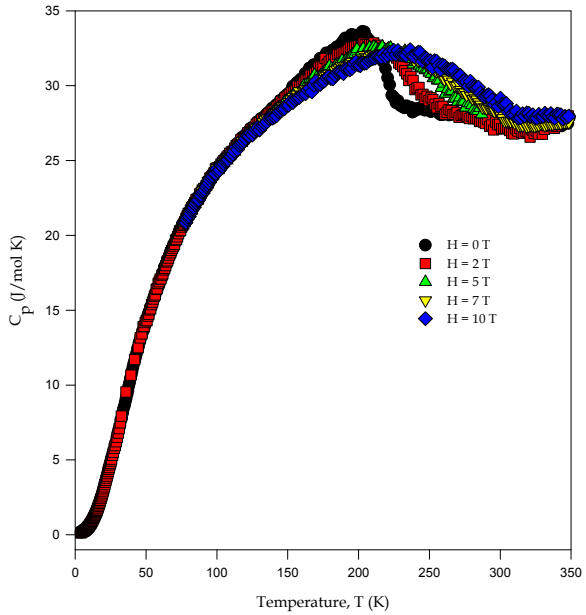

Figure 6.S1. The heat capacity of a single crystalline sample of $Gd_5Ga_{0.7}Ge_{3.3}$ oriented along its (010) axis as a function of temperature in 0, 2, 5, 7, and 10 T magnetic fields.

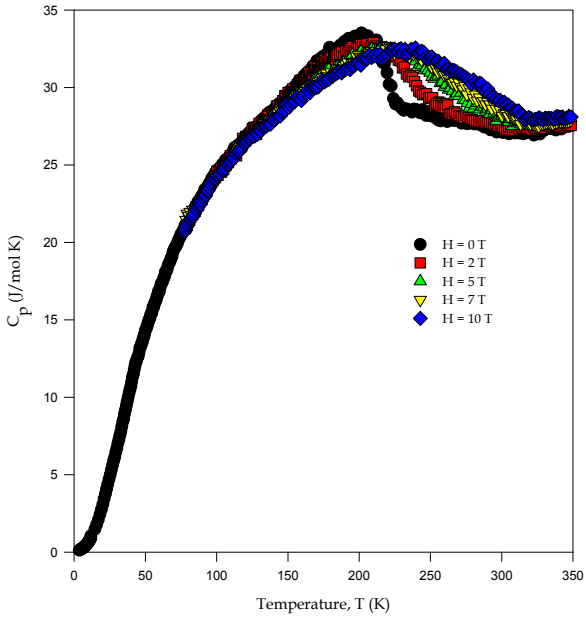

Figure 6.S2. The heat capacity of a single crystalline sample of $Gd_5Ga_{0.7}Ge_{3.3}$ oriented along its (100) axis as a function of temperature in 0, 2, 5, 7, and 10 T magnetic fields.

Table 6.S2. Lattice parameters for $Gd_5Ga_{1.0}Ge_{3.0}$ as obtained by powder X-ray diffraction (space group *Pnma* (No. 62), Mo K_α radiation, 2θ range = 9-42°, Z = 4) and from single crystal X-ray diffraction.

Temperature (K)	Sample	*a*, Å	*b*, Å	*c*, Å	*V*, Å^3	*b*/*a*	*c*/*a*
298	powder	7.563(2)	14.944(5)	7.908(2)	893.8(5)	1.9759(4)	1.0456(4)
	crystal*	7.548(3)	14.916(4)	7.894(2)	888.8(6)	1.9761(5)	1.0458(5)
323	powder	7.564(2)	14.949(5)	7.910(2)	894.3(5)	1.9763(4)	1.0457(4)
373	powder	7.567(2)	14.961(4)	7.912(2)	895.6(4)	1.9771(4)	1.0456(4)
	crystal*	7.554(2)	14.930(4)	7.898(2)	890.8(5)	1.9764(4)	1.0455(4)
423	powder	7.571(2)	14.980(4)	7.915(2)	897.7(4)	1.9786(4)	1.0454(4)
473	powder	7.573(2)	14.989(5)	7.915(2)	898.5(4)	1.9793(4)	1.0452(4)
	crystal*	7.565(2)	14.952(4)	7.908(2)	894.5(5)	1.9765(4)	1.0453(4)
523	powder	7.575(2)	14.993(5)	7.916(2)	899.0(5)	1.9793(4)	1.0450(4)
	crystal*	7.576(3)	14.963(5)	7.904(2)	896.0(6)	1.9750(5)	1.0433(5)
533	powder	7.580(2)	15.001(5)	7.917(2)	900.2(5)	1.9790(4)	1.0445(4)
	crystal*	7.623(7)	15.04(2)	7.895(6)	905.0(2)	1.9729(16)	1.0357(12)
543	powder	7.582(2)	15.007(5)	7.915(2)	900.6(4)	1.9793(4)	1.0439(4)
553	powder	7.587(2)	15.012(5)	7.913(2)	901.3(5)	1.9786(4)	1.0430(4)
563	powder	7.588(2)	15.011(5)	7.911(2)	901.1(5)	1.9782(4)	1.0426(4)
573	powder	7.590(2)	15.012(5)	7.912(2)	901.4(5)	1.9779(4)	1.0424(4)
583	powder	7.589(2)	15.015(5)	7.909(2)	901.1(5)	1.9785((4)	1.0422(4)
593	powder	7.591(2)	15.016(5)	7.909(2)	901.6(5)	1.9781(4)	1.0419(4)
623	powder	7.587(2)	15.000(4)	7.907(2)	899.9(4)	1.9771(4)	1.0422(4)

* The lattice parameters are from the matrix composed of 3 runs of 30 frames each.

Table 6.S3. Lattice parameters for $Gd_5Ga_{1.0}Ge_{3.0}$ as obtained by single crystal X-ray diffraction. The parameters are from the matrix composed of 3 runs of 30 frames each.

Temperature (K)	*a*, Å	*b*, Å	*c*, Å	*V*, Å^3	*b*/*a*	*c*/*a*
298	7.547(2)	14.924(4)	7.892(3)	888.9(5)	1.9775(4)	1.0457(5)
250	7.541(2)	14.912(3)	7.891(3)	887.4(5)	1.9775(3)	1.0464(5)
200	7.535(1)	14.895(3)	7.884(2)	884.8(4)	1.9768(2)	1.0463(3)
165	7.532(1)	14.889(3)	7.877(3)	888.3(4)	1.9768(2)	1.0458(4)
155	7.533(1)	14.890(3)	7.875(2)	883.3(4)	1.9766(2)	1.0454(3)
150	7.532(1)	14.887(3)	7.875(2)	883.0(4)	1.9765(2)	1.0455(3)
143	7.532(1)	14.885(3)	7.872(2)	882.5(4)	1.9762(2)	1.0451(3)
120	7.531(1)	14.880(3)	7.871(2)	882.1(4)	1.9758(2)	1.0451(3)

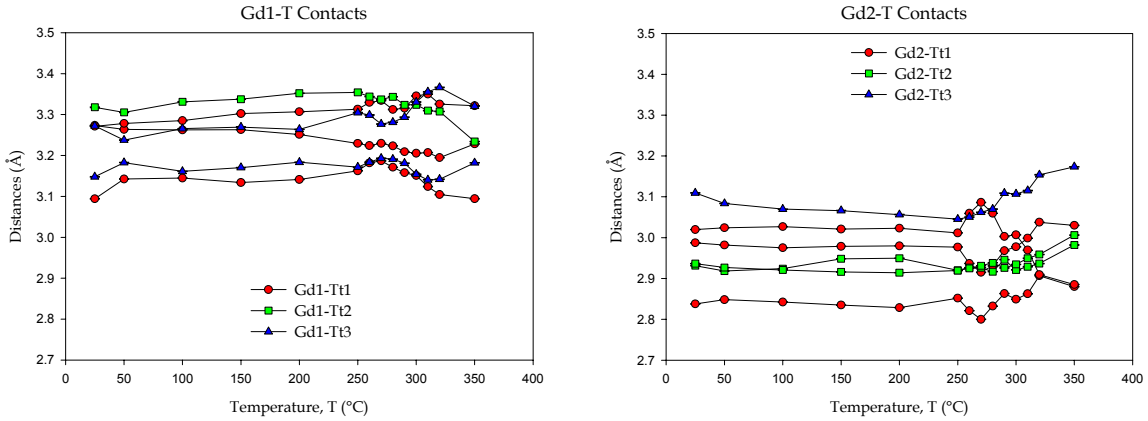

Figure 6.S3. Interatomic distance variations with temperature in $Gd_5Ga_{1.0}Ge_{3.0}$ as obtained from powder X-ray diffraction experiment.

Chapter 7

Conclusions

The work presented in this dissertation involving RE_5T_4 materials has resulted in the successful synthesis, characterization, property measurements and theoretical analyses of various new intermetallic compounds. The results provide significant insight into the fundamental magnetic and structural behavior of these materials and help us better understand the complex link between a compound's composition, its observed structure and its properties. Our work specifically presents the following results:

(1) Substitution of Gd with Y in $Gd_{5-x}Y_xTt_4$ (Tt = Si, Ge): A detailed structural and theoretical investigation provided the understanding that the interplay among the site preferences for Gd and Y, the local symmetry features of an individual slab that make up these structures, and the local electronic structures of Gd and Y atoms drives the structural transition from a well-known orthorhombic, Sm_5Ge_4-type to an unprecedented monoclinic, $U_2Mo_3Si_4$-type crystal structure. The magnetic properties of some of the $Gd_{5-x}Y_xTt_4$ phases were also measured. Germanides with $x \leq 2$ show a metamagnetic-type transition similar to Gd_5Ge_4. On the other hand, as the Y concentration increases ($3 \leq x \leq 4$), these phases exhibit ferromagnetic ordering showing a Curie-Weiss behavior at high temperatures.

(2) Synthesis of a mixed rare-earth system, $Nd_{5-x}Er_xTt_4$ (Tt = Si, Ge): A systematic investigation of a mixed rare-earth system comprised of a lighter and larger rare-earth, Nd; and a heavier and smaller rare-earth, Er, reveal a partially ordered arrangement of Nd and Er atoms in case of all the structures existing for both tetrelide systems. In the Si-system, there is a structural variation from the tetragonal, Zr_5Si_4-type to the orthorhombic Gd_5Si_4-type. On the other hand, for the Ge-system, a transition from orthorhombic, Sm_5Ge_4-type to monoclinic, $U_2Mo_3Si_4$-type is revealed, much like in the case of $Gd_{5-x}Y_xGe_4$. The magnetic properties of some of the

$Nd_{5-x}Er_xTt_4$ phases were also measured. Nd_4ErGe_4 shows an AFM-type transition similar to Gd_5Ge_4 but as the Er concentration increases ($2 \leq x \leq 4$), these phases exhibit ferromagnetic-type ordering showing a Curie-Weiss behavior at high temperatures.

(3) Distribution of Si-Ge in $Gd_5(Si_xGe_{1-x})_4$ materials: The structural transition in this series was due to a correlation between the nature of the *Tt*···*Tt* interslab contacts and the distribution of Si and Ge at the *Tt*-sites between the slabs: Si has a preference for the intraslab sites and Ge prefers the interslab positions. The distribution of the tetrelide (Si and Ge) atoms at each site impacts the fractions of possible homonuclear and heteronuclear Si-Si, Si-Ge and Ge-Ge dimers in the various structures and this correlates well with observed room temperature crystal structures for the entire series of $Gd_5(Si_xGe_{1-x})_4$.

(4) Phase Transformations in $Gd_5Ga_xGe_{4-x}$ materials: The role of temperature in the phase transformations for two compositions: $Gd_5Ga_{0.7}Ge_{3.3}$ and $Gd_5Ga_{1.0}Ge_{3.0}$ were investigated by *in situ* single crystal and powder X-ray diffraction. The former shows a transformation from Sm_5Ge_4-type → $Gd_5Si_2Ge_2$-type → Gd_5Si_4-type as the temperature decreases, whereas the latter shows a variation from the Pu_5Rh_4-type to Gd_5Si_4-type as the temperature rises.

All these results go to show the immense flexibility that these RE_5T_4 materials possess and reveal the uniqueness of these systems, as it stabilizes a variety of structure types.

For future work, it would be interesting to experimentally study the energetics and thermodynamic stability of some of the structure types observed for RE_5T_4 materials. This essentially will allow us to target new rare-earth based materials, probably with promising properties.

Appendix A

Controlling Magnetism of a Complex Metallic System via Predicted Atomic Replacements[†]

An article to be submitted in *Advanced Materials*

Yaroslav Mudryk, Durga Paudyal, Vitalij K. Pecharsky, Karl A. Gschneidner, Jr., Sumohan Misra,[‡] Gordon J. Miller

A.1. Introduction

The effect of chemical substitution of Gd by nonmagnetic La, Lu, and Y in Gd_5Ge_4 were studied. Each system had small quantities (ca. 5%) of nonmagnetic rare-earths as substituent: $(Gd_{0.95}La_{0.05})_5Ge_4$, $(Gd_{0.95}Lu_{0.05})_5Ge_4$, $(Gd_{0.95}Y_{0.05})_5Ge_4$. The samples studied were both as-cast and heat treated (at 1000°C for two days). Studies included single crystal X-ray diffraction at room-temperature, low-temperature powder X-ray diffraction under applied magnetic fields and using the SQUID magnetometer to determine the magnetic properties on bulk polycrystalline samples.

A.2. Discussion

Details of the single crystal data collection parameters and crystallographic refinement results for both as-cast and heat treated samples of $(Gd_{0.95}La_{0.05})_5Ge_4$, $(Gd_{0.95}Lu_{0.05})_5Ge_4$, and $(Gd_{0.95}Y_{0.05})_5Ge_4$ are included in Tables A.1, A.3, and A.5. The resulting atomic coordinates, site occupancies and isotropic displacement parameters are listed in Tables A.2, A.4, and A.6. The structures were refined using the *SHELXTL*[1] package of crystallographic programs.

[†] Only single crystal X-ray refinement data are included here as the manuscript is still under preparation.

[‡] My contribution to this work involved room-temperature single crystal X-ray diffraction experiments on samples of $(Gd_{0.95}La_{0.05})_5Ge_4$, $(Gd_{0.95}Lu_{0.05})_5Ge_4$, and $(Gd_{0.95}Y_{0.05})_5Ge_4$.

Table A.1. Crystallographic data for $Gd_{4.75}La_{0.25}Ge_4$ as obtained by single crystal X-ray diffraction (space group *Pnma* (No. 62), Mo *Kα* radiation, 2θ range = 4-57°, $Z = 4$)

Sample	As-cast	Heat treated
Refined Composition	$Gd_{4.75(8)}La_{0.25}Ge_4$	$Gd_{4.83(6)}La_{0.17}Ge_4$
***a* (Å)**	7.706(3)	7.696(3)
***b* (Å)**	14.824(6)	14.829(5)
***c* (Å)**	7.828(3)	7.787(2)
***V* (Å^3)**	894.2(6)	888.8(5)
No. of Independent Reflections	1105	1106
No. of Parameters	49	48
Final R indices	R1 = 0.0282,	R1 = 0.0433,
[I>2sigma(I)]	wR2 = 0.0560	wR2 = 0.0814
Peak/hole (e/Å^3)	2.412 / -1.676	3.251 / -2.374
b*/*a	1.9237(11)	1.9268(10)
c*/*a	1.0158(10)	1.0118(5)
***T*1-*T*1 (Å)**	3.605(2)	3.599(3)

Table A.2. Atomic coordinates and isotropic displacement parameters for $Gd_{4.75}La_{0.25}Ge_4$ as obtained by single crystal X-ray diffraction.

Atom		***x***	***y***	***z***	**occupancy**[a]	$\mathbf{U_{eq}}$, (**Å**^{2})[b]
			As-cast- $Gd_{4.75(8)}La_{0.25}Ge_4$			
M1	8d	0.9784(1)	0.4003(1)	0.1786(1)	0.883(19)	0.010(1)
M2	8d	0.6258(1)	0.3829(1)	0.8385(1)	0.99(2)	0.008(1)
Gd3	4c	0.2079(1)	¾	0.4993(1)	1	0.009(1)
Ge1	8d	0.7847(1)	0.4562(1)	0.5346(1)	1	0.010(1)
Ge2	4c	0.0796(2)	¾	0.1136(2)	1	0.009(1)
Ge3	4c	0.3234(2)	¾	0.8662(2)	1	0.010(1)
			Heat Treated- $Gd_{4.83(6)}La_{0.17}Ge_4$			
M1	8d	0.9786(1)	0.4004(1)	0.1788(1)	0.92(3)	0.010(1)
Gd2	8d	0.6260(1)	0.3828(1)	0.8384(1)	1	0.009(1)
Gd3	4c	0.2075(1)	¾	0.4994(1)	1	0.009(1)
Ge1	8d	0.7848(2)	0.4563(1)	0.5350(2)	1	0.010(1)
Ge2	4c	0.0792(3)	¾	0.1133(3)	1	0.010(1)
Ge3	4c	0.3234(3)	¾	0.8662(3)	1	0.010(1)

[a]All M1 and M2 sites are fully occupied with a mixture of Gd and La atoms. Only Gd occupations are listed.

[b]U(eq) is defined as one third of the trace of the orthogonalized U_{ij} tensor.

Table A.3. Crystallographic data for $Gd_{4.75}Lu_{0.25}Ge_4$ as obtained by single crystal X-ray diffraction (space group *Pnma* (No. 62), Mo *Kα* radiation, 2θ range = 4-57°, $Z = 4$)

Sample	As-cast	Heat treated
Refined Composition	$Gd_{4.75}Lu_{0.25(6)}Ge_4$	$Gd_{4.77}Lu_{0.23(7)}Ge_4$
***a* (Å)**	7.675(1)	7.677(3)
***b* (Å)**	14.797(3)	14.799(6)
***c* (Å)**	7.769(2)	7.763(3)
***V* (Å^3)**	882.4(3)	881.9(6)
No. of Independent Reflections	1107	1085
No. of Parameters	49	49
Final R indices	R1 = 0.0325,	R1 = 0.0327,
[I>2sigma(I)]	wR2 = 0.0701	wR2 = 0.0695
Peak/hole (e/Å^3)	2.576 / -2.345	2.838 / -2.073
b*/*a	1.9279(5)	1.9277(11)
c*/*a	1.0122(5)	1.0112(5)
***T*1-*T*1 (Å)**	3.611(2)	3.611(2)

Table A.4. Atomic coordinates and isotropic displacement parameters for $Gd_{4.75}Lu_{0.25}Ge_4$ as obtained by single crystal X-ray diffraction.

Atom		***x***	***y***	***z***	**occupancy**[a]	$\mathbf{U_{eq}}$, **(Å^2)**[b]
			As-cast- $Gd_{4.75}Lu_{0.25(6)}Ge_4$			
Gd1	8d	0.9769(1)	0.4002(1)	0.1783(1)	1	0.010(1)
M2	8d	0.6246(1)	0.3829(1)	0.8387(1)	0.051(18)	0.008(1)
M3	4c	0.2089(1)	¾	0.4990(1)	0.15(2)	0.009(1)
Ge1	8d	0.7833(1)	0.4559(1)	0.5335(1)	1	0.009(1)
Ge2	4c	0.0805(2)	¾	0.1133(2)	1	0.010(1)
Ge3	4c	0.3256(2)	¾	0.8651(2)	1	0.009(1)
			Heat Treated- $Gd_{4.77}Lu_{0.23(7)}Ge_4$			
Gd1	8d	0.9767(1)	0.4002(1)	0.1783(1)	1	0.009(1)
M2	8d	0.6244(1)	0.3829(1)	0.8387(1)	0.05(2)	0.008(1)
M3	4c	0.2092(1)	¾	0.4991(1)	0.13(3)	0.008(1)
Ge1	8d	0.7832(2)	0.4560(1)	0.5335(2)	1	0.009(1)
Ge2	4c	0.0805(2)	¾	0.1131(2)	1	0.009(1)
Ge3	4c	0.3259(2)	¾	0.8648(2)	1	0.009(1)

[a]All M2 and M3 sites are fully occupied with a mixture of Gd and Lu atoms. Only Lu occupations are listed.

[b]U(eq) is defined as one third of the trace of the orthogonalized U_{ij} tensor.

Table A.5. Crystallographic data for $Gd_{4.75}Y_{0.25}Ge_4$ as obtained by single crystal X-ray diffraction (space group *Pnma* (No. 62), Mo *Kα* radiation, 2θ range = 4-57°, $Z = 4$)

Sample	As-cast	Heat treated
Refined Composition	$Gd_{4.81(4)}Y_{0.19}Ge_4$	$Gd_{4.87(2)}Y_{0.13}Ge_4$
***a* (Å)**	7.702(2)	7.705(2)
***b* (Å)**	14.837(3)	14.859(4)
***c* (Å)**	7.788(2)	7.792(2)
***V* (Å^3)**	890.0(3)	892.0(6)
No. of Independent Reflections	1099	1119
No. of Parameters	50	49
Final R indices	R1 = 0.0335,	R1 = 0.0332,
[I>2sigma(I)]	wR2 = 0.0594	wR2 = 0.0624
Peak/hole (e/Å^3)	2.789 / -2.271	2.0938 / -1.691
b*/*a	1.9264(6)	1.9285(7)
c*/*a	1.0112(4)	1.0113(4)
***T*1-*T*1 (Å)**	3.632(2)	3.637(2)

Table A.6. Atomic coordinates and isotropic displacement parameters for $Gd_{4.75}Y_{0.25}Ge_4$ as obtained by single crystal X-ray diffraction.

Atom		***x***	***y***	***z***	**occupancy**[a]	$\mathbf{U_{eq}}$, **(Å^2)**[b]
			As-cast- $Gd_{4.81(4)}Y_{0.19}Ge_4$			
M1	8d	0.9760(1)	0.3999(1)	0.1779(1)	0.988(8)	0.011(1)
M2	8d	0.6235(1)	0.3832(1)	0.8386(1)	0.961(8)	0.010(1)
M3	4c	0.2095(1)	¾	0.4993(1)	0.917(8)	0.010(1)
Ge1	8d	0.7825(1)	0.4560(1)	0.5330(1)	1	0.011(1)
Ge2	4c	0.0822(2)	¾	0.1130(2)	1	0.011(1)
Ge3	4c	0.3259(2)	¾	0.8652(2)	1	0.010(1)
			Heat Treated- $Gd_{4.87(2)}Y_{0.13}Ge_4$			
Gd1	8d	0.9757(1)	0.3999(1)	0.1779(1)	1	0.012(1)
M2	8d	0.6233(1)	0.3832(1)	0.8386(1)	0.967(6)	0.010(1)
M3	4c	0.2096(1)	¾	0.4991(1)	0.934(7)	0.010(1)
Ge1	8d	0.7823(2)	0.4560(1)	0.5331(1)	1	0.011(1)
Ge2	4c	0.0820(2)	¾	0.1127(2)	1	0.010(1)
Ge3	4c	0.3263(2)	¾	0.8653(2)	1	0.011(1)

[a] All M1, M2 and M3 sites are fully occupied with a mixture of Gd and Y atoms. Only Gd occupations are listed.

[b] U(eq) is defined as one third of the trace of the orthogonalized U_{ij} tensor.

A.3. References

(1) *XRD Single Crystal Software*; Bruker Analytical X-ray Systems: Madison, USA, **2002**.

Appendix B

Crystal Structure of $Gd_2Sc_3Ge_4$

A report to be submitted in *Acta Crystallographica Section E: Structure Reports Online*

Sumohan Misra, Gordon J. Miller

B.1. Introduction

Continuing on our efforts to study the mixed rare-earth system bearing the formula RE_5T_4, we studied the effect of chemical substitution of Gd by nonmagnetic Sc. Studies included single crystal X-ray diffraction at room-temperature and refinements of the occupancies for two particular sites for Gd/Sc reveal a partially ordered arrangement of Gd and Sc atoms.

B.2. Discussion

$Gd_2Sc_3Ge_4$ crystallizes in the Pu_5Rh_4-type structure (see Figure B.1). This structure is characterized by the presence of *T*1-*T*1 bond distances of ca. 2.891(1) Å, which are intermediate between the Gd_5Si_4-type and Sm_5Ge_4-type structures. The details of the single crystal data collection parameters and crystallographic refinement results for $Gd_2Sc_3Ge_4$ are presented in Table B.1. The resulting atomic coordinates, site occupancies and isotropic displacement parameters are listed in Table B.2. The structure was refined using the *SHELXTL*[1] package of crystallographic programs.

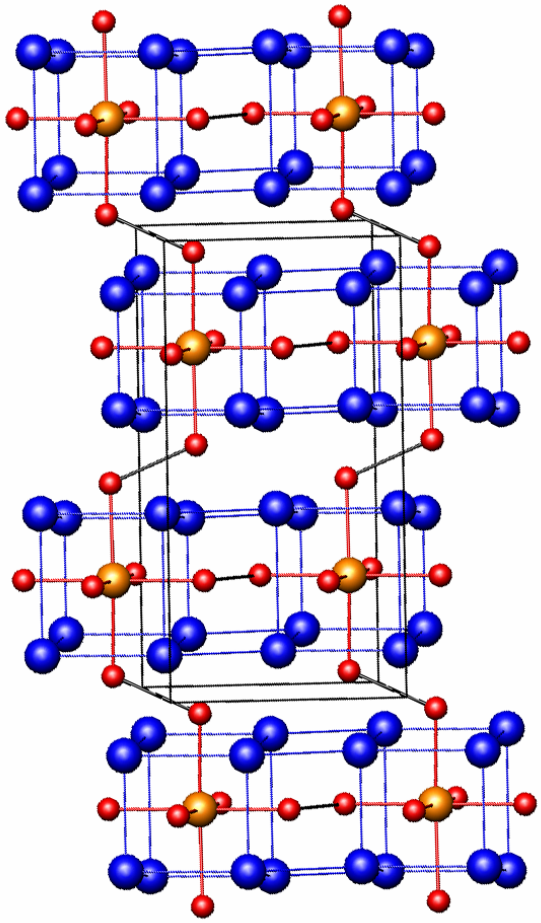

Figure B.1. Projection of the crystal structure of $Gd_2Sc_3Ge_4$ along (001) direction. Blue spheres are Gd, orange spheres are Sc and smaller red spheres are Ge.

Table B.1. Crystallographic data for $Gd_2Sc_3Ge_4$ as obtained by single crystal X-ray diffraction (Mo $K\alpha$ radiation, 2θ range = 4-57°, T = 298(2) K, Z = 4).

Refined Composition	$Gd_{2.00(1)}Sc_{3.00}Ge_4$
Structure-type	Pu_5Rh_4
Crystal system	orthorhombic
Space group	*Pnma*
***a* (Å)**	7.2445(13)
***b* (Å)**	14.101(3)
***c* (Å)**	7.4930(14)
***V* (Å^3)**	765.4(2)
Absorption coefficient	34.909 mm^{-1}
F(000)	1276
Crystal size	0.09 × 0.06 × 0.005 mm^3
Index ranges	$-9 \le h \le 9$, $-17 \le k \le 18$, $-9 \le l \le 9$
Reflections collected	6182
Independent Reflections	958 [R(int) = 0.0701]
Completeness to theta = 25.00°	100.0 %
Refinement method	Full-matrix least-squares on F^2
Data / parameters	958 / 49
Goodness-of-fit on F^2	1.048
Final R indices [I>2sigma(I)]	R1 = 0.0313, wR2 = 0.0618
R indices (all data)	R1 = 0.0410, wR2 = 0.0656
Peak/hole (e/Å^3)	2.204 / −1.442
b*/*a	1.9464(5)
c*/*a	1.0343(3)
***T*1-*T*1 (Å)**	2.891(1)

Table B.2. Atomic coordinates and isotropic displacement parameters for $Gd_2Sc_3Ge_4$ as obtained by single crystal X-ray diffraction.

Atom		***x***	***y***	***z***	**occupancy**[a]	$\mathbf{U_{eq}}$**, (Å^2)**[b]
M1	8d	0.9979(1)	0.4040(1)	0.1764(1)	0.967(4)	0.007(1)
M2	8d	0.6602(2)	0.3759(1)	0.8323(2)	0.031(3)	0.008(1)
Sc3	4c	0.1761(3)	¾	0.5005(3)	1	0.007(1)
Ge1	8d	0.8222(1)	0.4589(1)	0.5407(1)	1	0.009(1)
Ge2	4c	0.0400(2)	¾	0.1256(2)	1	0.008(1)
Ge3	4c	0.3068(2)	¾	0.8632(2)	1	0.008(1)

[a]All M1 and M2 sites are fully occupied with a mixture of Gd and La atoms. Only Gd occupations are listed.

[b]U(eq) is defined as one third of the trace of the orthogonalized U_{ij} tensor.

B.3. References

(1) *XRD Single Crystal Software*; Bruker Analytical X-ray Systems: Madison, USA, **2002**.

Appendix C

Ferromagnetism in the Mott Insulator Ba_2NaOsO_6

A paper published in the *Physical Review Letters*

Phys. Rev. Lett. **2007***, 99,* 016404.

A. S. Erickson, S. Misra,[†] G. J. Miller, R. R. Gupta, Z. Schlesinger, W. A. Harrison, J. M. Kim, and I. R. Fisher

C.1. Abstract

Results are presented of single crystal structural, thermodynamic, and reflectivity measurements of the double-perovskite Ba_2NaOsO_6. These characterize the material as a $5d^1$ ferromagnetic Mott insulator with an ordered moment of ~ 0.2 μ_B per formula unit and T_C = 6.8(3) K. The magnetic entropy associated with this phase transition is close to R ln2, indicating that the quartet ground state anticipated from consideration of the crystal structure is split, consistent with a scenario in which the ferromagnetism is associated with orbital ordering.

C.2. Introduction

The interplay between spin, orbital, and charge degrees of freedom in 3*d* transition metal oxides has proven to be a rich area of research in recent years. Despite the wide array of interesting physics found in these materials, much less is known about whether similar behavior can be found in related 4*d* and 5*d* systems, for which both the extent of the *d* orbitals and larger spin-orbit coupling cause a different balance between the relevant energy scales. In this respect, oxides of osmium are of particular interest because the element can

[†] My contribution to this paper involved variable temperature powder and single crystal X-ray diffraction experiments on samples of Ba_2NaOsO_6.

take formal valences from 4+ to 7+, corresponding to electron configurations $5d^4$ to $5d^1$. In this instance, we examine the simplest case of a $5d^1$ osmate for which the magnetic properties indicate that orbital ordering may indeed play a significant role.

Simple oxides of osmium are typically Pauli paramagnets due to the large extent of the 5*d* orbitals. Examples include the binary oxide OsO_2[1,2] and the simple perovskites $AOsO_3$ (A = Sr, Ba).[3] However, more complex oxides, including the double and triple perovskites La_2NaOsO_6,[4] Ba_2AOsO_6 (A = Li, Na),[5,6] and $Ba_3AOs_2O_9$ (A = Li, Na),[7] appear to exhibit local moment behavior. Presumably the large separation of Os ions in these more complex structures leads to a Mott insulating state, and indeed these and related materials are most often found to be antiferromagnetic. Of the above materials and their near relations containing no other magnetic ions, Ba_2NaOsO_6 distinguishes itself as the only osmate with a substantial *ferromagnetic* moment (~ 0.2 μ_B) in the ordered state.[5]

Weak ferromagnetism has been previously observed in other 5*d* transition metal oxides containing iridium. $BaIrO_3$ exhibits a saturated moment of 0.03 μ_B, which has been attributed to small exchange splitting associated with charge density wave formation.[8] Sr_2IrO_4 and $Sr_3Ir_2O_7$ exhibit similarly small saturated moments, attributed variously to either spin canting in an antiferromagnets due to the low crystal symmetry[9] or to a borderline metallic Stoner scenario.[10,11] The ferromagnetic moment in Ba_2NaOsO_6 is substantially larger than in these materials. Furthermore, at room temperature the material has an undistorted double-perovskite structure, space group $Fm\bar{3}m$ (inset to Figure C.1),[5] in which OsO_6 octahedra are neither distorted nor rotated with respect to each other or the underlying lattice.[12] Such a high crystal symmetry, if preserved to low temperatures, precludes the more usual mechanisms for obtaining a small ferromagnetic moment in an insulating antiferromagnet,[13] suggesting that a different mechanism is causing the ferromagnetism.

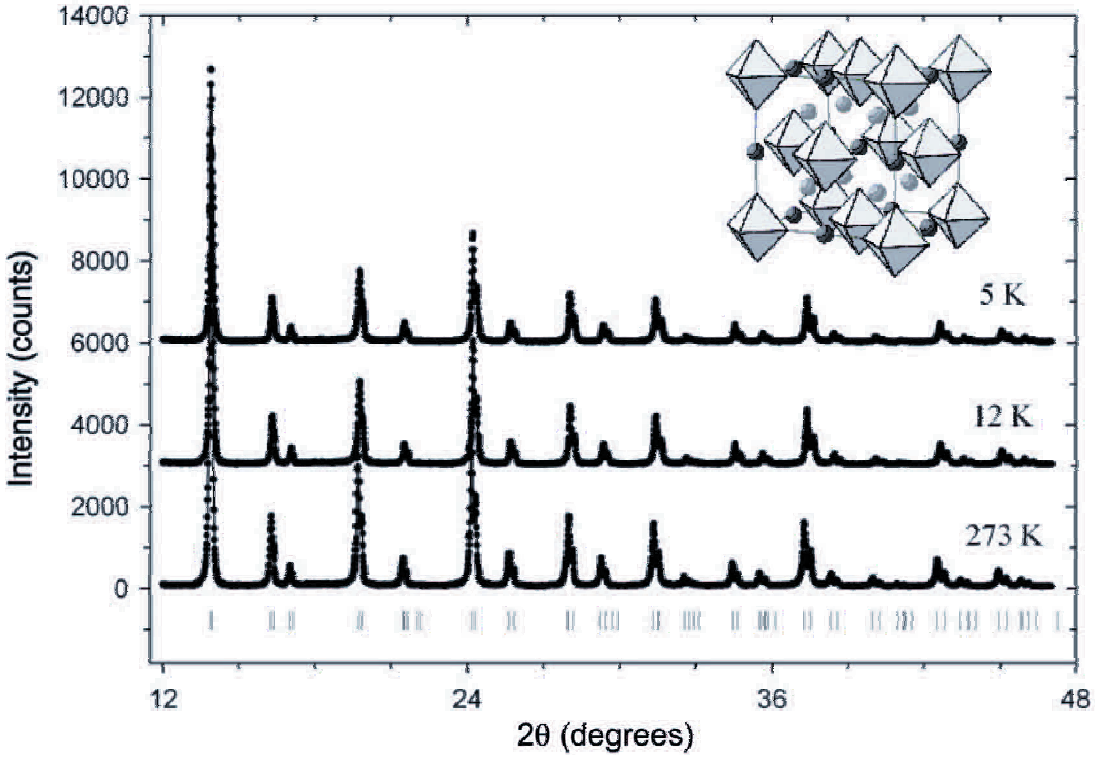

Figure C.1. Observed (dots) and calculated (line) X-ray powder diffraction patterns of Ba_2NaOsO_6 collected at 273, 12, and 5 K. Vertical bars under the observed and calculated diffraction patterns indicate calculated positions of Bragg peaks. The inset depicts the refined crystal structure, showing OsO_6 octahedra, Ba (light gray), and Na (dark gray) atoms.

C.3. Results and Discussion

Black, shiny, single crystals of Ba_2NaOsO_6 up to 2 mm in diameter and with a truncated octahedral morphology were grown from a molten hydroxide flux following a method similar to that presented in Ref. 5. Single crystal X-ray diffraction data were collected at room temperature using both a STOE Image Plate Diffractometer (IPDS II) and a Bruker Smart Apex CCD diffractometer. Data were taken for a crystal with dimensions 0.23 × 0.18 × 0.01 mm^3, and for a smaller piece broken from this larger crystal with dimensions 0.058 × 0.039 × 0.022 mm^3, more closely approximating a sphere. In each case, a large number of reflections were collected (3074 and 2166, respectively), and the structure was refined using the SHELXTL package of crystallographic programs.[14] Refinement to the published fully occupied, stoichiometric $Fm\bar{3}m$ structure[5] consistently gave the lowest R

values (0.0147) against a number of variable parameters, including partial occupancy, mixed site occupancy, and lower space group symmetry. These measurements were repeated at temperatures of 243, 223, 198, and 183 K, with no difference in the refined structures. Additional powder diffraction measurements were taken at temperatures of 273, 30, 12, and 5 K (Figure C.1), using a Rigaku TTRAX powder diffractometer, equipped with a helium-flow cryostat. The structure obtained by Rietveld refinement using the Rietica LHPM software[15] agreed with the single crystal structural refinement at all temperatures. Goodness of fit parameters were constant through the magnetic transition, indicating no discernable change in the crystal structure.

With one electron per osmium site, one might naively expect that Ba_2NaOsO_6 would be a metal. DC resistivity measurements consistently showed insulating behavior, but concern over the quality of the electrical contact to the samples led us to verify this observation by infrared reflectivity. Measurements were carried out using a scanning Fourier transform interferometer with a bolometer detector at 4.2 K, for arbitrary crystal orientations with the sample held at room temperature (Figure C.2). An evaporated Ag film, adjacent to and coplanar with the sample, provided a reference used to obtain absolute reflectivity versus frequency. The data show low overall reflectivity, with no indication of a metallic plasma edge down to the lowest measured frequency of 400 cm^{-1}. The strong variations in the reflectivity between 400 and 1000 cm^{-1} are a signature of unscreened optical phonons. These data suggest that Ba_2NaOsO_6 is a Mott insulator, which is supported by the following tight-binding analysis.

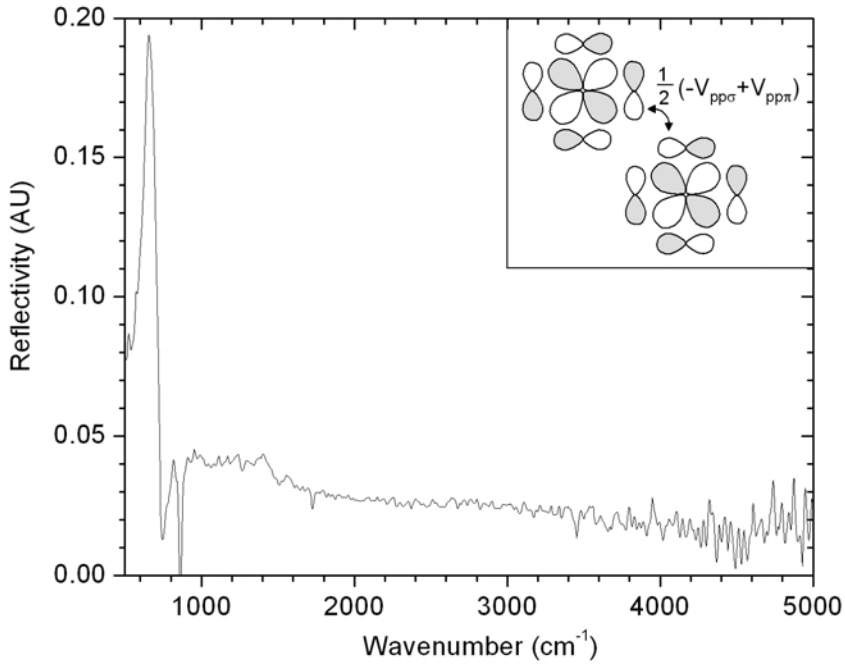

Figure C.2. IR reflectivity data as a function of wave number for Ba_2NaOsO_6. The inset shows coupling between two adjacent OsO_6 orbitals of d_{xy} symmetry for $k = 0$.

The crystal structure of Ba_2NaOsO_6 can be pictured as an fcc lattice of isolated OsO_6 octahedra separated by Ba and Na ions (inset to Figure C.1). The *s* orbitals of Ba and Na are so high in energy that they can be neglected, and the electronic structure is primarily determined by the OsO_6 octahedra, which form the usual set of molecular orbitals. The bonding and nonbonding states are filled, leaving one electron in the triply degenerate t_{2g} antibonding orbitals. Using the known energies for the Os and O orbitals we find that this molecular orbital is at −13.43 eV,[16] relative to E_p (O) = −16.77 eV for oxygen 2*p* states and E_d (Os) = −16.32 eV.[17] Since the Os *d* and O *p* orbitals are close in energy, these molecular orbitals have almost equal 5*d* and 2*p* character.

Adjacent OsO_6 octahedra in Ba_2NaOsO_6 are coupled by the matrix elements $\frac{1}{2}(-V_{pp\sigma} + V_{pp\pi})$ (inset to Figure C.2). Using values obtained for similar cluster separations in other materials,[16] modified appropriately for this particular lattice, and neglecting spin-orbit

coupling, we obtain $t = \frac{1}{4} \times \frac{1}{2}(-V_{pp\sigma} + V_{pp\pi}) \sim 0.05$ eV for the hopping matrix elements coupling adjacent octahedra. In contrast, the Coulomb energy associated with moving one electron from an OsO_6 octahedron to its neighbor is found to be $U \sim 3.3$ eV.[18] More detailed treatments could presumably refine these values, but since we find $U >> t$ it is clear that the material is a Mott insulator and that a local moment description of the magnetism is appropriate.

Magnetization measurements as a function of applied field at 1.8 K (Figure C.3) show ferromagnetic behavior, as previously reported for polycrystalline samples.[5] These data were obtained for applied fields oriented along high-symmetry directions using a Quantum Design Superconducting Quantum Interference Device magnetometer for single crystals weighing between 2 and 7 mg. The magnetization rises rapidly in low fields and levels off for fields above 1 T, beyond which there is no discernable hysterisis. However, the absolute value of the magnetization at this field is relatively small (approximately 0.2 μ_B) and does not appear to saturate in fields of up to 5 T. Extrapolating a linear fit to the magnetization between 3 and 5 T, we obtain a zero-field magnetization of 0.175(2), 0.191(1), and 0.223(1) μ_B for fields oriented along [100], [111], and [110], respectively. This anisotropy is confirmed by angle-dependent measurements at a constant field using a rotating sample holder and rotating in the $(01\bar{1})$ plane, which contains all three high-symmetry directions (inset to Figure C.3).

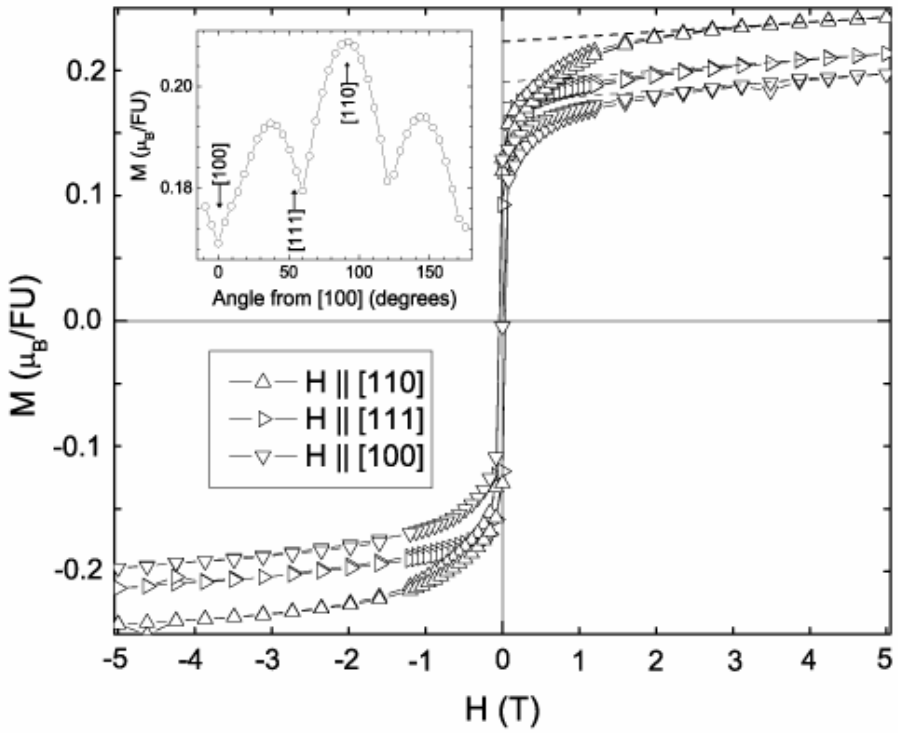

Figure C.3. Magnetization of Ba_2NaOsO_6 along high-symmetry directions as a function of applied field at 1.8 k for a full hysterisis loop. "f.u." refers to one formula unit. The inset shows magnetization as a function of angle in the $(00\bar{1})$ plane at a temperature of 1.8 K and a field of 2 T. A line is drawn between data to guide the eye.

Temperature-dependent magnetization measurements in fields above 1 T, for which there is no hysterisis, show an upturn below approximately 8 K (Figure C.4.), consistent with ferromagnetic behavior. The inverse susceptibility at high temperature shows a moderate amount of curvature [panel (a) of the inset to Figure C.4]. Data between 75 and 200 K can nevertheless be fit by a Curie-Weiss law if a constant offset, nominally attributed to Van Vleck paramagnetism, is included: $\chi = \frac{C}{(T-\theta)} + \chi_0$ [panel (b) of the inset to Figure C.4]. This fit results in relatively small effective moments μ_{eff} of 0.602(4), 0.596(1), and 0.647(3) μ_B for fields oriented in the [100], [111], and [110] directions, respectively, indicative of substantial spin-orbit coupling, and Weiss temperatures of −10(2), −10(1), and −13(1) K. Values

of χ_0 are found to be 3(1) × 10^{-5}, 1.7(1) × 10^{-4}, and 1.76(9) × 10^{-4} emu / mol Oe for fields oriented in these same directions.

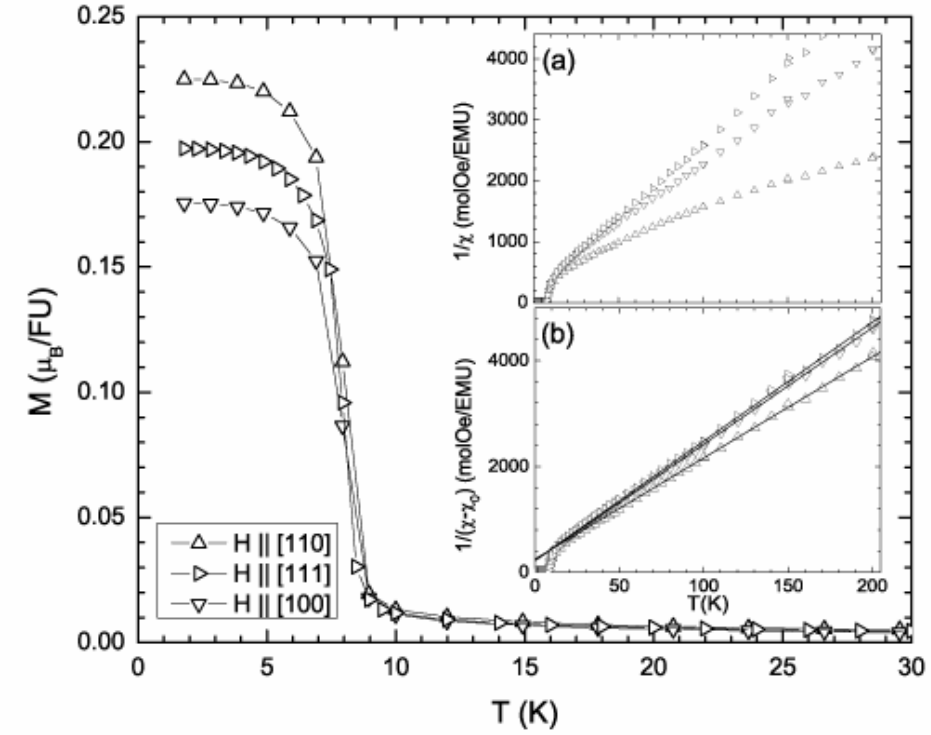

Figure C.4. Low temperature magnetization of Ba_2NaOsO_6 as a function of temperature in a field of 2 T. Insets show (a) inverse susceptibility and (b) the inverse susceptibility with a constant offset χ_0, subtracted. Lines show fits to Curie-Weiss behavior. f.u. refers to one formula unit.

The magnetic phase transition is most clearly seen in the heat capacity (Figure C.5). Data were taken using the relaxation method for 3-4 single crystals weighing a total of 2-3 mg, oriented at arbitrary angles to each other, for temperatures from 0.3 to 300 K. A sharp anomaly is seen with a peak at 6.8(3) K, which defines the critical temperature T_C. The magnetic contribution to the heat capacity was estimated by subtracting a polynomial extrapolation of the higher temperature phonon heat capacity, fit between 14.5 and 18 K [$C_{ph} = 0.065(7)T + 0.00262(6)T^3 - 2.6(1) \times 10^{-6}T^5$, shown in Figure C.5]. Since the magnetic contribution is significantly larger close to T_C, this crude subtraction results in only small

systematic errors. The total magnetic contribution to the entropy S_{mag} through the transition is found to be 4.6 J / mol K (right axis, Figure C.5), falling slightly short (80%) of R ln2 = 5.76 J / mol K. No additional anomalies are observed up to 300 K (inset to Figure C.5).

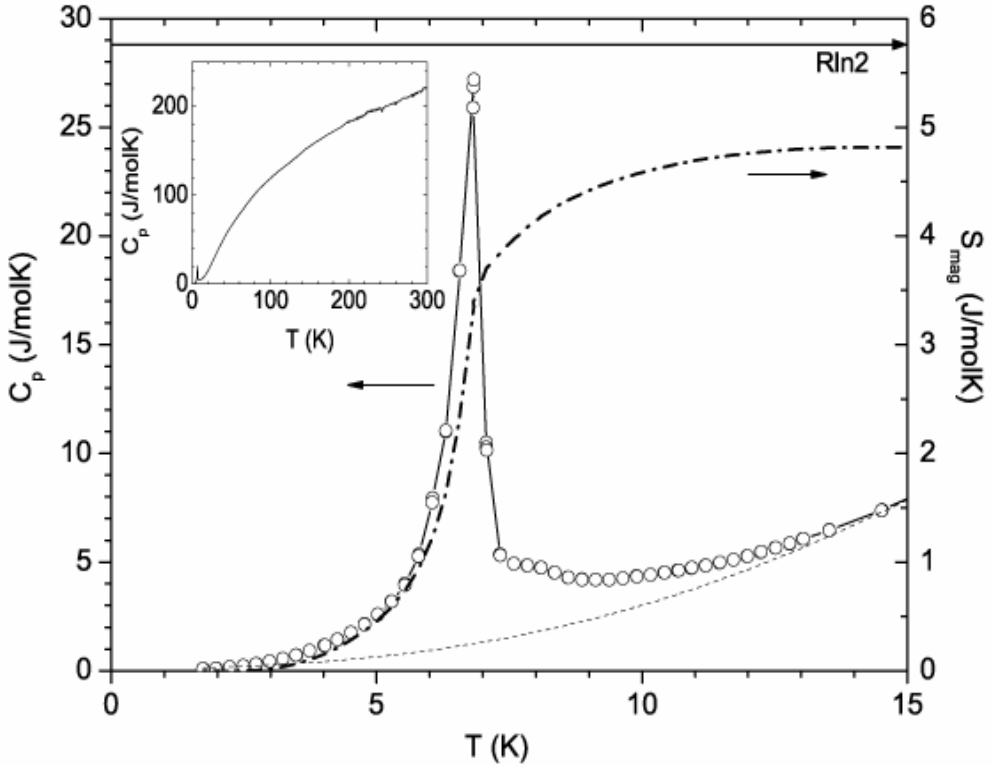

Figure C.5. Heat capacity (left axis) and magnetic contribution to the integrated entropy (right axis) for the magnetic transition in Ba_2NaOsO_6. The dashed line (left axis) shows an extrapolation of a fit to the phonon background, the solid horizontal line (right axis) indicates the theoretical entropy of R ln2 for a doublet ground state. The inset shows the heat capacity to 300 K. The upper axis shows the Dulong-Petite value of 249 J / mol K.

The triply degenerate t_{2g} orbitals of OsO_6 octahedra in the undistorted Ba_2NaOsO_6 crystal structure constitute an effective unquenched angular momentum **L** = 1. The matrix elements of the orbital angular momentum operator **L** within the t_{2g} manifold are the same as those of −**L** within states of P symmetry.[19] Application of spin-orbit coupling therefore results in a quartet ground state $J = \frac{3}{2}$ and a doublet excited state $J = \frac{1}{2}$.[19-21] Since the

integrated entropy through the magnetic phase transition is ~ R ln2, we can surmise that the quartet must be split into two Kramers doublets at a temperature $T_t > T_C$.

Xiang and Whangbo have recently suggested that both the insulating behavior and the ferromagnetism in Ba_2NaOsO_6 can be attributed to the combined effect of electron correlation and spin-orbit coupling.[22] However, the authors were unable to account for the magnitude of the saturated moment, the observed anisotropy, or the negative Weiss temperature. Furthermore, their assumption that the exchange energy is substantially larger than the spin-orbit coupling is not justified in light of the small value of T_C. These factors all indicate that a different mechanism is responsible for the ferromagnetism in this material.

The quartet ground state in Ba_2NaOsO_6 anticipated from consideration of the spin-orbit coupling is unstable to a Jahn-Teller distortion. Our observation of a doublet ground state certainly indicates that the anticipated degeneracy has been lifted, while the absence of any additional features in the heat capacity implies that $T_t > 300$ K. That this does not reveal itself in x-ray diffraction presumably reflects both the extremely subtle nature of the associated distortions (since the t_{2g} orbitals are not elongated along the bond directions they couple more weakly to the oxygen ligands than do e_g orbitals) and also the weak scattering power of the coordinating oxygen ions. The relative orientation of Os orbitals on adjacent sites will have a profound effect on the magnetically ordered state, via both the magnetic anisotropy and the superexchange,[23] which was not considered in the previous calculations. The small negative Weiss temperature deduced from susceptibility measurements clearly indicates that Ba_2NaOsO_6 is not a simple ferromagnet but rather has a nontrivial magnetic structure, which can then be understood in terms of an orbitally ordered state with a nonzero ordering wave vector.

If a scenario in which orbital order drives the ferromagnetism in Ba_2NaOsO_6 is indeed appropriate, then the fact that the isostructural, isoelectronic analog Ba_2LiOsO_6 is found to be antiferromagnetic[5] indicates that the factors determining the orbital order in these two compounds are remarkably finely balanced. It is intriguing to think that a similarly complex interplay between spin and orbital degrees of freedom might be present in these $5d^1$ Mott insulators as in their better-studied 3*d* analogs, for which spin-orbit coupling has a

much weaker effect. Resonant x-ray scattering experiments are in progress to directly address this possibility.

C.4. Acknowledgements

The authors thank R. M. White, Z. Islam, D. Mandrus, and A. Sleight for useful conversations. This work is supported by the DOE, Office of Basic Energy Sciences, under Contract No. DE-AC02-76SF00515, and the NSF under Grants No. DMR-0134613 and No. DMR-0554796. The authors would also like to thank Professor V. K. Pecharsky and Dr. Y. Mudryk for using their Rigaku PXRD. A part of this work was carried out at the Ames Laboratory, which is operated for the U. S. Department of Energy by Iowa State University under Contract No. W-7405-ENG-82.

C.5. References

(1) Greedan, J. E.; et al., *Inorg. Chem.* **1968**, *7*, 2461.

(2) Belova, V. I.; Syrkin, Y. K., *Zh. Neorg. Khim.* **1958**, *3*, 2016.

(3) Chamberland, K. L., *Mater. Res. Bull.* **1978**, *13*, 1273.

(4) Gemmill, W. R.; et al., *Inorg. Chem.* **2005,** *44*, 2639.

(5) Stitzer, K. E.; et al., *Solid State Sci.* **2002,** *4*, 311.

(6) Sleight, A.W.; et al., *Inorg. Chem.* **1962,** *1*, 245.

(7) Stitzer, K. E.; et al., *Inorg. Chem.* **2003,** *42*, 947.

(8) Brooks, M. L.; et al., *Phys. Rev. B* **2005,** *71*, 220411.

(9) Crawford, M. K.; et al., *Phys. Rev. B* **1994,** *49*, 9198.

(10) Cao, G.; et al., *Phys. Rev. B* **1998,** *57*, R11 039.

(11) Cao, G.; et al., *Phys. Rev. B* **2002,** *66*, 214412.

(12) The tolerance factor calculated from ionic radii = 0.99, indicating that the structure is very stable.

(13) Moriya, T., in *Magnetism*, edited by Rado, G. T.; Suhl, H., Academic: New York, **1963**, *Vol. 1*, 85.

(14) *XRD Single Crystal Software*; Bruker Analytical X-ray Systems, Madison, WI, USA, **2002**.

(15) Hunter, B. A., *International Union of Crystallography Commission on Powder Diffraction Newsletter*, **1998**, *20*, 21.

(16) Harrison, W. A., *Elementary Electronic Structure*, World Scientific, Singapore, **2004**.

(17) The bare value for Os is − 13.74 eV.[16] Charge transfer between Os and O results in a shift in energy which can be calculated in a self-consistent manner. The shift in energy in E_d(Os) is given by $\Delta E = U_d \Delta Z_d$, with U_d = 3.4 eV[16] and ΔZ_d = 0.76, from which E_d(Os) = − 13.74 − (3.4 × 0.76) = − 16.32 eV.

(18) Since the Os d orbitals are much smaller than the 4-atom O *p*-orbital cluster associated with one t_{2g} molecular orbital, the dominant contributions to U will come from the Os site. The antibonding orbital has only a weak polarization, characterized by α_P = 0.067,[16] such that roughly half of the charge resides in the Os *d*-orbital and half in the 4-atom O *p*-orbital cluster. U will therefore contain contributions from the self-energy of the two half electrons on the Os site, ¼ U_d, the Coulomb repulsion between the Os ½ e^- and the ½ e^- in the *p*-orbital cluster a distance d away, ¼ e^2 / d, and the Coulomb attraction between the Os ½ e^- and the positive charge on the electron-deficient neighbor a distance r away, ½ e^2 / r, where r ~ 2√2d. The resulting total contribution U = ¼ U_d + ¼ e^2 / d + ½ e^2 / r = 3.32 eV.

(19) Goodenough, J. B., *Phys. Rev.* **1968**, *171*, 466.

(20) Stevens, K.W. H., *Proc. R. Soc. A* 1953, *219*, 542.

(21) Ishihara, S., in *Physics of Transition Metal Oxides*, Springer Series in *Solid State Sciences, Vol. 144*, Springer, New York, **2004**.

(22) Xiang, H. J.; Whangbo, M.-H., *Phys. Rev. B* **2007,** *75*, 052407.

(23) Kugel, K. I.; Khomskii, D. I., *Sov. Phys. JETP* **1973**, *37*, 725.

Table C.1. Reaction composition and product identification.

Sample Code	Reaction Stoichiometry	Heating Methods	Reaction Products	Analysis
SM111	Gd_5InGe_3	Arc melting	Sm_5Ge_4-type	SXRD
SM112	$Gd_5In_2Ge_2$		Sm_5Ge_4-type	
SM113	Gd_5In_3Ge		Tetragonal cell: a = 11.7406 c = 15.3533; Incomplete structure solution	
SM321	Gd_5AlGe_3	Arc melting	The reaction failed as everything did not melt properly	
SM322	$Gd_5Al_2Ge_2$			
SM323	Gd_5Al_3Ge			
SM741	Gd_5SbGe_3	Arc melting	Sm_5Ge_4-type	PXRD
SM742	$Gd_5Sb_2Ge_2$		Mn_5Si_3-type	SXRD
SM743	$Gd_5Sb_{2.05}Ge_2$		Gd_2Ge_3-type	
SM951	Gd_5InSi_3	Arc melting	Could not find good quality single crystals	
SM952	$Gd_5In_2Si_2$			
SM953	Gd_5In_3Si			
SM1161	Gd_5AlSi_3	Arc melting	The reaction failed as everything did not melt properly	
SM1162	$Gd_5Al_2Si_3$			
SM1163	Gd_5Al_3Si			
SM1371	$Gd_5Si_{2.4}Ge_{1.6}$	Arc melting	Gd_5Si_4-type	PXRD, SXRD

Table C.1. (continued)

Sample Code	Reaction Stoichiometry	Heating Methods	Reaction Products	Analysis
SM1372	$Gd_5Si_{2.8}Ge_{1.2}$			
SM1373	$Gd_5Si_{3.2}Ge_{0.8}$	Arc melting	Gd_5Si_4-type	PXRD, SXRD
SM1374	$Gd_5Si_{3.6}Ge_{0.8}$			
SM1581	Gd_4YSi_4			
SM1582	$Gd_3Y_2Si_4$			
SM1583	$Gd_2Y_3Si_4$	Arc melting	Gd_5Si_4-type	PXRD, SXRD
SM1584	GdY_4Si_4			
SM1585	$Gd_2Y_3Si_4$			
SM1791	Gd_4YGe_4		Sm_5Ge_4-type	
SM1792	$Gd_3Y_2Ge_4$		Sm_5Ge_4-type	
SM1793	$Gd_2Y_3Ge_4$		Sm_5Ge_4-type	
SM1794	GdY_4Ge_4		$U_2Mo_3Si_4$-type, Sm_5Ge_4-type	PXRD, SXRD, SEM-EDS
SM1795	GdY_4Ge_4	Arc melting	$U_2Mo_3Si_4$-type, Sm_5Ge_4-type	
SM19101	$Gd_{1.2}Y_{3.8}Ge_4$		$U_2Mo_3Si_4$-type, Sm_5Ge_4-type	
SM19102	$Gd_{1.4}Y_{3.6}Ge_4$		$U_2Mo_3Si_4$-type, Sm_5Ge_4-type	
SM19103	$Gd_{1.6}Y_{3.4}Ge_4$		Sm_5Ge_4-type, $U_2Mo_3Si_4$-type	
SM19104	$Gd_{1.8}Y_{3.2}Ge_4$		Sm_5Ge_4-type, $U_2Mo_3Si_4$-type	
SM21111	Y_5Ge_4	Arc melting	Sm_5Ge_4-type	PXRD, SXRD

Table C.1. (continued)

Sample Code	Reaction Stoichiometry	Heating Methods	Reaction Products	Analysis
SM21112	Y_5Si_4	Arc melting	Sm_5Ge_4-type	PXRD, SXRD
SM23121	Gd_4ZrSi_4	Arc melting	Gd_5Si_4-type	PXRD
SM23122	$Gd_3Zr_2Si_4$			
SM23123	$Gd_2Zr_3Si_4$			
SM23124	$GdZr_4Si_4$			
SM25131	Gd_4ZrGe_4	Arc melting	Sm_5Ge_4-type	PXRD
SM25132	$Gd_3Zr_2Ge_4$			
SM25133	$Gd_2Zr_3Ge_4$			
SM25134	$GdZr_4Ge_4$			
SM27141	$Gd_{0.8}Y_{4.2}Ge_4$	Arc melting	$U_2Mo_3Si_4$-type, Sm_5Ge_4-type	PXRD, SXRD, SEM-EDS
SM27142	$Gd_{0.6}Y_{4.4}Ge_4$		Sm_5Ge_4-type, $U_2Mo_3Si_4$-type	
SM27143	$Gd_{0.4}Y_{4.6}Ge_4$		Sm_5Ge_4-type	
SM27144	$Gd_{0.2}Y_{4.8}Ge_4$		Sm_5Ge_4-type	
SM29151	Nd_4ErSi_4	Arc melting	Zr_5Si_4-type	PXRD, SXRD
SM29152	$Nd_3Er_2Si_4$		Gd_5Si_4-type, Zr_5Si_4-type	
SM29153	$Nd_2Er_3Si_4$		Gd_5Si_4-type, Zr_5Si_4-type	
SM29154	$NdEr_4Si_4$		Gd_5Si_4-type	
SM31161	Nd_4ErGe_4	Arc melting	Sm_5Ge_4-type	PXRD, SXRD
SM31162	$Nd_3Er_2Ge_4$		Sm_5Ge_4-type	

Table C.1. (continued)

Sample Code	Reaction Stoichiometry	Heating Methods	Reaction Products	Analysis
SM31163	$Nd_2Er_3Ge_4$	Arc melting	Sm_5Ge_4-type, $U_2Mo_3Si_4$-type	PXRD, SXRD
SM31164	$NdEr_4Ge_4$		$U_2Mo_3Si_4$-type	
SM33171	$Nd_{1.2}Er_{3.8}Ge_4$		Sm_5Ge_4-type, $U_2Mo_3Si_4$-type	PXRD
SM33172	$Nd_{1.4}Er_{3.6}Ge_4$		$U_2Mo_3Si_4$-type	PXRD, SXRD
SM33173	$Nd_{1.6}Er_{3.4}Ge_4$	Arc melting	$U_2Mo_3Si_4$-type	PXRD
SM33174	$Nd_{1.8}Er_{3.2}Ge_4$		$U_2Mo_3Si_4$-type	PXRD, SXRD
SM33175	$Nd_{1.2}Er_{3.8}Ge_4$		Sm_5Ge_4-type, $U_2Mo_3Si_4$-type	PXRD
SM35181	Nd_4HoGe_4			
SM35182	$Nd_3Ho_2Ge_4$	Arc melting	Sm_5Ge_4-type	PXRD
SM35183	$Nd_2Ho_3Ge_4$			
SM35184	$NdHo_4Ge_4$			
SM37191	$Gd_4YbSiGe_3$			
SM37192	$Gd_3Yb_2SiGe_3$	Tube furnace fitted		
SM37193	$Gd_2Yb_3SiGe_3$	with a flow tube	Reaction failed as the Ta-tubes were oxidized	
SM37194	$GdYb_4SiGe_3$	under argon		
SM37195	Yb_5SiGe_3			
SM37196	$Gd_3Yb_2SiGe_3$	Induction Furnace	Gd_5Si_4-type	SXRD
SM39201	Gd_5GaSn_3	Arc melting	Mn_5Si_3-type	PXRD
SM39202	$Gd_5Ga_2Sn_2$		Could not find good quality single crystals	

Table C.1. (continued)

Sample Code	Reaction Stoichiometry	Heating Methods	Reaction Products	Analysis
SM39203	Gd_5Ga_3Sn	Arc melting	Could not find good quality single crystals	
SM41211	Gd_5GeSn_3	Arc melting	Sm_5Ge_4-type	PXRD, SXRD
SM41212	$Gd_5Ge_2Sn_2$			
SM41213	Gd_5Ge_3Sn			
SM43221	Gd_5GaSb_3	Arc melting	Could not find good quality single crystals	
SM43222	$Gd_5Ga_2Sb_2$		P_4Th_3-type	SXRD
SM43223	Gd_5Ga_3Sb		P_4Th_3-type	
SM45231	Gd_5GaGe_3	Arc melting	Pu_5Rh_4-type	HT & LT-PXRD, HT&LT-SXRD
SM45232	$Gd_5Ga_{0.5}Ge_{3.5}$		Sm_5Ge_4-type	
SM45233	Gd_5GaGe_3		Pu_5Rh_4-type	
SM45234	$Gd_5Ga_2Ge_2$		Gd_5Si_4-type	
SM45235	Gd_5GaGe_3		Pu_5Rh_4-type	
SM47241	Gd_5Si_4	Arc melting	Gd_5Si_4-type	SXRD
SM49251	Tb_5Ge_4	Arc melting	Sm_5Ge_4-type	SXRD
SM49252	$Tb_5Si_{0.44}Ge_{3.56}$		Sm_5Ge_4-type	
SM49253	$Tb_5Si_{1.84}Ge_{2.16}$		$Gd_5Si_2Ge_2$-type	
SM49254	$Tb_5Si_{2.40}Ge_{1.60}$		$Gd_5Si_2Ge_2$-type	
SM49255	$Tb_5Si_{3.20}Ge_{0.80}$		Gd_5Si_4-type	
SM49256	Tb_5Si_4		Gd_5Si_4-type	

Table C.1. (continued)

Sample Code	Reaction Stoichiometry	Heating Methods	Reaction Products	Analysis
SM51261	Dy_5Ge_4	Arc melting	Sm_5Ge_4-type	SXRD
SM51262	$Dy_5Si_{0.44}Ge_{3.56}$		Sm_5Ge_4-type	
SM51263	$Dy_5Si_{1.84}Ge_{2.16}$		Sm_5Ge_4-type	
SM51264	$Dy_5Si_{2.40}Ge_{1.60}$		Sm_5Ge_4-type	
SM51265	$Dy_5Si_{3.20}Ge_{0.80}$		$Gd_5Si_2Ge_2$-type	
SM51266	Dy_5Si_4		Gd_5Si_4-type	
SM53271	$Gd_5Ga_{0.5}Ge_{3.5}$	Arc melting	Sm_5Ge_4-type	HT & LT-PXRD, HT&LT-SXRD
SM53272	Gd_5GaGe_3		Pu_5Rh_4-type	
SM53273	$Gd_5Ga_{0.5}Ge_{3.5}$		Sm_5Ge_4-type	
SM55281	$Gd_5Zn_{0.5}Ge_{3.5}$	Induction Furnace	Mn_5Si_3-type	PXRD, SXRD
SM55282	Gd_5ZnGe_3	Induction Furnace	Mn_5Si_3-type	SXRD
SM55283	$Gd_5Zn_2Ge_2$	Induction Furnace	Could not find good quality single crystals	
SM55284	Gd_5Zn_3Ge	Induction Furnace		
SM55285	$Gd_5Zn_{3.5}Ge_{0.5}$	Induction Furnace		
SM57291	$Tb_5Ga_{0.5}Ge_{3.5}$	Arc melting	Sm_5Ge_4-type	SXRD
SM57292	Tb_5GaGe_3		Sm_5Ge_4-type	
SM57293	$Tb_5Ga_2Ge_2$		Gd_5Si_4-type	
SM57294	Tb_5Ga_3Ge	Not analyzed		
SM57295	$Tb_5Ga_{3.5}Ge_{0.5}$			

Table C.1. (continued)

Sample Code	Reaction Stoichiometry	Heating Methods	Reaction Products	Analysis
SM59301	$NdEr_4SiGe_3$	Arc melting	Sm_5Ge_4-type	PXRD, SXRD
SM59302	$NdEr_4Si_2Ge_2$		Sm_5Ge_4-type	
SM59303	$Nd_2Er_3SiGe_3$		Sm_5Ge_4-type	
SM59304	$Nd_2Er_3Si_2Ge_2$		$Gd_5Si_2Ge_2$-type	
SM59305	$Nd_3Er_2SiGe_3$		$Gd_5Si_2Ge_2$-type	
SM59306	$Nd_3Er_2Si_2Ge_2$		$Gd_5Si_2Ge_2$-type	
SM59307	$Nd_4ErSiGe_3$		$Gd_5Si_2Ge_2$-type	
SM59308	$Nd_4ErSi_2Ge_2$		Gd_5Si_4-type	
SM61311	Gd_5Si_3Ge	Arc melting	Gd_5Si_4-type	SXRD
SM63321	$NdEr_4Si_3Ge$	Arc melting	Gd_5Si_4-type	SXRD
SM63322	$Nd_2Er_3Si_3Ge$			
SM63323	$Nd_3Er_2Si_3Ge$			
SM63324	Nd_4ErSi_3Ge			
SM71363	Y_5Ge_4	Arc melting	Sm_5Ge_4-type	PXRD, SXRD
SM75381	$Gd_{2.5}Sc_{2.5}Ge_4$	Arc melting	Not analyzed	PXRD, SXRD
SM75382	$Gd_2Sc_3Ge_4$		Pu_5Rh_4-type	
SM75383	$Gd_{1.5}Sc_{3.5}Ge_4$		Not analyzed	

CURRICULUM [redacted]

NAME OF AUTHOR: Sumohan Misra

[redacted]

DEGREES AWARDED:

- Ph. D., Inorganic Chemistry, Iowa State University, Ames, IA, USA, 2008.
- M.S., Inorganic Chemistry, Michigan State University, East Lansing, MI, USA, 2004.
- B.S., Chemistry *with Honors*, St. Stephen's College, University of Delhi, India, 2000.

HONORS AND REWARDS:

- Iowa State University Research Excellence Award, 2008.
- Nominated to the Sigma Xi, The Scientific Research Society, 2007.
- Arthur P. Hellwig Memorial Endowment Award, Department of Chemistry, Iowa State University, 2005.

PROFESSIONAL EXPERIENCE:

- Research Assistant, Ames Laboratory, Iowa State University, 2005–2008.
- Teaching Assistant, Iowa State University, 2004–2005.
- Research Assistant, Michigan State University, 2003–2004.
- Teaching Assistant, Michigan State University, 2002–2003.

PROFESSIONAL PUBLICATIONS:

- *Controlling Magnetism of a Complex Metallic System via Predicted Atomic Replacements*. Mudryk, Y.; Paudyal, D.; Pecharsky, V. K.; Gschneidner, K. A. Jr.; Misra, S.; Miller, G. J., *Adv. Mater.* **2008**, submitted.
- *On the Crystal Structure, Metal Atom Site Preferences, and Magnetic Properties of* $Nd_{5-x}Er_xTt_4$ *alloys (Tt = Si, Ge*). Misra, S.; Poweleit, E.; Miller, G. J., *Z. Anorg. Allg. Chem*. **2008**, submitted.
- $Gd_{5-x}Y_xTt_4$ *(Tt = Si, Ge): Effect of Metal Substitution on Structure, Bonding, and Magnetism.* Misra, S.; Miller, G. J., *J. Am. Chem. Soc*. **2008**, *130*, 13900–13911.
- *Magnetic Phase Diagram of* Ce_2Fe_{17}. Janssen, Y.; Chang, S.; Kreyssig, A.; Kracher, A.; Mozharivskyj, Y.; Misra, S.; Canfield, P. C., *Phys. Rev. B* **2007**, *76*, 054420.
- *Ferromagnetism in the Mott Insulator* Ba_2NaOsO_6. Erickson, A. S.; Misra, S.; Miller, G. J.; Gupta, R. R.; Schlesinger, Z.; Harrison, W. A.; Kim, J. M.; Fisher, I. R., *Phys. Rev. Lett*. **2007**, *99*, 016404.
- *On the Distribution of Tetrelide Atoms (Si, Ge) in* $Gd_5(Si_xGe_{1-x})_4$. Misra, S.; Miller, G. J., *J. Solid State Chem*. **2006**, *179*, 2290–2297.